Growth mechanisms of $CuInS_2$ formed by the sulfurization of thin metallic films

vorgelegt von
Diplom-Ingenieur
Humberto Rodriguez Alvarez
aus Bogotá, Kolumbien

Von der Fakultät III-Prozesswissenschaften
der Technischen Universität Berlin
zur Erlangung des akademischen Grades
Doktor der Ingenieurwissenschaften
-Dr.-Ing.-

genehmigte Dissertation

Promotionsausschuss:

Vorsitzende: Prof. Dr.-Ing. C. Fleck
Gutachter: Prof. Dr. rer. nat. W. Reimers
Gutachter: Prof. Dr.-Ing. H.-W. Schock

Tag der wissenschaftlichen Aussprache: 15.02.2010

Berlin 2010
D 83

Zusammenfassung

Gegenstand dieser Arbeit ist das Wachstum von dünnen $CuInS_2$-Schichten mittels eines schnellen thermischen Syntheseprozesses. $CuInS_2$ dient als absorbierende Schicht in Dünnschichtsolarzellen. Die Herstellung erfolgt durch eine Sulfurisierung von Cu und In Vorläuferschichten. Dieses Verfahren stellt eine kostengünstigere und ertragreichere Möglichkeit zu anderen Herstellungstechnologien dar und wird, dank iterativer Optimierung der resultierenden Solarzellen, in der großflächigen Massenherstellung von Solarmodulen benutzt. Die Mikrostrukturentwicklung während eines solchen Herstellungsverfahrens ist bisher allerdings unbekannt. Dieses Wissen ist notwendig für die weitere Optimierung und für die zukünftige Gestaltung neuartiger Prozesse.

Diese Dissertation liefert zwei Beiträge zur Sulfurisierungstechnologie. Erstens zeigt sie eine *in situ* Methode zur Überwachung der Dünnschichtmikrostruktur während Festkörperumwandlungen und Reaktionen mit einer Gasphase. Diese Methode basiert auf der energiedispersiven Röntgenbeugung. Sie eignet sich sowohl für die Untersuchung von isolierten Festkörpermechanismen als auch für die Analyse von kompletten schnellen thermischen Sulfurisierungen. Zweitens schlägt die Arbeit eine Zerlegung des komplizierten Sulfurisierungsprozesses in fünf unabhängige Wachstumsmechanismen vor. Die Analyse von deren Interaktion erlaubt eine nachvollziehbare Beschreibung der Mikrostrukturbildung in Abhängigkeit von den Prozesseinflussgrößen. Die Wachstumsmechanismen sind: 1) die Bildung einer Metalllegierung, 2) die Sulfurisierung einer Metalllegierung, 3) die Reaktion zwischen den Sulfiden, 4) die Rekristallisation der Dünnschicht und, 5) die Interdiffusion der Sulfide.

Jeder Mechanismus wirkt sich anders auf die Schichtmikrostruktur aus und wird in dieser Dissertation *in situ* und mit anderen Charakterisierungsmethoden untersucht. Der erste Schwerpunkt der Untersuchungen betrifft die Bildung von Schichtsytemen während der Sulfurisierung einer $Cu_{16}In_9$-Legierung. Die Temperatur und der Schwefeldruck bestimmen sowohl die Sulfidschichtreihenfolge als auch deren Morphologie. Als Zweites studiert diese Arbeit die Kinetik der Reaktion zwischen $Cu_{2-x}S$ und $CuIn_5S_8$ Dünnschichten. Diese Reaktion verbraucht die Fremdphase $CuIn_5S_8$, die zusammen mit der Hauptphase $CuInS_2$ koexistieren kann. Die Rekristallisation der Dünnschicht ist das dritte Schwerpunktthema. Dieser Mechanismus bewirkt strukturell defektarme Körner, die eine Größe von einigen Mikrometern im Durchmesser aufweisen. In diesen Körnern befinden sich die Kupfer- und Indiumkationen in der Chalkopyritordnung. Die Rekristallisation von $CuInS_2$-Schichten wurde das erste Mal *in situ* beobachtet. Diese Arbeit schlägt ein Modell zur Beschreibung dieses Mechanismus vor.

Die neue *in situ* Methode erlaubt die Erforschung schneller thermischer Sulfurisierungen. Anhand der untersuchten Wachstumsmechanismen kann die Mikrostrukturbildung der $CuInS_2$-Schicht erklärt werden. Die vorgeschlagenen Pfade zur Kontrolle aller Mechanismen unterstützen die Weiterentwicklung der Sulfurisierungstechnologie und ermöglichen die Entstehung von neuartigen Herstellungsprozessen.

Abstract

The focus of this thesis is the growth of $CuInS_2$ films from a rapid thermal sulfurization process. This material is used as the absorber layer in thin-film solar cells. The rapid thermal sulfurization of thin Cu-In films is a technology that represents a low cost alternative to other chalcopyrite thin-film fabrication technologies. This technology has evolved to industrial maturity thanks to the optimization of the resulting solar cell devices. However, the knowledge concerning the formation of the film microstructure during this kind of processing is scarce. This knowledge is necessary for further optimization and future process design.

This thesis makes two contributions to the sulfurization technology. First, it presents an experimental method to monitor in real-time the microstructural changes of a thin-film during solid-solid or solid-gas reactions. This *in situ* method was developed on the basis of the energy-dispersive X-ray diffraction. It is used to follow and quantify isolated solid state mechanisms and complete rapid thermal sulfurizations. Second, it divides the sulfurization process into five independent growth mechanisms. The microstructure formation can be clarified by the analysis of their interaction. The mechanisms are: 1) the alloying of the metals, 2) the sulfurization of the metallic alloy, 3) the reaction of the sulfides, 4) the thin-film recrystallization and 5) the sulfide interdiffusion.

These growth mechanisms are investigated by means of the *in situ* and complementary characterization methods. The experimental results reveal the impact that each mechanism has on the film microstructure. Detailed attention is firstly given to the sulfide layered stack formation during the sulfurization of a $Cu_{16}In_9$ alloy. The layer sequence and the morphology are functions of the temperature and the sulfur pressure. The second focus concerns the kinetics of the reaction between $CuIn_5S_8$ and $Cu_{2-x}S$. This reaction consumes the secondary $CuIn_5S_8$ phase that may segregate during sulfurization. The thin-film recrystallization is the third central point of these investigations. This mechanism ensures grain sizes of the order of the thickness of the films, low structural defect densities and the chalcopyrite ordering of the Cu and In cations. This mechanism is monitored *in situ* for the first time. A model is presented that describes the thin-film recrystallization together with its prerequisites and enhancement factors.

The rapid thermal sulfurization of thin metallic Cu-In films is investigated by means of the *in situ* method developed in this thesis. The investigations concentrate on the growth mechanisms during the formation of the $CuInS_2$ films. The impact of each mechanism on the film microstructure is exemplified. Paths to control the growth mechanisms are proposed. These paths support the further development of the sulfurization technology and enable the design of innovative fabrication processes.

Contents

1. Introduction and motivations

The concentration of CO_2 in the earth's atmosphere has oscillated between 180 ppm and 280 ppm during the last 400,000 years[97]. Under the highly optimistic scenario that the CO_2 emissions are reduced to zero by 2050, its concentration will achieve 350 ppm by that date[74]. Other optimistic scenarios estimate that it will stabilize at 550-750 ppm. This CO_2 enrichment generated by men will have dramatic environmental consequences.

Knowing this, the use of carbon-free energy to satisfy our growing needs is unavoidable. The sun provides the earth in one hour with the amount of energy that is consumed by the humans in one year. One way to convert the energy of the sun directly into electrical power is photovoltaics. Chapin *et al.* presented in 1954 one of the first solar cell devices capable of converting solar light into electricity[25]. These devices were based on silicon. Meanwhile, other materials have emerged as an alternative to silicon due to their higher absorption coefficients[111]. This means that less material is necessary to absorb the same amount of light and results in material savings on one hand and in a reduction of the fabrication costs on the other. These materials are deposited as films of some micrometers of thickness. This thin-film approach offers a large cost-reduction potential for the production of photovoltaic modules.

One example of this approach is the $CuInS_2$-based module production[82]. High-yield and low production costs are at the basis of this technology. A key step in this fabrication technology is the formation of the $CuInS_2$ absorber-film from metallic precursors. This is done by means of a rapid thermal process (RTP) where the Cu-In thin films are brought to reaction with elementary sulfur vapor. The thin-film formation during such a process has long been looked at as a black box. The film microstructure has mainly been evaluated through the characteristics of the resulting solar cells or even solar modules. Even though this efficiency-oriented approach has brought the material to a competitive level, it does not allow a critical assessment of the processing itself. This, in contrast, is of clear importance to increase the reproducibility, to optimize the existent and to design new fabrication processes.

Figure 1.1 presents an idealized $CuInS_2$ absorber with few microstructural defects and a typical $CuInS_2$ absorber when fabricated by means of RTP. The RTP-$CuInS_2$ film presents defects in its microstructure that affect the performance of the film as a solar cell absorber. For further development of this technology it is necessary to:

1. Understand the formation of the microstructure;
2. Lay the ground for the engineering of the film.

These two points constitute the main objectives of this thesis. To attain these objectives two tools were developed and will be presented throughout the following chapters:

- An experimental method based on the energy-dispersive X-ray diffraction[41]. This method allows to monitor *in situ* the microstructural changes of a thin film as a function of time, temperature and pressure. Complete sulfurizations or isolated solid state transitions can be investigated by this method.
- A breakdown of the complex sulfurization process in independent mechanisms. Each mechanism can be studied individually in terms of its origin and impact on the microstructure

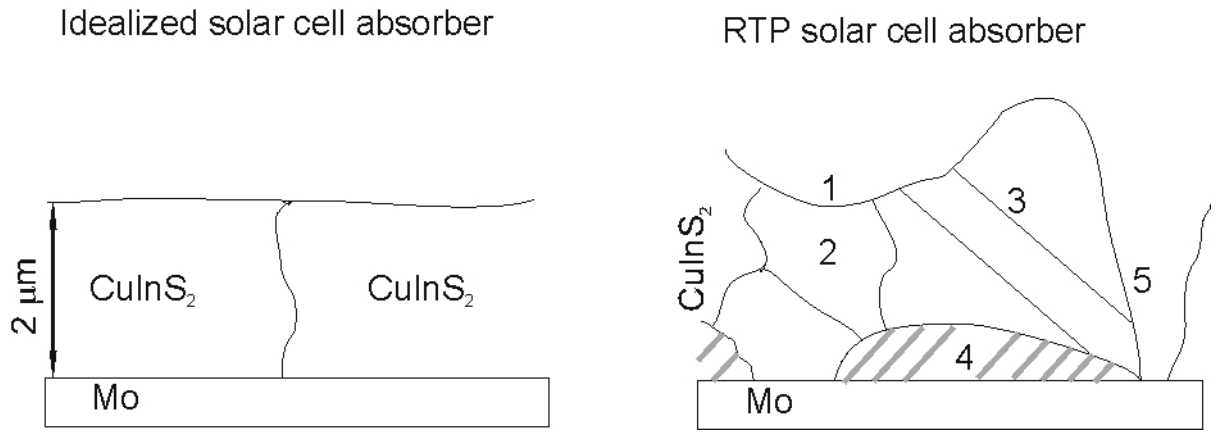

Figure 1.1.: Idealized and typical RTP-$CuInS_2$ thin films[120]. The numbers indicate the microstructural features that affect the performance of the film as a solar cell absorber: 1) surface, 2) point defect concentration and gradient, 3) grain boundaries and other planar and linear defects, 4) voids at the back contact, 5) pinholes that traverse the entire film.

of the resulting $CuInS_2$ thin film.

The investigations on these growth mechanisms by means of the *in situ* method are the pillars of this work. This thesis is structured as follows:

- Chapter 2 begins with an introduction to the $CuInS_2$-based solar cell. The following sections review the main structural, physical, chemical and microstructural features of $CuInS_2$ thin films. The chapter ends with a description of the rapid thermal processing technology to fabricate such films.
- Chapter 3 presents the experimental method that was developed and optimized during this thesis. This method consists of a custom-made rapid thermal processing chamber coupled to a synchrotron-based energy-dispersive X-ray diffraction setup. The theory, the technology, the possibilities and resolution limits of this method will be presented in this section. This experimental setup is currently unique in its ability to monitor rapid thermal chalcogenizations.
- Chapter 4 presents the breakdown of the sulfurization process in five growth mechanisms: the alloying of the metals, the sulfurization of the metallic alloy, the reaction of the sulfides, the thin-film recrystallization and the sulfide interdiffusion. This chapter reviews in five sections the theory and the results reported in the literature concerning each one. It concludes with a summary of the unresolved issues and the open questions that will be addressed by the experiments.
- Chapter 5 presents the investigations on the growth mechanisms based on the X-ray diffraction method. The issues and questions stated in the previous chapter are addressed in detail. The impact of each mechanism on the microstructure of the $CuInS_2$ films is discussed. Paths for the exploitation of these mechanisms to purposely modify the microstructure of the films are proposed in this chapter.
- Chapter 6 presents a new rapid thermal process that bypasses the void formation at the back of the $CuInS_2$ film. This chapter serves as an example of film engineering based on the information gained in Chapter 5.

To summarize, little or no tools are available to monitor the microstructure formation of $CuInS_2$ thin films from a rapid thermal sulfurization process and to control it. This thesis endeavors to

establish two such tools. The first one consists of an experimental method to monitor *in situ* the changes in the microstructure of thin metallic films during annealing or sulfurizing in a closed space. The second consists of a breakdown of the sulfurization process into five mechanisms whose interaction determines the final microstructure of the film. These mechanisms are investigated by means of the *in situ* method and concrete information for the film engineering is extracted. This thesis serves as a basis for future design of processes that are based on the sulfurization of metallic thin films.

2. $CuInS_2$ Thin-Film Devices and Material Properties

$CuInS_2$ thin films are used as solar cell absorbers. This means that when such a film absorbs photons, free charge carriers are generated in the material. The carriers can be collected by an appropriate device[144]. A heterojunction solar cell is an example of such a collecting device. The first two sections of this chapter give a brief introduction to $CuInS_2$ based thin films solar cells and to their main technological characteristics. The next sections concentrate on the structural and physico-chemical properties of the $CuInS_2$ material as well as on the microstructural properties of the corresponding thin films. The last section of this chapter presents their fabrication technology.

2.1. Definition of a solar cell

A solar cell is an electrical device that converts sunlight into electricity. It delivers a maximal current I_{ph} that is a function of:

- The intensity and energy distribution of the incoming light. This is determined by the solar irradiance, in watts per area per wavelength, at the measuring location. To standardize the characterization of solar cells a standard spectrum is used. This is the AM 1.5 spectrum and corresponds to the spectrum measured when the sun is at an angle of 45° with respect to the normal of the earth at the measuring location.
- The absorption of the semiconductor. This is a material property and is a function of the energy of the incoming photons. In the idealized case it is zero for photons of energy below the bandgap and a constant for photons of energies above the bandgap of the material. The constant is called absorption coefficient. The absorption coefficient of $CuInS_2$ is $\sim 10^5 cm^{-1}$ for photons of energy larger than ~1.5eV. The absorption coefficient of silicon is approximately two orders of magnitude smaller.
- The quality of the semiconductor. This is characterized by the diffusion lengths of the charge carriers in the material. These diffusion lengths must be of the order of magnitude of the thickness of the device. This ensures that the carriers that are generated within the cell achieve the collecting contacts. Diffusion lengths of $CuInS_2$ are of the order of $1\mu m$. For silicon diffusion lengths must be of the order of some hundreds of micrometers.

A solar cell will deliver less current to an external load depending on the operating point on the current-voltage characteristic of the device. The ideal current-voltage $(I-V)$ characteristic of a solar cell is

$$I = I_s \cdot (exp(\frac{q \cdot V}{k \cdot T}) - 1) - I_{ph} \ , \tag{2.1}$$

where I_s is called the saturation current, q is the elemental charge and k the Boltzmann constant. In real solar cells the following must be considered:

- The carrier recombination within the space-charge region cannot be neglected. This is quantified by a diode quality factor, A, that takes values between 1 and 2.
- The resistance at the contacts and interconnectors and the bulk resistance of the film is not negligible. These resistances sum up to form the series resistance, R_S.
- The shunt resistance, R_{SH}, is not infinite. This can be caused by pinholes, large precipitates or any other source of current leakage.

The current-voltage characteristic of a real solar cell can be better approximated by (using a one-diode model)[83]:

$$I = I_s \cdot (exp(\frac{q \cdot (V - I \cdot R_S)}{A \cdot k \cdot T}) - 1) + \frac{V - I \cdot R_S}{R_{SH}} - I_{ph} \ . \tag{2.2}$$

The performance of a solar cell can be characterized by its current-voltage characteristic under AM 1.5 illumination. The basic parameters that can be read from such a measurement are:

1. The short circuit current I_{SC}: it corresponds to the current at V=0. From Equation 2.2, I_{SC} equals I_{ph} if the series resistance is zero and if the saturation current is negligible.

2. The open circuit voltage V_{OC}: it corresponds to the voltage when I=0. The open circuit voltage is a function of the band alignments and recombination mechanisms in the solar cell[49].

3. The fill factor ff: it is defined as the ratio between the maximal power output of the device, $I_{mp} \cdot V_{mp}$, and the idealized power output of the device $I_{SC} \cdot V_{OC}$:

$$ff = \frac{I_{mp} \cdot V_{mp}}{I_{SC} \cdot V_{OC}} \ . \tag{2.3}$$

   The fill factor characterizes the curvature of the current-voltage characteristic. It is sensitive to series and shunt resistances but also to recombination mechanisms within the cell.

4. The efficiency: it is defined as the ratio between the maximal power output and the power of the incoming light.

2.2. The $CuInS_2$ solar cell

The $CuInS_2$ solar cell is composed of a stack of layers that are deposited on a substrate (typically soda-lime glass). These are:

- the back contact layer: 500nm Mo;
- the absorber layer: 2μm $CuInS_2$ (p-type semiconductor);
- the puffer layer: 50nm CdS (n-type semiconductor);
- the window layer: 100nm intrinsic ZnO (n-type) + 500nm Al doped ZnO (n^+-type semiconductor);
- The Ni/Al front grid for contacting.

Figure 2.1 shows the current voltage characteristic and the main electrical parameters of a solar cell based on a $CuInS_2$ film. This film was fabricated by means of rapid thermal processing in the experimental setup described in Section 3.1 of Chapter 3 during a beamtime at the EDDI beamline of BESSY II. The $CuInS_2$ layer was optimized to present a double-layered morphology where a large-grained $CuInS_2$ layer covers a small-grained $CuInS_2$ layer (details on the growth of such films will be given in Chapter 6).

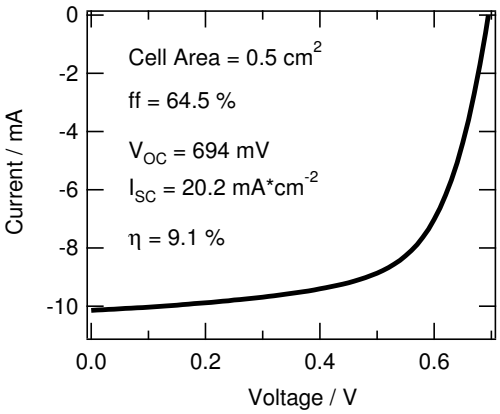

Figure 2.1.: Current-voltage characteristic of a Mo/$CuInS_2$/CdS/ZnO solar cell. The absorber layer was prepared by means of rapid thermal processing in the experimental setup described in Section 3.1 of Chapter 3 during a beamtime at the EDDI beamline of BESSY II. The reaction path for the fabrication of this $CuInS_2$ film will be presented in Chapter 6.

2.3. Structural properties of $CuInS_2$

$CuInS_2$ belongs to the group of the $A^IB^{III}X_2^{VI}$ ternary chalcopyrite compounds. The structure of the chalcopyrite compounds derives from the cubic sphalerite structure in accordance to the Grimm-Sommerfeld rule, i.e. average of 4 valence electrons per atomic site. Each X anion is sp^3 bonded to two A and two B cations and form together a tetrahedron. The sphalerite structure can be considered as two inter-penetrating face-centered cubic lattices, one with cations and one with anions, separated by a translation vector $(\frac{1}{4},\frac{1}{4},\frac{1}{4})$. In the chalcopyrite structure the cation sublattice is made of ordered group I and group III cations. This reduced symmetry leads to a primitive cell composed of eight atoms compared to a primitive cell of two atoms in the sphalerite structure. Figure 2.2 gives a representation of the crystal structures of sphalerite and chalcopyrite $CuInS_2$.

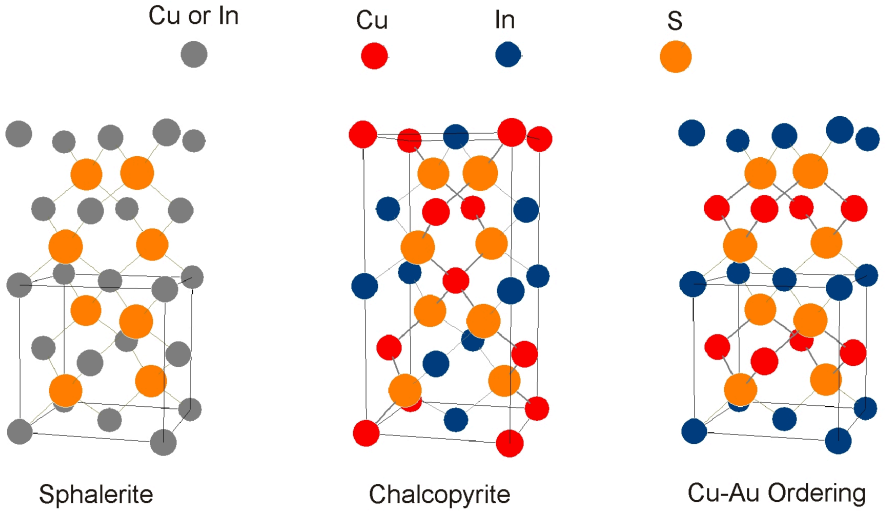

Figure 2.2.: Crystal structures of sphalerite, chalcopyrite and Cu-Au ordered $CuInS_2$.

The chalcopyrite structure belongs to the space group I-42d. Its unit cell is tetragonal and is distorted along the c-axis so that c/a is no longer equal to 2 as is the case in the sphalerite structure. In the chalcopyrite structure the anion does not occupy the ideal position inside the tetrahedron. The anion displacement parameter u is used to characterize this distortion; if u=0.25 there is no distortion. Note that c/a and u are independent. Table 2.1 gives the lattice parameters, the c/a ratios, the displacement parameters u and the bandgaps of $CuInS_2$, $CuGaS_2$, $CuInSe_2$ and $CuGaSe_2$.

Table 2.1.: Survey of structural properties[123], melting points[46] and bandgaps[127] of selected chalcopyrite materials.

Material	a/nm	c/nm	c/a	u	T_m/ °C	E_g(300K)/eV
$CuInS_2$	0.552[115]	1.1135[115]	2.017	0.227[113]	1079[15]	1.5[90]
$CuGaS_2$	0.536	1.043	1.948	0.275	1200	2.5
$AgInS_2$	0.583[15]	1.120[15]	1.922	0.25[54]	871[15]	2
$CuInSe_2$	0.578	1.161	2.008	0.224	986	1.05
$CuGaSe_2$	0.561	1.103	1.965	0.250	1040	1.7

Figure 2.3a) shows the angle-dispersive X-ray diffraction spectrum of $CuInS_2$. This was calculated with the software POWDERCELL[70]. The reflections of the chalcopyrite phase fall into three groups[89]:

- Reflections having h, k, and l/2 all even or odd. These reflections correspond to the sphalerite structure. Due to the tetragonal distortion (c/a≠2) the splitting of some reflection is observed: for example $(2,0,0)_{Sphalerite} \rightarrow (0,0,4)/(2,0,0)_{Chalcopyrite}$. A $CuInS_2$ compound having a random occupation of cations would present only this type of reflections without any splitting.

- Reflections having h and k even and l/2 odd or vice versa. This reflections depend on the anion displacement. If u=0.25 these reflections vanish.

- Reflections having h even and k, l odd, or k even and h, l odd. These reflections contain a cation term and reflect the ordering in the action sublattice. These reflections are also called super lattice reflections. If the cations occupy the lattice sites randomly these reflections vanish.

The Grimm-Sommerfeld rule can also be fulfilled by cation orderings which are different from the chalcopyrite structure. Alternating A^I and B^{III} cations in the [001] direction leads to the copper-gold (Cu-Au) ordering (space group P-4m2)[3]. Figure 2.2 presents the crystal structure of Cu-Au ordered $CuInS_2$. Rudigier[103] identifies the Cu-Au ordering in $CuInS_2$ films at room temperature. She observes that the presence of this phase is not compatible with high-efficiency devices. The X-ray diffraction spectra of both structures are similar. Figure 2.3 shows the calculated angle-dispersive X-ray diffraction spectra of chalcopyrite-ordered and Cu-Au-ordered $CuInS_2$ in the 15°-19° and 36°-38° ranges. Alvarez-Garcia[3] uses the reflections in these 2θ ranges to distinguish both structures.

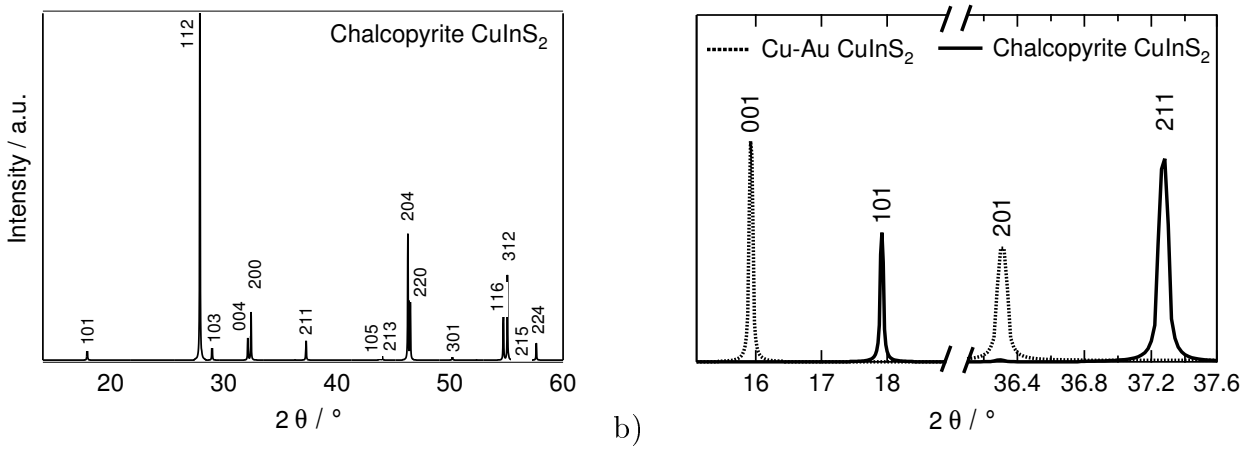

Figure 2.3.: a) Angle-dispersive X-Ray diffraction spectrum of chalcopyrite $CuInS_2$, b) selected reflections of the chalcopyrite and the Cu-Au ordering of $CuInS_2$. The spectra were calculated with the software POWDERCELL[70].

2.4. Physical and chemical properties of $CuInS_2$

Appendix A gives a review on the thermodynamics of the Cu-In-S system, including the phase diagrams of the Cu-In, Cu-S, In-S, and Cu-In-S systems. Table 2.2 gives the density, the thermal expansion coefficient, the bulk modulus, the electronic affinity, the absorption coefficient, and typical electrical characteristics like resistivity and charge carrier diffusion lengths of $CuInS_2$ thin films.

Table 2.2.: Physical properties of $CuInS_2$ at room temperature.

Property	Units	Values	Reference
Density	$g \cdot cm^{-3}$	4.71-4.75	[46]
Thermal Expansion Coefficient	K^{-1}	$(1.1 \pm 0.2) \times 10^{-5}$	[98]
Bulk modulus	GPa	62 ; 75	[72];[130]
Electronic Affinity	eV	4.7	[88]
Density of States Valence Band	cm^{-3}	$\sim 1 \times 10^{19}$	[66]
Density of States Conduction Band	cm^{-3}	$\sim 1 \times 10^{19}$	[66]
Absorption coefficient	cm^{-1}	10^5	[105]
Electron / Hole mobilities	cm^2/Vs	200 (n-type) /10 (p-type)	[126]
Conductivity	$(\Omega \cdot cm)^{-1}$	0.1	[37]
Diffusion lengths of electrons /holes	μm	0.9 / 2.5	[105]

The conductivity type and the carrier concentration of $CuInS_2$ materials are fixed by their intrinsic defect concentration[127]. Two parameters describe at best the deviation in composition of a $Cu_xIn_wS_z$ phase: the deviation in molecularity Δm and the deviation in valence stoichiometry Δy (see Figure A.6 in Appendix A). They are defined as

$$\Delta m = \frac{x}{w} - 1; \ \Delta y = \frac{2z}{x + 3w} - 1 \ . \tag{2.4}$$

Binsma[12] shows that Δy (anion poor- or richness) affects the level and conductivity type. Look[75] shows that single $CuInS_2$ crystals can be made n-type by annealing in indium atmosphere and p-type by annealing in sulfur atmosphere. As a general observation, anion vacancies lead to donor and cation vacancies to acceptor type doping. Other defects including interstitials, In_{Cu} and Cu_{In} also affect the conductivity. $CuInS_2$ fabricated by the sulfurization of thin metallic films normally exhibit p-type conductivity with charge carrier concentrations between 10^{16} and $10^{17}cm^{-3}$[37].

2.5. Microstructure of $CuInS_2$ thin films

Thin-film absorbers for solar cells based on $A^I B^{III} X_2{}^{VI}$ and $C^{II} X^{VI}$ materials are polycrystalline. The grain boundaries affect the electronic (or hole) transport in the material [91]. The mean grain size may affect the efficiency[125], but a large mean grain size is not a necessary condition for a high-efficiency $Cu(In,Ga)Se_2$ device[53]. In $Cu(In,Ga)Se_2$ devices, grain size and Ga content are coupled[1]. Abou-Ras *et al.*[2] analyze grain size distributions in $CuInS_2$ films from a sulfurization process by means of EBSD (electron backscatter diffraction). He finds a mean grain size of $\sim 0.5\mu m$.

Abou-Ras *et al.*[1] measure the crystallographic texture of the polycrystalline $Cu(In,Ga)(S,Se)_2$ films by means of EBSD. They find that $CuInS_2$ films fabricated through a sulfurization process present no particular preferred orientation.

Evaporated thin $Cu(In,Ga)Se_2$ and $CuInS_2$ films present good adhesion to the Mo back-contact. Chakrabarti *et al.*[24] estimate that stresses between 10MPa and 30MPa are present in evaporated $CuInSe_2$ films. Alvarez-Garcia[3] estimates the maximal tensile stress in $CuInS_2$ films from a sulfurization process to be 170MPa. These films present a bad adhesion to the back Mo contact. Large voids between absorber material and molybdenum, as those presented in Figure 1.1 of Chapter 1, are typically observed in $CuInS_2$ films fabricated through a sulfurization process[120].

2.6. Fabrication of $CuInS_2$ thin films

$CuInS_2$-based solar modules are being produced on a large scale[82]. They are currently fabricated by means of a rapid thermal process (RTP) where previously sputtered metallic precursors are sulfurized in a closed volume[120]. There are other fabrication processes at the laboratory scale like thermal evaporation[139] or spray pyrolysis[71]. However the RTP technology is the only one that has bridged the gap to the industrial production. This is thanks to a significant cost-reduction potential in terms of the deposition chambers, scalability and through-puts.

The rapid thermal sulfurization is composed of two steps:

1. Placing the glass/Mo/Cu/In stacks, with [Cu]/[In]>1, together with elementary sulfur pellets, so that sulfur excess conditions are ensured, in a evacuated and closed reaction box.
2. Heating the reaction box by means of high-performance halogen lamps. The total heating times are of the order of some minutes (2-5min), and the top temperatures oscillate between 550°C and 600°C.

The excess copper segregates at the surface as Cu-S phases[67] that can be removed by a chemical etching treatment with KCN[141]. The optimization of the RTP-based $CuInS_2$ films has been done through the analysis of the resulting solar cells and the adjustment of time-temperature profile.

The typical microstructure of the RTP-based $CuInS_2$ fabricated at the baseline of the Helmholtz Zentrum Berlin was schematically presented in Figure 1.1 of Chapter 1. Solar cells based on such films have achieved world record efficiencies of 11.4%[64, 120].

Alvarez-Garcia *et al.*[5] expose void formation between the $CuInS_2$ films and the metals during RTP sulfurization. They propose that these voids coalesce and form the large cavities near the Mo back contact that are responsible for a bad adhesion. Other than the adhesion problems, the state of the art $CuInS_2$-based solar cells present efficiencies that are well below the theoretical efficiency of these films[49, 119, 66]. The microstructure of these films can be improved in terms of (see Figure 1.1 of Chapter 1 for a representation of the microstructural defects in these films):

- the presence of secondary phases within the films (phases other than chalcopyrite $CuInS_2$);
- the crystalline quality of the films (long range cation order, low defect densities and large grain sizes);
- the presence of pinholes;
- the point defect distribution near the surface;
- the presence of large voids near the back contact.

This thesis proposes two tools that should support the scientists and engineers when addressing these issues in the future: first, a method for the monitoring of microstructural changes in $CuInS_2$ thin films and second, a logical decomposition of the sulfurization process in independent and quantifiable solid state mechanisms.

3. Method

During this thesis the method of the energy-dispersive X-ray diffraction[41] was extended to monitor in real-time the evolution of thin films during annealing or sulfurizing in a closed volume. This task consisted in the development, assessment and optimization of two experimental tools:

- a rapid thermal processing (RTP) chamber;
- a method based on the energy-dispersive X-ray diffraction to monitor processes *in situ* inside this chamber.

The analysis of the energetic positions, widths and intensities of the diffraction signals delivers information concerning the microstructure of the thin films[132]. Their dependence on temperature, time and pressure can be used to study a wide range of solid state mechanisms. Table 3.1 presents some of the information that can be gained thanks to the *in situ* energy-dispersive X-ray diffraction method.

The first section of this chapter presents the RTP chamber. The second one exposes the principles of X-ray diffraction and particularly of the energy-dispersive X-ray diffraction of thin films. The third section describes the *in situ* energy-dispersive X-ray diffraction method.

Table 3.1.: Relevance of the in situ energy-dispersive X-ray diffraction method for the studies of $Cu(In,Ga)(S,Se)_2$ thin-film materials. The main characteristics of the diffraction signals (energetic position, broadening and intensity) give a wide spectrum of information concerning the microstructure of the films. The table is not exhaustive. For information on the correlation between microstructure and X-ray diffraction see [132].

Signal characteristic	Information	Examples
Energetic position	Phase identification	Section 5.2
	Thermal expansion	Section 5.3.1
	Chemically induced strains	Section 5.1
	Mechanically induced strains	[41]
Width	Domain sizes	Section 5.4
	Microstrains	
	Chemical gradients	
	Twinning	
	Point defects	
Intensity	Reaction progression	Section 5.3.1.1
	Preferred orientation analysis	Section 5.3.1.2

3.1. Rapid thermal processing chamber

Figure 3.1 shows a representation of the RTP-chamber used to fabricate the $CuInS_2$ films during this work. The base pressure is lower than $1x10^{-3}$mbar. The chamber contains a reaction box composed of a graphite ring and two quartz membranes closing a sealed $107cm^3$ cylindrical volume. This reaction box is fixed to the chamber walls via a quartz table. A motor valve controls the sulfur pressure inside the box. Two sets of four lamp heaters each are placed on top and on bottom of the reaction box, 35mm apart from the top and bottom membranes respectively. The heaters allow heating rates up to 8.6K/s measured by thermocouples placed 1mm away from the respective lamps. The walls of the chamber are water cooled. The temperature measurement at the sample position is a challenge in RTP[52]. The temperature was measured by a thermocouple in contact with the samples.

The use of a closed volume that is heated isothermally to sulfurize the Cu-In thin films has two important consequences:

1. The temperature of the sample and the sulfur offer are coupled.
2. The sulfur pressure evolves from $p_S<10^{-3}$mbar to ~10mbar. The exact pressure inside the reaction box is unknown. However, if the box is perfectly sealed the pressure can be calculated (see Fig. A.1 of Appendix A). From this calculations the maximal pressure inside the reaction box is estimated to be in the 1 to 10mbar range.

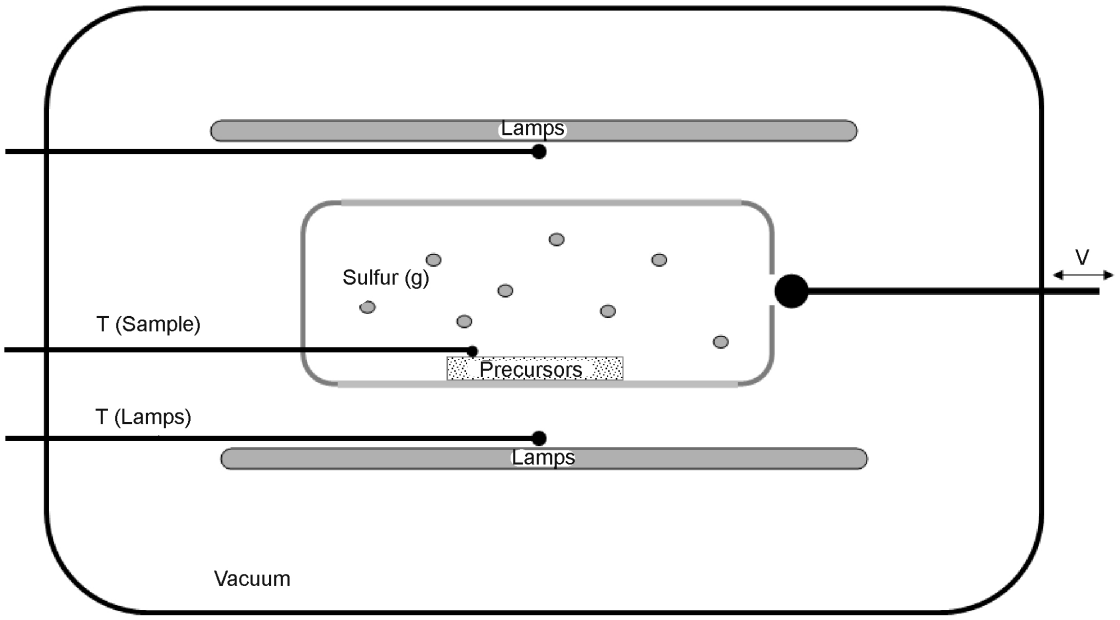

Figure 3.1.: RTP-chamber used during this work. The vacuum chamber has a base pressure $p_S<10^{-3}$mbar. Inside the vacuum chamber a cylindrical graphite reaction box ($107cm^3$) is placed between two lamp sets. The reaction box has a valve that controls the pressure inside of it. The temperatures are measured near the lamps and near the samples.

3.2. X-Ray diffraction

X-ray diffraction (XRD) is based on the elastic scattering of electromagnetic waves of energies E between ∼0.1keV and ∼100keV by periodically spaced structures. Because these energies correspond to wavelengths λ of the order of 100nm to 10pm, this process can be used to study crystalline structures. An incident X-ray beam of wave number $\mid \vec{k} \mid = \frac{2\pi}{\lambda}$ will be diffracted by an arrangement of planes periodically separated by the distance d_{hkl} (where h,k,l are the miller indices of the crystalline structure considered) if the Bragg condition is satisfied. The Bragg condition can be written as:

$$\overrightarrow{k} - \overrightarrow{k}' = \overrightarrow{G_{hkl}} \tag{3.1}$$

where $\overrightarrow{k}$, $\overrightarrow{k'}$and $\overrightarrow{G_{hkl}}$ are the incident beam vector, diffracted beam vector, and scattering vector respectively. The latter is given by

$$\mid \overrightarrow{G_{hkl}} \mid = \frac{2\pi n}{d_{hkl}} \tag{3.2}$$

where n is an natural integer. The Bragg condition for diffraction can be simplified to

$$n \cdot \lambda = 2d_{hkl} \cdot sin\theta \tag{3.3}$$

where θ is the angle between incident beam and the lattice planes.

The total intensity of a Bragg reflection is[140]

$$I_{hkl} \propto V \cdot \mid F_{hkl} \mid^2 \tag{3.4}$$

where V is the volume of diffracting crystallites. F_{hkl} is the structure factor, that is written as

$$F_{hkl} = \sum_{\alpha} f_\alpha \cdot exp(-M_\alpha) \cdot exp(-i\overrightarrow{G_{hkl}} \cdot \overrightarrow{r_\alpha}) \tag{3.5}$$

where α stands for the atoms in the lattice, $\overrightarrow{r_\alpha}$ for the vector that gives their atomic position in terms of components along the basis vectors of the lattice, and f_α for the atomic form factors. The factor M_α accounts for thermal vibrations and can be written as[28]

$$M_\alpha = B_\alpha \cdot (\frac{sin\theta}{\lambda})^2 \ . \tag{3.6}$$

The isotropic temperature factor, B_α, can be estimated by Rietveld refinement of powder diffraction experiments. Table 3.2 shows the results of such refinements at room temperature and at 868°C[113]. The values of B_α can be linearly interpolated between both temperatures[1]. These interpolations are necessary to calculate the temperature dependency of the diffracted intensities. Figure 3.2 shows the calculated angle-dispersive X-ray diffraction spectra at room temperature and at 500°C of $CuInS_2$ based on the data of Table 3.2. Table 3.3 summarizes the intensity ratios of the most prominent $CuInS_2$ reflections at room temperature and at 500°C.

[1]The isotropic temperature factors of $CuInSe_2$ were measured as a function of temperature and a linear dependency was observed for temperatures below the chalcopyrite to sphalerite phase transformation[114]. This linear dependency is also assumed for $CuInS_2$ below 900°C given that the chalcopyrite to sphalerite phase transformation takes place at ∼950°C (see phase diagram in Figure A.7 of Appendix A).

Table 3.2.: Rietveld refinement of $CuInS_2$ powder at room temperature and at 868°C[113].

Temperature	a/nm	c/ nm	B_{Cu}/nm^2	B_{In}/nm^2	B_S/nm^2
25°C	0.5521	1.1135	1.568×10^{-2}	1.077x10^{-2}	0.952×10^{-2}
868°C	0.5581	1.1228	7.246×10^{-2}	2.802x10^{-2}	3.606×10^{-2}

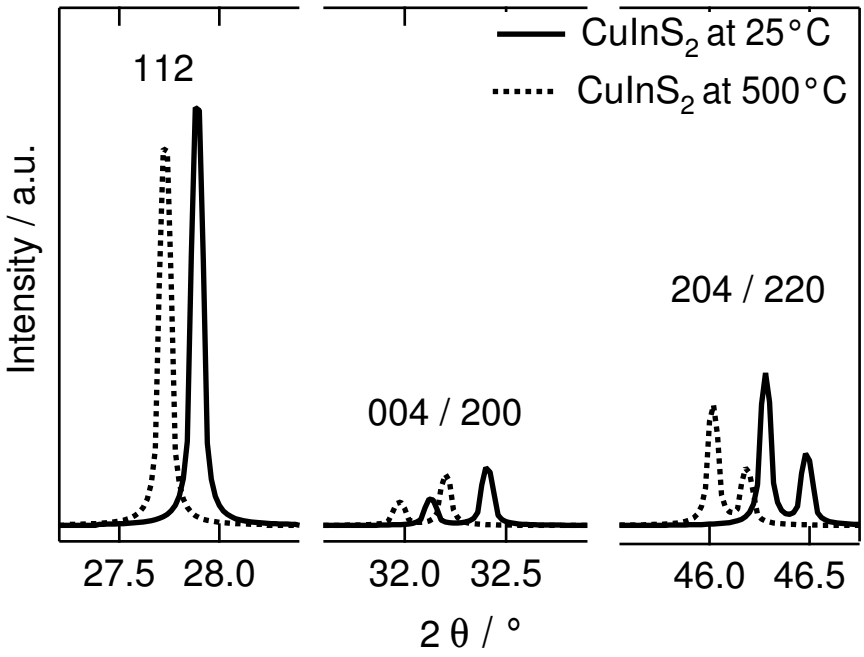

Figure 3.2.: Angle-dispersive X-ray spectra of $CuInS_2$ at room temperature and at 500°C calculated with the software POWDERCELL[70].

Table 3.3.: Calculated integral intensity ratios of the most prominent $CuInS_2$ reflections at room temperature and at 500°C.

hkl	112	004/200	204/220	116/312
$\frac{I_{hkl}^{500°C}}{I_{hkl}^{25°C}}$ / %	90	88	79	71

3.2.1. Energy-dispersive X-Ray diffraction (EDXRD)

As a consequence of Equation 3.3 the characteristic lattice plane distances d_{hkl} can be obtained when irradiating a crystalline material with X-rays of constant energy and observing intensity maxima whilst scanning θ. This is the angle-dispersive configuration (ADXRD). θ can also be kept constant while scanning the energy of the diffracted X-rays. This is the energy-dispersive configuration (EDXRD). Bremsstrahlung of an X-ray anode or white light from synchrotron facilities are used as X-ray sources in EDXRD. The collection of all diffracted photons and their

separation in energy by an adequate detector leads to complete spectra of d_{hkl}. Bragg's equation is transformed in the energy-dispersive case to (for the first order of the reflection)

$$E_{hkl} = \frac{h \cdot c}{2d_{hkl} \cdot sin\theta} \ . \tag{3.7}$$

3.2.1.1. X-Ray source

The majority of the experiments were carried out at the energy-dispersive beamline EDDI[41] of the Berlin synchrotron facility (BESSY II). The source is a 7 Tesla multipole wiggler that delivers a spectrum of X-rays going from ∼5keV to ∼100keV with reasonable intensities for diffraction experiments. Figure 3.3 presents the X-ray spectrum of this source. The ring current of the BESSY II synchrotron facility decreases exponentially with a $1.934\text{x}10^{-3}\text{min}^{-1}$ time constant. The ring current determines the total intensity available for the diffraction experiments.

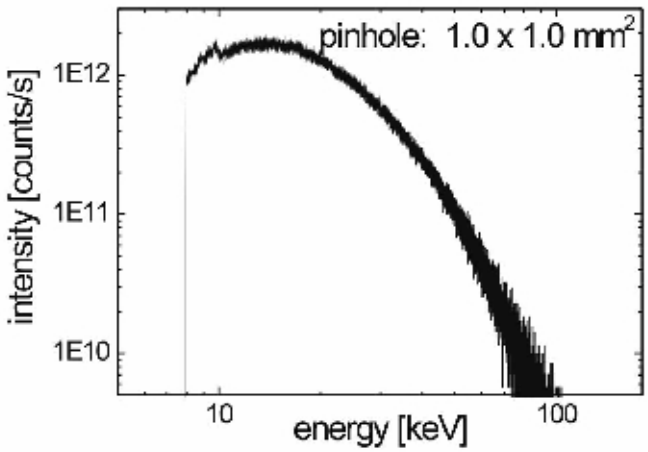

Figure 3.3.: X-Ray spectrum available at the energy-dispersive beamline (EDDI) at BESSY II from [41]. The spectrum was acquired in the low current ring modus (1mA) and was extrapolated to the normal current ring modus (∼250mA).

3.2.1.2. Geometry

The geometry of the diffraction experiments is given in Figure 3.4. The beam is collimated by a mask at 19m and a pair of slits S_1/S_2 at 26.8m and 29m from the source respectively. The detector is placed in a diffractometer, at a fixed scattering angle 2θ, whose center is at 30m from the source[41]. The diffracted beams travel through a double slit system S_3/S_4 before they arrive at the energy-dispersive detector. For the experiments of this thesis the slits S_1, S_2, S_3 and S_4 were fixed at the values of 1, 0.5, 0.12 and 0.12mm respectively in the axial direction ($\vec{z}$ in Fig. 3.4 for S_1 and S_2) and of 1mm in the equatorial direction ($\vec{y}$ in Fig. 3.4). The intersection of the incoming X-ray beam and the region of space seen by the detector form the active volume. Only the volume of the sample that is within this active volume will contribute to the collected diffraction signals. Figure 3.5 shows the section of the active volume (hatched area) of the experimental setup used in this thesis.

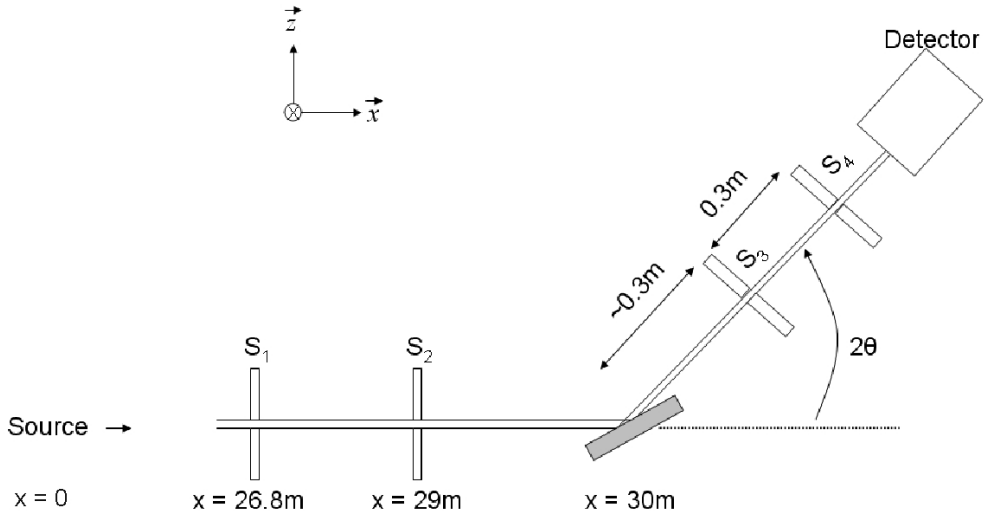

Figure 3.4.: Geometry of the energy-dispersive X-ray diffraction (EDXRD) setup (see also [41]).

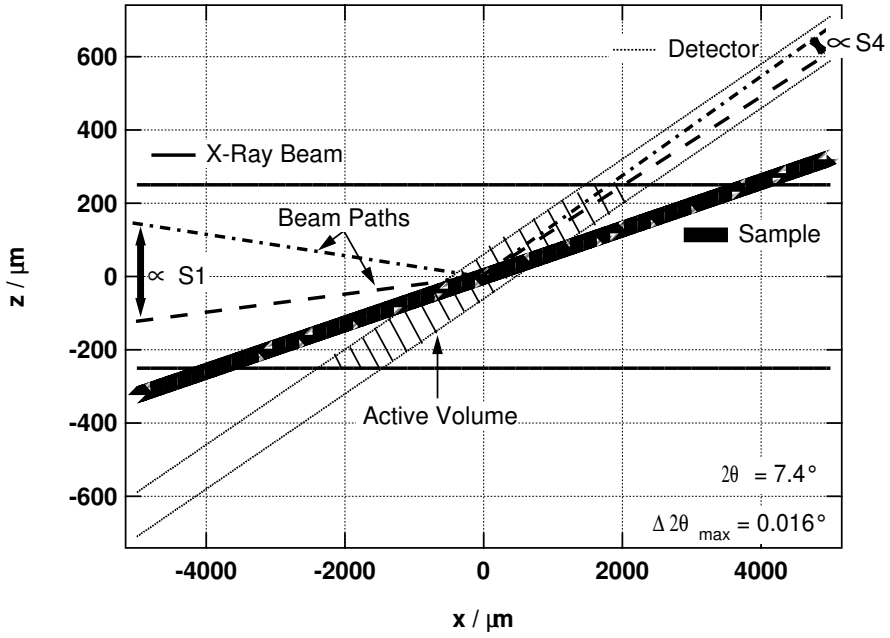

Figure 3.5.: Active volume (hatched parallelogram) of the EDXRD setup.

The lack of parallelism of the incoming and diffracted X-ray beams results in an uncertainty of the diffraction angle 2θ. This is fixed by the slit system. The extreme possible beam paths are plotted in Figure 3.5 as dashed-dotted and dashed lines. For the geometry shown in Fig. 3.4 and the given slit system the uncertainty of 2θ is

$$\Delta 2\theta = 0.016°. \tag{3.8}$$

The uncertainty of 2θ is related to the uncertainty of the diffracted energy by (from Eq. 3.7)

$$\Delta\theta = \frac{tan\theta}{E} \cdot \Delta E. \tag{3.9}$$

For $\theta = 3.7°$ (chosen diffraction angle) the Equation 3.9 is visualized in Figure 3.6. The uncertainty in the determination of the energetic position due to $\Delta\theta$ can be read from the lines intersecting the dashed line: at 30keV the uncertainty is of ∼0.05keV and at 60keV it is of ∼0.11keV.

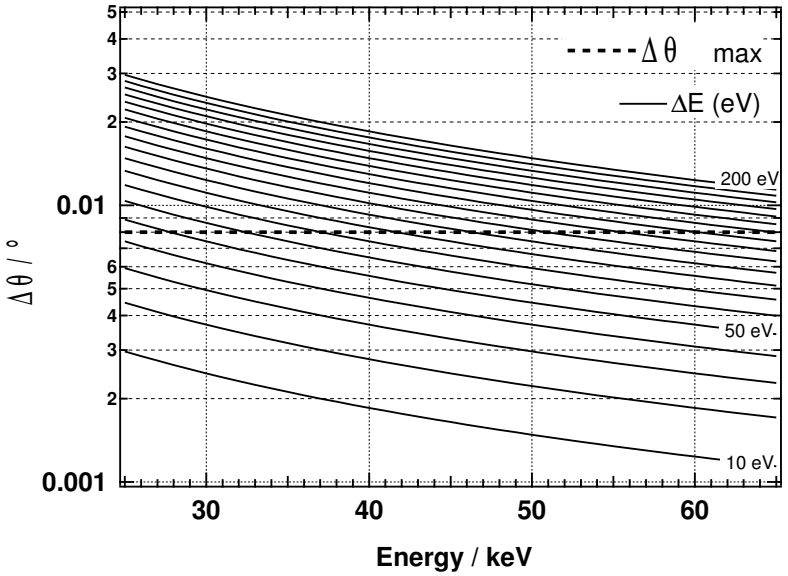

Figure 3.6.: Uncertainty of the energetic position of a measured reflection, ΔE, due to the uncertainty of the diffraction angle $\Delta\theta$. The intersection of the dashed line ($\Delta 2\theta_{max} = 0.016°$) with the corresponding energy error hyperbola gives the uncertainty as a function of the energy.

3.2.1.3. Temperature dependence

Both the intensity and the energetic of the Bragg reflection depend on the temperature. On the one hand the energetic position, E_{hkl}, of a hkl Bragg reflection depends on the temperature T following the law

$$\alpha_{hkl} = \frac{1}{\Delta T} \cdot \frac{\Delta d_{hkl}}{d^{T_0}_{hkl}} = \frac{1}{\Delta T} \cdot \frac{\frac{1}{E^T_{hkl}} - \frac{1}{E^{T_0}_{hkl}}}{\frac{1}{E^{T_0}_{hkl}}} = \frac{1}{\Delta T} \cdot (\frac{E^{T_0}_{hkl}}{E^T_{hkl}} - 1) \ , \tag{3.10}$$

where α_{hkl} is the expansion coefficient of the considered lattice planes, d_{hkl}. Chalcopyrite structures present in general expansion coefficients that are anisotropic. This means that the thermal

expansion in the parallel, $\alpha_{parallel}$, or in the perpendicular, $\alpha_{perpendicular}$, directions of the $\vec{c}$-axis are not equivalent[62, 63]. The thermal expansion of a hkl plane, whose normal forms an angle φ with the $\vec{c}$-axis, can be written as[15]

$$\alpha_{hkl} = \alpha_{parallel} \cdot cos^2\varphi + \alpha_{perpendicular} \cdot sin^2\varphi \ . \tag{3.11}$$

For $CuInS_2$ $\alpha_{parallel}$ and $\alpha_{perpendicular}$ lie in a narrow range (0.9x10^{-5}K^{-1} and 1.1x10^{-5}K^{-1} at 30°C after[14]). Therefore, the expansion coefficient is taken as isotropic with a mean value of (1±0.1)x10^{-5}K^{-1}. This means that α_{hkl} can be replaced by this value (with the given uncertainty) in Equation 3.10 for every hkl. This assumption is no longer valid for strongly anisotropic chalcopyrites like $AgInS_2$[15].

The intensity of the Bragg reflections decreases with temperature. The decrease in the intensity comes from the thermal vibrations of the atoms in the lattice and it is described by the structure factor (Equation 3.5). A similar behavior as the one shown in Figure 3.2 and summarized in Table 3.3 is expected in EDXRD.

3.2.1.4. Energy-dispersive detector

The energy-dispersive detector is capable of collecting and identifying photons of different energies during a short period of time. The collection of a complete spectrum is possible with a time resolution that can go down to 1 second. These short acquisition times are a clear advantage of the energy-dispersive method when compared to the angle-dispersive one. The energy-dispersive detector consists of a contacted and exposed semiconducting single crystal (Ge in the case of the EDDI beamline) where an output voltage is produced, proportional to the energy of the incoming photons[21].

The following issues are relevant for the *in situ* experiments:

- Escape peaks: The use of a Ge single crystal is accompanied by the apparition of escape peaks that are situated 9.8keV below the diffraction signals. This peaks correspond to the absorption of the K_α energy levels of germanium.
- Efficiency: The detector has an efficiency that is a function of the energy. The efficiency given by the manufacturer is: 4% at ∼10keV and a 6% plateau from ∼25keV to ∼100keV.
- Resolution: The resolution depends on the collection settings. For the settings used during this thesis the resolution of the detector was obtained by analyzing the full width at half maximum (FWHM) of the radioactive decay lines of ^{55}Fe, ^{241}Am, and ^{133}Ba. The FWHM dependence on the energy E is well described by the linear relationship:

$$FWHM(keV) = 0.241 + 2.4715 \cdot 10^{-3} \cdot E(keV) \ . \tag{3.12}$$

- Deadtime: An important parameter of the EDXRD method is the deadtime. Denks *et al.*[30] show that the deadtime influences the energy positions of the reflections. To avoid this effect, the experiments were carried out under constant deadtime conditions. The realization of this will be explained in Section 3.3.1. The deadtime, DT, is defined as

$$DT(\%) = 1 - \frac{time^{collection}}{time^{real}} \ . \tag{3.13}$$

3.2.1.5. Reflection profile

The measured X-ray diffraction profile $h(E)$ is a convolution of the instrumental profile $g(E)$ and the structural profile $f(E)$ of the sample[13]. The convolution of two functions is defined as:

$$h(E) = \int_{-\infty}^{+\infty} f(y) \cdot g(E-y)dy \ . \tag{3.14}$$

A deconvolution gives a relation between the breadths of the two contributions and the measured breadth:

$$\beta_h = \Psi(\beta_f, \beta_g) \tag{3.15}$$

where Ψ is a function that depends on the profile form. An infinite perfect crystal has a structural profile $f(E)$ that is identical to a delta function of the energy. Real crystals have defects, impurities and present nonuniform strains. In the general case, both f and g can be described by a Voigt function[2]. The Voigt function is a convolution of a Gauss function and a Cauchy function (see Appendix C for the definition of the functions). The convolution of two Voigt functions is also a Voigt function. This means that if $h(E)$, $f(E)$ and $g(E)$ are Voigt functions they are characterized by a Gauss and a Cauchy-breadth, β^G and β^C respectively. Deconvolution of h yields in this case[13]:

$$\beta_h^C = \beta_f^C + \beta_g^C \tag{3.16}$$

and

$$(\beta_h^G)^2 = (\beta_f^G)^2 + (\beta_g^G)^2 \tag{3.17}$$

where the subindices refer to the profile (h, f, g) and the superindices (G, C) to the Gauss or Cauchy contributions.

The ^{241}Am radioactive decay line can be used to asses the instrumentation profile $g(E)$ because in this case the structural profile $f(E)$ is a delta function of energy. Figure 3.7a) shows the measurement and a Gauss-fit of the ^{241}Am radioactive decay line. The residual (difference between the fits and the measurements) reveals the quality of the fit. The figure shows that $g(E)$ is well approximated by a pure Gauss function and that β_g^C is negligible.

Energy-dispersive X-ray diffraction lines are commonly fitted by pure Gauss functions [21, 30, 42, 76, 36]. Figure 3.7b) shows the measurement and a Gauss fit of the $CuInS_2$ 112 diffraction line. However, in the case where the domain size of coherent scattering is small, for example of the order of some tens of nanometers, a Cauchy contribution of the Bragg reflection becomes evident (see Section 5.31a)). In this case the general Voigt approach must be used. Dehlez *et al.*[29] propose a numerical method (described in Appendix E) to obtain the Gauss and Cauchy contributions of an underlying Voigt function from the measured breadth and full width at half maximum of a measured reflection.

[2]There are two functions that can reproduce a Voigt profile and that are numerically easier to manipulate: the Pseudo-Voigt and the simplified Pearson VII function. The first is a sum of a Gauss and a Cauchy function with a weighting factor η. The second, given in Appendix C) is a function that was not developed for XRD profile analysis at its origin. However, it is adapted to fit XRD profiles and recent investigations have given a physical foundation for its use [145].

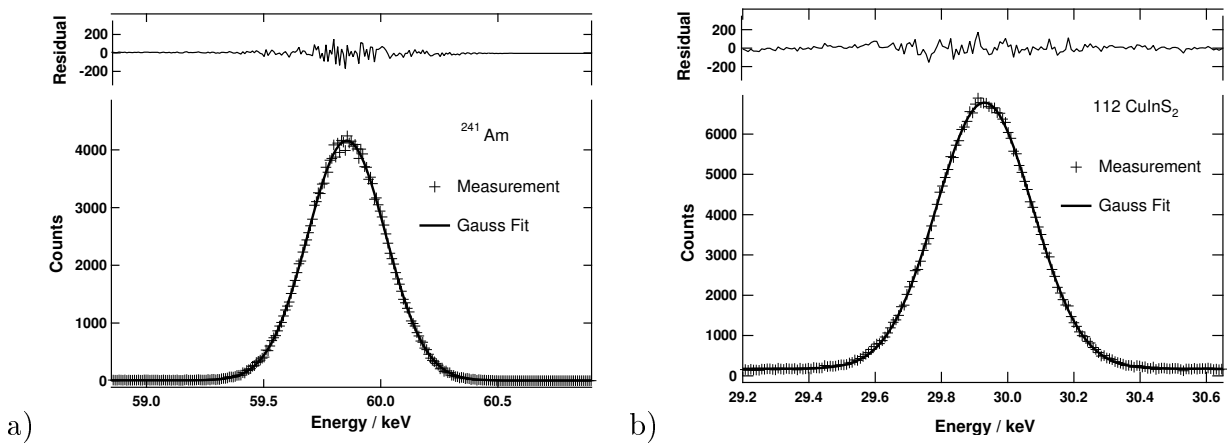

Figure 3.7.: a) Instrumentation profile taken from the collection of the ^{241}Am radioactive decay line and b) typical $CuInS_2$ 112 diffraction profile. Both profiles are well fitted by a Gaussian. The quality of the fits can be assessed by the corresponding residuals.

3.2.1.6. EDXRD of thin $CuInS_2$ films

The scattering angle $2\theta = 7.4^{\circ}$ is adequate to record EDXRD spectra of $CuInS_2$, and by similarity of $Cu(In,Ga)(Se,S)_2$ materials. This angle ensures an optimal use of the X-ray spectrum (between 10keV and 70keV, see Figure 3.3) and a clear energetic separation of the fluorescence lines[3] (in the low energy range $<$ 30keV) and the diffraction lines (at higher energies $>$30 keV). Figure 3.8 presents an EDXRD spectrum taken at 500°C of a 0.5 μm Mo/ 2 μm $CuInS_2/Cu_{2-x}S$ thin-film stack. The acquisition time for this spectrum was 5 seconds.

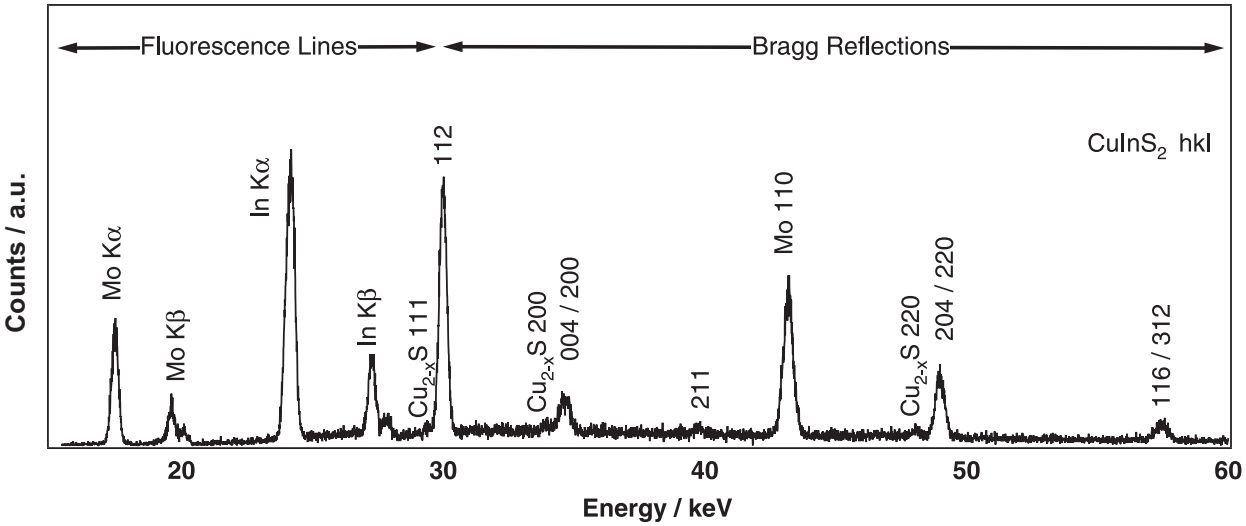

Figure 3.8.: Energy-dispersive X-ray diffraction spectrum of a $\sim$2μm thick $CuInS_2/Cu_{2-x}S$ film at 500°C. 5sec recording time, 20% deadtime. The fluorescence lines of Mo and In emerge in the low energy range. The diffraction signals emerge on the $E >$ 30keV energy range. Indexing of the reflections was made based on the Joint Committee of Powder Standards (JCPDS) database.

[3]The fluorescence consists in the absorption of a photon of energy higher as the absorption edge of a species, expulsion of an electron from the ground levels, relaxation of an electron to the ground level accompanied by an emission of a photon with a characteristic energy[76].

In the low energy range the Mo $K\alpha$, Mo $K\beta$, In $K\alpha$, In $K\beta$ fluorescence lines emerge at 17.4keV, 19.6keV, 24.2keV and 27.3keV respectively. In the higher energy range ($E_{Photon} > \sim$30keV) the Bragg reflections emerge. The lattice plane distances d_{hkl} can be extracted using Equation 3.7. Phase identification is possible by comparison of the d_{hkl} with the values reported in the database of the Joint Committee of Powder Standards (JCPDS). Table 3.4 gives the *hkl* values and the corresponding energetic positions of the reflections of the most common phases in the Cu-In-S system.

Table 3.4.: Expected diffraction lines at room temperature for the scattering angle θ=3.7° and the corresponding JCPDS files of the most common phases in the Cu-In-S system.

Phase	*hkl* reflections	Energy (keV)	JCPDS File
Cu	111, 200, 220	46.0, 53.1, 75.1	004-0836
In	101, 110, 112	35.3, 41.7, 57.0	005-0642
$CuIn_2$	002, 211, 112	35.8, 36.9, 41.2	[56]
$Cu_{11}In_9$	311, 312, 313	31.0, 34.8, 44.6	041-0883
$Cu_{16}In_9$	101, 002, 102	31.3, 36.4, 44.6	042-1475
α-InS	011, 101, 110, 004	23.4, 26.0, 32.5, 36.0	019-0588
β-In_2S_3	400, 511, 440	35.8, 46.4, 50.6	032-0456
CuS	103, 006, 110	34.2, 35.3, 50.7	078-2121
α-Cu2S	630, 106	48.6, 51.4	023-0961
β-Cu2S	220, 110	47.6, 51.2	026-1116
$Cu_{2-x}S$	200, 220	33.6, 47.6	Calc. (Fm-3m, a= 5.628[34])
$CuInS_2$	112, 200, 220	29.6, 34.3, 48.5	027-159
$CuIn_5S_8$	400, 511, 440	35.9, 46.6, 50.8	024-361

Absorption of the film

The intensity I of an X-ray beam that traverses a solid of thickness x is

$$I = I_0 \cdot exp(-\alpha \cdot x) \tag{3.18}$$

where I_0 is the initial intensity and α the mass absorption coefficient[4]. A signal generated at the depth d from the surface of a sample will be attenuated by the absorption of the film itself. The path within the film increases with decreasing scattering angle theta. Figure 3.9a) shows an X-ray signal generated within the film and the path that it follows to leave it. To evaluate the depth of the material that is being probed by the diffraction experiments, it is useful to define the $d_{\xi\%}$ information depth. This is the depth of the film where a generated signal is absorbed to $\xi\%$, or:

$$\frac{I(d_\xi)}{I_0} = 1 - \xi\% \ . \tag{3.19}$$

Figure 3.9b) shows the $d_{99\%}$, $d_{90\%}$, $d_{10\%}$ and $d_{1\%}$ for $CuInS_2$ under θ =3.7° as a function of the energy. It shows that for energies higher than 35keV, the $d_{10\%}$ is larger than 1μm. This means that when analyzing films of 1μm the structural information comes from the whole thickness with

[4]The mass absorption coefficients are tabulated in the website of the National Institute for Standard and Technology (NIST)[51]

a maximal lost of 10% in intensity. Therefore, for films thinner than 1μm, energy dependent self-absorption effects can be neglected (within 10% error). The figure also shows that films thicker than 200μm absorb completely the whole spectrum. Energy-dependent self-absorption effects cannot be neglected in this case.

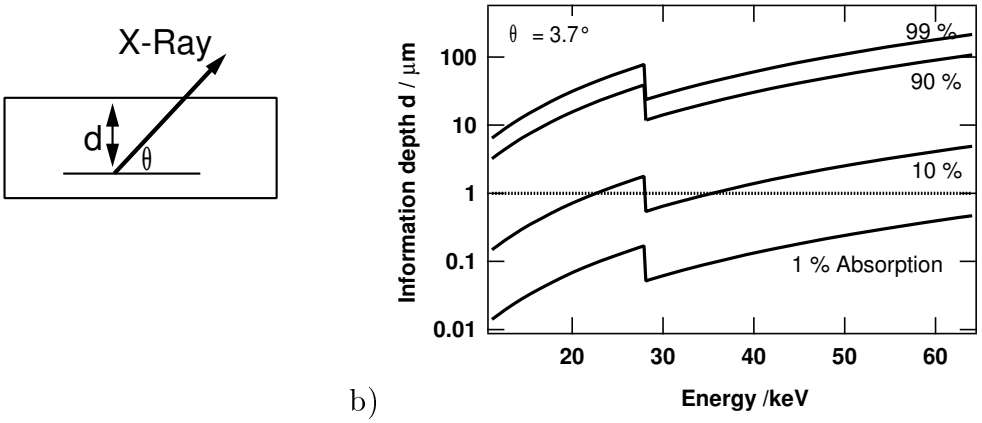

a) b)

Figure 3.9.: a) Definition of the information depth d. An X-ray generated at the depth d will traverse $d/sin\theta$ before exiting the sample. In this path in can be absorbed. b) Information depths of 99%, 90%, 10% and 1% absorption for $CuInS_2$ with an exit angle θ=3.7°. Calculations are based on the data reported in [51]. The step at ~28keV corresponds to the In K absorption edge. For energies ≥35keV the information depth with 10% absorption is larger than 1μm. For thin films of this thickness the generated information traverses the whole sample with maximal 10% absorption. For films with thicknesses ≥200μm self-absorption effects must be taken into account.

3.3. *In situ* EDXRD at BESSY II

Buras *et al.*[21] and Gerward[42] pioneered in the field of *in situ* energy-dispersive X-ray diffraction. Ellmer *et al.*[36] and Pietzker [98] adapted this technique for the analysis of thin-film growth. During this research thesis the EDXRD setup at the energy-dispersive beamline of BESSY II[41, 30] was extended to monitor annealings and sulfurizations of thin films in a closed volume. This included monitoring rapid thermal processes for the first time. To achieve this, the chamber presented in Figure 3.1 is placed at the center of the diffractometer of Figure 3.4. The chamber has 1mm thick Al windows for the incoming X-rays and the outgoing diffraction signals. The X-rays also traverse the cylindrical graphite reaction box. The graphite absorbs X-rays with energies mainly below 10keV. X-rays diffracted by the sample and fluorescence lines generated within the sample exit the chamber and are recorded by an energy-dispersive detector in the 10keV to 80keV energy range. Temperature profiles can be programmed and the sulfur pressure inside the reaction box can be regulated by means of an externally controlled valve (see Figure 3.1). The characteristics of the *in situ* experiments are outlined below.

3.3.1. Thermal drift of the sample position

The components inside the chamber expand when the chamber is heated. Due to this, the sample placed in the reaction box drifts in the $\vec{z}$-direction of Fig. 3.4 and Fig. 3.5. This thermal drift is between 100 to 200μm depending on the experimental conditions. Figure 3.10 shows the effect of such a drift on the intensities of the chalcopyrite 112 reflection and the Mo $K\alpha$ fluorescence line.

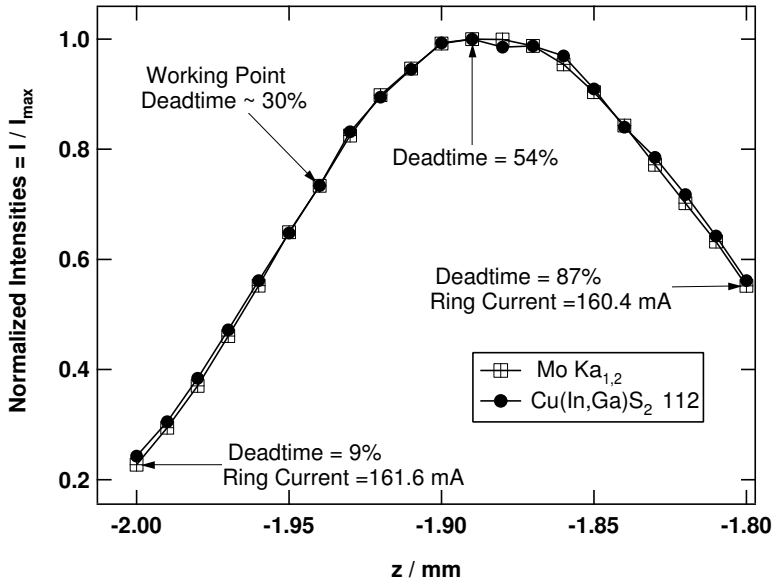

Figure 3.10.: Intensities of the chalcopyrite 112 Bragg reflection and the Mo $K\alpha$ fluorescence line as a function of the position of the sample in the $\vec{z}$ direction (see Figure 3.4 for the definition of the coordinates). The intensities are a function of the volume of the films and of the amorphous glass substrate in the active volume (see Figure 3.5).

The lowest position (z = -2mm) in Figure 3.10 corresponds to a film that has just entered the active volume (see Figure 3.5). Both the Bragg reflection and fluorescence line increase in intensity with increasing z because the film penetrates further in the active volume. At z = -1.9mm there is a maximum of both signals. As z increases further the background stemming from the glass

substrate increases steadily whereas the volume of the film in the active volume remains constant. The signal to background ratio decreases. This yields a decrease of the measured signals for $z \geq -1.9$. This decrease is related to: a) the background subtraction and b) the increase in the deadtime.

A programmed routine corrects the position of the sample during heating to compensate this thermal drift. The routine uses the deadtime of the collected spectra as a regulation parameter, assuring a constant position of the sample. This is the case if the ring current does not fall significantly during the heating experiment. For long experiments this correction routine introduces a new error: a ring current induced z-shift, called from now on rc-shift (the definition of short and long heating experiments will be given in the next section).

3.3.1.1. Ring-current induced shift

The deadtime is a function of the incoming photons. To maintain a constant deadtime when the ring current falls considerably, the correction routine moves the sample to higher z positions. This ring-current induced shift (rc-shift) is negligible ($\sim$1μm) if the experiments are no longer than 30min and small ($\sim$13μm) for experiments of 300min of duration.

Figure 3.11 shows the effect of the correction routine on the EDXRD signals of the $CuInS_2$ and Mo, together with the ring current and the shift in z position (rc-shift) during a complete injection (480min). The deadtime (DT) was kept constant during the injection. The maximal rc-shift was 18μm.

The rc-shift:

- induces a drift in the energetic positions of the Bragg reflections. This shift is equal to 10eV for the reflection at $\sim$ 30keV and 20eV for the reflection at $\sim$43keV and small if compared to the shift due to the thermal expansion of the $CuInS_2$ 112 reflection (from 25°C to 500°C $\sim$200eV);
- correlates with an increase of 4eV of the full widths at half maximum (FWHM). This is negligible because it falls below 2% of the measured width;
- affects the intensities of the reflections. The intensities of the reflections in the lower energy range (E $<\sim$30keV) behave differently from those in the higher energy range (E $> \sim$40keV).

To summarize, the thermal drift correction used in this work is based on a fixed deadtime. This correction is stable and does not introduce significant errors for experiments that are shorter than 30min. For experiments of 300min of duration the thermal drift correction introduces no significant error for the determination of the full widths at half maximum. However it introduces a 10eV error in the determination of the energy position and a 7% error in the determination of the intensity.

3.3.2. Noise to signal ratio

The ratio between the maximal intensity of a signal and the noise, or noise to signal ratio, is a source of inaccuracy in the determination of a signal's energetic position, width and intensity. In some cases a relatively high noise to signal ratio is unavoidable because integration times as short as five seconds are necessary to study fast processes and because the initial reflection intensity increases proportionally to the volume of the phase when it appears as a product of a chemical reaction (see Eq. 3.4). Figure 3.12 shows the Mo 110 reflection of the same sample recorded with

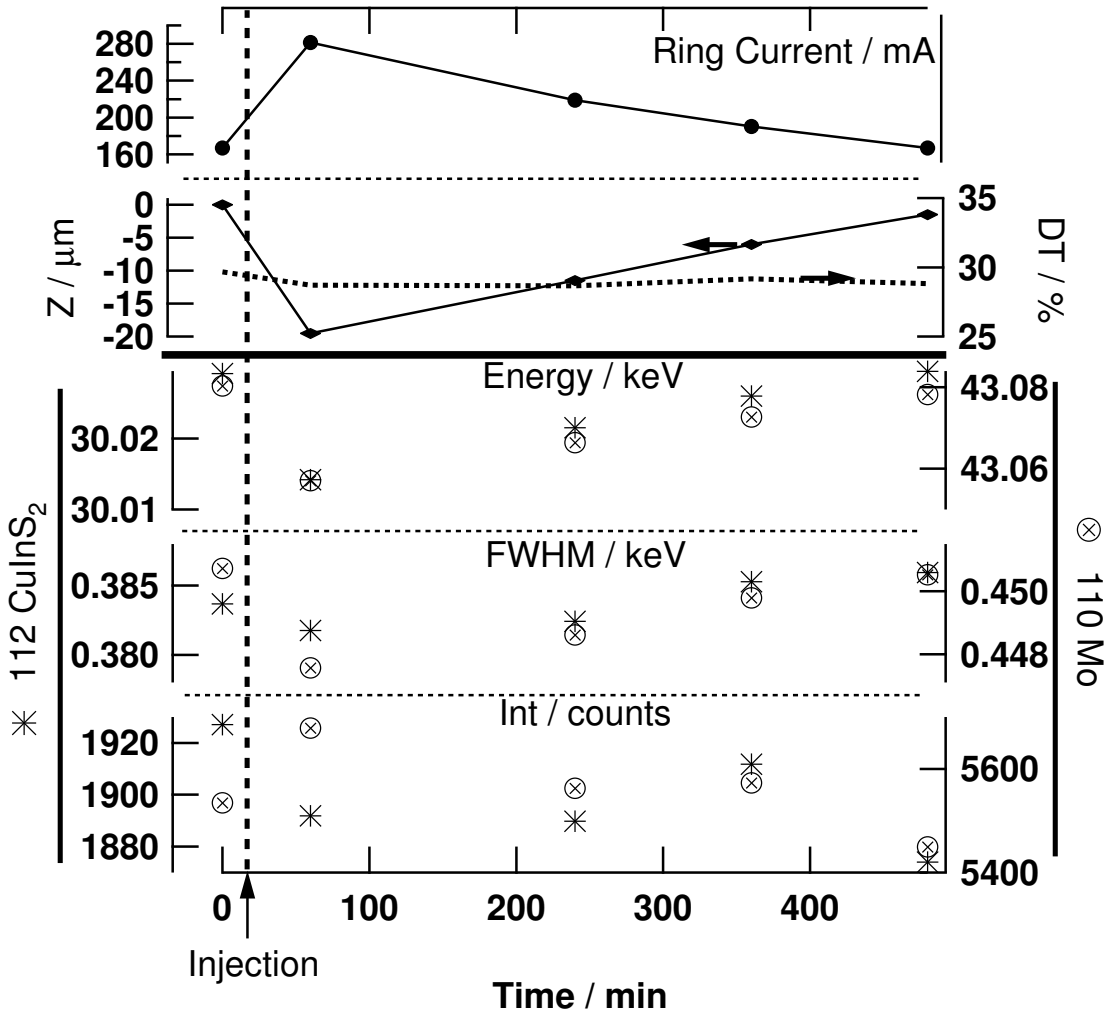

Figure 3.11.: Ring-current induced errors in the determination of the energetic positions, the full widths at half maximum (FWHM) and the intensities of the diffraction signals introduced by fixing the deadtime at 30% during the *in situ* experiments. The errors introduced in the experiment are a function of its duration.

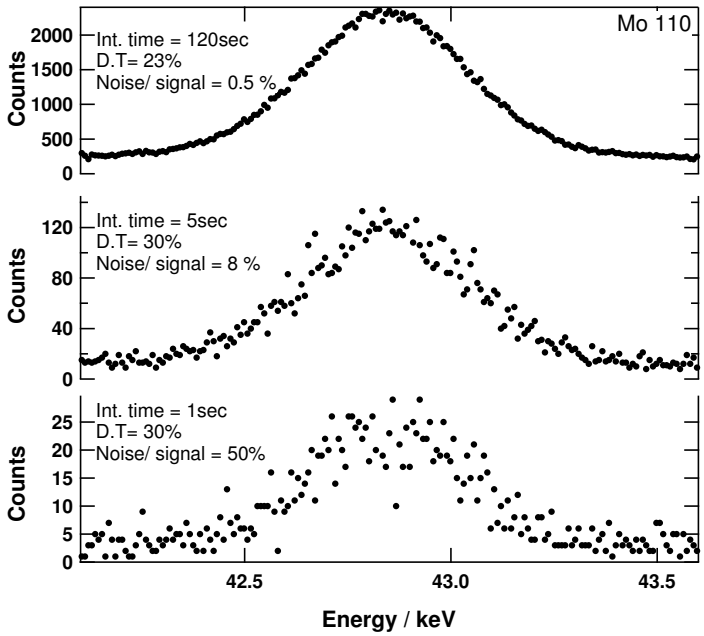

Figure 3.12.: Evolution of the the noise to signal ratio as a function of the integration time for a Mo 110 reflection. The energetic position, the width and the intensity of the reflection can be extracted with more accuracy at lower noise to signal ratios.

increasing integration times and the corresponding noise to signal ratios. Short integration times are coupled to a larger noise to signal ratio. This ratio determines the inaccuracy of the values extracted by the fitting procedure.

A numerical simulation was done to quantify the inaccuracy of the values extracted by fitting a signal with decreasing noise to signal ratios. Figure 3.13 shows the energetic position, the full width at half maximum and the intensity extracted from a Gauss fit of a simulated reflection as a function of the noise to signal ratio. The simulated reflection consists of an ideal Gauss profile plus random noise. For each fit the noise was randomized. Figure 3.13 is the result of 1000 fits made after consecutive randomization. The noise to signal ratio decreases from left to right. The figure shows that the energetic position of the reflection is defined within 75eV at high noise to signal ratios, ∼50%. Therefore, phase identification is possible at very short integration times, for example one second (see Figure 3.12). The relative energetic position is the most accurate measurement in energy-dispersive X-ray diffraction. The incertitude on the FWHM is under 0.02keV when the noise to signal ratio is lower than 10%. The intensity is the most inaccurate measurement. At noise to signal ratios of ∼ 50% it introduces an uncertainty of 40%.

To summarize, the noise to signal ratio is a key parameter that determines the accuracy of the information that can be obtained from a fit of a measured signal. For noise to signal ratios of 50% only the determination of the energetic position of a signal can be attempted. For other noise to signal ratios, the errors can be quantified using Figure 3.13.

3.3.3. Errors in the *in situ* EDXRD setup

During this work two main configurations of the *in situ* EDXRD setup were chosen:

- Configuration 1: Short experiment duration, ≦30 min, with short integration times of ∼5 seconds. The investigations on the metallic alloy sulfurization (Section 5.2 of Chapter 5) and on the RTP processing (Chapter 6) were done using this configuration.

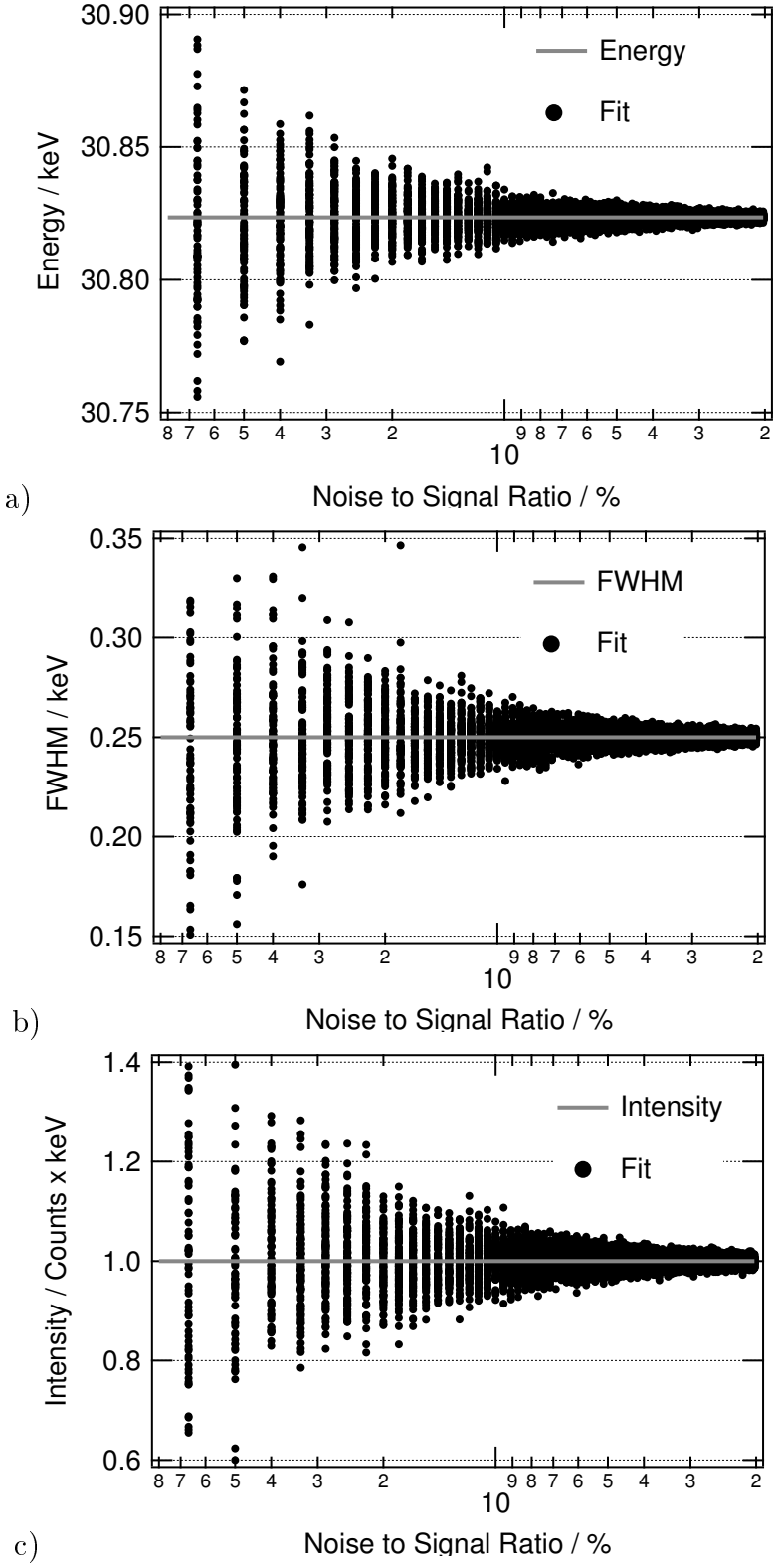

Figure 3.13.: a) Energetic positions, b) full widths at half maximum (FWHM) and c) intensities extracted from a fit (using the software IGOR Pro) of a simulated signal as a function of the noise to signal ratio (decreasing from left to right). The simulated signal is composed of a pure Gauss profile plus random noise. The points correspond to 1000 fits of the simulated signal where the noise was re-randomized after each fit.

- Configuration 2: Long experiment duration, ∼300 min, with long integration times of ∼120 seconds. The recrystallization studies (Section 5.4) were done using this configuration.

The deadtime was held constant in both cases.

Assuming a Gaussian convolution of the sources of error, the total absolute error Δ of a measurement is

$$\Delta = \sqrt{\sum_i \Delta_i^2} \, . \tag{3.20}$$

Δ_i represent the absolute errors stemming from different sources.

The main sources of error for the extraction of energetic positions, FWHMs and intensities in the in situ EDXRD setup are:

- noise to signal ratio;
- ring current shift;
- diffraction angle ($\Delta\theta$).

These depend on the configuration of the measurement and on the energetic positions of the signals. Table 3.5 summarizes the incertitudes in the configurations 1) and 2) for EDXRD signals at ∼17keV and ∼30keV. The table shows that both configurations are well adapted for the determination of energetic positions. Configuration 2 is better adapted for the determination of FWHMs. The error in the intensity measurement is determined by the sum of the relative errors. The total relative error in the determination of the intensity is 10% in both configurations and depends strongly on the noise to signal ratio (see also Figure 3.13).

Table 3.5.: Summary of errors of the in situ EDXRD experiment as a function of the experimental configurations and the energetic positions of the signals. The total absolute error in the determination of the energetic position and full widths at half maximum are calculated by Equation 3.20. The total relative error in the determination of the intensities is calculated by the sum of the individual relative errors.

Conf.	1 (short experiments, ∼30min)						2 (long experiments,∼300min)					
Energy	17 keV			30keV			17keV			30keV		
Param.	E /eV	FWHM/eV	I/%	E	FWHM	I	E	FWHM	I	E	FWHM	I
Noise	10	20	10	10	20	10	2	3	3	2	3	3
rc- shift	-	-	-	-	-	-	10	4	7	10	4	7
$\Delta\theta$	25	-	-	55	-	-	25	-	-	55	-	-
Δ	27	20	10	56	20	10	27	5	10	56	5	10

3.3.4. Mo normalization and background subtraction

A 0.5μm thick Mo thin film serves as a back contact in the Glass/Mo/$CuInS_2$/ZnO solar cell. Mo has a low chemical reactivity. Therefore the signal of the Mo $K\alpha$ line at 17.47keV is used for the normalization of the EDXRD data. This normalization corrects for overall intensity variations. This procedure has no effect in the determination of the energetic position or the FWHM of a given reflection. When determining the intensity of a normalized reflection, the incertitude in the determination of the intensity of the Mo $K\alpha$ line must be taken into account.

The background stems mainly from the underlying amorphous glass substrate. To extract the energetic position, the FWHMs and the intensities of the Bragg reflections, this background is removed. To do this, an energy range comprehending the signal to be analyzed is chosen and a linear background is subtracted.

4. The Growth Mechanisms

This thesis proposes the breakdown of the complex sulfurization process in independent but interacting mechanisms. This procedure allows a sequential description of the microstructure formation. Deliberate modification of the microstructure can be achieved if the different mechanisms are controlled.

The mechanisms are:

1. the alloying of the metals;
2. the sulfurization of the metallic alloy;
3. the reaction of the sulfides;
4. the thin-film recrystallization;
5. the sulfide interdiffusion.

The independent mechanisms can be analyzed individually but it is their interaction that defines the final microstructure of the film. Figure 4.1 presents their sequence. This chapter reviews the theory and the reported results concerning each mechanism. At the end of the chapter the unresolved issues and open questions will be summarized.

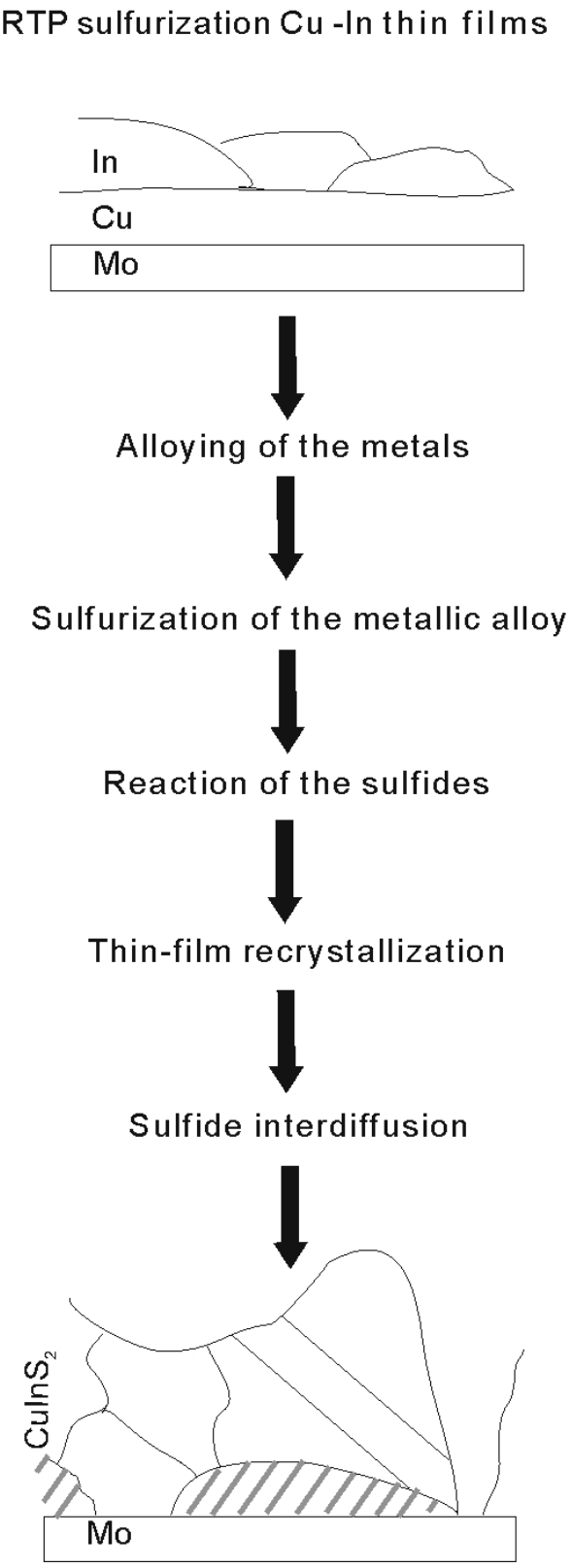

Figure 4.1.: Active mechanisms during the rapid thermal sulfurization of Cu-In thin films. The mechanisms are studied independently in this work. The final microstructure of the $CuInS_2$ film is a result of their interaction. The typical microstructure of the RTP processed $CuInS_2$ presents deficiencies that can be addressed if the different mechanisms are controlled.

4.1. Alloying of the metals

The alloying of Cu-In thin films has been studied by Somadossi[122], Pietzker[98] and Neisser[89]. After at most three days of storage at room temperature the Cu/In stack is transformed in $Cu/CuIn_2$. During heating of this stack, two reactions are typically identified:

$$CuIn_2(s) \rightarrow Cu_{11}In_9(s) + In(l) \mid T = 148°C \tag{4.1}$$

and

$$Cu_{11}In_9(s) \rightarrow Cu_{16}In_9(s) + In(l) \mid T = 307°C\ . \tag{4.2}$$

Both reactions liberate free In in the liquid state.

Interdiffusion experiments between pure copper and pure indium films[89] show that below 150°C the diffusion of Cu into the In supports the formation of the $CuIn_2$ phase. Above 150°C the intermetallic compound formation is governed by diffusion of In along grain boundaries of more Cu-rich phases[98]. Mainz *et al.*[77] show that alloying is of crucial importance during the sulfurization Cu-In-Ga thin films. He postulates that the strains in the $Cu_9(In,Ga)_4$ phase are responsible for the void formation as well as for the subsequent sulfurization stop that is observed in these films.

Chemically induced strains of the Cu-In metallic phases are expected if the metals become so Cu-rich that the solid solution of In in Cu appears. Indeed, the Cu(In) phase expands and contracts proportionally to the In content. At 650°C Cu dissolves 10.4 at.% In and expands hereby 2.5% (room temperature measurements)[124]. An estimation of the possible expansion or contraction of this phase during the sulfurization is missing in the literature. This issue will be addressed in Section 5.1 of Chapter 5. Large strain differences between the metallic phases and the sulfide phases could be at the origin of void or crack formation in the $CuInS_2$ films.

4.2. Sulfurization of the metallic alloy

During the sulfurization of a metallic alloy, a stack composed of sulfide layers may appear. The layer sequence and its morphology determines the applicability of the resulting film as a solar cell absorber. The idealized configuration of sulfide phases forming single plane layers above a plane Cu_xIn_y film (as shown in Figure 4.2) will be considered in the following. In a situation where ϕ_2 corresponds to CuS, the film would be unusable as a solar cell absorber. This phase would introduce on one hand a recombination path for charge carriers and on the other short circuits within the film. Indeed a difficulty in fabricating $Cu(In,Ga)Se_2$ films is that when they are Cu-rich, Cu-Se phases segregate within the film. Therefore a prerequisite for $Cu(In,Ga)Se_2$ thin-film fabrication is that they are Cu-poor[112]. In the sulfur system the Cu-S phases and the $CuIn_5S_8$ phase are susceptible of segregating when sulfurizing in Cu-rich conditions[107, 108, 9].

The sulfide layer sequence is determined by the sulfurization mechanism. The sulfurization of alloys is a common subject in corrosion of metallic materials[137, 138, 101, 84, 85, 86, 87, 19]. To address this mechanism it is necessary to refer to theoretical reflections and empirical observations on the sulfurization of pure metals and on their extension to the case of metallic alloys.

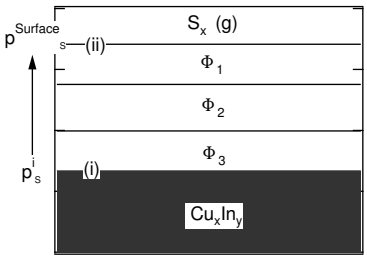

Figure 4.2.: Layer sequence during the sulfurization of a Cu-In alloy. Φ_i stands for the different sulfide phases, (i) and (ii) represent the alloy/sulfide and sulfide/gaseous sulfur interfaces respectively. The sulfur activity (or pressure) increases from interface (i) to interface (ii).

4.2.1. Theory of the sulfurization of pure metals

Rickert[101] identifies three steps in the reaction between a solid metal Me and a chalcogen[1] X in the gas phase to form a MeX film (see Figure 4.3):

1. Transition of metal across the Me/MeX interface (i);
2. Diffusion of metal or chalcogen ions and electrons (or holes) through the MeX film;
3. Incorporation of X at the MeX/X interface (ii).

The interaction between these three steps determines the growth mechanism. The film thickness, x, characterizes the kinetics of the growth. If the rate determining step is a reaction at one of the two interfaces, (i) or (ii), a linear rate law of the type:

$$\frac{dx}{dt} = k \tag{4.3}$$

is observed[116]. This is the case of a slow surface reaction due to low chalcogen impingement. In this case an increase in chalcogen pressure increases the velocity of the film growth.

If the rate determining step is the diffusion in the film, a parabolic rate law is observed [116] where

$$\frac{dx}{dt} = \frac{k}{x} \ . \tag{4.4}$$

This equation was originally developed in a detailed analysis of transport during oxidation.[2]

If:

a) equilibrium exists at the interfaces;

b) equilibrium conditions are locally achieved at every point in the MeX film;

c) the stoichiometry deviations in the MeX film are small;

[1] Chalcogens are the chemical elements belonging to the group 16 of the periodic table, i.e O, S, Se, Te etc.

[2] The parabolic law can also be obtained using Fick's first law $\vec{j} = D\overrightarrow{gradC}$. Considering that the flux of the rate determining species contributes to the increase of film's thickness, $\vec{j}$ can be replaced by $(dx/dt)\vec{x}$. On the other hand the concentration gradient of this species can be linearized by taking the concentrations at the boundaries: $\overrightarrow{gradC} = (\Delta C/x)\vec{x}$. Therefore $dx/dt \propto x^{-1}$.

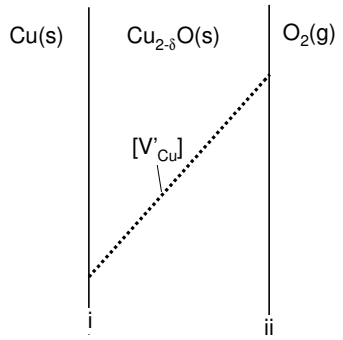

Figure 4.3.: Steady state oxidation of Cu from [109]. (i) and (ii) represent the $Cu/Cu_{2-\delta}O$ and $Cu_{2-\delta}O/O_2$ interfaces respectively. During the growth of the oxide film a constant cation vacancy gradient is established.

d) the MeX film is thicker than ∼100nm (for thinner films a logarithmic law is observed[101]);

then the parabolic rate constant is

$$k = \frac{1}{2}\int_{p^i_{X_2}}^{p^{ii}_{X_2}} \left\{ \frac{z_{cat}}{z_{an}} \cdot D_M + D_X \right\} dlnP_{X_2} \ . \tag{4.5}$$

Here D stands for the diffusion coefficients in the MeX film of the metal and chalcogen ions, z for their valence and p_{X_2} for the pressure of the chalcogen at the interfaces (i) and (ii). Equation 4.5 shows that the growth of the film is driven by the concentration gradient of the chalcogen. At the interface (i) the chalcogen pressure (interpreted as an activity) equals the dissociation pressure of the metal. At the interface (ii) the chalcogen pressure is fixed by the working pressure. The matter transport is determined by the diffusion coefficients: if $D_M >> D_X$, growth is supported by the out diffusion of the cations. In this case and for a p-type MeX film where D_M is independent of the chemical potentials, Schmalzried[109] shows that

$$k \propto p^{\nu}_{X_2} \tag{4.6}$$

with $\nu > 0$. This means that increasing the chalcogen pressure increases the velocity of the film growth.

In this model local thermodynamic equilibrium is achieved at every point in the film. Therefore local defect concentrations are coupled. A gradient in the chalcogen activity imposes a gradient of in the concentration of other defects. Figure 4.3 shows the charged cation vacancy concentration during the oxidation of Cu[109] where growth is controlled by the diffusion of Cu cations. In this case a chalcogen gradient imposes a cation vacancy gradient.

In sulfurizing pure copper metallic films, the sulfur pressure fixes the rate determining step[11]. If the pressure is low, the rate determining step is the sulfur offer (linear growth rate). If the pressure is high, the rate determining step is the cationic diffusion. This leads to a parabolic growth.

4.2.2. Theory of the sulfurization of metallic alloys

Chalcogenization of an A-B alloy is a process that depends on[109, 85, 101]:

1. Alloy composition;

2. Number and type of A-B-X compounds;
3. Chemical potentials of the A, B and X species in all A-B-X compounds;
4. Diffusion coefficients of the A, B and X species in all A-B-X compounds;
5. Stability of the interfaces;
6. Porosity of the layers.

No general solution for the alloy chalcogenization problem is available and each case must be looked at individually. Concerning the sulfurization two approaches can be underlined:

- A thermodynamic approach[43, 44, 45];
- A kinetic approach[84, 85, 86, 87].

4.2.2.1. Thermodynamic approach

This approach is the extrapolation of the analysis made for pure metals. In the steady state[3] sulfurization, a local thermodynamic equilibrium is achieved. The chemical potential, or pressure, of sulfur evolves from that imposed at the surface (interface (ii) of Fig. 4.3) to that imposed at the interface alloy/sulfide (interface (i) of Fig. 4.3). The sulfur pressure at the alloy/sulfide interface is fixed by the equilibrium

$$Alloy + S_2 \rightleftharpoons Sulfide(s) \ . \tag{4.7}$$

Gesmundo *et al.*[44] propose that a phase diagram chalcogen pressure vs. composition describes the chalcogenization. The analysis of such a diagram gives the possible reaction paths for the steady state sulfurization, i.e. the combination of sulfides that satisfy all transport equations and equilibrium conditions. When the points 1 - 6 listed at the beginning of this section are known the reaction path can be calculated[110].

No chalcogen pressure vs. composition diagram is available in the literature for the Cu-In-S system. Such a diagram would be very helpful to understand the layer sequence formation during sulfurizations of Cu-In thin films.

4.2.2.2. Kinetic approach

This approach is based on experimental observations done by Mrowec[85]. He finds that:

- When the sulfides form a solid solution, a compact film of $A_xB_{1-x}S$ is formed, independent of alloy composition. The growth occurs via the out diffusion of cations. This is the case for Fe-Ni alloys.
- When the sulfides form solid solutions within limited concentration ranges or when they form spinels, a bilayered film is formed. This film is composed of: a compact layer of the less stable sulfide on the surface covering a layer of mixed sulfides or of the ternary spinel phase. The underlying layer is compact if the outer layer deforms plastically with increasing thickness. If not, an inner porous layer is observed. In both cases the growth occurs via the out diffusion of cations. This is the case of Ni-Cr alloys.

[3] Steady state means that the fluxes (ionic, electronic) and that the intensive variables (p,T) are independent of time.

- When sulfides are insoluble and do not form spinels, the film consists of two layers: a compact layer of the less stable sulfide covering a porous layer containing both A and B sulfides. In this case the growth of the outer film is supported by the out diffusion of cations and that of the inner porous layer by the in-diffusion of sulfur. This is the case of Cu-Zn alloys.

Most of the cases studied by Mrowec presented a parabolic growth kinetic, the rate determining step being the diffusion of the slowest ion through one of the sublayers.

Mrowec[85] and Brueckmann[19] propose the free energy of formation as a kinetic criterion to justify faster growth rates and the formation of an exclusive surface sulfide layer. In the majority of the sulfides the cation sublattices are more defective than the anion sublattices. Hence, growth is supported by the diffusion of cations. The more defective the sublattice the faster the growth. Because the free energy of formation is a measure of the energy needed to pull an atom or ion out of its lattice point, it is also an indicator of the lattice defectiveness. Mroweck[85] postulates that sulfides, having lower absolute free energies of formations grow faster than their oxides analogues.

Table 4.1[40] gives the standard free energies of formation of the principal sulfide phases in the Cu-In-S system. The CuS phase presents the lowest absolute free energy of formation.

Table 4.1.: Free standard formation energies of the principal sulfides in the Cu-In system[40].

Compound	$-\triangle G^0_{298K}(kJmol^{-1})$
CuS	73
$Cu_{2-x}S$	114
α-InS	154
$CuInS_2$	275
β-In_2S_3	404
$CuIn_5S_8$	1133

4.2.3. Sulfurization of Cu-In alloy thin films

Klopmann *et al.*[69], Rudigier[104] and Mainz[76] study by means of in situ experiments the sulfurization of Cu-In-(Ga) thin films in the low sulfur pressure regime where $p_s < 10^{-3}$mbar. Klopmann *et al.* find that in the Cu-rich case and under 425°C, a temperature gradient is needed to support growth of a sulfide layer. They attribute this to a stress-induced growth. Based on the reported diffusion coefficients (see Table 4.2) they postulates that the growth determining step is the diffusion of cations through the $CuInS_2$ film and that at lower temperature this is only possible through crack formation. Diffusion of cations to the surface and reaction to $CuInS_2$ without intermediate phases is also postulated by Neisser[89] and confirmed by Mainz. Alvarez-Garcia *et al.*[4] show that during the sulfurization of Cu-In thin films at low chalcogen pressures ($p < 10^{-4}$ mbar) the reaction front is at the surface and the growth of $CuInS_2$ is supported by the out diffusion of cations.

Rudigier also studied the formation of the Cu-Au ordering (see Section 2.3 of Chapter 2 for the definition of this cation ordering) during sulfurization of thin Cu-In films. She observes the transition Cu-Au ordering to chalcopyrite ordering starting at 400°C and assisted by secondary Cu-S phases on the surface.

Mainz is the only author that addresses the sulfur offer dependence of the growth. He controls the sulfur offer by controlling the time when the temperature of an external sulfur source achieves

Table 4.2.: Diffusion coefficients of Cu and In in $CuInS_2$. For comparison the diffusion coefficient of S in $CuGaS_2$ is also given.

	Cu	In	S (in $CuGaS_2$)
D / cm^2sec^{-1}	5.3 x 10^{-5} - 3.3 x 10^{-7}	1 x 10^{-9}- 3.2 x 10^{-7}	2 x 10^{-12}
Temperature / K	298	923	700
Reference	[65]	[143]	in [89]

190°C. If sulfur is offered early, with respect to the sample temperature, he observes the formation of a binary $Cu_{2-x}S$ phase together with the $CuInS_2$ formation. In this case he observes the formation of an intermediate $CuIn_5S_8$ phase that is consumed at the top temperature. If sulfur is offered late, with respect to the sample temperature, he observes the exclusive formation of $CuInS_2$.

Barcones *et al.* address the growth of Cu-rich $CuInS_2$ from an rapid thermal sulfurization process (RTP) by means of break-off experiments[9]. In RTP the sulfur pressure evolves from $\sim 10^{-3}$mbar to ~10mbar at the top temperature (see Section 3.1). Barcones *et al.* postulate that in this case $CuIn_5S_8$ forms as an intermediate phase. She supposes the formation of a CuS phase at the surface from the beginning of the sulfurization. Contrary to Rudigier, Barcones *et al.* observe a Cu-Au ordering → chalcopyrite ordering transition that is not correlated to the presence of Cu-S phases. These experimental evidences point to different growth mechanisms when sulfurizing at low ($p_s < 10^{-3}$mbar) or high ($p_s >$ 1mbar) sulfur pressures. The growth models that have been developed by Pietzker, Neisser and Rudigier cannot be translated to the case of the high pressure sulfurization.

The sulfide layer sequence and its morphology has important consequences for the performance of the thin film. Section 5.2 of Chapter 5 will present that the stack formation during the sulfurization of a $Cu_{16}In_9$ alloy is a function of the temperature and the sulfur pressure. A general approach to reconstruct the layered stacks will be presented. This will be based on the thermodynamic and kinetic approaches presented in this section.

4.3. Reaction of the sulfides

Jost[55] has identified three sulfide reactions when sulfurizing Cu-In thin films. These are labeled A, B and C in Table 4.3 where the standard reaction free energies[4] based on the data of Appendix B are also shown. Reactions D and E were identified during this thesis and are given for comparison.

The $2Cu_2S + CuIn_5S_8 \rightarrow 5CuInS_2$ reaction (B in Table 4.3) was identified in this thesis as being the most relevant sulfide reaction for the rapid thermal process as described in Section 2.6 of Chapter 2.1 because it consumes the secondary $CuIn_5S_8$ phase that may appear during the sulfurization of the metallic alloys. On one hand, a kinetic investigation gives the velocity of its consumption. On the other, the structural relations between the $CuIn_5S_8$ phase and the $CuInS_2$ phase can indicate if texture manipulation of the films is possible by controlling the educt phase. Such a manipulation was already reported for the selenium system[27].

No kinetic or structural investigations concentrate on the reactions listed in Table 4.3. Kim et.al.[58, 59, 60, 61] investigate the kinetics of some reactions in the Cu-Se/In-Se system. Table 4.4

[4]The free energies of reactions indicate the energy gain by the system after the reaction has occurred.

summarizes the selenide reactions together with the activation energies that they obtain. A usual approach to obtain the kinetics of a solid state reaction is to use Avrami's overall transformation equation.

Table 4.3.: Possible sulfide reactions and their free energy of reaction at 298 K from the dataset of Appendix B.

Label	Reaction	ΔG_{298K} / kJmol^{-1}
A	$CuS + InS \rightarrow CuInS_2$	-47
B	$2Cu_2S + CuIn_5S_8 \rightarrow 5CuInS_2$	-13
C	$Cu_2S + 2InS + S \rightarrow 2CuInS_2$	-117
D	$Cu_2S + 3In_2S_3 \rightarrow CuInS_2 + CuIn_5S_8$	-80
E	$2CuS + 5In_2S_3 \rightarrow 2CuIn_5S_8 + S$	-107

Table 4.4.: Selenide reactions from bilayered thin films and their activation energies from [59, 58].

Reaction	E$_a$ /kJmol^{-1}
$2CuSe + In_2Se_3 \rightarrow 2CuInSe_2 + Se$	162±5
$CuSe + InSe \rightarrow CuInSe_2$	66

4.3.1. Avrami's overall transformation kinetics

Avrami derives an equation that describes the kinetics of a solid state transformation as a function of temperature and time[7, 8] (see also[52]). To derive the Avrami's equation the concept of extended volume, V_{ext}^{ψ}, must be introduced. The extended volume is defined as the volume of the transformation product ψ formed after a time t, without taking into account the consumption of the total volume. The infinitesimal evolution of the real volume of the transformation product V^{ψ} is equal to the infinitesimal evolution of the extended volume times the probability of finding untransformed regions:

$$dV^{\psi} = dV_{ext}^{\psi} \cdot (1 - \frac{V^{\psi}}{V}) \ . \tag{4.8}$$

This equation can be integrated into

$$\alpha(t) = \frac{V^{\psi}}{V} = 1 - exp(-\frac{V_{ext}^{\psi}(t)}{V}) = 1 - exp(-(k_p t)^n) \tag{4.9}$$

which is called the Avrami equation, where α is the fractional reaction, k_p the thermally activated transformation constant, and n the Avrami exponent. k_p can be written as $k_p = k_{p0} exp(-\frac{E_a}{kT})$ where k is the Boltzmann constant, k_{p0} is the preexponential factor and E_a is the activation energy. k_p and n fully describe the kinetics of the reaction, whereas E_a characterizes the mechanism through which the reaction occurs.

Table 4.5.: Avrami's exponents for site saturation or constant nucleation, for linear of parabolic growth rates, and for one, two and three dimensioned geometries of the growing phase.

	Site saturation		Constant nucleation	
	Linear growth	Parabolic growth	Linear growth	Parabolic growth
3D	3	$\frac{3}{2}$	4	$\frac{5}{2}$
2D	2	1	3	2
1D	1	$\frac{1}{2}$	2	$\frac{3}{2}$

The kinetics of the transformation depends on the nucleation rate, the growth rate, and the geometry of the growing volume. The time exponent n in Avrami's equation reflects the interaction between these contributions. Table 4.5 summarizes the Avrami exponents for the cases of zero (site saturation) and constant nucleation rate, linear and parabolic growth and one, two and three dimensioned geometries. These are obtained by the analysis of the evolution of the extended volume with time under the given growth and nucleation conditions. Table 4.5 shows that the Avrami exponents takes the same values for different cases. The mechanism of growth cannot be unambiguously identified from a kinetic analysis alone.

Even though kinetic and structural information concerning all of the reactions of Table 4.3 is missing and should be addressed in the future, the reaction $2Cu_2S + CuIn_5S_8 \rightarrow 5CuInS_2$ was identified as being the most relevant sulfide reaction in the rapid thermal sulfurization of Cu-In thin films. This reaction consumes the secondary $CuIn_5S_8$ phase that may appear during sulfurization. The kinetic parameters of this reaction are essential for any process design that includes a step where both ternary phases coexist. The possible structural relationship between the $CuIn_5S_8$ and the $CuInS_2$ phases can justify further studies that attempt to manipulate the texture in these films. These two points will be addressed in Section 5.3 of Chapter 5.

4.4. Thin-film recrystallization

Gottstein[47] defines primary recrystallization as the formation of a new microstructure characterized by the nucleation and growth of nuclei from a plastically deformed bulk metal or alloy. Thompson[128] defines recrystallization of thin films of semiconductors in a similar manner leaving out the necessary condition of the plastic deformation. In the literature concerning thin semiconducting films[133, 131, 50, 71], the term recrystallization is used to describe the formation of a new microstructure characterized by an increase in domain and grain size. This relaxation in the definition of the recrystallization of thin films is due to the fact that this mechanism is monitored in most cases via the apparent grain size and no conclusion are made (or can be made) concerning new nucleation, grains size distributions or dislocation densities.

Through out this thesis the term "thin-film recrystallization" is used to describe the formation of a new microstructure accompanied by an increase in grain size.

This definition of thin-film recrystallization covers mechanisms like primary recrystallization, normal and abnormal grain growth as defined by Gottstein[47] for bulk materials[5]. Furthermore, a

[5]Gottstein defines normal grain growth as the self-similar growth of grains where the grain size distribution remains unchanged, and abnormal grain growth as the growth of particular type of grains accompanied by a splitting of the grain size distribution.

possible healing of structural defects by dislocation movement (or recovery as defined by Gottstein [47]) can also be included in the formation of a new microstructure. Clearly, it is a relaxed definition of the recrystallization and shows that that these mechanisms are not easily discernible and that in the case of chalcopyrite thin films they have not been well studied.

In contrast to this, the thin-film recrystallization is a mechanism that has a major impact on the final microstructure. The average grain size profoundly affects the chemical, physical and electrical properties of polycrystalline thin semiconducting films[129]. For example grain sizes lower than the thickness of the film deteriorate the performance of CdTe/CdS solar cell devices[78]. Linear and planar structural defects may act as recombination centers for charge carriers. The thin-film recrystallization is exploited in a whole range of fabrication techniques to produce $Cu(In,Ga)(Se,S)_2$ materials for solar cells including: thermal evaporation methods[112], electrodeposition plus thermal treatment[135], spray-based deposition[71], ink-based deposition[48] and sulfurization of metallic films[89]. However, no report has isolated and studied the recrystallization of chalcopyrite thin films. Therefore the questions of the driving forces, prerequisites and enhancement factors are not often treated in the literature.

As defined, the thin-film recrystallization mechanism includes the growth of some grains at expenses of others. Therefore the movement of the grain boundaries between growing grains and shrinking grains are at the microscopical basis of this mechanism. This section begins with the theory of grain boundary motion. This is followed by the microscopical models that were proposed to account for experimental observations of new microstructure formation and grain growth.

4.4.1. Theory of grain boundary motion

The movement of a grain boundary is supported by the reduction of the free energy, G^{Gibbs}, of the polycrystalline material when the boundary moves covering the volume dV. This driving force f is defined as:

$$f = -\frac{dG^{Gibbs}}{dV} \ . \tag{4.10}$$

The driving force can have different origins resumed in Table 4.6.

The driving force for the motion of the grain boundaries determines the mechanism for the growth of the grains. As an example, normal grain growth as defined by Gottstein[47] is driven by the reduction of the overall grain boundary energy. This is achieved by the suppression of grain boundaries. The driving force is in this case:

$$f_{normal} = \frac{2\gamma_{GB}}{R} \tag{4.11}$$

where γ_{GB} is the grain boundary energy per unit area and R the mean radius of curvature. For the primary recrystallization as defined by Gottstein[47] the driving force is the reduction of the dislocation density introduced during deformation:

$$f_{Prim.Recrystallization} = \frac{\rho \cdot G \cdot b^2}{2} \tag{4.12}$$

where ρ is the dislocation density, G the shear modulus and b the burgers vector. For a highly defective microstructure (high deformation state) the forces for primary recrystallization are generally larger than those for normal grain growth[6]. This is why recrystallization is observed prior

Table 4.6.: Driving forces for grain boundary motion.

Force Origin	Definition	Remarks
Deformation[47]	$f = \frac{\rho \cdot G \cdot b^2}{2}$	ρ:Dislocation density G: Shear Modulus b: Burgers vector
Stacking faults	$f = n \cdot \gamma_{SF}$	n:Stacking fault density γ_{SF}: Stacking fault energy
Grain boundary energy and curvature[47]	$f = \frac{2\gamma_{GB}}{R}$	γ_{GB}:Grain boundary energy R: Mean grain radius
Elastic[47]	$f = \frac{\sigma^2}{2}(\frac{1}{E_2} - \frac{1}{E_1})$	σ:Stress E:Young's moduli of growing and shrinking grain
Electrochemical	$f = \sum_i kT(c_2^i ln(\frac{c_2^i}{c_0^i}) - c_1^i ln(\frac{c_1^i}{c_0^i})) + Ze(c_2^i\varphi_2 - c_1^i\varphi_1)$	c^i:Concentration of the ith species in growing and shrinking grain φ:Electrical potential in growing and shrinking grain Z: Oxidation State e: Elemental charge

to normal grain growth in deformed metals and alloys. However it must be noted that the growth processes may overlap.

The velocity v at which the grain boundaries move is

$$v = m \cdot f \tag{4.13}$$

where m is called the mobility of the boundary. Grain boundary mobilities have been quantified in the case of normal grain growth as defined by Gottstein[47] in pure and impure metallic systems[6]. It is accepted that:

$$m = m_o \cdot exp(-\frac{Q_G}{kT}) \tag{4.14}$$

where Q_G is the activation energy for grain boundary movement and m_0 a preexponential factor that depends very weakly on temperature. The expression for the velocity of the grain boundary movement is

$$\frac{dr}{dt} = m_o \cdot exp(-\frac{Q_G}{kT}) \cdot f \tag{4.15}$$

where r is average grain radius. Enhancement of grain growth means that, following Equation 4.15, annealing at the same temperature during the same time yields larger grain sizes. This can be achieved by: reducing the activation energy, increasing the driving force or the preexponential factor of the mobility, m_o.

In a simplified microscopic approach for single phase pure systems[47], the movement of the grain boundary is supported by self-diffusion processes. In this case the activation energy for grain boundary motion coincides with the activation enthalpy of self diffusion Q_{SD}. The Bugakov-van Liempt rule states that the activation enthalpy of self-diffusion is linearly proportional to the melting point[81]. According to this rule single phase pure materials with lower melting points should present enhanced grain boundary motion.

4.4.2. Thin-film recrystallization of semiconductors

Thin-film recrystallization of semiconductors can be enhanced by controlled doping and/or controlled annealing[131]. Three microscopical approaches attempt to explain the experimental observations concerning the formation of a new microstructure and the grain growth of thin films of semiconductors:

- The liquid phase approach: a liquid phase placed between the grains is capable of dissolving the primary phase and serves as a growth accelerator. This model is analogous to the V-L-S (vapor-liquid-solid) theory of crystal growth, where the liquid phase serves as a dissolving and transfer agent of all the species transported by the gas phase while the solid phase grows only in contact with the liquid one. Ni and Pa enhance WS_2 crystal growth through intermediate liquid Ni-S and Pa-S phases[20]. Brunken *et al.* find that the liquid phase is necessary for the onset of the thin-film recrystallization of WS_2. Klenk *et al.*[68] use this approach to explain the grain growth of Cu-rich Cu(In,Ga)Se_2 material. However, they is careful in not making any hypothesis concerning an eventual nucleation. Nishiwaki *et al.* finds that when depositing $CuGaSe_2$ in Cu and Se excess conditions, Cu_xSe phases are found between the resulting $CuGaSe_2$ grains[92]. Such observations could support this approach for the thin-film recrystallization of Cu(In,Ga)Se_2 materials. The consequences for the microstructure of $CuInS_2$ films, if the recrystallization occurs following this model, should be twofold: i) if there is new nucleation in the liquid phase, the preferred crystallographic orientation may change ii) secondary phases may remain within the film creating possible paths of preferred electronic transport.
- The topotaxial approach: This model was proposed for $CuInSe_2$ thin films and is also based on the growth of grains supported by a secondary phase, in this case solid $Cu_{2-x}Se$. Wada *et al.*[136] propose that $CuInSe_2$ grows through a topotaxial reaction between $Cu_{2-x}Se$ and $CuInSe_2$. A three-dimensional relationship between the Se anion sublattices of both phases supports cation transport. The cubic $Cu_{2-x}Se$ phase that is lattice matched to the chalcopyrite phase enhances transport of cations from a liquid phase into a growing grain, while the anion sublattice remains unchanged. In the second step of this approach the unordered cations reorganize to form the stable chalcopyrite structure. Abou-Ras[1] proposes that a zero lattice mismatch between the $Cu_{2-x}Se$ phase and the Cu(In,Ga)Se_2 phase correlates with larger grains. The consequences for the microstructure of $CuInS_2$ films if the recrystallization occurs following this mechanism are threefold: i) a structural

relation between the secondary $Cu_{2-x}S$ and the $CuInS_2$ phase should correlate with the same degree of recrystallization; ii) preferred orientation of grains should be similar before and after growth of grains; iii) $Cu_{2-x}Se$ phases should remain within the film creating paths of preferred electronic transport.

- The bulk diffusion approach: the mobility of the grain boundary is correlated to diffusion processes in the bulk of the material. Increasing the mobility of the diffusing species enhances the movement of the grain boundaries and the thin-film recrystallization. Vacancy formation and migration supports self-diffusion in pure crystals (mainly because other diffusion mechanisms have higher activation energies[47]). The addition of dopants, or change in the molecularity determines the point defect concentrations. Increasing the concentration of defects that are relevant for the diffusion enhances the grain boundary mobility. This model predicts a compensation effect when doping n and p at the same time. This compensation was observed for secondary recrystallizations (as defined by Gottstein[47]) in CdS films[50] and for normal grain growth (as defined by Gottstein[47]) in Si thin films[57].

4.4.3. Recrystallization of $CuInS_2$ thin films

Neisser[89] addresses the recrystallization of $CuInS_2$ thin films based on the liquid phase approach described above. He proposes a recrystallization front consisting of the cubic $Cu_{2-x}S$ phase that leaves behind a large-grained material. He presents no experimental evidence to this approach. In contrast to this hypothesis CuS segregates on the surface during deposition of Cu-rich $CuInS_2$ thin films. No secondary Cu-S phase has been observed within or underneath the matrix phase[120, 108, 106].

Silver has been introduced in $CuInS_2$ because it was supposed that it could enhance the thin-film recrystallization. This stems from the fact that $AgInS_2$ has a melting point ~210K lower than $CuInS_2$[16]. On one hand the first results[142] of Ag alloying were discouraging because no observable microstructural changes were detected and an increase in the resistivity of the film was observed. On the other hand, recent investigations on $Cu(In,Ga)Se_2$[39] thin films revealed for the first time a decrease in the microstructural disorder when alloying with Ag. It remains unclear if the alloying with a cation with high mobility like Ag enhances the recrystallization of $CuInS_2$ thin films.

Concerning the recrystallization of $CuInS_2$ thin films, no experimental evidence supports the liquid phase approach, the topotaxial approach or the bulk diffusion approach presented above. Therefore it is not clear what are the prerequisites, driving forces and enhancement factors of this mechanism. This lack of knowledge has limited the possibilities of controlling this mechanism. These questions are addressed in Section 5.4 of Chapter 5.

4.5. Sulfide interdiffusion

When two phases that present a limited solubility range within each other or that can form a mixed phase are in contact, an interdiffusion process at the interface is observed. Smith[121] describes the possible morphologies of the interfaces between the two phases in question. A particular case is the dissolution of one phase by another due to asymmetrical solubilities.

The dissolution proceeds by solid-state diffusion across the interface. This is a process that depends among others on time and temperature. The interdiffusion of the $CuInS_2$-$Cu_{2-x}S$ couple is considered in the following. Neisser[89] estimates the solubility of $CuInS_2$ in Cu_2S at 1 mol %

at 500°C. He does not consider the pressure dependence of the $Cu_{2-x}S$ stoichiometry. There is practically no solubility of Cu_2S in $CuInS_2$ (see Figure A.7 of the Appendix A). This is a clear case of asymmetrical solubilities where the $Cu_{2-x}S$ is capable of dissolving the $CuInS_2$ phase.

The question if the dissolution of $CuInS_2$ by $Cu_{2-x}S$ affects the performance of the solar cells has not been addressed in the literature. Evidence of this dissolution and the possible parameters that control it will be given in Section 5.5 of Chapter 5.

4.6. Summary and unresolved issues

The breakdown of the complex sulfurization of Cu-In thin films in independent mechanisms allows a sequential description of the microstructure formation. The mechanisms are: the alloying of the metals, the alloy sulfurization, the reaction of the sulfides, the thin-film recrystallization and the sulfide interdiffusion. Regarded as independent mechanisms each one has an impact on the microstructure of the $CuInS_2$ films. Their interaction determine the final microstructure of the film after a sulfurization process. Chapter 5 addresses the following unresolved issues concerning each mechanism:

1. Alloying of the metals: the possible opposite strains between the metals and the sulfide films caused by the solid solution of In in Cu.
2. Alloy sulfurization: the formation of the sulfide layered-stack during sulfurization as a function of temperature and pressure.
3. Sulfide reaction: the kinetics of the $2Cu_2S + CuIn_5S_8 \rightarrow 5CuInS_2$ reaction and the structural relationship between the $CuIn_5S_8$ and the $CuInS_2$ phases.
4. Thin-film recrystallization: the description of this mechanism together with its prerequisites and enhancement factors; the enhancement of this mechanism by Ag.
5. Sulfide interdiffusion: the proof of the dissolution of $CuInS_2$ by $Cu_{2-x}S$.

These issues are investigated by means of the *in situ* EDXRD method presented in Chapter 3 and by complementary characterization methods including scanning and transmission electron microscopy (SEM and TEM) and energy-dispersive X-ray spectroscopy (EDS). The main experimental efforts concern the sulfurization of a metallic alloy, the reaction between $Cu_{2-x}S$ and $CuIn_5S_8$ and the thin-film recrystallization.

5. Investigations on the Growth Mechanisms

This chapter presents experimental results that address the unresolved issues and the open questions concerning the growth mechanisms exposed in Chapter 4. This was done (except for the sulfide interdiffusion) by means of the *in situ* EDXRD method described in Chapter 3. Each section begins with the details on the experimental procedures, followed by the presentation of the results and a discussion in terms of their impact on the microstructure. Paths for the exploitation of these mechanisms to purposely modify the microstructure of the $CuInS_2$ films are proposed. The focus of the experimental efforts was placed on the alloy sulfurization, the $2Cu_2S + CuIn_5S_8 \rightarrow 5CuInS_2$ reaction and the thin-film recrystallization. The latter is a process that was monitored for the first time *in situ* for any chalcopyrite thin film. Its investigation led to a thin-film recrystallization model. The model is relevant for every fabrication process that includes a step where both ternary $CuIn_5S_8$ and $CuInS_2$ phases are present as a mixed nanocrystalline layer.

5.1. Alloying of the metals

This section is dedicated to the metal alloying in Cu-In films. During heating, Cu and In react to form alloy phases following the phase diagram from Bolcavage (Fig. A.2 of Appendix A). The phase formation path was given in Section 4.1 of Chapter 4. It includes two transitions: $CuIn_2(s) \rightarrow Cu_{11}In_9(s) + In(l)$ and $Cu_{11}In_9(s) \rightarrow Cu_{16}In_9(s) + In(l)$. If the Cu-rich metals become Cu richer by the consumption of Cu and In in equal amounts, the phases Cu_7In_3 and a solid solution of In in Cu may also appear. The Cu(In) phase will expand and contract proportionally to the In content[124]. This can lead to opposite strains between the solid solution and the sulfide film.

The expansion of the solid solution Cu(In) is the focus of the following investigations. To expose this effect, the particular case of an incomplete sulfurization of a copper-rich Cu-In thin film was studied. This corresponds to an extreme case where the sulfur pressure is very low. If the incomplete sulfurization forms $CuInS_2$, the metals become Cu richer as the sulfurization proceeds. The Cu(In) solid solution should form if enough metallic Cu and In remain. The expansion or contraction of the Cu(In) phase should be triggered by the migration of In.

To obtain the incomplete sulfurization, a Cu-In thin film was heated in a closed reactor that was not previously cleaned by a high temperature step. This means that the rest sulfur inside the reactor is enough to start the sulfurization but not sufficient to finish it.

5.1.1. Cu enrichment of a metallic alloy studied by means of *in situ* EDXRD

$Mo/Cu/CuIn_2$ films on soda-lime glass were obtained by DC magnetron sputtering of 500nm of Mo, 692nm of Cu and 655nm of In and subsequent room temperature storage. Considering the nominal thicknesses and densities, this precursors were Cu-rich with [Cu]/[In]≈2.3. Figure 5.1 presents the evolution of the energy-dispersive X-ray diffraction spectra during heating. In this figure the normalized diffraction intensity is color coded. In this case the sulfurization occurs by means of the rest sulfur present in the reactor. The phase evolution can be followed in the figure:

- At room temperature the layer stack is $Mo/Cu/CuIn_2$. The reflection at ∼46keV results from the overlapping of the $CuIn_2$ 202 and the Cu 111 reflections. The formation of $CuIn_2$ from pure Cu and In thin films is known to happen at room temperature[89]. During heating both peritectic transitions take place forming $Cu_{11}In_9$(s) and $Cu_{16}In_9$(s) .
- Sulfurization starts consuming Cu and In in similar amounts to form $CuInS_2$.
- At nominally 280°C a reflection appears at ∼44.3keV. This reflection was identified by Mainz[76] and Djordjevik *et al.*[32] as the Cu_7In_3 phase. This phase shares reflections with the $Cu_{16}In_9$ phase. The formation of this phase coincides with an increase in the intensity of Cu 111 signal. The alloy becomes more Cu-rich during the formation of $CuInS_2$.
- Between 390°C and 434°C the Cu 111 intensity presents a strong increase accompanied by a shift to lower energies (larger lattice constants), whereas the $Cu_{16}In_9$ reflection decreases in intensity. This is coherent with a continuous copper enrichment of the metallic alloy. The copper phase increases in volume and accommodates increasing amounts of In in its lattice. Note that three intermetallic phases are identified in this temperature range: $Cu_{16}In_9$, Cu_7In_3 and Cu(In). This outlines the fact that thermodynamic equilibrium conditions are not achieved during this heating.

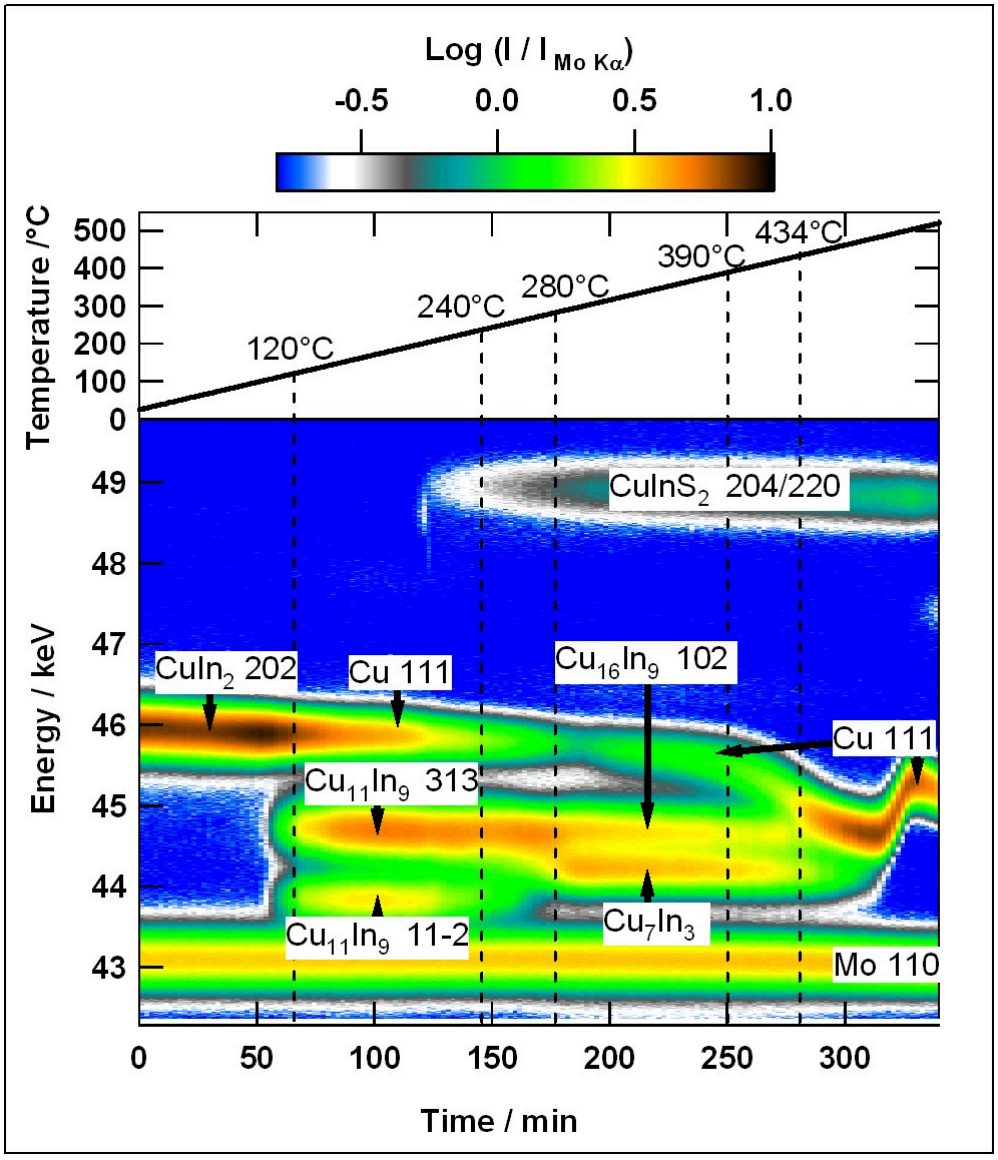

Figure 5.1.: Time-resolved EDXRD spectra of the alloying of a Mo/Cu/$CuIn_2$ ([Cu]/[In]∼2.3) bilayer during an incomplete sulfurization. Two peritectic reactions are identified: $CuIn_2(s) \rightarrow Cu_{11}In_9(s) + In(l)$ and $Cu_{11}In_9(s) \rightarrow Cu_{16}In_9(s) + In(l)$. As sulfurization continues, the alloy becomes more Cu rich forming Cu_7In_3 and Cu(In). The latter phase presents large volume expansions and contractions depending on the In content.

- The Cu-enrichment continues until the $Cu_{16}In_9$ and Cu_7In_3 phases have disappeared. Then the Cu signal shifts in the reverse direction (smaller lattice constants). This means that the In that was dissolved in the Cu lattice leaves it to form further $CuInS_2$. The shift corresponds to a lattice contraction of 1.4%. Such a contraction opposes the thermal expansion of the $CuInS_2$ phase. In the same temperature range $CuInS_2$ expands 1.6 x 10^{-2}%. This can introduce stresses during growth of the $CuInS_2$ film and may result in cavity formation between the metals and the sulfide film.

5.1.2. Conclusions

The Cu-In phase diagram (see Fig. A.2 of Appendix A), with inclusion of the $CuIn_2$ phase, can be used to understand the phase formation during Cu-In alloying even if this takes place out of the thermodynamic equilibrium. There are two reactions that liberate In in the liquid state. This should be kept in mind when heating such samples. When sulfurizing a Cu-In alloy, the composition of the alloy may change. If the sulfide is pure $CuInS_2$, a Cu-rich alloy becomes more Cu-rich during sulfurization. The phase transitions $Cu_{16}In_9$(s) to Cu_7In_3(s) to Cu(In)(s) are observed as expected from the phase diagram. The presence of a solid solution of In in Cu may result in volume contractions or expansions depending on the In content. These can be up to 100 times the expansion of the $CuInS_2$ phase and can be deleterious for the growing sulfide film. Therefore, it would be desirable to design sulfurization processes that avoid the formation of the Cu(In) solid solution in the metallic alloy.

5.2. Sulfurization of the metallic alloy

This section treats the sulfurization of a Cu-In alloy. The sulfurization leads to a layer system of sulfides stacked on top of each other. The composition of the alloy, the temperature and the sulfur pressure determines the sulfide layer sequence (in the following referred as layer sequence) and its morphology. A general approach to the sulfurization of Cu-In alloys will be developed. Such an approach can explain and predict the layer sequence formation during the steady state sulfurization[1] at different pressures and temperatures. This sulfurization approach is founded on:

a) the mass conservation of the cations (Cu and In);

b) the experimental results concerning the steady state sulfurizations of a $Cu_{16}In_9$ thin film;

c) the thermodynamic and kinetic approaches to the sulfurization presented in Section 4.2 of Chapter 4. For the thermodynamic approach a sulfur pressure vs. composition phase diagram is necessary. This was calculated with the software CHEMSAGE[38] for T= 330°C and T= 500°C. Appendix B gives the parameter set and the results of the calculations. The effects of the temperature on the phase diagram are twofold:

- The equilibrium pressures increase with temperature.
- At 330°C there is a two-phase region ($CuIn_5S_8$ and metals) that is absent at 500°C.

Neglecting the second point (that is not relevant for these studies) and keeping in mind a translation in the pressure axis with increasing temperature, the overall form of the phase diagram remains unchanged. Figure 5.2 shows a schematic sulfur pressure vs. Cu composition phase diagram at 330°C. The vertical lines separate regions of two condensed phases: 1) $CuIn_5S_8$-CuS, 2) $CuIn_5S_8$-$CuInS_2$, 3) $CuInS_2$-CuS, 4) $CuInS_2$-$Cu_{2-x}S$, and 6) $Cu_{2-x}S$ and α-Cu(In). Region 5) is composed of at least 3 subregions.

The alloy/sulfide equilibrium (noted as equilibrium 4.7 of Chapter 4) should be defined in region 5) of Figure 5.2. However, the definition of this equilibrium was not possible through the calculations because the thermodynamic data of the intermetallic phases was estimated (see Appendix B). Equilibrium

$$Cu_{16}In_9 + \frac{25}{4}S_2 \rightleftharpoons 9CuInS_2 + \frac{7}{2}Cu_2S \tag{5.1}$$

is assumed as the relevant alloy/sulfide equilibrium of region 5) in Figure 5.2 because the growth of $CuInS_2$ from a $Cu_{16}In_9$ alloy was observed in the literature[98] and during low pressure ($p_S < 10^{-5}$mbar) annealings during this work.

At higher pressures the equilibrium

$$5CuInS_2 + S_2 \rightleftharpoons 4CuS + CuIn_5S_8 \tag{5.2}$$

is clearly identified.

[1] Steady state means that the fluxes (ionic, electronic) and that the intensive variables (p,T) are independent of time.

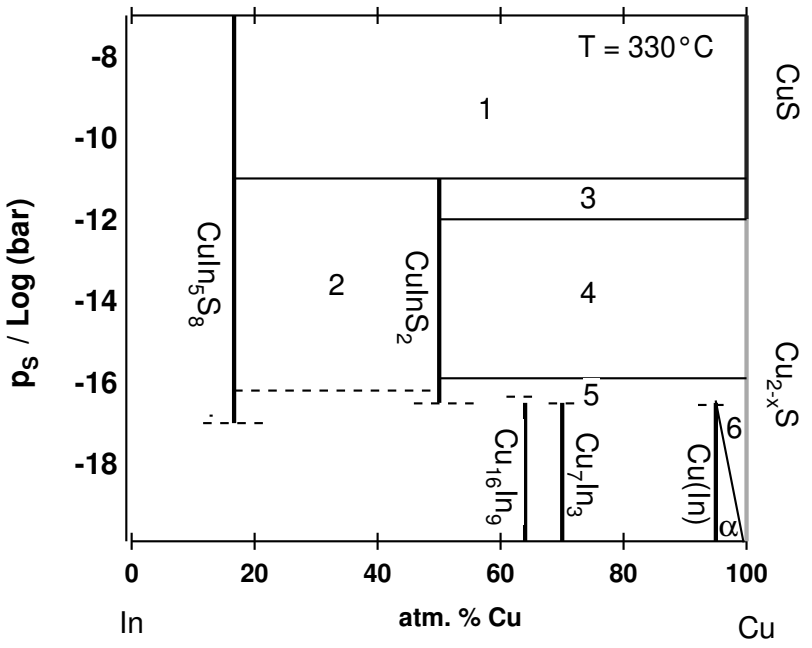

Figure 5.2.: Schematic p_S vs. composition phase diagram at 330°C based on equilibrium calculations made with the software CHEMSAGE[38]. The input data are given in Appendix B. The numbers indicate regions of two condensed phases: 1) $CuIn_5S_8$-CuS, 2) $CuIn_5S_8$-$CuInS_2$, 3) $CuInS_2$-CuS, 4) $CuInS_2$-$Cu_{2-x}S$, and 6) $Cu_{2-x}S$ and α-Cu(In). Region 5 is composed of three sub regions.

5.2.1. Sulfurizations of a $Cu_{16}In_9$ alloy at 175°C, 330°C and 530°C studied by means of *in situ* EDXRD

Precursor films were deposited on soda-lime glass by DC magnetron sputtering in the following order: 500nm Mo, 529nm Cu and 648nm In. Considering the nominal thicknesses and densities, this precursors films were Cu-rich with [Cu]/[In]≈1.8. In a second step the precursors were annealed in a vacuum chamber (base pressure $<10^{-5}$mbar) for 10 min at nominally 450°C. At this temperature (higher than 389°C, see Figure A.2 of Appendix A) the $Cu_{16}In_9$ alloy should be present in the stable η' hexagonal phase. Figure 5.3 shows an energy-dispersive X-ray diffraction spectrum of the layer stack after the vacuum annealing step together with the diffraction lines expected from the JCPDS cards 42-1475 ($Cu_{16}In_9$-hexagonal), 26-0523 ($Cu_{16}In_9$-orthorhombic) and 26-0522 ($Cu_{16}In_9$-orthorhombic). The main reflexions correspond to the hexagonal $Cu_{16}In_9$ indicating that this phase is the main intermetallic phase in the film. However, some lines that do not correspond to the hexagonal phase (indicated by the arrows). This indicates that a small volume percentage of the orthorhombic $Cu_{16}In_9$ phase remains in the sample. The shoulder at ∼44,7 keV also indicates the presence of the Cu_7In_3 phase (see Figure 5.1). No traces of the $Cu_{11}In_9$ or $CuIn_2$ phases are visible.

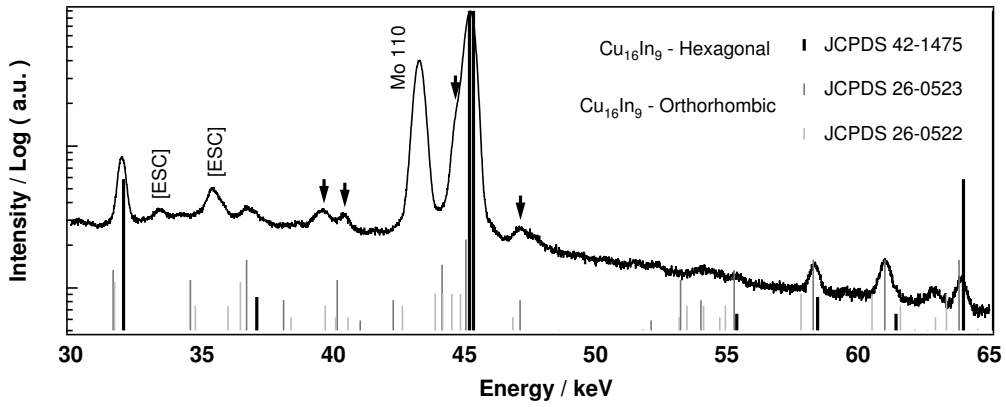

Figure 5.3.: Energy-dispersive X-ray diffraction spectrum (10 min integration time) of a $Cu_{16}In_9$ alloy film precursor for the sulfurization experiments.

To achieve the steady state sulfurization conditions, a controllable and constant sulfur offer is necessary. To do this, two sources that separate sulfur offer and substrate temperature were installed in the in situ chamber presented in Figure 3.1 of Chapter 3: an internal and an external one.

- The internal source contains pure sulfur and forms together with the reaction box a closed volume. The source itself is shielded from the lamps and can be heated separately to 210°C. In the ideal case of no condensation, the pressure inside the volume (source plus reaction box) corresponds to that of the saturated sulfur vapor at 210°C, i.e. $\geq$1 mbar (see Fig. A.1 of Appendix A). This source has the disadvantage that no complete separation of the sulfur offer and the samples is achieved and therefore can only be used in a low temperature range. It was used for the sulfurizations at 175°C and 330°C (see Table 5.1).
- The external source contains pure sulfur and is heated to 190°C. The sulfur vapor leaves the source through a 2mm orifice, fills the vacuum chamber and is pumped by the main pumping system. This configuration has the advantage that a complete separation of sulfur offer and sample temperature can be achieved by the use of the valve that separates the reaction box from the vacuum chamber. It has the disadvantage that the sulfur pressure is lower than 10^{-3}mbar. This source was used for the sulfurization at 530°C (see Table 5.1).

Figure 5.4 presents schematically both sulfur sources. Table 5.1 summarizes the sulfurization experiments: their names, the sulfur sources, the estimated pressures and the annealing temperatures.

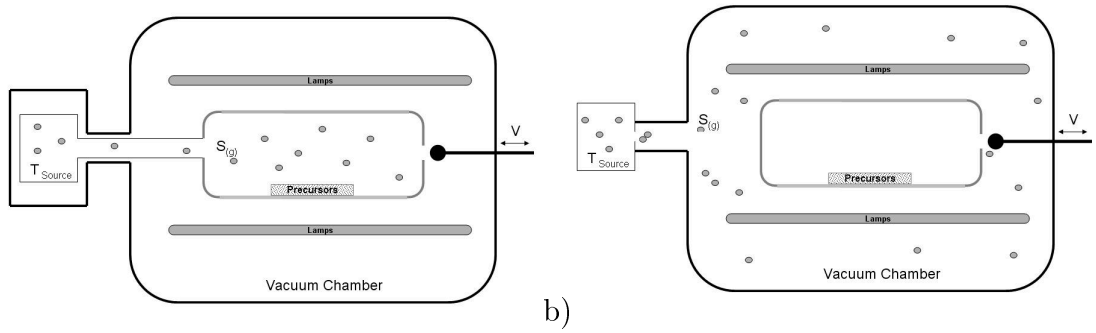

Figure 5.4.: Representation of the a) internal and b) the external sulfur source for the sulfurizations under a controlled atmosphere.

Table 5.1.: Sulfur sources, estimated pressures and temperatures of the sulfurization experiments.

Experiment Name	Alloy	Sulfur source	Pressure / mbar	Temperature / °C
$Alloy_{175°C}$	$Cu_{16}In_9$	Internal	∼1	175
$Alloy_{330°C}$	$Cu_{16}In_9$	Internal	∼1	330
$Alloy_{530°C}$	$Cu_{16}In_9$	External	$< 1x10^{-3}$	530

Sulfurization at 175°C

Figure 5.5 presents the sulfurization of the $Cu_{16}In_9$ precursor alloy (see Figure 5.3) at 175°C using the internal sulfur source, i.e. experiment $Alloy_{175°C}$ of Table 5.1. Sulfurization starts before the steady state conditions are reached (assumed between markers (a) and (b)) with the formation of a CuS phase. Sulfurization continues with the formation of $\alpha-$InS. The alloy is completely consumed by the formation of CuS and InS. The inset of Figure 5.5 presents the evolution of the intensities of the CuS 103 line, the $\alpha-$InS 110 line and of the metallic alloy phase (labeled as $Cu_{16}In_9$ 102). Assuming no texture effects are present, these intensities can be used as a measure of the volume of the diffracting phase (see Equation 3.4 of Chapter 3). The inset of Figure 5.5 shows that both the CuS and InS intensities evolve linearly and with the same time constants. This reaction can be written as

$$Cu_{16}In_9 + \frac{25}{x}S_x \rightarrow 16CuS + 9InS \ . \tag{5.3}$$

Reaction 5.3 also occurs when sulfurizing $Cu/CuIn_2$ stacks with [Cu]/[In]≈1.6 at 150°C in the external source configuration. In this case the stack reacts first to $Cu/Cu_{11}In_9$ + In(l) before it transforms to CuS and InS in a similar manner as that shown in Figure 5.5. Figure 5.6 shows an SEM image and mappings of the In L and Cu L fluorescence lines of such a film. An almost complete separation of the Cu and In species is observed. The CuS is situated at the surface of the sample covering the underlying $\alpha-$InS layer.

If the sulfur pressure is low ($p_S<10^{-3}$mbar), reaction 5.3 does not occur at the same velocity. Low-pressure sulfurizations while heating at constant rates of $30Kmin^{-1}$ realized during this thesis showed no presence of CuS or InS. Pietzker[98] and Mainz[76] report on low pressure sulfurizations done with constant heating rates of $24Kmin^{-1}$ and $18Kmin^{-1}$ without the appearance of CuS or InS. On the other hand, high pressure sulfurizations (alloy in contact with liquid sulfur) reported by Jost[55] show a reaction to CuS and InS below 250°C while heating at a rate of $48Kmin^{-1}$.

$CuInS_2$ thin films were fabricated from the CuS/InS bilayers resulting from this type of sulfurization. To achieve this, the bilayers similar to the one presented in Figure 5.6 were heated in a closed volume to 500°C. The layers presented as a general rule an inhomogeneous, small-grained and porous morphology. Pinholes of large dimensions were present through out the film. Figure 5.7 presents an example of such a morphology.

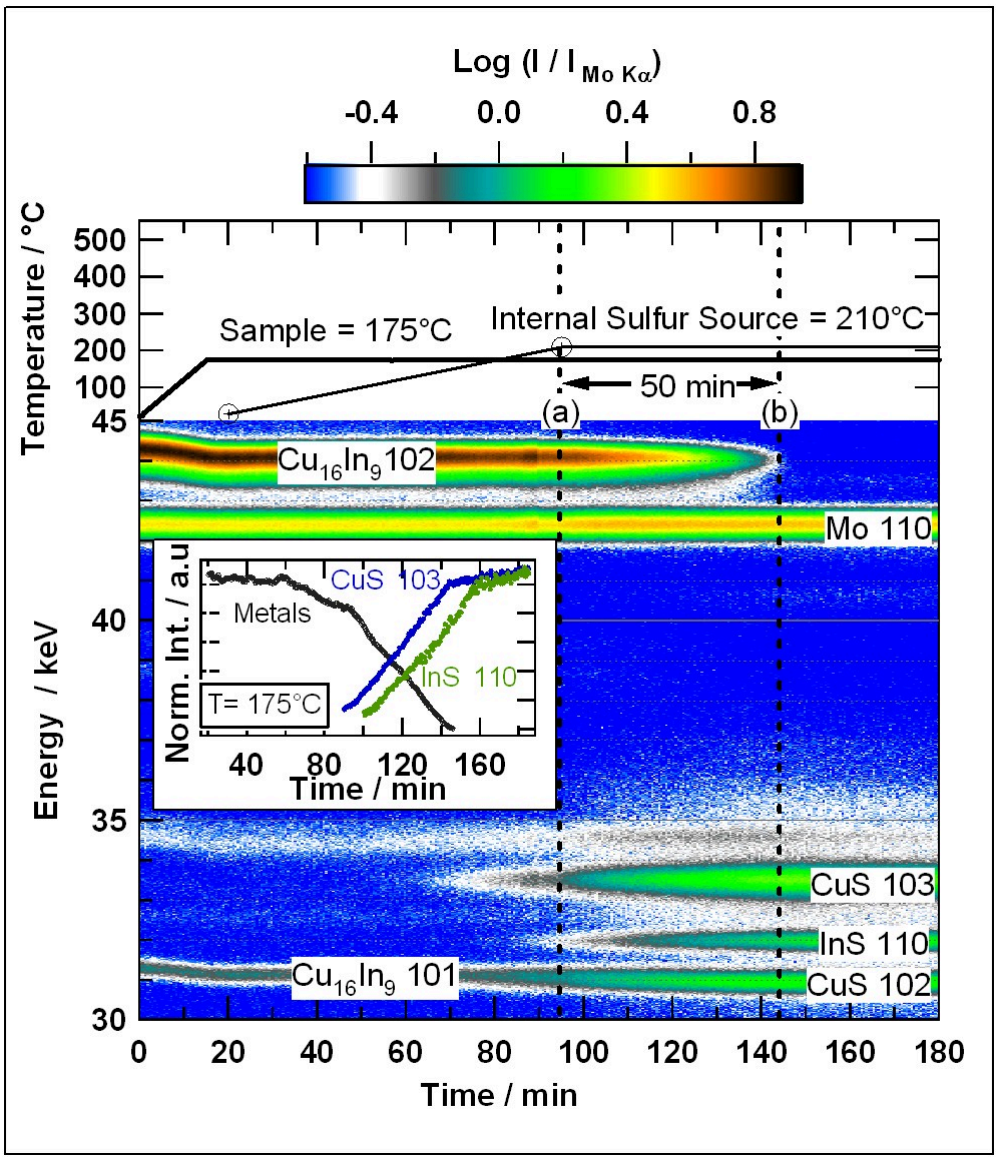

Figure 5.5.: Time-resolved EDXRD spectra of the sulfurization of a $Cu_{16}In_9$ film at 175 °C by means of the internal sulfur source. Marker (a) indicates the point where steady state sulfurization conditions are achieved, marker (b) the time where the metals have disappeared. The inset shows the evolution of the metallic reflection intensity at ∼44keV and of the CuS 103 and InS 110 reflection intensities.

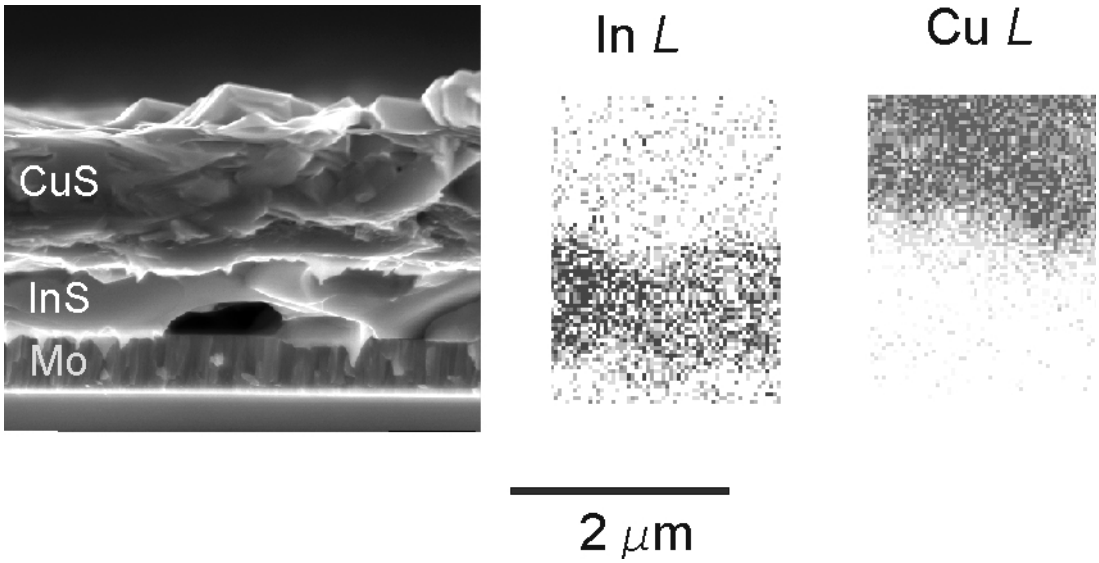

Figure 5.6.: CuS and InS after sulfurization at $p_S < 10^{-3}$mbar and T=150°C. On the left a cross-section of the sample. On the right energy-dispersive X-ray fluorescence mappings of the In L and Cu L lines.

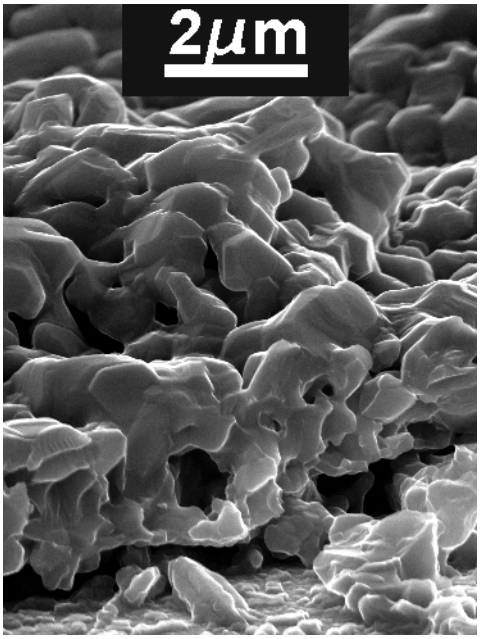

Figure 5.7.: $CuInS_2$ obtained by sulfurization of Cu-In metals. The characteristic of this sulfurization was that the film completely reacted to CuS and InS at 200°C before reacting to $CuInS_2$ at higher temperatures (T_{max}=550°C). The morphology of the film is very perturbed with large pinholes and pores and presents small grains.

Sulfurization at 330°C

Figure 5.8 presents the sulfurization of the $Cu_{16}In_9$ alloy (see Figure 5.3) at 330°C using the internal sulfur source, i.e. experiment $Alloy_{330°C}$ of Table 5.1. Sulfurization starts before the steady state conditions are reached (marker (a)). The shift to higher energies of the 220 $Cu_{2-x}S$ reflection (indicated as red markers at approximately 48.5keV in the figure) indicates that the sulfur pressure is still increasing before marker (a)[2]. In the steady state (assumed between markers (a) and (b)) sulfide phases are $CuInS_2$, $CuIn_5S_8$ and CuS. The reflection attributed to the metallic alloy is slightly shifted to lower energies indicating the presence of the Cu_7In_3 phase. From break-off experiments of sulfurizations that followed the same reaction path and EDS (energy-dispersive spectroscopy) analysis of the corresponding cross-sections, it was concluded that the CuS phase forms a closed layer on the surface of the films. The In L signals disappear at the surface layer where the Cu L signals are continuous and more intense. Such break-off experiments are analyzed in detail in Chapter 6.

Sulfurization at 530°C

Figure 5.9 presents the sulfurization of the $Cu_{16}In_9$ alloy (see Figure 5.3) at 530°C using the external sulfur source, i.e. experiment $Alloy_{530°C}$ of Table 5.1. No sulfurization takes place before the steady state conditions (assumed between markers (a) and (b)) are reached. This was achieved by opening the valve of the reaction box at marker (a). During the steady state sulfurization the only sulfide detected is $CuInS_2$. The growth follows a linear rate (see the linear fit of the $CuInS_2$ 112 reflection at the the beginning of the sulfurization in the inset of Figure 5.9). The metallic alloy enriches in Cu. The alloy reacts following the schema depicted in Section 5.1: first to Cu_7In_3 and then to a solid solution of In in Cu. $Cu_{2-x}S$ forms at the end of the reaction when the only metallic phase present is Cu.

Figure 5.10 presents the morphology in cross-section of the sample sulfurized at 530°C. The film is characterized by the presence of grains of approximately 1μm in dimensions and by a poor adhesion to the Mo.

[2] A shift to higher energies means a contraction of the lattice constants (see Equation 3.7 of Chapter 3). The lattice constants of this phase contract with increasing sulfur pressures[102].

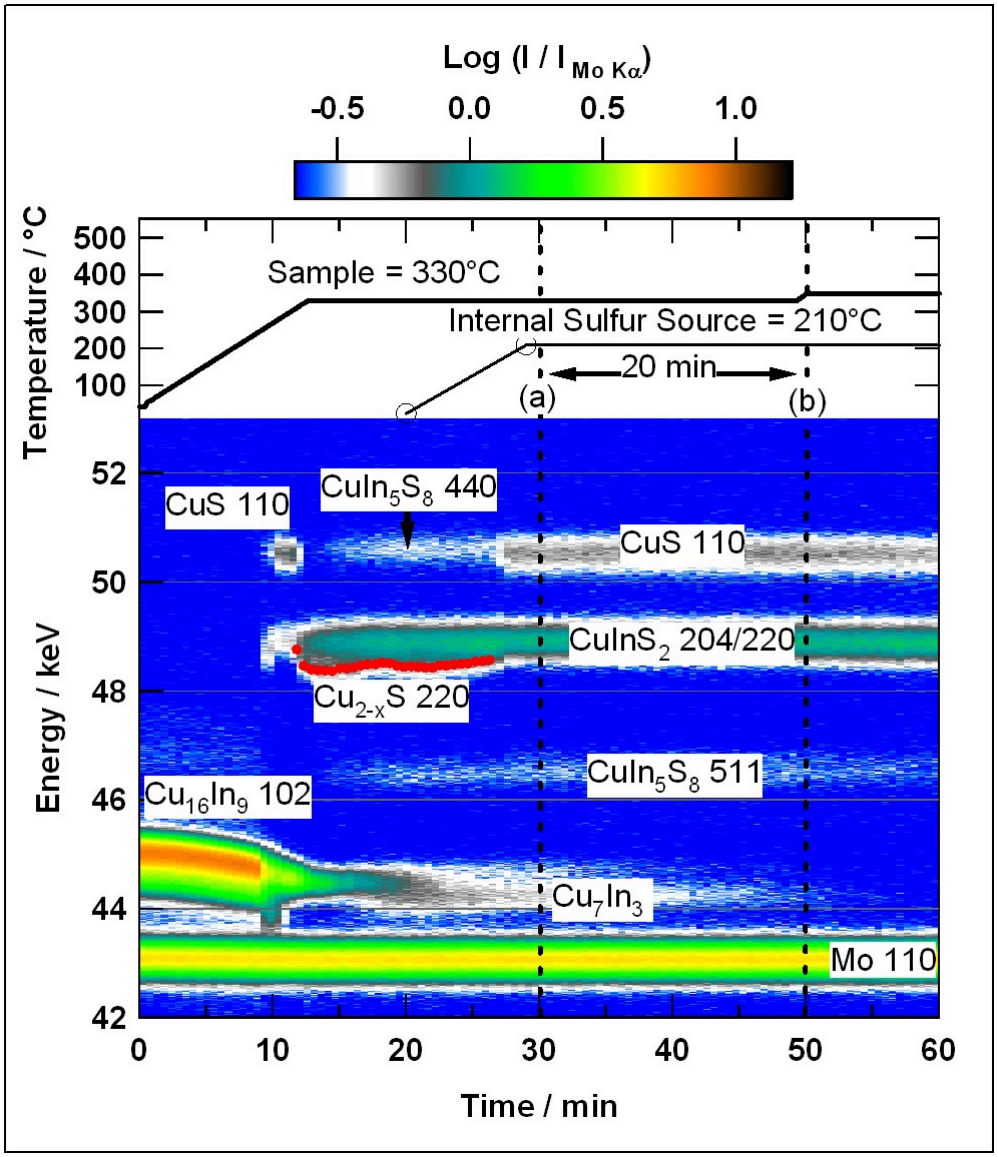

Figure 5.8.: Time-resolved EDXRD spectra of the sulfurization of a $Cu_{16}In_9$ film at 330 °C by means of the internal sulfur source. Markers (a) an (b) indicate the possible time frame of the steady state conditions.

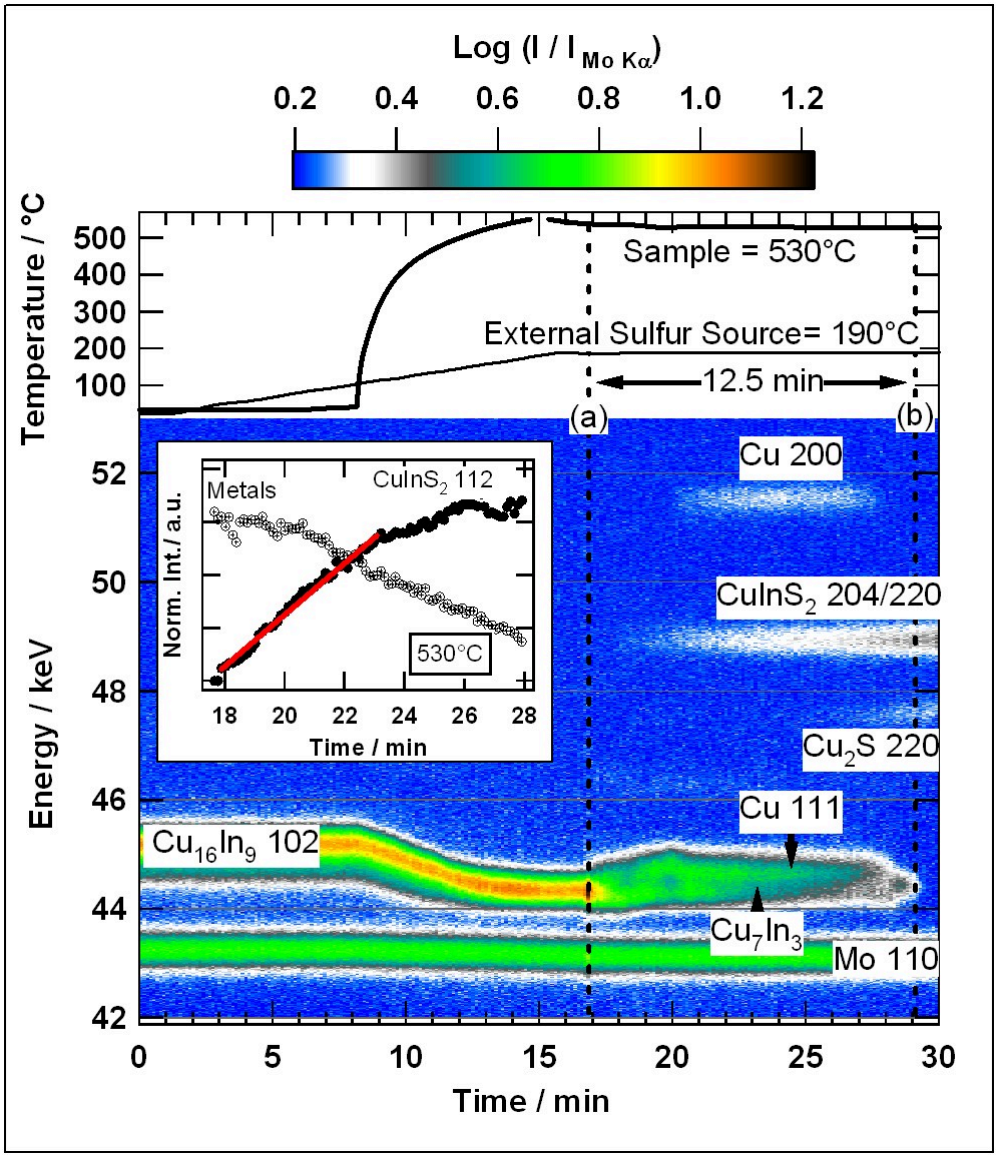

Figure 5.9.: Time-resolved EDXRD spectra of the sulfurization of a $Cu_{16}In_9$ film at 530 °C by means of the external sulfur source. Markers (a) an (b) indicate the possible time frame of the steady state conditions. The inset shows the evolution of the metallic intensity at ∼44keV and of the $CuInS_2$ 112 reflection. The latter is well fitted by a line (in red) at the beginning of the sulfurization.

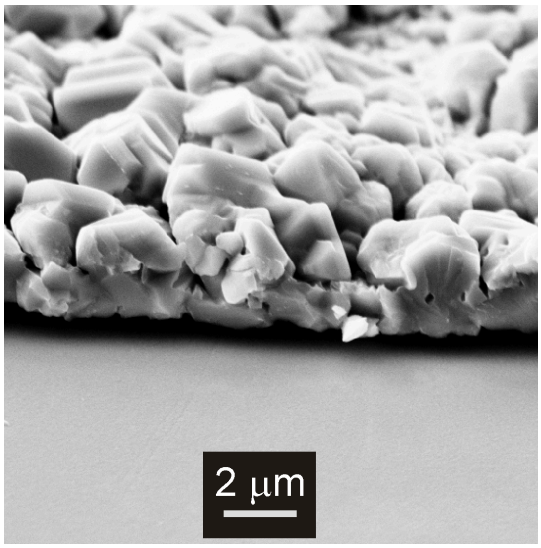

Figure 5.10.: Scanning electron microscope morphology of the $Cu_{16}In_9$ alloy sulfurized at 530°C.

5.2.2. Layer sequences of the sulfurizations

The experimental results show that the layer sequence formation during the sulfurization of a $Cu_{16}In_9$ alloy depends critically on the temperature and on the sulfur pressure. Figure 5.11 gives a simplified representation of the observed layer sequences as a function of temperature and pressure.

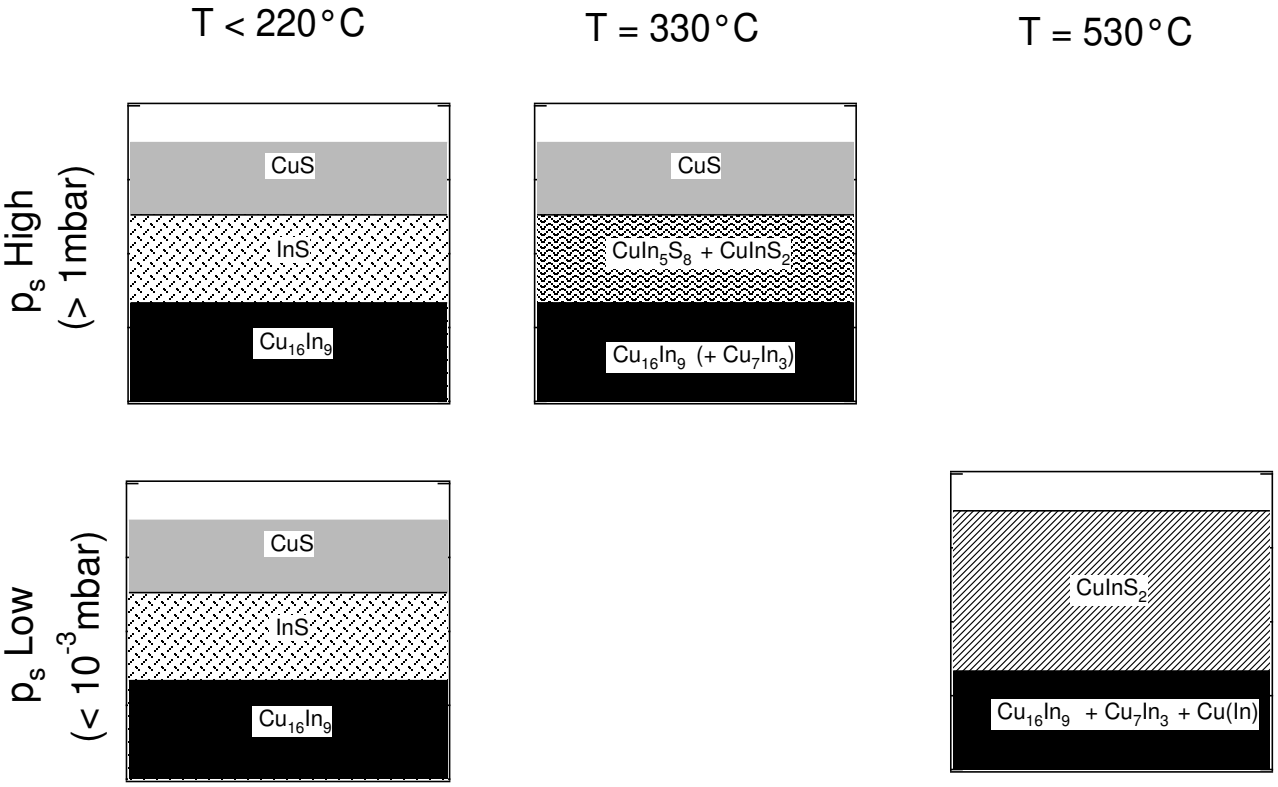

Figure 5.11.: Summary of the layer sequences observed during the steady state sulfurizations of a $Cu_{16}In_9$ alloy as a function of temperature and pressure.

5.2.3. Kinetic, thermodynamic and semithermodynamic approach to the layer sequence formation

Based on the experimental results (summarized by Figure 5.11) and on the kinetic and thermodynamic approaches presented in Section 4.2 of Chapter 4, a general approach for the layer sequence formation is proposed in this section. This is based on the hypothesis that steady state conditions are achieved (constant pressure, temperature and fluxes) between the markers (a) and (b) of Figures 5.5, 5.8 and 5.9 and on the constancy of the number of cations (Cu and In). The general sulfurization approach is based on the division of the sulfurization in three modes whose applicability depend on the temperature:

1. A sulfurization purely governed by kinetics;
2. A sulfurization purely governed by thermodynamics;
3. A sulfurization where both kinetics and thermodynamics play a role.

Sulfurization governed by kinetics

At low temperatures (below 250°C) the sulfide formation depends on the growth velocity of the individual phases and not on their thermodynamic stability. Figure 5.5 shows the formation of CuS and InS from the $Cu_{16}In_9$ alloy. These two phases are not expected at equilibrium at any sulfur pressure (see calculated phase diagram 5.2). CuS is the most unstable sulfide in the whole system (see Table 4.1). If only kinetics and not thermodynamics are governing the sulfurization, the CuS nuclei (that grow faster than others[85, 19], see also Section 4.2.2.2 of Chapter 4) are expected to form a closed surface layer. Further growth of the CuS layer occurs thanks to the diffusion of Cu through the CuS layer to the surface. However, the diffusion is not the rate limiting step because a linear growth is observed (see inset of Figure 5.5). In analogy to chalcogenization of pure substances it is the reaction at the CuS/S_x interface or at the alloy/CuS interface. The most probable rate limiting step is the reaction at the CuS/S_x surface. This explains that the sulfurization is slower at lower pressures and that In sulfurizes to α-InS with the same time constants.

Sulfurization governed by thermodynamics

At high temperatures (higher than 400°C[3]) the sulfide formation depends on the local thermodynamic stability of each phase. The sulfur activity decreases within the film from the value imposed by the working pressure at the surface (interface (ii) of Figure 4.2 of Chapter 4)[4] to the value at the alloy/sulfide interface (interface (i) of Figure 4.2 of Chapter 4). The latter is fixed by equilibrium $Cu_{16}In_9 + \frac{25}{4}S_2 \rightleftharpoons 9CuInS_2 + \frac{7}{2}Cu_2S$. Under this approach, the layer sequence can be read in a S pressure (understood in this case as activity) vs. composition phase diagram [44].

The following steps can be used to reconstruct the layer sequence in the case of a thermodynamic sulfurization:

[3]Raman measurements reported by Rudigier[104] and recrystallization experiments reported in this thesis, show that at least 400°C are necessary to transform the metastable CuAu- ordered $CuInS_2$ in the stable chalcopyrite phase. It is reasonable to postulate that this is a characteristic temperature of the Cu-In-S system where the system can achieve the thermodynamic equilibrium.

[4]The value of the sulfur pressure imposed at the surface is correlated but not equal to the working pressure. Indeed Appendix B shows that the calculated equilibrium sulfur pressure values are orders of magnitude lower as that of the usual working pressures (10^{-4} to 10mbar). The effective surface sulfur pressure depends on adsorption, dissociation and evaporation processes (steps 1 and 2 of the sulfurization steps) and on the temperature[121].

1. Placing the working coordinates (surface pressure, p_S, and the alloy composition, x) in the p_S vs. composition phase diagram. They can fall in a two-phase region.

2. Identifying the sulfide with the highest absolute free energy. This sulfide grows at the surface.

3. Identifying the underlying sulfides. They must be stable at sulfur pressures lower than the one imposed at the surface, and must satisfy the mass conservation of the cations. Possible composition variations of the metallic alloy must be taken into account.

Following these steps, the layer sequence during the steady state sulfurization at low pressure (p_S<10^{-3}mbar) and 530°C shown in Figure 5.11 can be reconstructed. The experiment showed that:

a) The only sulfide is $CuInS_2$: it can be deduced that the working coordinates fall in the $CuInS_2$ - Cu_xS region (regions 3 or 4 from Fig. 5.2). The absolute free energy of formation of the $CuInS_2$ phase is larger than that of the Cu-S phases. This justifies *a posteriori* (following the step 2 of the layer sequence reconstruction) that the surface layer is $CuInS_2$.

b) The metals react to Cu-richer phases during sulfurization. This is indeed the only possibility to satisfy mass conservation without the formation of another sulfide.

Note that the equilibrium $Cu_{16}In_9 + \frac{25}{4}S_2 \rightleftharpoons 9CuInS_2 + \frac{7}{2}Cu_2S$ imposes the presence of Cu_2S at the interface alloy/sulfide (interface (i) of Figure 4.2). This phase can be present at the interface but is no longer present within the film (it is not detected in the X-ray spectra). This leads to the important conclusion:

- equilibrium 5.1 does not imply considerable volume percentage of the Cu_2S phase at the interface (i).

Figure 5.12 shows the reconstructed layer sequence. The possible working coordinates are marked as a cross. In the steady state, the layered stack is composed of a Cu-enriched alloy and a $CuInS_2$ film. The arrow indicates the increasing sulfur activity (pressure). Under this approach there exists a strong sulfur activity gradient within the film. This gradient supports the diffusion of cations as described for pure metallic systems in Section 4.2.1 of Chapter 4.

The rate limiting step is not the cation diffusion itself but the reaction at the surface given the linear evolution of the $CuInS_2$ intensity in the inset of Figure 5.9. In analogy to the sulfurization of Cu, it can be expected that increasing the S pressure should lead to a crossover, where the rate limiting step becomes the diffusion of the cations. However if the S pressure is increased above the pressure of equilibrium $5CuInS_2 + S_2 \rightleftharpoons 4CuS + CuIn_5S_8$ other sulfide phases are expected. Indeed, following the phase diagram in Figure 5.12 it is expected that at 530°C and sulfur pressures high enough to enter the $CuIn_5S_8$-CuS region, the thermodynamic sulfurization leads to a layer sequence where $CuIn_5S_8$ grows at the surface. This prediction should be verified in the future with an experimental setup that allows to study this sulfurization conditions.

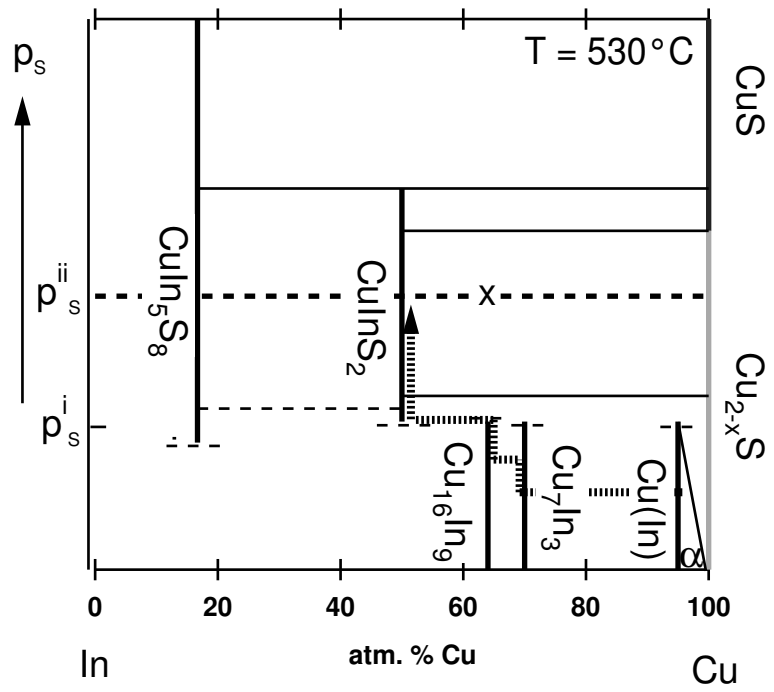

Figure 5.12.: Layer sequence formation during the steady state sulfurization of $Cu_{16}In_9$ at 530°C and low sulfur pressures. The layer stack is composed of a Cu-enriched alloy and a $CuInS_2$ film. The cross indicates the possible working coordinates and the arrow indicates the increasing sulfur activity (pressure) in the stack. The arrow goes through the different layers in the idealized stack: from the metallic alloy to the surface of the $CuInS_2$ phase.

Semithermodynamic sulfurization

At intermediate temperatures, a pure thermodynamic approach does not describe the steady state sulfurization. The following hypothesis are used in this semithermodynamic mode of the sulfurization:

- The surface sulfide layer is determined by the fastest growing sulfide between those of the relevant two-phase region.
- The underlying sulfides are at local thermodynamic equilibrium and can be read in a p_S vs. composition phase diagram.
- The sulfur activity (pressure) decreases from the surface of the stack (interface (ii) of Figure 4.2 of Chapter 4) to the alloy/sulfide interface (interface (i) of Figure 4.2 of Chapter 4) determined by equilibrium 5.1. As pointed out in the previous paragraph, this does not imply the presence of considerable amounts of Cu_2S at the interface (i).

Given these working hypothesis, the p_s vs. composition phase diagram shown in Fig. 5.2 serves to identify possible layer sequences. The following steps can be used to reconstruct the layer sequence in the case of a semithermodynamic sulfurization:

1. Placing the working coordinates (surface pressure, p_S, and the alloy composition, x) in the S pressure vs. composition phase diagram. They can fall in a two-phase region;

2. Identifying the sulfide with the lowest absolute free energy. This sulfide will grow at the surface.
3. Identifying the underlying sulfides. They must be stable at sulfur pressures lower than the one imposed at the surface, and must satisfy the mass conservation of the cations. Possible composition variations of the metallic alloy must be taken into account.

Following these points, the layer sequence during the steady state sulfurization at high pressures (p_S>1mbar) and 330°C shown in Figure 5.11 can be reconstructed. The experiment shows that the steady state sulfide phases are $CuInS_2$, $CuIn_5S_8$ and CuS. CuS forms a closed layer at the surface (see break-off experiments of Section 6 of Chapter 6). From this it is deduced that the working coordinates fall in the $CuIn_5S_8$- CuS region (region 1 from Fig. 5.2).

CuS is more unstable than $CuIn_5S_8$. This justifies a posteriori the fact that it forms the surface layer (because it is expected to grow faster [85, 19], see also Section 4.2.2.2 of Chapter 4). At a certain point within the stack the phases $CuIn_5S_8$, CuS and $CuInS_2$ must be stable according to equilibrium 5.2. Both $CuInS_2$ and $CuIn_5S_8$ are stable at continuously decreasing sulfur pressures and may grow side by side as the sulfur activity decreases within the film.

Figure 5.13 shows the reconstructed layer sequence in the S pressure vs. composition diagram of the steady state sulfurization at 330°C and high pressures (p_S>1mbar). The possible working coordinates are marked by a cross. In the steady state, the layered stack is composed of a Cu-enriched alloy, a $CuInS_2$-$CuIn_5S_8$ mixed layer whose composition cannot be defined through this approach (the possible coexistence is represented by the hatched area in the figure), and a closed CuS layer on the surface. The arrow indicates the increasing sulfur activity within the layered film.

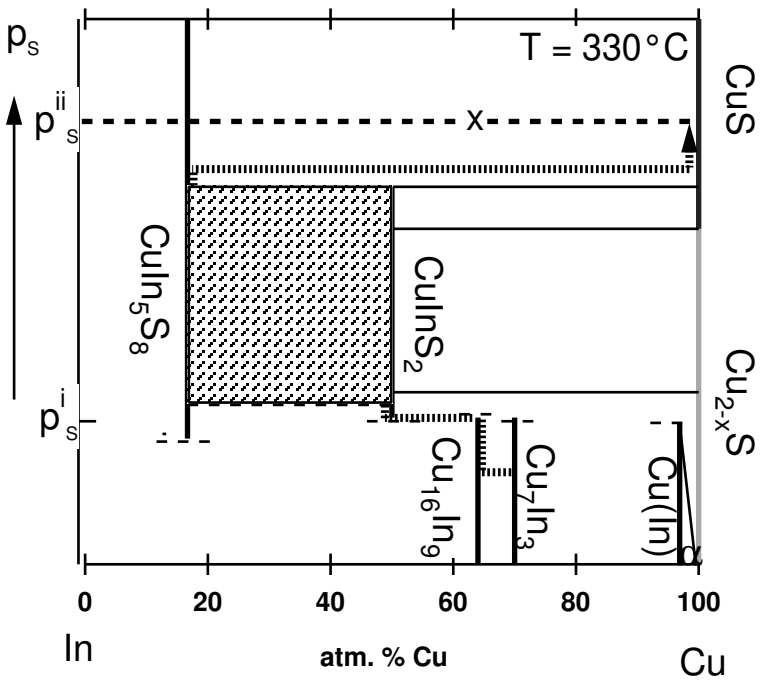

Figure 5.13.: Layer sequence formation during the steady state sulfurization of $Cu_{16}In_9$ at 330°C and high sulfur pressures. The layer stack is composed of a Cu enriched alloy, a mixture of $CuInS_2$ and $CuIn_5S_8$ whose composition is undefined (represented by the hatched area) and a CuS film on the surface. The cross indicates the possible working coordinates, and the arrow indicates the increasing sulfur activity (pressure) within the stack. The arrow goes through the different layers in the idealized stack: from the metallic alloy through a mixed $CuInS_2$-$CuIn_5S_8$ layer to the surface of the CuS phase.

5.2.4. Conclusions

In the Cu-In-S system two characteristic temperatures, T_D and T_C, separate three steady state sulfurization modes: a kinetic, a semithermodynamic and thermodynamic one.

- Below a decomposition temperature T_D, around 220°C and 250°C, the layer sequence formation is determined by the growth rate and not by the thermodynamic stability of the phases. A criterion for a fast growth rate is a low absolute free energy of formation. The CuS phase presents the lowest free energy of formation and therefore is expected to form the surface layer during this type of sulfurizations. This process will decompose the alloy through the formation of CuS and InS. If this process is not avoided the final $CuInS_2$ film resulting from the reaction between CuS and InS will present a small-grained and porous morphology. Such a morphology makes the $CuInS_2$ film inadequate for its use as a solar cell absorber.
- Above a critical temperature T_C, between 330°C and 500°C (probably around 400°C), the local thermodynamic stability of the phases control the sulfurization. This approach is based on the hypothesis that the sulfur activity decreases from the surface of the film to the sulfide/alloy interface. The layer sequence during steady state sulfurization can be

reconstructed based on the sulfur pressure (interpreted as activity) vs. composition phase diagram shown schematically in Figure 5.2.

- Between both temperatures a cross over between a sulfurization governed by kinetics and one governed by thermodynamics is expected. It was proposed that the p_S vs. composition phase diagram can be used to predict the layer sequence also above T_D. Between T_D and T_C, a lower free energy of formation can be used as a criterion to determine which of the sulfides of the relevant two-phase region grows at the surface.

This general approach is a tool to understand and reconstruct the sulfide layered-stack that forms during the sulfurization of a Cu-In alloy. Future investigations should, based on this qualitative approach, attempt to quantify the thickness of the layers and their eventual compositional gradients. A particular case of this layered stack formation is observed when sulfurizing at T$\sim$330°C and high S pressures (higher than 1mbar). In this case an intermediate layer where both ternary phases $CuInS_2$ and $CuIn_5S_8$ coexist is formed. The $CuIn_5S_8$ phase must be consumed to obtain films containing only $CuInS_2$ (and eventually Cu-S phases on the surface that can be removed by a chemical etching treatment). The consumption of $CuIn_5S_8$ phase by the solid state reaction with the $Cu_{2-x}S$ phase will be analyzed in the next section.

5.3. Sulfide reaction: $2Cu_2S + CuIn_5S_8 \rightarrow 5CuInS_2$

The reaction

$$2Cu_2S + CuIn_5S_8 \rightarrow 5CuInS_2 \tag{5.4}$$

(reaction B of Table 4.3 of Chapter 4) is of particular interest for any $CuInS_2$ fabrication process that includes a step where both ternary phases may coexist. The $CuIn_5S_8$ phase can be consumed through this reaction. The kinetics of this reaction and the possible structural relationship between the $CuIn_5S_8$ and the $CuInS_2$ phases will be studied in this section.

5.3.1. In-S / Cu-S thin-film reactions studied by means of *in situ* EDXRD

To study the mechanism and kinetics of Reaction 5.4, precursors consisting of a In-S/Cu-S bilayer were deposited by means of thermal evaporation on soda-lime glass coated with 500nm of Mo. The two steps of the evaporation deposition were:

- the evaporation of In (source temperature 920°C) under constant sulfur offer (source temperature 190°C) at a substrate temperature of 300°C and p$<10^{-4}$mbar;
- the evaporation of Cu (source temperature 1410°C) under constant sulfur offer (source temperature 190°C) at a substrate temperature 100°C and p$<10^{-4}$mbar.

Figure 5.14 shows an angle-dispersive X-ray spectrum of such a bilayer. According to the JCPDS files listed in Table 3.4 the phases present in the precursors corresponded to $\beta-In_2S_3$ and CuS. Figure 5.15 presents the SEM cross-section of the precursor bilayer. From these measurements the total thickness of the bilayer was approximately 2.7μm. Two morphologically different layers are visible in the cross-section: a small-grained compact $\beta-In_2S_3$ layer and a pyramidal, compact CuS layer phase. From the measured thicknesses and the reported densities ($\rho_{CuS} = 4.7gcm^{-3}$ and $\rho_{\beta-In_2S_3} = 4.9gcm^{-3}$) the Cu to In ratio of the films was estimated to be: 1< [Cu]/[In]<1.3.

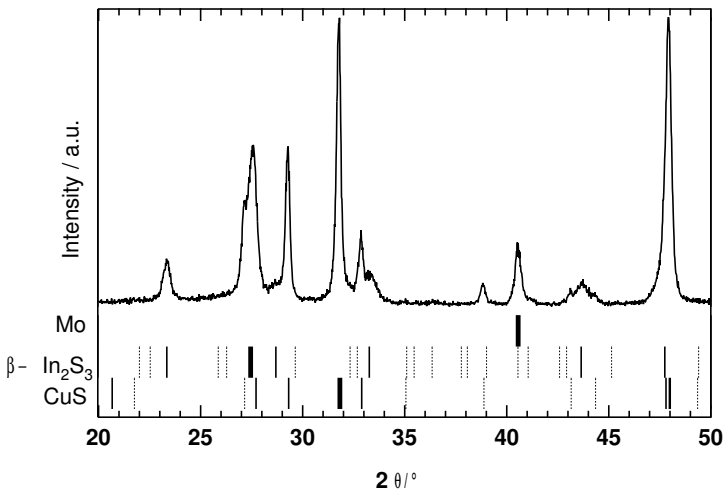

Figure 5.14.: Angle-dispersive X-ray spectrum of the Mo/β-In_2S_3/CuS precursor stack.

The precursors were annealed in vacuum conditions (p$<10^{-3}$mbar) in the *in situ* chamber (see Figure 3.1 of Chapter 3). The annealing programs included an annealing step of 2 minutes at

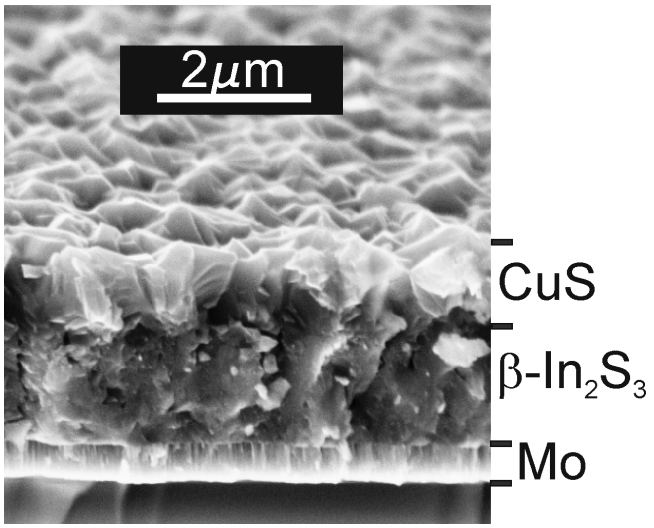

Figure 5.15.: Scanning electron microscope cross-section of the Mo/β-In_2S_3/CuS precursor stack.

nominally 40°C to assure the same starting conditions for all experiments. Energy-dispersive X-ray diffraction spectra were recorded with an exposure time of 5 seconds. For the data treatment, 20 to 100 consecutive spectra were added depending on the total transformation times. This led to effective integration times between 1.6 and 8.3 minutes. This procedure implied loosing in time resolution but gaining in the accuracy of the intensity determination by the fitting procedure mainly because the noise to signal ratio was reduced (see Figure 3.13 of Chapter 3). The intensity of the diffraction signals was obtained by fitting the data with Gaussian profiles exclusively. Table 5.2 summarizes the experiments names, the processing parameters and the effective integration times.

Table 5.2.: Experiments names, layer stacks, annealing parameters and effective integration times for the EDXRD data collection for the kinetic investigations of reaction $2Cu_2S + CuIn_5S_8 \rightarrow 5CuInS_2$. Experiment $Texture_{320}$ included a more complex heating program in presence of elementary sulfur depicted in Figure 5.21.

Name	Stack	Pressure/mbar	Temp./ °C	Integration time / min
$Binary_{300}$	Mo/β−In_2S_3/CuS	$< 1x10^{-3}$	300	∼8.3
$Binary_{325}$	Mo/β−In_2S_3/CuS	$< 1x10^{-3}$	325	∼4.2
$Binary_{340}$	Mo/β−In_2S_3/CuS	$< 1x10^{-3}$	340	∼1.6
$Texture_{320}$	Mo/β−In_2S_3/CuS	-	320	0.08

Evolution of the Mo, $CuIn_5S_8$ and $CuInS_2$ reflections

Figure 5.16 shows the evolution of the energetic position of the Mo 110 reflection during experiments $Binary_{300}$, $Binary_{325}$ and $Binary_{340}$. During the annealing at 40°C, all signals coincided at approximately the same energy position. The signals shifted to lower energies (larger lattice constants) as the samples were heated and annealed. Once the annealing temperature was achieved, the signals remained at a constant energetic position.

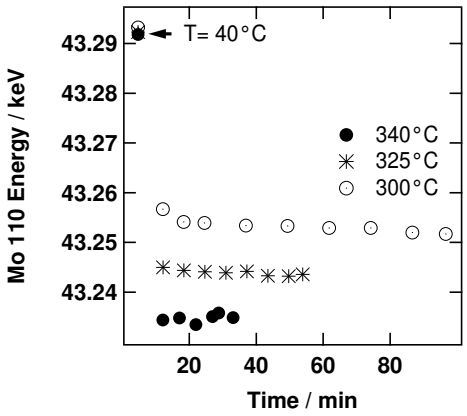

Figure 5.16.: Energy position of the Mo 110 reflection during annealing experiments $Binary_{300}$, $Binary_{325}$ and $Binary_{340}$. At 40°C the position of the reflections coincide. During annealing the position shifts to lower energies (higher lattice constants). The final position depends on the annealing temperature. Due to the constancy of the energetic position during annealing other possible strain relaxation effects are neglected.

The nominal temperature does not coincide with the temperature of the film. The temperature of the film was approximated by temperature of the Mo thin film. This can be estimated by the evolution of the energetic position of the Mo 110 reflection. Table 5.3 gives the energetic positions at room and annealing temperatures of the Mo 110 line and the resulting estimated temperatures from these analysis, T_{Cal}. This calibration is based on equation 3.10 of Chapter 3, and on the supposition of an isotropic expansion of the Mo layer, α^{Mo} equal to 5x10^{-6}K^{-1}[93].

Table 5.3.: Temperature calibration for the annealing experiments based on the energetic position of the Mo 110 reflection.

Experiment	$E_{T=40^{\circ}C}{}^{Mo\,110}$/ keV	$E_T{}^{Mo\,110}$/keV	T_{Cal}/°C
$Binary_{300}$	42.293 ±0.001	43.253 ±0.001	220 ±15
$Binary_{325}$	42.292 ±0.001	43.244 ±0.001	260 ±15
$Binary_{340}$	42.292 ±0.001	43.234 ±0.001	299 ±15

Figure 5.17 shows the evolution of the energy-dispersive X-ray diffraction spectra during annealing at nominally 300°C (experiment $Binary_{300}$ of Table 5.2). In this figure the normalized diffraction intensity is color coded and the reflections corresponding to the different phases are labeled. The transition CuS to $Cu_{2-x}S$ occurs during heating. It correlates with the formation of $CuIn_5S_8$ and $CuInS_2$. The identification of $CuIn_5S_8$ is not straight forward. Figure 5.18 presents the normalized sum of all spectra taken at room temperature and the normalized sum of all spectra taken within three minutes after the annealing temperature was achieved in the energy range 45.5 to 47.5keV. The energetic shift translates in a lattice contraction from the room to the annealing temperature. This is used to distinguish between the $\beta-In_2S_3$ and $CuIn_5S_8$ phases.[5] In the next step, the

[5]The main reflections of the $CuIn_5S_8$ and $\beta-In_2S_3$ phases overlap. The two phases present the same spinel structure and can coexist in a wide temperature range (see Figure A.7 of Appendix A). However, there is a clear evolution of the signals corresponding to the spinel phase before and after the CuS to $Cu_{2-x}S$ transformation. It

intensities of the $CuInS_2$ phase increase steadily. In contrast, those corresponding to the $CuIn_5S_8$ phase decrease steadily.

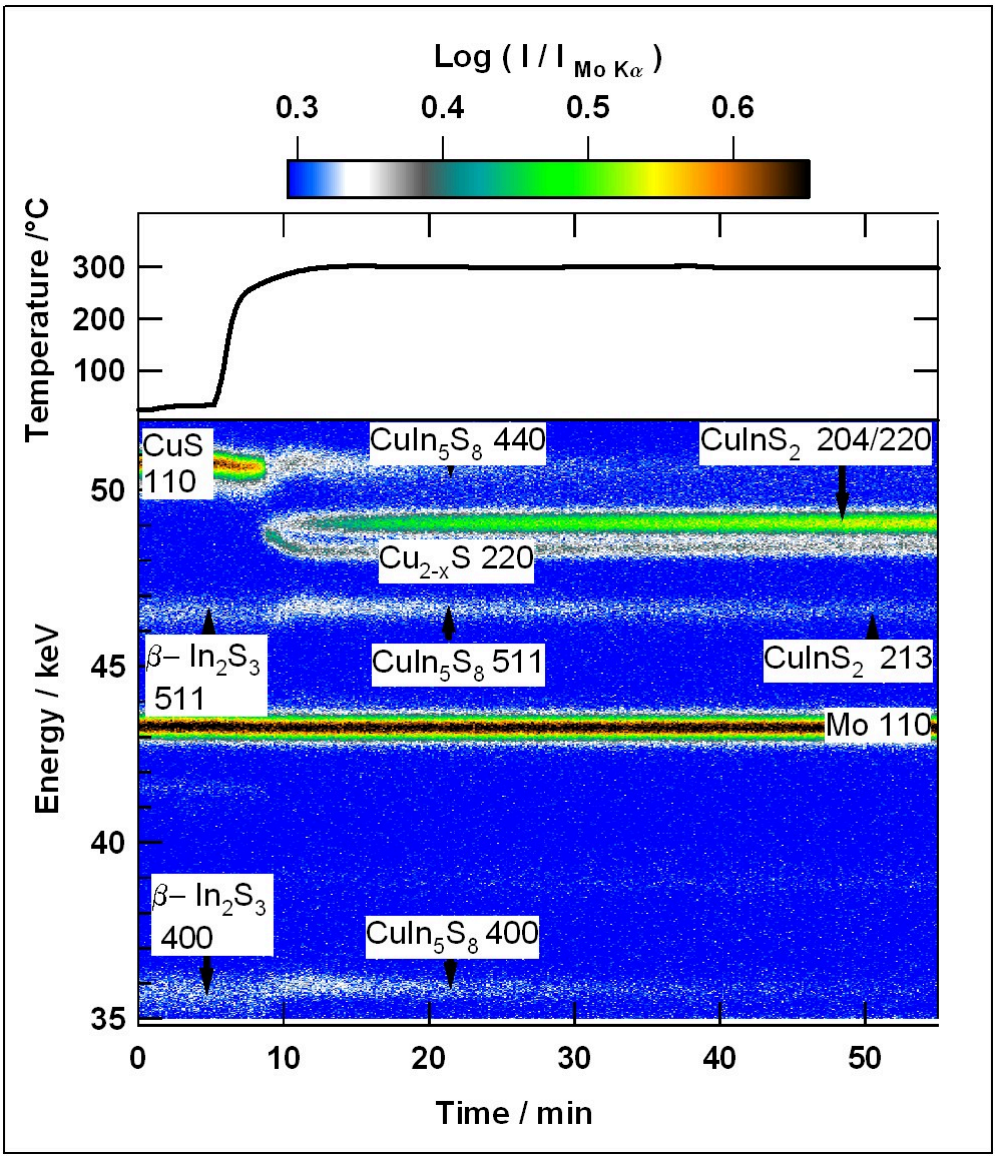

Figure 5.17.: Time-resolved EDXRD spectra during the heating and annealing of a Mo/β−In_2S_3/CuS stack (experiment *Binary*$_{300}$ of Table 5.2). The CuS to $Cu_{2-x}S$ transition is coupled to the formation of $CuIn_5S_8$ and $CuInS_2$. The formation of further $CuInS_2$ from the consumption of $CuIn_5S_8$ is observed starting from t=10min.

corresponds to a contraction of the lattice constants. The energy positions are used to calculate the contraction of the (511) lattice planes of the spinel phase despite the low intensity of the reflections. It results that the lattice parameter of the (511) planes of the spinel phase contracted of 0.4% whilst the sample temperature had increased from the room to the annealing temperature. This contraction can be explained with the β−In_2S_3 to $CuIn_5S_8$ phase transformation. The contraction between the (511) lattice parameter of the β−In_2S_3 phase at room temperature and the (511) lattice parameter of the $CuIn_5S_8$ phase at 200°C (or 240°C) is of 0.4%(or of 0.5%). This confirms the formation of $CuIn_5S_8$ from β−In_2S_3. To do this calculation, an isotropic thermal expansion coefficient of 1.6x10^{-5} K^{-1}[69] for the $CuIn_5S_8$ phase was assumed. The room temperature lattice parameters were taken from the JCPDS files listed in Table 3.4 of Chapter 3.

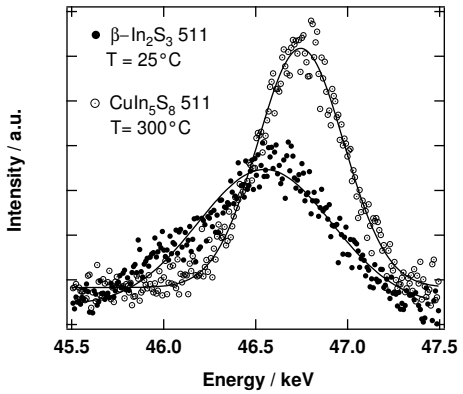

Figure 5.18.: β-In_2S_3 to $CuIn_5S_8$ transformation during experiment $Binary_{300}$ of Table 5.2. The symbols correspond to the normalized sum of the spectra taken: at 25°C (filled) and within three minutes after nominally 300°C were achieved (empty). The lines correspond to Gauss fits. The energetic positions indicate a contraction of 0.4%.

Figure 5.19 presents the expected energetic positions of the $CuInS_2$ and $CuIn_5S_8$ phases from the given JCPDS files. The largest $CuInS_2$ reflection that does not overlap with a $CuIn_5S_8$ one is the 204/220 reflection. Figure 5.20a) shows that the $CuInS_2$ 204/220 intensity correlates linearly with the $CuIn_5S_8$ 400 intensity during the experiment $Binary_{300}$. The 400 reflection was chosen because it does not overlap with CuS or $CuInS_2$ reflections (see also Table 3.4 of Chapter 3).

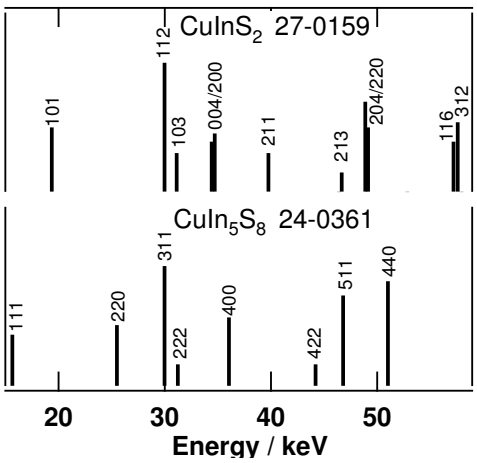

Figure 5.19.: JCPDS files of the chalcopyrite $CuInS_2$ and the spinel $CuIn_5S_8$ phases. The strongest $CuInS_2$ reflection (112) overlaps with a $CuIn_5S_8$ one. The second strongest $CuInS_2$ reflection is the combination of the 204 and 220 ones. This double reflection is used for further analysis.

Figure 5.20b) presents the $CuInS_2$ 204/220 intensity normalized to Mo $K\alpha$ during experiments $Binary_{300}$, $Binary_{325}$ and $Binary_{340}$ together with the imposed temperature.

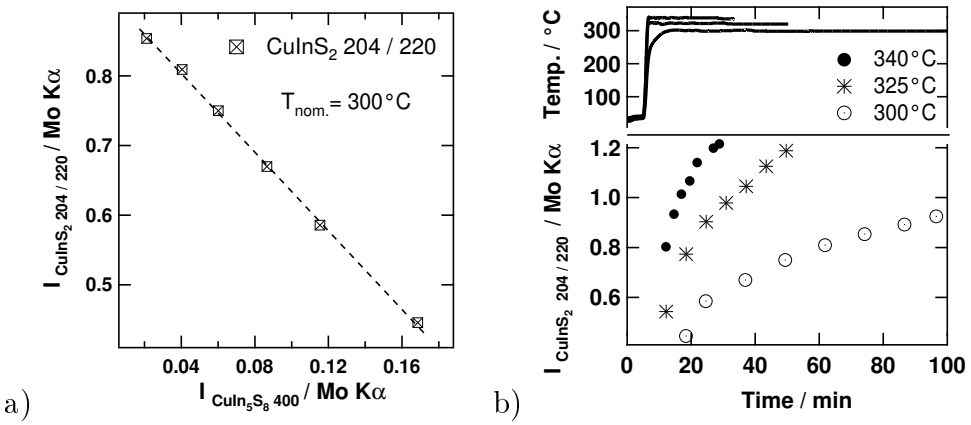

Figure 5.20.: a) Correlation between the $CuInS_2$ 204/220 and the $CuIn_5S_8$ 400 intensities during the annealing experiment at nominally 300°C; b) $CuInS_2$ 204/220 intensity evolution during annealing at nominally 300°C, 325°C and 340°C.

Formation of $CuInS_2$ from a precursor showing a preferred orientation

The growth of $CuInS_2$ through the reaction $2Cu_2S + CuIn_5S_8 \rightarrow 5CuInS_2$, where the $CuIn_5S_8$ precursor presented a preferred orientation, was studied in experiment $Texture_{320}$. One step deposition of In and S at lower nominal temperatures and subsequent Cu and S deposition at T$\sim$100°C yielded a textured β-In_2S_3/CuS precursor stack. Figure 5.21 shows the program used to heat this bilayer in the closed volume (see closed volume description in paragraph 3.1 of Chapter 3). Figure 5.22 shows the energy-dispersive X-ray spectra of the points indicated in Figure 5.21.

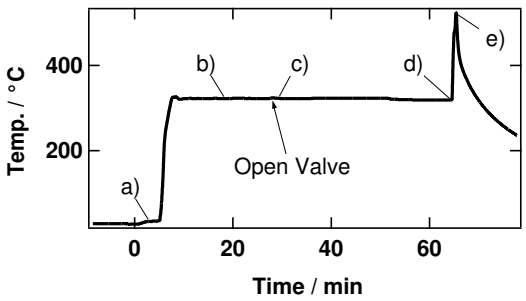

Figure 5.21.: Heating program for the growth of $CuInS_2$ with a preferred orientation. The points indicate the time and temperatures of the EDXRD spectra presented in Figure 5.22. The heating was done in a closed volume in presence of elementary sulfur. Short before c) the valve was opened and the sulfur vapor removed by the main pumping system.

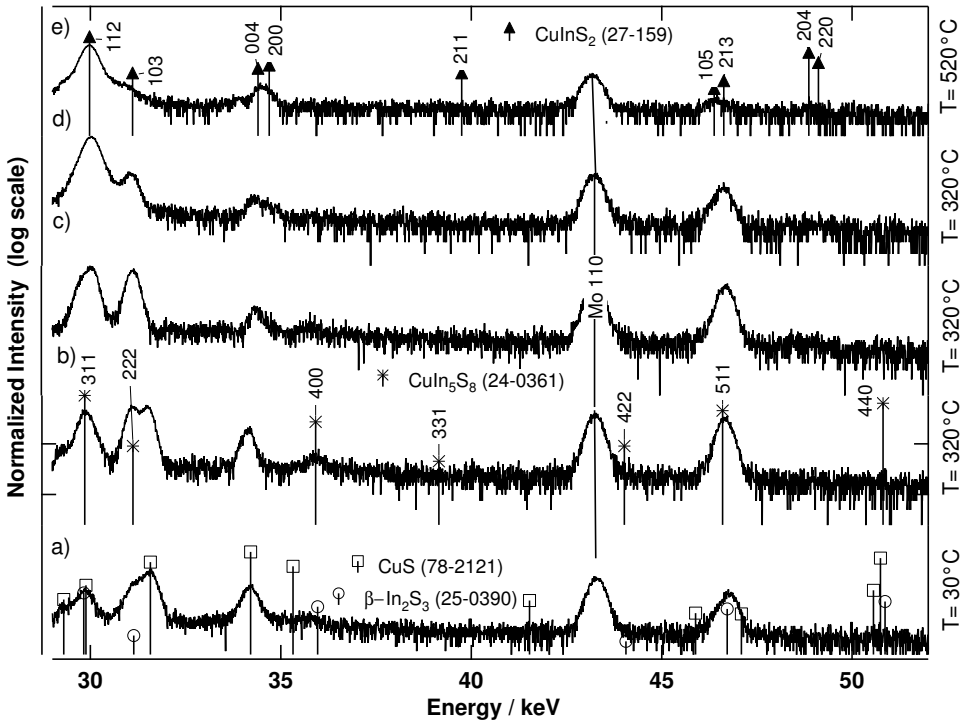

Figure 5.22.: Formation of $CuInS_2$ from a textured precursor, i.e. experiment $Texture_{320}$ of Table 5.2. The heating profile and the time where the spectra were taken are shown in Figure 5.21. In a first step (heating with excess sulfur) the β-In_2S_3 to $CuIn_5S_8$ transition is observed. Opening the valve (spectrum b to c) induces the CuS to $Cu_{2-x}S$ transition (characterized by the disappearance of the CuS lines). This is accompanied by the formation of $CuInS_2$. In a next step the $CuIn_5S_8$ phase is consumed following the reaction $2Cu_2S + CuIn_5S_8 \rightarrow 5CuInS_2$. To complete the reaction the sample was heated shortly to 500°C.

Reflections of both the β-In_2S_3 and the CuS phases are missing in Figure 5.22a) (at T=30°C). The sample was then heated in the presence of excess sulfur to nominally 320°C. This lead to the formation of the ternary $CuIn_5S_8$, still showing a preferred orientation. The absence of a 440 reflection and the presence of a strong 222 reflection are underlined. No $CuInS_2$ was formed in this step. Once the temperature was stable, the transition CuS to $Cu_{2-x}S$ was induced by opening the valve of the reaction box (see Section 3.1 of Chapter 3), leading to a strong decrease of the sulfur pressure. This was accompanied by the growth of the $CuInS_2$ phase that continued with time at expenses of the $CuIn_5S_8$ phase (evolution of the diffraction signal at ~31keV in spectrum c to d of Figure 5.22. After heating the sample rapidly to 520°C the only phase observed was a strongly textured $CuInS_2$. The absence of a 204/220 reflection and the presence of a strong 112 reflection are underlined.

5.3.1.1. Reaction kinetics

Definition of the fractional reaction

To address the kinetics of this reaction, a fractional reaction α, with

$$\alpha(t) = \frac{V^{CuInS_2}_{formed\ at\ t}}{V^{CuInS_2}_{formed\ at\ t=\infty}} \tag{5.5}$$

must be identified. In energy-dispersive X-ray diffraction the intensity of one $CuInS_2$ reflection is proportional to the volume of the diffracting grains whose lattice planes are parallel to the sample normal. For the following it is supposed that orientation effects are negligible. This is based on two points:

1. In the next paragraph it will be shown that preferred orientation is transferred, meaning that the reaction does not favor the growth of grains with a particular orientation.

2. If orientation effects were present, a non-linear correlation between random reflections of the consumed and the formed phase could be expected. Figure 5.20 shows the correlation between the $CuInS_2$ 204/220 intensities and the $CuIn_5S_8$ 400 intensity during annealing at 300°C. The $CuIn_5S_8$ 400 reflection does not overlap with a chalcopyrite one (see Fig. 5.19). Clearly there is a linear correlation between the $CuInS_2$ 204/220 intensity and the $CuIn_5S_8$ 400 intensity.

As a consequence, the 204/220 intensity is interpreted as being proportional to the overall volume of $CuInS_2$ formed from the $CuIn_5S_8$ phase.

Figure 5.23a) presents the correlations between the $CuInS_2$ 204/220 intensity and the $CuIn_5S_8$ 400 intensity during annealing at nominally 300°C, 325°C and 340°C. The linear extrapolation of the $CuInS_2$ 204/220 intensity at zero $CuIn_5S_8$ 400 intensity is used to define $V^{CuInS_2}_{formed\ at\ t=\infty}$. Figure 5.23b) presents the evolution of the fractional reaction α obtained by means of this normalization.

The fractional reactions exceed 1.0 in Figure 5.23b). This is interpreted as a effect of the recrystallization of the thin film. Recrystallization implies the formation of a new microstructure and the growth of grains at expenses of others. Depending on the driving forces and on the microstructure of the films it is possible that some orientation effects appear or that an increased crystalline quality (or consumption of X-ray amorphous regions) enhances the intensity of an X-ray diffraction signal during recrystallization. Any of these two effects can explain the over shooting of α. A clear separation between the reaction and the recrystallization is not possible. However, for the following it is assumed that the recrystallization only starts once the reaction $2Cu_2S + CuIn_5S_8 \rightarrow 5CuInS_2$ has come to an end. This assumption is valid if the consumption of the $CuIn_5S_8$ is a prerequisite for the recrystallization. This is indeed one conclusion of section 5.4. Based on this assumption, α values higher than 0.95 are excluded from further analysis.

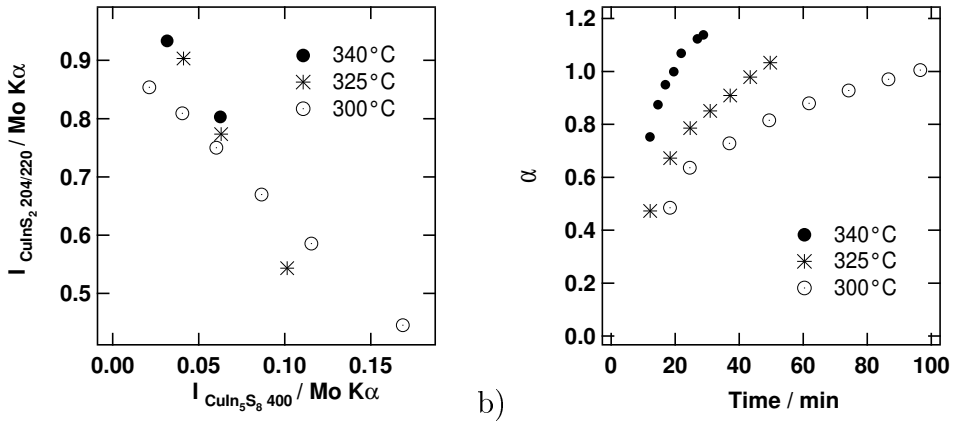

Figure 5.23.: a) correlation between the $CuInS_2$ 204/220 intensity and the $CuIn_5S_8$ 400 intensity during annealing at 300°C, 325°C and 340°C and b) the respective fractional reactions. With increasing temperatures the fractional reactions exceed 1.0. This is interpreted as a recrystallization effect.

Determination of the kinetic parameters

The kinetic parameters of the reaction $2Cu_2S + CuIn_5S_8 \rightarrow 5CuInS_2$ were determined following Avrami's approach described in Section 4.3 of Chapter 4. Avrami's equation was modified to:

$$\alpha(t) = 1 - exp(-(k_p(t-\tau))^n) \tag{5.6}$$

where $t - \tau$ is the time that corresponds purely to the annealing at the constant temperature. Plotting $ln(-ln(1-\alpha))$ against $ln(t-\tau)$ must give a straight line with a slope equal to the Avrami exponent n, and a cut at the origin equal to $nln(k_p)$. Figure D.1 of Annexe D presents the data and the procedure used to extract the Avrami exponents and the reaction constants.

The reaction constant k_p was plotted in an Arrhenius plot to obtain the activation energy of the reaction (k_p can be written as $k_p = k_{p0}exp(-\frac{E_a}{kT})$, where k is the Boltzmann constant, k_{p0} is the pre-exponential factor and E_a is the activation energy). The temperatures used were those obtained by the Mo-calibration. The temperature incertitude introduces an error in the determination of the activation energy. This is taken into account by graphically determining the maximal and minimal slope that fits all data points and error bars. For the determination of the activation energy two approaches were explored, a physical and an empirical one.

- The physical approach: the Avrami exponents presented in Table 4.5 of Section 4.2 are based on physical models of nucleation and growth rates. The kinetic data taken at nominally 300°C and 325°C are well fitted by an Avrami coefficient of 0.84. An Avrami exponent $n = 1$ corresponds to a model with: site saturation and 1D linear growth or site saturation and 2D parabolic growth. Plate-like growing grains satisfy both growing geometries. In both cases there is no new nucleation taking place: the grains available at the beginning of the reaction grow further. Assuming that this is valid for the three temperatures studied, the activation energy is 66 (-16 +34)kJmol^{-1}.
- The empirical approach: an Avrami exponent of 0.84 fits at best the data at 300°C and 325°C. Assuming that this value ($n = 0.84$) is valid for the three temperatures studied, the activation energy is 68 (-11 +32)kJmol^{-1}.

Figure 5.24 presents the k_p values in an Arrhenius plot for both approaches. Table 5.4 shows the corresponding activation energies. The values are similar in both cases. The activation energy is

expected to fall between the extreme values, i.e. between 50 and 100kJmol^{-1} (or 0.52 and 1.0eV). This activation energy is coherent with those obtained for the solid state reaction of selenides (Table 4.4 of Chapter 4).

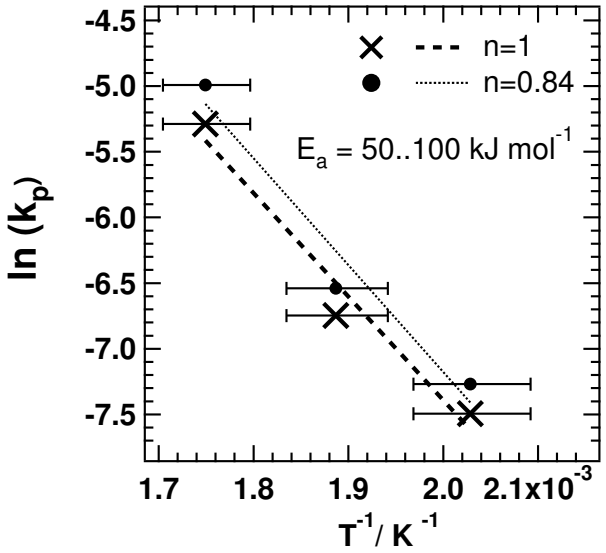

Figure 5.24.: Arrhenius plot of the reaction constant k_p(sec) for the determination of the activation energy from the kinetic data of the reaction $2Cu_2S + CuIn_5S_8 \rightarrow 5CuInS_2$.

Table 5.4.: Activation energy of the reaction $2Cu_2S + CuIn_5S_8 \rightarrow 5CuInS_2$ for a physical (n=1) and an empirical (n=0.84) approach.

Avrami exponent	Activation energy / kJmol^{-1} (eV)	Extreme values / kJmol^{-1} (eV)
0.84	68 (0.70)	57...100 (0.59 ... 1)
1	66 (0.68)	50...100 (0.52 ... 1)

Reaction $2Cu_2S + CuIn_5S_8 \rightarrow 5CuInS_2$ is much faster than the direct metallic sulfurization to produce $CuInS_2$ at low pressures (p_s<10^{-3}mbar) even if the reaction free energy of the latter is larger: ∼-500 kJmol^{-1} (from the thermodynamic data of Appendix B) compared to -13kJmol^{-1}. It would seem that the free energies of activation are large enough so that the reaction free energies play no determining role in the reaction velocity. Figure 5.10 shows that at nominally 530°C the formation of ∼2μm of $CuInS_2$ takes place in approximately 12.5min through a direct sulfurization. Figure 5.23 shows that at nominally 340°C the formation of ∼2μm of $CuInS_2$ takes place in approximately 12min through reaction $2Cu_2S + CuIn_5S_8 \rightarrow 5CuInS_2$. Extrapolating the kinetic data to 550°C results in total reaction times of tens of seconds. This is an upper limit for the fabrication rate of processes that include in one of their steps both $CuInS_2$ and $CuIn_5S_8$ as intermediate phases.

5.3.1.2. Structural relationship between $CuIn_5S_8$ and $CuInS_2$

Figure 5.25 presents the sulfur sublattices of the chalcopyrite $CuInS_2$, the sphalerite $CuInS_2$ and the spinel $CuIn_5S_8$ structures. The sulfur anions are organized in a face-centered cubic sublattice

in the three structures.

Figure 5.25 reveals the structural equivalences between the three sublattices. They are made visible by choosing 4 unit cells of the chalcopyrite structure, 8 of the sphalerite structure and 1 of the spinel structure. The simplified structure of the chalcopyrite $CuInS_2$ phase is the sphalerite structure with a cubic unit cell so that $2a_{Sphalerite}^{CuInS_2} \sim 1.1$nm (see Figure 2.2 of Chapter 2 for a representation of both structures). In this structure the splitting of the 204 and 220 reflection disappears simplifying to 220 and the 112 reflection simplifies to 111. This is due to the fact that the cations are statistically distributed in the cation sublattice and that the unit cell is cubic (see Section 2.3 of Chapter 2). The spinel $CuIn_5S_8$ structure belongs to the cubic system and presents a lattice parameter $a_{cubic}^{CuIn_5S_8} \sim 1.1$nm. In the spinel structure the cations occupy octahedral and tetrahedral sites of the anion sublattice. The elementary cell is twice that of the sphalerite $CuInS_2$ one, but the anion sublattice is similar (see Figure 5.25). Figure 5.25 shows that the 111 and 220 lattice planes of the sphalerite structure are equivalent to the 222 and 440 of the spinel one respectively.

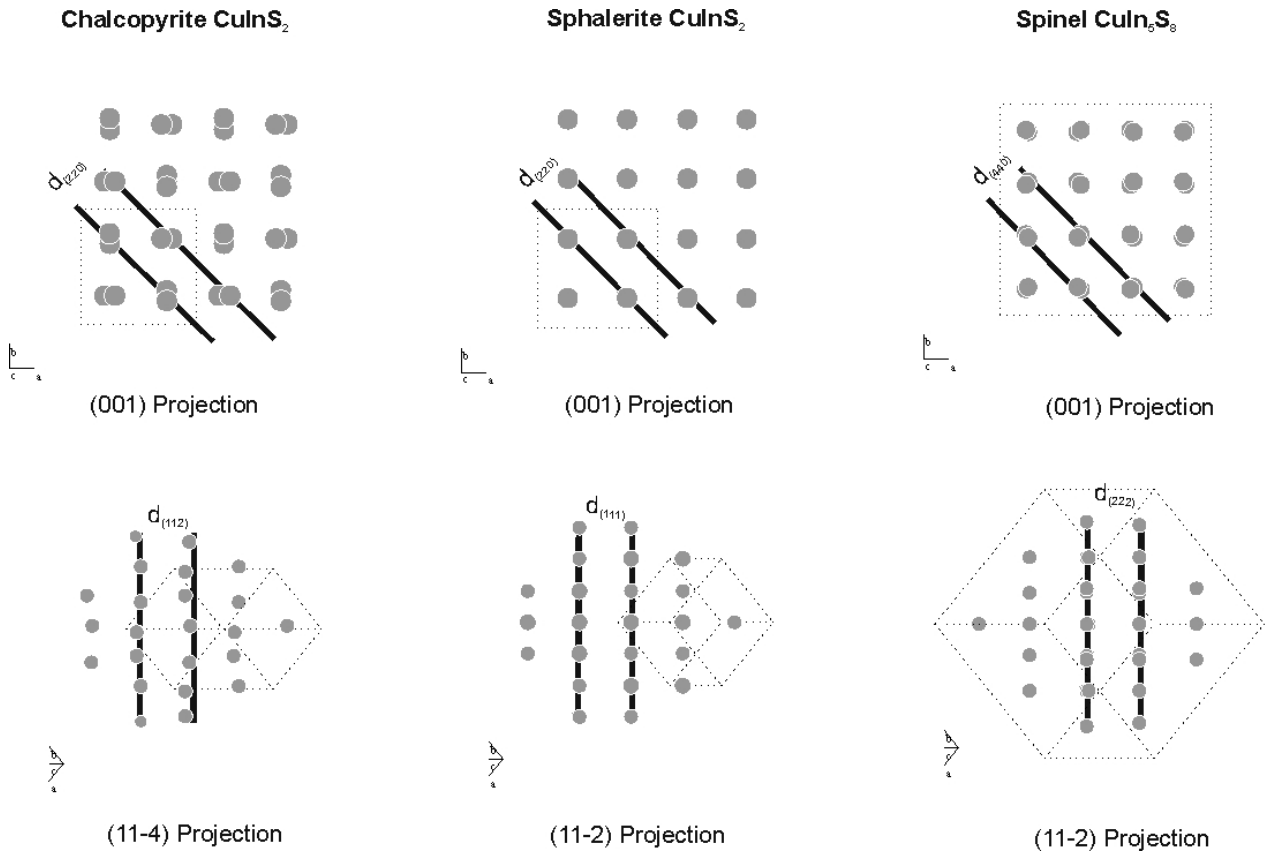

Figure 5.25.: Sulfur sublattices in the $CuInS_2$ chalcopyrite, $CuInS_2$ sphalerite and $CuIn_5S_8$ spinel structures obtained with the software POWDERCELL[70]. The sublattices are projected to reveal the lattice planes that contribute to the 220 and 112 reflections of the chalcopyrite, the 220 and 111 reflections of the sphalerite and the 440 and 222 reflections of the spinel structure. The 220 chalcopyrite, 220 sphalerite and 440 spinel are equivalent, as are the 112 chalcopyrite, 111 sphalerite and 222 spinel ones.

Figure 5.22 presents the reaction of a $CuIn_5S_8$ precursor showing a strong 222 reflection and the absence of the 440 reflection. The resulting $CuInS_2$ product presents a strong 112 reflection and no 220 reflection. In the simplified structure this corresponds to the 111 and 220 reflections.

In this experiment ($Texture_{320}$) the reaction product ($CuInS_2$) preserves the initial preferred orientation of the $CuIn_5S_8$ phase. This means that the anion sublattice remains qualitatively with the same orientation throughout the reaction $2Cu_2S + CuIn_5S_8 \rightarrow 5CuInS_2$. On the basis of these results it is reasonable to postulate that the reaction is supported by the diffusion of cations through a relatively rigid sulfur matrix. This is coherent with the slower mobility of the anions as compared to that of the cations (see Table 4.2 of Chapter 4).

5.3.2. Conclusions

The formation of $CuInS_2$ from a $\beta-In_2S_3/CuS$ bilayer was studied. The chalcopyrite formation can be divided into two reactions:

1. $Cu_2S + 3In_2S_3 \rightarrow CuInS_2 + CuIn_5S_8$(reaction D of Table 4.3 of Chapter 4);
2. $2Cu_2S + CuIn_5S_8 \rightarrow 5CuInS_2$(reaction B of Table 4.3 of Chapter 4).

The first reaction is very fast and occurs together with the CuS to $Cu_{2-x}S$ transition. This transition is sulfur pressure dependent. The second reaction is slower. The kinetic analysis yielded an activation energy of between 50 and 100kJmol^{-1} (between 0.5 and 1 eV). The kinetic data fit acceptably well a site-saturated, one-dimensional linear growth rate or a two-dimensional parabolic growth rate model. Plate-like growing grains satisfy both geometries. Site-saturated means that there is no new nucleation taking place and that existing grains or nuclei, those formed through the first reaction, grow further. The studies of the reaction of a precursor showing a preferred orientation revealed that the resulting $CuInS_2$ phase preserves the preferential orientation of the $CuIn_5S_8$ one. This indicate that the formation of $CuInS_2$through reaction B of Table 4.3 is supported by the diffusion of Cu and In cations through a relatively rigid sulfur matrix.

The reaction $2Cu_2S + CuIn_5S_8 \rightarrow 5CuInS_2$ plays a major role in the fabrication of $CuInS_2$ thin films because it ensures, even at low pressures ($p_s < 10^{-3}$mbar), high $CuIn_5S_8$ consumption and $CuInS_2$ growth rates. Once the $CuIn_5S_8$ phase is consumed, the recrystallization of the single phase thin-film material can take place. This will be analyzed in the next section.

5.4. Thin-film recrystallization

This section treats the recrystallization of $CuInS_2$ thin films. This mechanisms is understood as the formation of a new microstructure accompanied by an increase in grain size. It will be shown that the thin-film recrystallization ensures grain sizes of the order of the film thickness ($\sim 2\mu$m) and a good crystalline quality. With crystalline quality is understood a low density of linear and planar structural defects and a long range cation ordering in the stable chalcopyrite structure. The driving forces, prerequisites and enhancement factors of this mechanism will be addressed. The question if Ag enhances recrystallization of the $CuInS_2$ thin films will be answered.

5.4.1. Recrystallization of $CuInS_2$ thin films studied by means of *in situ* EDXRD

To study the thin-film recrystallization bilayers composed of

- Cu-poor $CuInS_2$ and
- CuS

were prepared by means of thermal evaporation. The deposition sequence consisted in three steps:

1. evaporation of indium in a sulfur atmosphere on a Mo-coated soda-lime glass heated to 275°C;
2. evaporation of Cu during a heating ramp to 580°C. Evaporation of Cu was made until the stoichiometry of the sample was [Cu]/[In]$\sim$0.9 (measured separately by means of X-ray fluorescence analysis). The nominal thickness of the Cu-poor $CuInS_2$ film was of $\sim 1.7\mu$m;
3. evaporation of Cu at a substrate temperature of 100°C in presence of sulfur.

Figure 5.26 shows a transmission electron micrograph (TEM) of the bilayers. An energy-dispersive X-ray spectrum of the samples revealed the phases: $CuInS_2$, $CuIn_5S_8$ and CuS. The CuS phase is on the surface of the film and the ternary phases coexist in the bottom layer. $CuInS_2$ has a restricted range of stability on the Cu-poor side of the Cu_2S- In_2S_3 pseudo-binary tie line (see Figure A.7 of Appendix A). If the film is richer in In the $CuIn_5S_8$ phase segregates. In the TEM image it is not possible to distinguish between $CuIn_5S_8$ and $CuInS_2$ grains. However, regions of lamellar morphology were found evenly distributed through out the sample. Figure 5.27 presents the evidence of such regions within the $CuInS_2$-$CuIn_5S_8$ layer. Cattarin *et al.* [22] report on $CuInS_2$ lamellae (made of nanocrystals) separated by the $CuIn_5S_8$ phase. It is possible that this is also the case in the regions of lamellar morphology. The volume fraction of $CuIn_5S_8$ in the bottom layer was estimated from the X-ray diffraction spectrum to be 10%. No cation ordering reflection (see Figure 2.3 of Chapter 2 for the expected positions of this type of reflection) can be detected by the energy-dispersive X-ray diffraction setup. Highly resolved *ex situ* angle-dispersive X-ray diffraction spectra showed only traces of the Cu-Au ordering in the bottom layer.

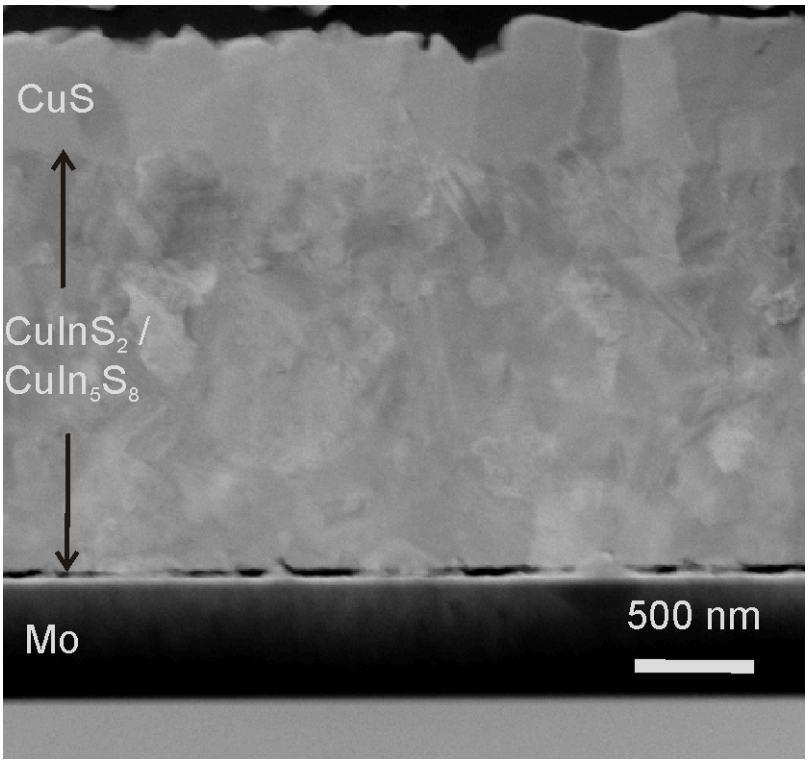

Figure 5.26.: Transmission electron microscope cross-section of the Cu-poor $CuInS_2$/CuS bilayer. The [Cu]/[In] ratio of the bottom layer is approximately 0.9. The volume percentage of the $CuIn_5S_8$ phase is to be 10% in this layer. The overall [Cu]/[In] ratio of both layers is approximately 1.4.

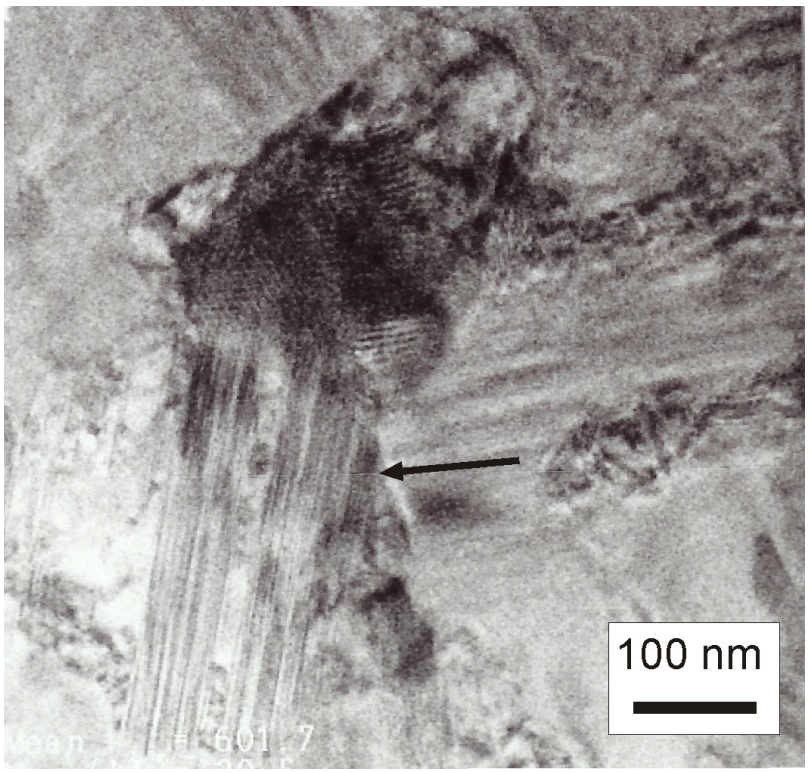

Figure 5.27.: Lamellar regions (indicated by the arrow) in the $CuInS_2$-$CuIn_5S_8$ layer.

Together with the Cu-poor $CuInS_2$/CuS bilayers also Cu-poor $CuInS_2$/Cu and Cu-poor $CuInS_2$/Ag bilayers were prepared by evaporating pure metals on similarly deposited Cu-poor $CuInS_2$ films.

The bilayered films were heated at a constant rate of 1.44Kmin^{-1} to 500°C and passively cooled down in the *in situ* reaction chamber (see Figure 3.1 of Chapter 3). The time resolution of the *in situ* energy-dispersive X-ray diffraction experiments was of 2min/spectrum. The experimental setup allowed to investigate three pressure conditions during heating. These were:

i) Heating in vacuum where the sulfur pressure was determined by the chamber pressure (p $<10^{-3}$mbar);

ii) Heating in a closed volume without any sulfur;

iii) Heating with an internal sulfur source (see Section 5.2 for the description and Figure 5.4 for the schematic representation).

These three pressure conditions are named in the following as: vacuum, closed volume and closed volume with sulfur source respectively. Table 5.5 summarizes the names, the layer sequences, their stoichiometry (determined from SEM analysis, assuming the $CuIn_5S_8$ phase occupies 10% of the volume of the Cu-poor layer and taking as densities $\rho_{CuInS_2} = 4.75 gcm^{-3}$and $\rho_{CuIn_5S_8} = 4.86 gcm^{-3}$) and the pressure conditions used in the different experiments.

Table 5.5.: Layer sequences, stoichiometry and pressure conditions for the recrystallization experiments of $CuInS_2$ thin films. The Cu-poor $CuInS_2$ layers are equivalent to those shown in Figures 5.26 and 5.27.

Name	Layer Seq:	[Cu]/[In]	Pressure Conditions
a	$CuInS_2$	0.9±0.1	Closed Volume
b	$CuInS_2$/CuS	1.4±0.2	Vacuum
c and *d*	$CuInS_2$/CuS	1.4±0.2	Closed Volume, Sulfur Source
e	$CuInS_2$/Cu	1.9±0.3	Vacuum
f and *g*	$CuInS_2$/Cu	1.1±0.2	Vacuum, Closed Volume
h	$CuInS_2$/Ag	([Cu]+[Ag])/[In]=1.8±0.3	Vacuum

For the recrystallization experiments careful attention was given to the evolution of the diffraction line at ∼30keV of the $CuInS_2$ phase. In this range the reflections of the $CuInS_2$, $CuIn_5S_8$, CuS and $Cu_{2-x}S$ phases overlap. The Cauchy contribution to the broadening of this reflection was extracted via a multiple line fit, combined with the method proposed by Dehlez *et al.*[29]. Appendix E summarizes this methodology. The Cauchy contribution to the broadening of the $CuInS_2$ 112 reflection (in the following just Cauchy-breadth) was used to monitor the thin-film recrystallization.

Monitoring the thin-film recrystallization

Figure 5.28 shows a TEM image of a bilayered Cu-poor $CuInS_2$/CuS sample after heating to 500°C at a 1.44Kmin^{-1} rate in the closed volume pressure conditions, i.e. experiment *c* of Table 5.5. Large $CuInS_2$ grains with dimensions of about 2μm are visible. Some crystals present twinning (indicated by the arrow in the TEM image) but there are large regions with no evident stacking faults and/or dislocations. A secondary phase, CuS, segregates at the surface of the sample forming islands that do not cover completely the underlying $CuInS_2$. CuS aggregates are also present at the bottom of the film. After removal of the Cu-S phases by KCN etching, pinholes are made visible in complementary SEM analysis proving that Cu-S phases were present throughout the thickness of the films.

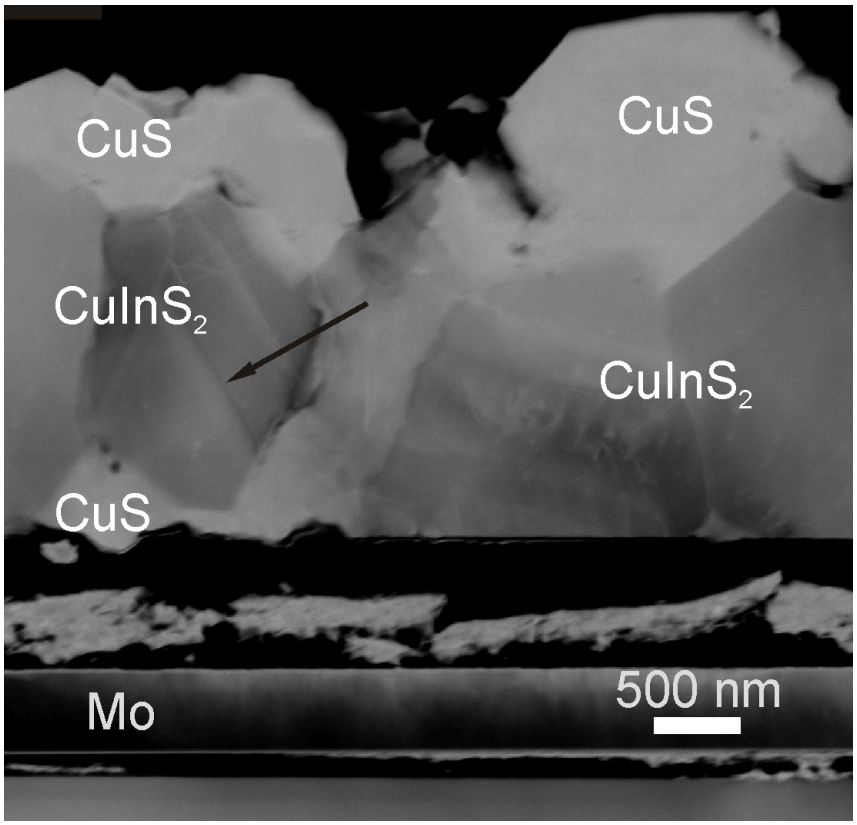

Figure 5.28.: Transmission electron microscope cross-section of the bilayer shown in Figure 5.26 after heating to 500°C with a 1.44Kmin^{-1} rate. Large $CuInS_2$ grains with possible twinning (indicated by the arrow) are revealed. CuS segregates at the surface as islands, but also at the back of the film. The delamination of the film from the Mo occurred during the preparation of the sample.

Figure 5.29 presents the evolution of the microstructure during the recrystallization of Cu-poor $CuInS_2$ thin film as function of copper excess. The figure presents EBSD quality mappings of a cross-section of a sample similar to that shown in Figure 5.26 but where the CuS layer was removed partially by means of KCN etching. The resulting film is seen schematically on the left of Figure 5.29. The film was then heated to 500°C under the same conditions of experiment *c* of Table 5.5. The figure shows that the thin-film recrystallization is characterized by the formation of a new microstructure and the growth of some grains at expenses of others.

Figure 5.30 presents the evolving energy-dispersive diffraction spectra during the heating of a sample similar to that shown in Figure 5.26 and that lead to the sample shown in Figure 5.28, i.e experiment *c* of Table 5.5. In this figure the normalized diffraction intensity is color coded

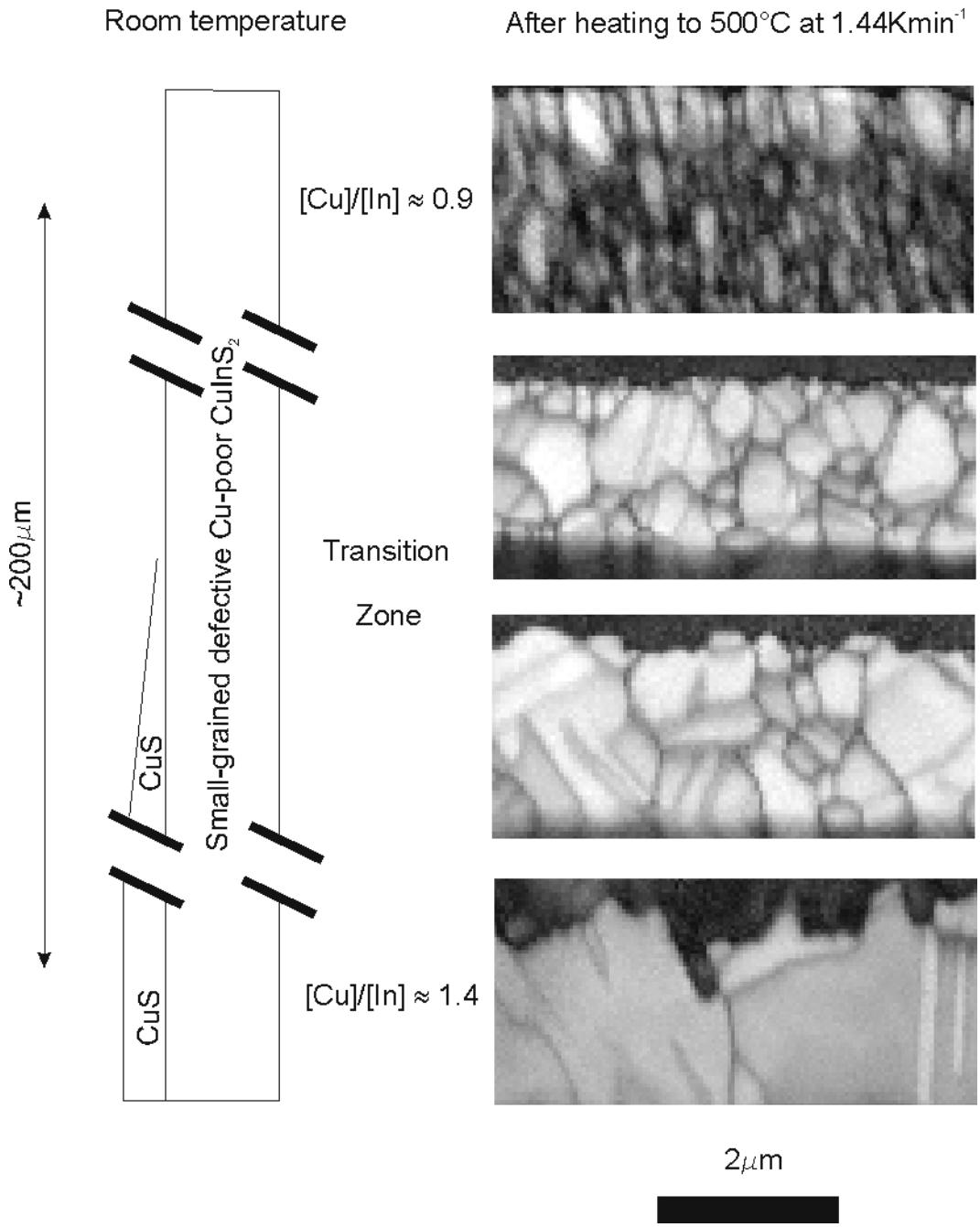

Figure 5.29.: Lateral thin-film recrystallization of a Cu-poor $CuInS_2$ ([Cu]/[In]≈0.9) where excess copper (so that [Cu]/[In]≈1.4) was assured by means of a thin CuS layer that was deposited only to half of the sample. The film schematically shown on the left of the figure was heated to 500°C. The polished cross-sections on the right side of the figure correspond to quality maps of EBSD measurements that reveal the evolution of the microstructure within the sample in the case where the sample had no Cu excess (top cross-section), in the case where the Cu excess was approximately 1.4 (bottom cross-section) and in the transition zone.

and the reflections corresponding to the different phases are labeled. The evolution of the $CuInS_2$ 112, 200/004, 204/220, the $CuIn_5S_8$ 400, 511, 440, CuS 102, 110 and the $Cu_{2-x}S$ 220 reflections are plotted against time together with the imposed temperature (top of the graph). The pressure dependent CuS to $Cu_{2-x}S$ phase transition (see Section A.3.2 of Appendix A) takes place at 280°C. The reflections corresponding to the $CuIn_5S_8$ phase disappear during heating. The reflections corresponding to the $CuInS_2$ phase are always present. Of particular interest is the appearance of a reflection at ∼39keV at 300°C and its disappearance at expenses of another reflection at ∼39.5keV at 400°C. This effect will be treated in detail in the paragraph 5.4.1.3 (cation ordering).

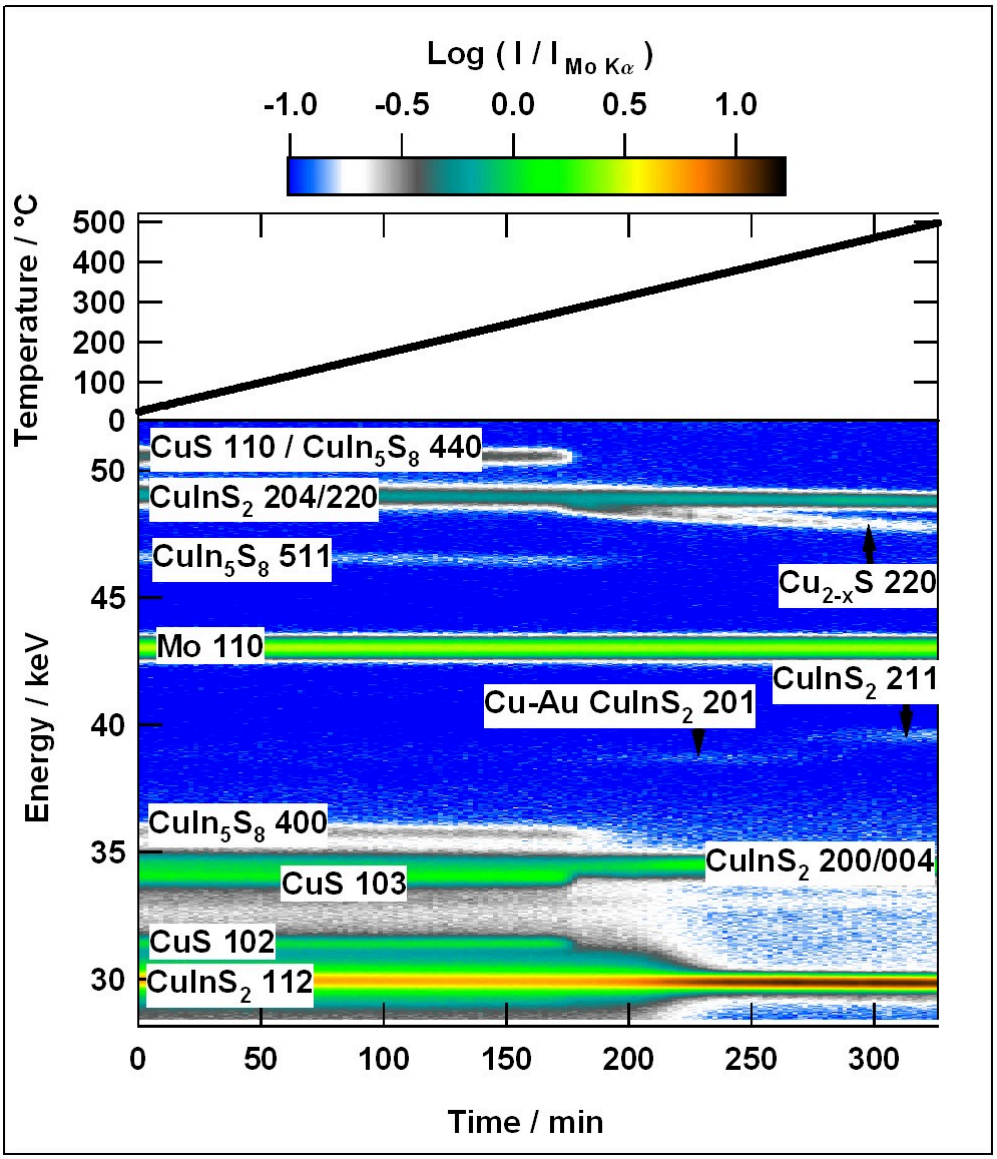

Figure 5.30.: Time-resolved EDXRD spectra during the heating of a Cu-poor $CuInS_2$([Cu]/[In]≈0.9) layer covered with a CuS layer (overall [Cu]/[In]≈1.4). In the bottom layer the ternary $CuIn_5S_8$ phase is present. This phase disappears after the CuS to $Cu_{2-x}S$ transition and before the decrease of the breadth of the 112 reflection (at ∼30keV) observed between t=200min and t=250min. At t=200min a reflection appears at ∼39keV that is attributed to the Cu-Au ordering of $CuInS_2$. This reflection vanishes and gives rise to a reflection at ∼39.5keV that is attributed to the chalcopyrite ordering of $CuInS_2$.

Monitoring the domain and grain growth by means of X-ray diffraction

The evolution of the Cauchy-breadth with temperature can be used to monitor the domain and grain growth during the recrystallization of $CuInS_2$ thin films (see Appendix E). This was done for the first time for a chalcopyrite thin film thanks to the in situ method described in Chapter 3.

Figure 5.30 shows how the breadth of 112 reflection of the $CuInS_2$ phase (∼30keV) evolves with increasing temperature between t=200min and t=250min. Figure 5.31 presents the energy-dispersive X-ray spectra in the energy range 28.5keV to 32.5keV at 30°C and at 500°C of this experiment. The multiple-line fit made to extract the Cauchy-breadth, β^C, following the procedure described in Appendix E is also shown.

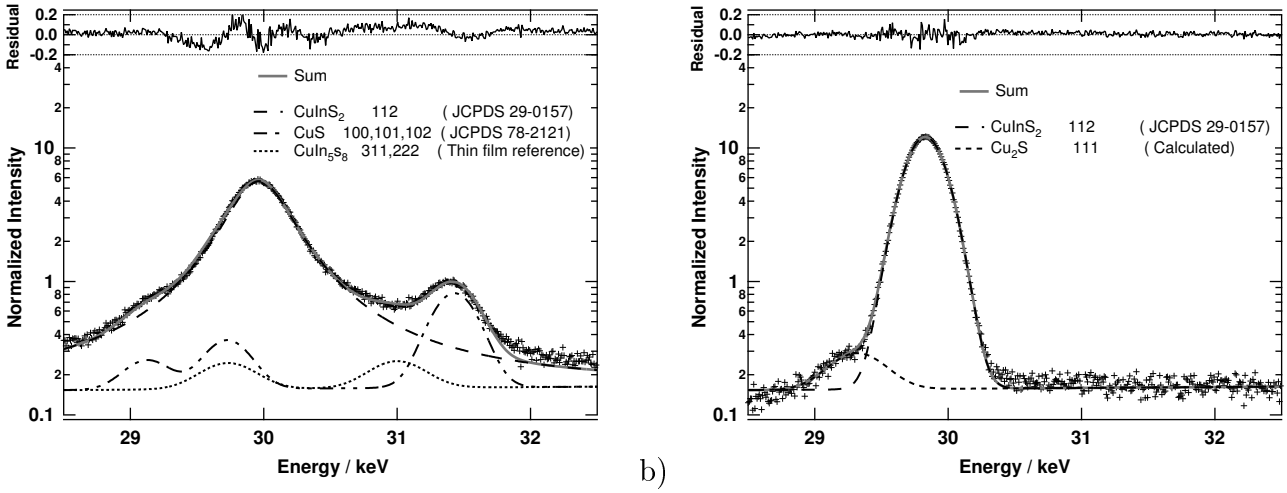

Figure 5.31.: EDXRD spectra and multiple-line fit before (a) and after (b) heating to 500°C. The broadening of the $CuInS_2$ reflection decreases considerably, the low intensity $CuIn_5S_8$ reflections disappear, and the CuS reflections are replaced by the $Cu_{2-x}S$ one.

Figure 5.32a) presents the evolution of the Cauchy-breadth and a phase existence plot[6] of an experiment where a similar Cu-poor $CuInS_2$ layer as that shown in Figure 5.26 but without the top CuS layer was heated to 500°C at a rate of 1.44Kmin^{-1} under the close volume pressure conditions, i.e. experiment *a* of Table 5.5. No detectable changes in the width of the reflection are observable in this case. Figure 5.32b) shows the evolution of the Cauchy-breadth with temperature together with a phase existence plot during the thin-film recrystallization shown in Figure 5.30, i.e. experiment *c* of Table 5.5. In this case (heating with a top CuS layer) the Cauchy-breadth decreases steadily from 0.8 keV to ∼0keV in the temperature range 250°C $<$ T $<$ 400°C. The CuS to $Cu_{2-x}S$ phase transition occurs at 280°C and the $CuIn_5S_8$ phase disappears before the Cauchy-breadth has fallen below 0.6keV. These two experiments correspond to the heating of a Cu-poor $CuInS_2$ with or without a CuS layer shown in Figure 5.29. The resulting microstructures correspond to those presented by the uppermost (no CuS layer) and the lowermost (CuS layer) cross-sections of of this figure.

[6]For the phase existence plots the intensities of the $CuInS_2$ reflections were corrected for their expected decline with increasing temperature (see Section 3.2 of Chapter 3). To do this, the measurements were corrected by a factor that was determined by the linear interpolation of the calculated intensities ratios at room temperature and at 500°C. These ratios are given in Table 3.3 of Chapter 3.

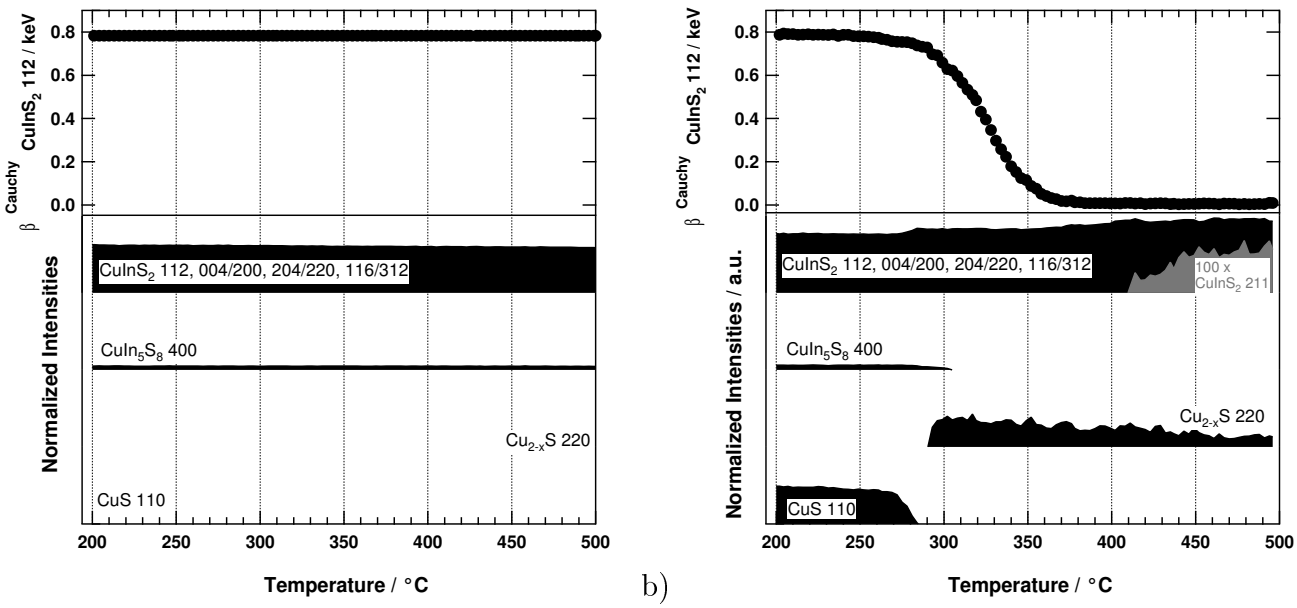

Figure 5.32.: Phase existence plot and Cauchy-breadth evolution of heating experiments without (a) and with (b) a CuS layer. Without the CuS no significant changes are observed in the X-ray diffraction spectra. With a CuS top layer: the CuS to $Cu_{2-x}S$ transition is observed, the $CuIn_5S_8$ phase is consumed and the $CuInS_2$ film recrystallizes (Cauchy-breadth β^C falls from 0.8keV to 0keV and 211 chalcopyrite cation ordering line emerges above 400°C). The $CuInS_2$ intensities were corrected to account for the expected temperature decrease (see 3.3 of Chapter 3).

5.4.1.1. Sulfur pressure dependence

The influence of the sulfur pressure on the thin-film recrystallization was studied by monitoring the heating of the same type of bilayers as the one shown in Figure 5.26 (Cu-poor $CuInS_2$ with a top CuS layer so that the overall [Cu]/[In]≈1.4) under different sulfur pressure conditions, i.e. experiments *b*, *c* and *d* of Table 5.5.

Table 5.6 presents the temperatures of the CuS to $Cu_{2-x}S$ transition, the temperatures where the intensity of the 440 $CuIn_5S_8$ falls below 20% of its maximum value and the temperatures where the Cauchy-breadth equals 0.4keV as a function of the sulfur pressure conditions. The sulfur pressure increases from the vacuum (experiment *b*), to the closed volume (experiment *c*), to the closed volume with sulfur source pressure conditions (experiment *d*). This is confirmed by the transition temperatures of the CuS to $Cu_{2-x}S$ transition. Table 5.6 shows that:

a) the temperature where the Cauchy-breadth equals 0.4keV is always preceded by the disappearance of the $CuIn_5S_8$ phase;

b) the temperature where the Cauchy-breadth equals 0.4keV does not correlate with the CuS to $Cu_{2-x}S$ phase transformation;

c) in presence of the $Cu_{2-x}S$ phase, sulfur pressure shifts the temperature where the Cauchy-breadth falls below 0.4keV to lower temperatures;

d) in the case of the highest sulfur pressure conditions, the Cauchy-breadth falls below 0.4keV before the CuS to $Cu_{2-x}S$ phase transformation.

Table 5.6.: Temperatures of the CuS to $Cu_{2-x}S$ phase transformation, of the consumption of the $CuIn_5S_8$ phase (defined as the temperature where the intensity of the 440 $CuIn_5S_8$ reflection falls below 20% of its maximum) and of the fall of the Cauchy-breadth (β^C=0.4keV) as a function of the increasing sulfur pressure conditions (experiments *b*, *c*, and *d* of Table 5.5).

Pressure Conditions	T(CuS-> $Cu_{2-x}S$) / °C	T($I_{CuIn_5S_8}$=20%I_{max}) /°C	T(β^C=0.4keV) /°C
Vacuum	245	325	349
Closed Volume	281	302	323
Sulfur Source	391	373	387

5.4.1.2. Cu excess dependence

The effect of copper excess on the recrystallization of $CuInS_2$ thin films was studied by monitoring the heating of a Cu-poor $CuInS_2$ with a top Cu layer so that the overall [Cu]/[In] ratio was approximately equal to 1.1 or 1.9. This was done under the vacuum pressure conditions, i.e. experiments *f* and *e* of Table 5.5.

Figure 5.33 shows the evolution of the Cauchy-breadths of both experiments. The bilayer with the higher Cu excess ([Cu]/[In]≈1.9) presented the secondary chalcocite phase Cu_2S during heating until T∼250°C and the digenite $Cu_{2-x}S$ phase at higher temperatures. No binary phase could be detected in the experiment with lower Cu excess conditions ([Cu]/[In]≈1.1). Figure 5.33 shows that whereas the temperature where the Cauchy-breadth equals 0.4keV remains qualitatively unchanged, the onset and the velocity of the transition change significantly with the copper excess. In the case where the nominal [Cu]/[In] ratio is ≈1.9, the transition starts at 410°C and ends at 440°C and in the case of [Cu]/[In]∼1.1 the transition starts at 375°C and does not come to the detection end (Cauchy-breadth ∼0keV) before the top temperature is achieved (500°C). Figure 5.34 shows that grain sizes (after passive cooling) are different in both films.

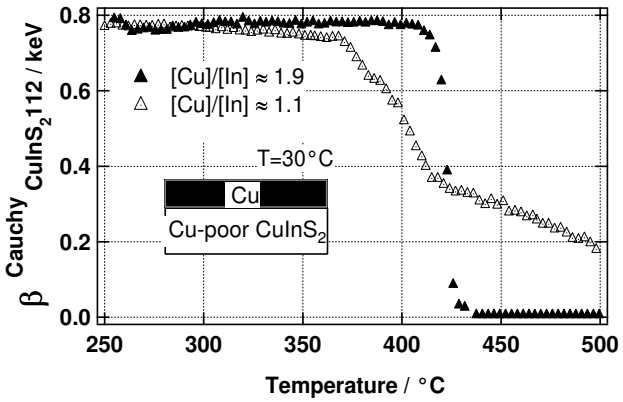

Figure 5.33.: Cauchy-breadth evolution during heating of a Cu-poor $CuInS_2$ layer with a pure Cu layer on top so that the overall [Cu]/[In] ratio was ≈ 1.1 or 1.9. For the film with the [Cu]/[In] ratio ≈1.1 the transition starts at 375°C and does not come to a detection end at T= 500°C. For the film with the [Cu]/[In]≈1.9 the transition starts at 410°C and ends at 440°C.

For the SEM image presented in Fig. 5.34 the sample with [Cu]/[In]≈1.9 was etched to remove secondary Cu-S phases. The image reveals grain sizes of at least 1μm. The $CuInS_2$ film is closed,

even and presents no pinholes. The film with nominally a [Cu]/[In]≈1.1 presents a much lower average grain size of the order of 160nm.

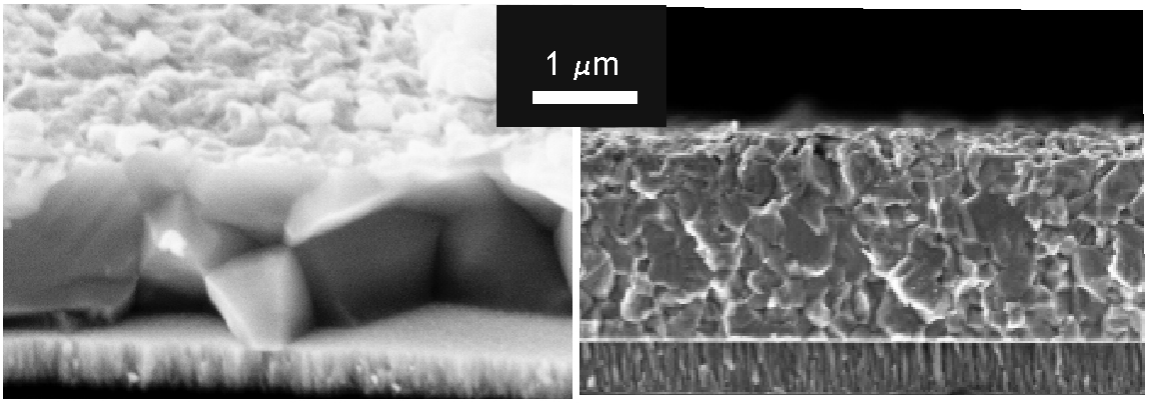

Figure 5.34.: Scanning electron microscope cross-sections of the samples with a [Cu]/[In]≈1.9 on the left (the Cu-S phases were etched with KCN and for the SEM analysis the sample was kipped 20° to reveal the surface) and [Cu]/[In]≈1.1 on the right. These cross-sections correspond to the thin-film recrystallization experiments of Figure 5.33.

5.4.1.3. Cation ordering

This section will show that the cation ordering makes part of the thin-film recrystallization. Figure 2.3 of Chapter 2 showed calculated angle-dispersive X-ray diffraction spectra of the chalcopyrite ordering and the Cu-Au ordering of $CuInS_2$. The figure outlines the 211 reflection of the chalcopyrite and the 201 reflection of the Cu-Au ordering. Each reflection mirrors a particular cation ordering. If no ordering is present, sphalerite type structure, the reflections vanish (see Section 2.3 of Chapter 2).

Figure 5.35 shows the evolution with temperature of the energy-dispersive X-ray diffraction spectra during heating of a Cu-poor $CuInS_2$ layer with a top CuS layer (experiment *c* of Table 5.5) in the energy range 37keV-42keV, together with the evolution of the Cauchy-breadth already presented in Figure 5.32. The continuous and dashed lines correspond to the calculated energetic positions of the chalcopyrite 211 and Cu-Au ordering 201 lines in this energy range on the basis of the energetic position of the $CuInS_2$ 112 reflection[7]. Figure 5.35 shows:

- a low intensity reflection that can be attributed to the Cu-Au ordering 201 between 300°C and 400°C;
- an emerging chalcopyrite 211 reflection at T > 400°C.

[7] The expected energetic position of a reflection E_2 based on a reflection E_1 can be obtained if the corresponding lattice constants d are known at room temperature:

$$\frac{E_1(T) - E_2(T)}{E_1(T)} = \frac{d_2(T) - d_1(T)}{d_2(T)} = \frac{d_2(RT) - d_1(RT)}{d_2(RT)} = const\ .$$

This assumes an isotropic thermal expansion coefficient. See Section 3.10 of Chapter 3 for the validity of this supposition.

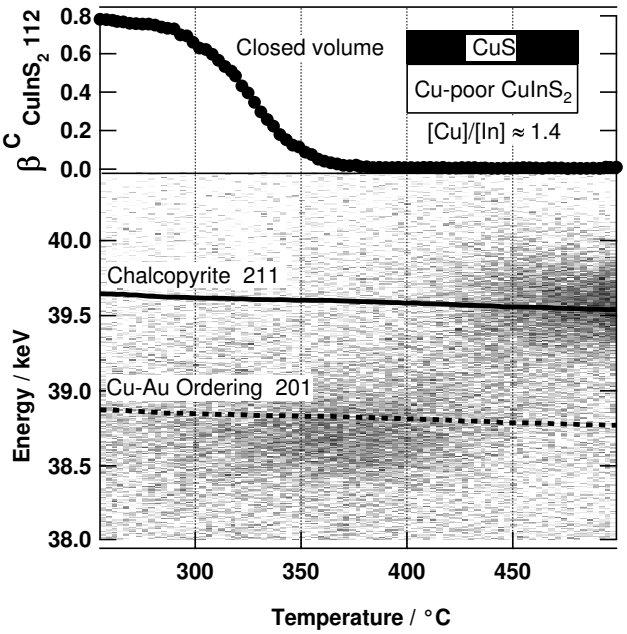

Figure 5.35.: Cu-Au ordering to chalcopyrite ordering transition during the thin-film recrystallization of a Cu-poor $CuInS_2$ layer with a top CuS layer with an overall [Cu]/[In]≈1.4. The continuous and dashed lines correspond to the expected positions of the chalcopyrite and Cu-Au cation ordering on the basis of the energy position of the $CuInS_2$ 112 reflection fitted to extract the Cauchy-breadth β^C.

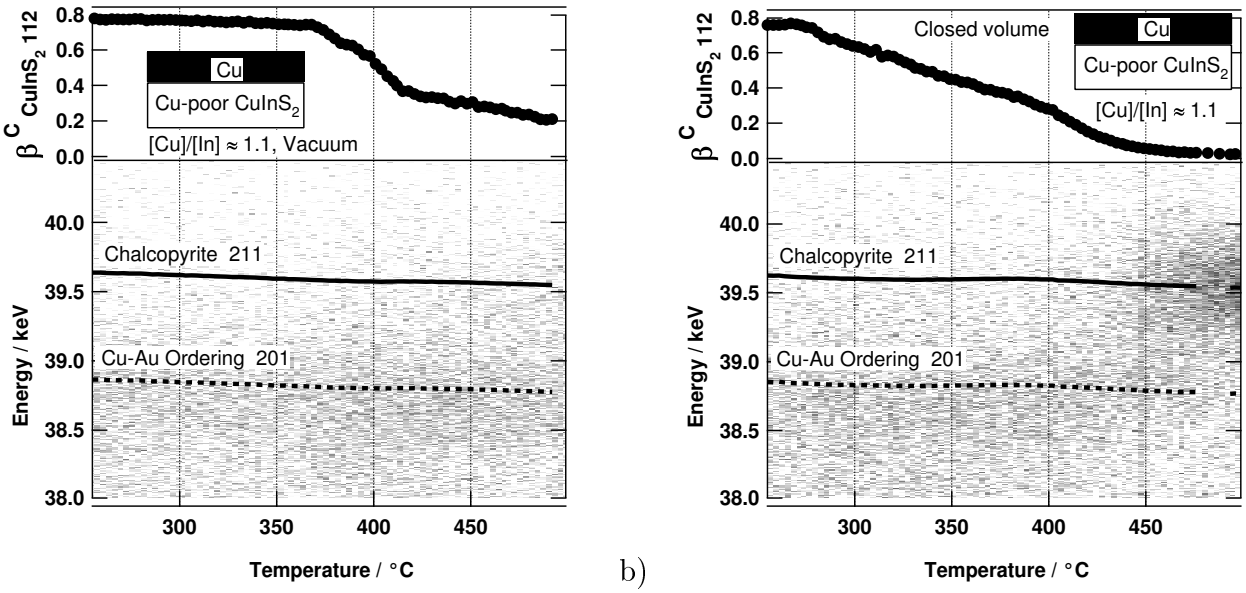

Figure 5.36.: Expected chalcopyrite 211 and Cu-Au 201 cation ordering reflections during thin-film recrystallization experiments with [Cu]/[In]≈1.1 and different sulfur pressure conditions: a) vacuum; b) closed volume. The sulfur pressure is higher in the closed volume conditions. The thin-film recrystallization of the Cu-poor $CuInS_2$, characterized by the decrease of the Cauchy-breadth β^C, is shifted to lower temperatures with the increased sulfur pressure. The fall of the Cauchy-breadth is coupled to the appearance of the chalcopyrite 211 ordering reflection. This ordering is not achieved in the vacuum annealing (left).

Figure 5.36 presents the evolution with temperature of the energy-dispersive X-ray diffraction spectra during heating of Cu-poor $CuInS_2$ layers with a top Cu layer (experiments *f* and *g* of Table 5.5) in the energy range 37 to 42keV, together with the evolution of the Cauchy-breadth of the $CuInS_2$ 112 reflection. The heatings were done under different sulfur pressure conditions: under vacuum conditions in experiment *f* (Fig. 5.36a) and under closed volume pressure conditions in experiment *g* (Fig. 5.36b). No cation ordering reflection emerges for the sample processed under the vacuum conditions and the Cauchy-breadth achieves 0.2keV at 500°C. For the sample heated in the closed volume no intermediate Cu-Au ordering reflection is detected and a chalcopyrite 211 reflection emerges at 450°C . The Cauchy-breadth achieves negligible values at 500°C in this case.

5.4.1.4. Ag assisted thin-film recrystallization

The question if silver enhances the recrystallization of $CuInS_2$ thin films was addressed by the following experiment. A Cu-poor $CuInS_2$ layer with a top Ag layer was prepared so that ([Cu]+[Ag]) / [In] $\approx$ 1.8. The sample was then heated in vacuum conditions with a heating rate of 1.44K/min, i.e. experiment *h* of Table 5.5. Given the similar ratio of group I to group III atoms (1.9 and 1.8), this Ag triggered thin-film recrystallization can be compared to the Cu triggered one (experiments *h* and *e* of Table 5.5).

Figure 5.37 presents the evolution of the energy-dispersive X-ray diffraction spectra together with the reflection indexing in the energy ranges 28.5keV to 31.5keV and 39keV to 47keV during heating of the Ag-containing bilayer. The energetic positions of the 112 reflections of $CuInS_2$ and of $(Cu_{1-x}Ag_x)InS_2$ are marked by the black cross-markers at ~30keV. These energetic positions were obtained after applying the fitting procedure described in Appendix E and assuming two possible chalcopyrite reflections. The evolution of the spectra with temperature can be divided into five stages whose limits are marked by a, b, c and d in Figure 5.37:

- After the deposition of the silver layer at room temperature, Ag-S phases were detected visually as small brown spots on the sample. They correspond to the α-Ag_2S monoclinic phase whose reflection signals (present in Fig. 5.37 at ~39keV) grow steadily until T=160°C where the phase transition to the body-centered cubic β-Ag_2S[33, 18] is observed (the expected transition temperature at normal pressure is T=178°C[117]).
- Between (a) and (b) the Ag signals decrease considerably. At (a) a shoulder appears at energies lower as the $CuInS_2$112 reflection and shifts continuously to lower energies. This can be attributed to a 311 $(Cu_{1-x}Ag_x)In_5S_8$ or a 112 $(Cu_{1-x}Ag_x)InS_2$ reflection that shifts to lower energies (larger lattice constants, see Bragg's equation 3.7 in Chapter 3) with increasing Ag content. At (b) all other reflections of the spinel $(Cu_{1-x}Ag_x)In_5S_8$ structure vanish (mainly visible at 35.9keV), and the reflection at 29.5keV can be unambiguously attributed to 112 $(Cu_{1-x}Ag_x)InS_2$.
- Between (b) and (c) the 112 $(Cu_{1-x}Ag_x)InS_2$ reflection shifts to higher energies (smaller lattice constants) and its breadth decreases. Note also that the intensity of the pure $CuInS_2$ decreases and vanishes in this temperature range. In the same period a light increase of the intensities of the β-Ag_2S phase are observed.
- At (d) the face-centered cubic $Ag_{1.2}Cu_{0.8}S$ phase appears. This phase disappears during cool down.

Figure 5.37 shows that a $(Cu_{1-x}Ag_x)InS_2$ phase appears before a decrease of the breadth of the $CuInS_2$ 112 has taken place. In a next step, the breadth the 112 reflection of the $(Cu_{1-x}Ag_x)InS_2$ phase decreases in presence of the body-centered cubic β-Ag_2S whilst the pure $CuInS_2$ phase is consumed. This is identified with the thin-film recrystallization observed for the case of pure $CuInS_2$.

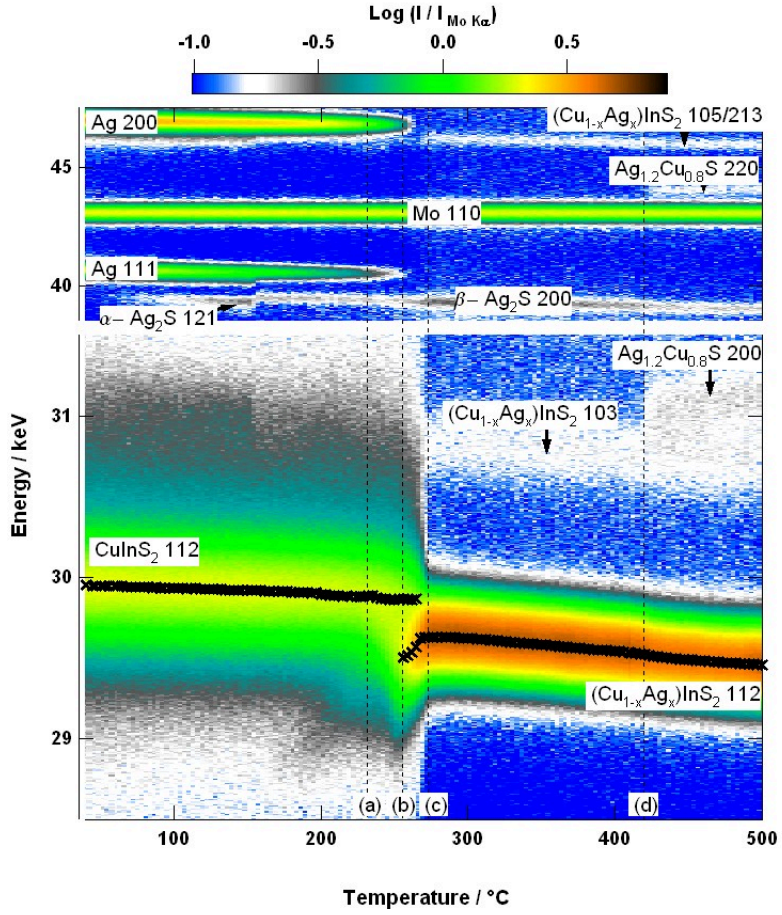

Figure 5.37.: Time-resolved EDXRD spectra during the heating of a Cu-poor $CuInS_2$ layer plus a Ag layer. The overall ([Ag]+[Cu])/[In]≈1.8. The thin-film recrystallization can be monitored through the reflections at ∼30keV. The energetic positions of these reflections (cross-markers) reveal that the $(Cu_{1-x}Ag_x)InS_2$ grows at expenses of the pure $CuInS_2$phase. The decrease of the $(Cu_{1-x}Ag_x)InS_2$ reflection's breadth occurs at 270°C and in presence of the body-centered cubic β-Ag_2S phase.

This process comes to the detection end (no further change in the broadening) at T=270°C. This is a much lower temperature in comparison to the case where pure Cu was deposited as a top layer (experiment *e* of Table 5.5 shown in Figure 5.33), i.e. T= 440°C.

5.4.2. Modeling the thin-film recrystallization

From the TEM investigations (Figs. 5.26 and 5.27) it can be inferred that the recrystallization of the thin-film is characterized by the formation of a new microstructure. The unrecrystallized film presents grain sizes of some tenths of nanometers and lamellar regions. These are completely replaced by large grains of some micrometers in dimensions of good crystalline quality (large regions with no clear presence of dislocations) presenting the chalcopyrite cation ordering (see Figure 5.30). The EBSD investigations of a laterally recrystallized thin film (see Figure 5.29) show that: a) the microstructure Cu-poor $CuInS_2$ is not maintained and b) the growth of the grains occurs homogeneously throughout the film.

The diffraction profiles (Fig. 5.31) coupled to the TEM and EBSD investigations (Figures 5.26 and 5.29) show that a large Cauchy-breadth (0.8keV) corresponds to grain sizes of the order of tenths of nanometers in magnitude and negligible Cauchy-breadths correspond to grain sizes larger than 500nm. Even if the Cauchy-breadth is known to be inversely proportional to the domain size of coherent scattering (see Section 5.4.1 of Chapter 4) these experimental results show that it in this case it can also be correlated to the grain size.

Therefore, the decrease of the Cauchy-breadth is taken as a measure of the increase in domain and grain size during the thin-film recrystallization.

This may also include the healing of structural defects by movement of dislocations (recovery as defined by Gottstein[47]). This mechanism cannot be distinguished by purely monitoring the Cauchy-breadth. Therefore, eventual healing of structural defects also makes part of the thin-film recrystallization as was presented in Section 4.4 of Chapter 4.

On the basis of the experimental results the prerequisites, the driving forces, and the enhancement factors for the recrystallization of Cu-poor $CuInS_2$ thin films will be discussed and a model that describes this mechanism will be presented.

5.4.2.1. Prerequisites

A necessary condition for the thin-film recrystallization is the consumption of the $CuIn_5S_8$ phase. The $CuIn_5S_8$ phase is always consumed before the Cauchy-breadth has achieved 0.6 keV, i.e. before significant increase in domain size. If the $CuIn_5S_8$ phase is stabilized by stabilizing the CuS phase the recrystallization will be delayed (see Figure A.8 of Appendix A for the thermodynamical prediction of such a stabilization and Figures 5.21 and 5.22 of the previous section for the experimental proof of the stabilization of the $CuIn_5S_8$ phase by an increase in the sulfur pressure).

5.4.2.2. Driving force and activation energy

The analysis of the driving force concentrates on the domain and grain growth monitored by means of the evolution of the Cauchy-breadth. This analysis is based on the following hypothesis:

- The microstructure of the thin film can be described by domains of coherent scattering;
- The smallness of the domain sizes is responsible for a Cauchy contribution of the breadth[13, 29];
- The strain effects fall purely in the Gauss contribution of the breadth[13, 29].

The TEM cross-section in Figures 5.26 and 5.27 expose the defective microstructure of the Cu-poor $CuInS_2$ material. Grain boundaries are visible in the CuS phase at the surface but are not

clear within $CuInS_2$ film. Co-existence of both ternary $CuInS_2$ and $CuIn_5S_8$ phases in a plate-like morphology can explain the periodic linear structures shown in Figure 5.27. A large density of stacking faults could also explain such structures. The Cu-poor $CuInS_2$ presents no Cu-Au or chalcopyrite cation ordering reflections. This indicates that no significant long range cation ordering is present within this layer and stresses the structural disorder of such films.

In analogy to equation 4.15 of Chapter 4 the evolution of the domain sizes, D_d, can be written as:

$$\frac{dD_d}{dt} = m_o^d \cdot exp(-\frac{Q_d}{kT}) \cdot f \tag{5.7}$$

where Q_d is the apparent activation energy for domain boundary movement, and m_0^d the pre-exponential factor of the domain boundary mobility. The pre-exponential factor also accounts for constant geometrical factors. The physical meaning of Q_d changes if the domain size is equivalent to the grain size or not. If this is the case then $Q_d = Q_g$. If not, Q_d is the activation energy for the diffusion of the slowest of the species involved in the motion of the relevant lattice defects. If f is assumed to be constant, equation 5.7 integrates to[26]

$$D_d(T) - D_d(25°C) = \frac{f \cdot m_o^d}{\varphi} \int_0^T exp(-\frac{Q_d}{kT})dT \approx \frac{f \cdot m_o^d}{\varphi} \cdot \frac{k \cdot T^2}{Q_d} exp(-\frac{Q_d}{kT}) \tag{5.8}$$

for constant heating rate experiments ($\varphi = \frac{dT}{dt}$). The Scherrer formula (Equation E.6 in Appendix E) relates Cauchy-breadth and domain size. Combining these two equations gives:

$$\beta^C(T) = \frac{1}{\frac{1}{\beta^C(25°C)} + \frac{2 \cdot sin\theta}{k^{Scherrer} \cdot h \cdot c} \cdot \frac{f \cdot m_o^d}{\varphi} \cdot \frac{k \cdot T^2}{Q_d} exp(-\frac{Q_d}{kT})} \ . \tag{5.9}$$

This equation was used to fit the temperature evolution of the Cauchy-breadth during heating of the Cu-poor $CuInS_2$/CuS bilayer with [Cu]/[In]≈1.4 under vacuum conditions, i.e. experiment *b* of Table 5.5. Figure 5.38 presents the result of this procedure. The fit was made for the Cauchy-breadths of the $CuInS_2$ reflection once the $CuIn_5S_8$ had disappeared (T>600 K). There are two sources of error in this fitting procedure: the Scherrer constant, $k^{Scherrer}$, and the temperature measurement. On one hand, $k^{Scherrer}$ does not significantly affect the determination of the activation energy because it is situated in the pre-exponential factor. On the other hand, the temperature does introduce a large error in the determination of the activation energy. To account for the inaccuracy of the temperature measurement, the fit was done for temperatures shifted ±20°C with respect to the measured values. This assumes that the real temperature of the sample might be shifted, but evolves linearly with the imposed nominal temperature. This assumption is valid because the expansion of the $CuInS_2$ 112 reflection evolves linearly with the imposed temperature (see Fig. 5.35). The fit yielded an apparent activation energy Q_d between 3 and 3.4eV.

Figure 5.38 also shows the fit of the data assuming a driving force that is inversely proportional to the domain size (as is the case of normal grain growth as defined by Gottstein[47]). The figure shows that a constant driving force yields a better fit of the experimental data.

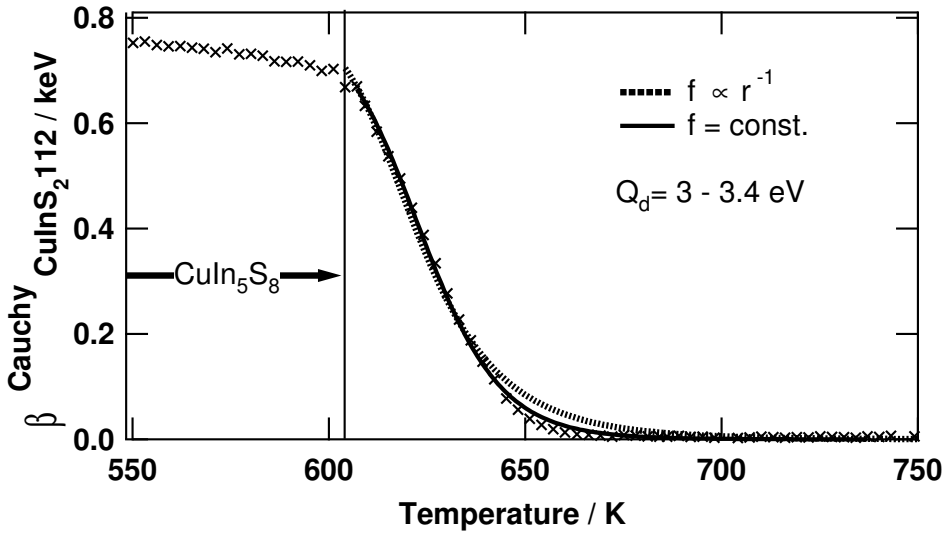

Figure 5.38.: Analytic modeling of the evolution of Cauchy-breadth during the annealing of a Cu-poor $CuInS_2$ layer covered with a CuS layer so that the overall [Cu]/[In]≈1.4. The annealing was done in vacuum with a heating rate of 1.44Kmin^{-1}. The continuous line corresponds to the fit of the data (after the consumption of the $CuIn_5S_8$ phase) with equation 5.9. Taking into account the large uncertainty in the temperature measurement, the activation energy extracted from the fit falls between 3 and 3.4eV. The dashed line corresponds to the best fit under the assumption that the driving force is not constant but inversely proportional to the domain size (as is the case for normal grain growth defined by Gottstein[47]).

The conclusions of this analysis are twofold:

a) The driving force for the domain and grain growth is well described by a constant. It could be supposed that the driving force is the density of linear and planar defects in the film, given the defective microstructure shown in Figures 5.26 and 5.27. However, other types of driving forces may also contribute to the domain and grain growth. The overall driving force is probably better described by the sum of the driving forces given in Table 4.6 of Chapter 2. These driving forces all tend to minimize the free energy of the thin film. Future investigations should focus on a clear identification of the driving force.

b) The activation energy for the domain and grain growth during the thin-film recrystallization measured by in situ X-ray diffraction was found to be between 3 and 3.4 eV. This indicates that the microscopical mechanism supporting the domain and grain growth is clearly different from the one supporting the evolution of the $2Cu_2S + CuIn_5S_8 \rightarrow 5CuInS_2$ reaction for which the activation energy was found between 0.5 and 1 eV.

5.4.2.3. Enhancement

This analysis concentrates of the enhancement of the domain and grain growth monitored by means of the evolution of the Cauchy-breadth. Enhancement means that the temperature of the growth is shifted to lower values or that the velocity of the transition is increased. This can be achieved by:

- Increasing the sulfur pressure in presence of the $Cu_{2-x}S$ phase: this was the case for the heating in presence of Cu-S phases with different sulfur pressure conditions (see Table 5.6

for the vacuum and close volume conditions) and was confirmed by experiment f and g of Table 5.5 shown in Figure 5.36. In these experiments the Cauchy-breadth profiles are qualitatively similar but shifted to lower temperatures (around 25K) when the pressure conditions increased from the vacuum to the closed volume one. Figure 5.9 shows the theoretical Cauchy-breadth temperature profiles from equation 5.9 as a function of the activation energy. With increasing activation energy the transition is shifted to higher temperatures but the profile remains qualitatively unchanged. Therefore it is postulated that the sulfur pressure reduces the activation energy Q_d for the domain and grain growth. This indicates that domain and grain growth are controlled by bulk diffusion processes. Enhancement of diffusion processes by increased chalcogen pressure was found by Matsushita[80] in $A^IB^{III}Se_2$ thin films. He measured a decreasing melting point with increasing Se pressure. Triboulet[131] also observed an enhanced grain growth of ZnS films by increasing the sulfur pressure during annealing.

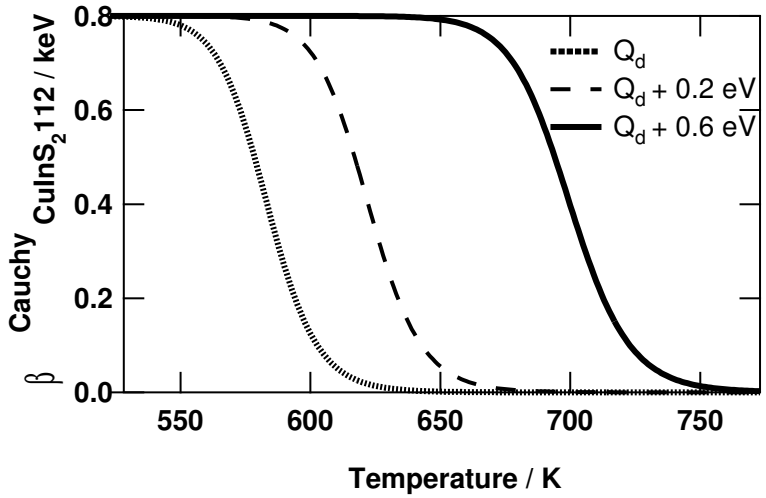

Figure 5.39.: Cauchy-breadth profiles from equation 5.9 as a function of the activation energy Q_d. An increase in the activation energy of 0.4eV shift the domain and grain growth ~80K to higher temperature. This shift is qualitatively observed when the trigger for the recrystallization is pure Cu (β^C(420°C)=0.4keV from Figure 5.33) or a CuS layer (β^C(340°C)=0.4keV from Figure 5.38) in vacuum conditions.

- Increasing the [Cu]/[In] ratio: Figure 5.33 shows that Cu excess controls the velocity of the growth. Accepting the validity of equation 5.9, Cu excess may not only affect the apparent activation energy but also the pre-exponential factor m_0^d. An increase in both the activation energy and the pre-exponential factor could explain the same transition temperatures but the shorter transition times with increasing Cu content. The [Cu]/[In] ratio may also affect the driving force f. For all of the analysis presented here this force was assumed to be constant. However, as discussed in the previous section, the driving force is not clearly identified and it may have a contribution of chemical nature.

- Increasing the cation mobility: Cation mobility can be enhanced by alloying with Ag. In this case the domain and grain growth occur at temperatures as low as 270°C. The mobility of the cations can be qualitatively compared by looking at the melting points of the ternary sulfides: $AgInS_2$, $CuInS_2$, and $CuGaS_2$ have melting points of 871°C, 1079°C, and 1200°C respectively. Correspondingly domains and grains of (Ag,Cu)InS_2 grow at lower temperatures compared to $CuInS_2$ ones (see Figure 5.37) and Cu(In,Ga)S_2 grains remain smaller than $CuInS_2$ ones[76,

89] at temperatures around 500°C. This indicates once again that domain and grain growth are controlled by bulk diffusion processes.

5.4.2.4. Microscopical approach

This section will evaluate the applicability of the microscopical approaches exposed in Section 4.4.2 of Chapter 4 to explain the recrystallization of $CuInS_2$ thin films.

1. Liquid phase approach: there are two points that question the validity of the liquid phase approach.
   a) The temperature of the transition CuS to $Cu_{2-x}S$ does not correlate with the enhancement of this mechanism, see Table 5.6. This is expected if the pseudo-liquid phase is necessary for growth.
   b) The presence of Cu-S phases within the film is not always given. Figure 5.28 shows that it is possible that CuS phases segregate within the film, but figure 5.34 shows that recrystallization may occur without this being a necessary consequence (no pinholes were revealed after etching of the Cu-S phases).
2. The topotaxial approach: the prerequisites of the topotaxial approach include the presence of a face-centered cubic phase that is lattice matched to the chalcopyrite phase. There are two points that do not support this hypothesis:
   a) Domain and grain growth of $(Cu_{1-x}Ag_x)InS_2$ was observed in presence of a body-centered cubic β-Ag_2S phase.
   b) Domain and grain growth has started short before the CuS to $Cu_{2-x}S$ phase transition in the case of the heating with a sulfur source, see Table 5.6.
3. The bulk diffusion approach: the bulk diffusion approach can explain the experimental observations. The last paragraph showed that the cation vacancy concentration and the cation mobility are capable of enhancing the domain and grain growth processes. This indicates that diffusion and point defects in the material are the key to this mechanism. A main conclusion of this work is that the domain and grain growth of Cu-poor $CuInS_2$ thin films is supported by the bulk diffusion of the cations.

The bulk diffusion approach

Wissmann[143] studied the bulk diffusion of cations in the $CuInS_2$ phase. He states that In is the slowest diffusing cation and finds that diffusion of In is coupled to the diffusion of Cu. He postulates that in the stable chalcopyrite structure diffusion of In occurs via Cu vacancies. Figure 5.35 shows that the films presented no long range cation ordering before recrystallization (within the detection limits of the instrumentation). Highly resolved ex-situ X-ray diffraction measurements show only traces of Cu-Au ordering. In a random cation configuration (sphalerite structure, see Section 2.3 of Chapter 2) no formation of antisite is necessary to support the diffusion of In. Only the formation of vacancies should be relevant. In a neutral defect model, cation vacancy concentration increases with increasing S activity[143]. In the $CuInS_2$ thin films presenting the sphalerite structure excess S could create cation vacancies that support diffusion of cations, and in particular of In cations. These vacancies can be created at the surface and must diffuse through the entire film to support domain and grain growth. The $Cu_{2-x}S$ phase on the surface may accelerate the cation vacancy formation at the surface. This phase is known to enhance the incorporation of sulfur in the $CuInS_2$ phase[119, 103].

5.4.2.5. Model of the recrystallization of $CuInS_2$ thin films

A qualitative model for the recrystallization of a film composed of $CuIn_5S_8$ and $CuInS_2$ and in presence of excess copper in a secondary Cu-S phase was developed. Figure 5.40 presents the morphology change and Figure 5.41 presents the model in a diagram free energy of the system vs. transition coordinate. The model consists of three steps:

1. Consumption of the $CuIn_5S_8$ phase: no significant growth of $CuInS_2$ domains will take place as long as the ternary $CuIn_5S_8$ phase is present within the film. This blockade is represented as an energy barrier for the system in Figure 5.41. This barrier is controlled by the presence of the CuS phase. Once the transition $2CuS \rightarrow Cu_2S + S$ occurs, the barrier will be removed and the $CuIn_5S_8$ phase will be consumed following the reaction studied in detail in the previous section of this Chapter, i.e. $2Cu_2S + CuIn_5S_8 \rightarrow 5CuInS_2$. This reaction is thermally activated with a free energy barrier G_a^R. The driving force for the reaction is ΔG_R (free energy of reaction). The result of this reaction is a defective (in terms of point, linear and planar defects) phase. In particular the cations present no long range ordering and the domains of coherent X-ray scattering are of the order of some tens of nanometers.

2. Domain and grain growth: this includes the healing of structural defects and the growth of the domains and grains. After this step the cations are found in the metastable Cu-Au ordering. The driving force for the domain and grain growth is well described by a constant, f. This can be the large density of structural defects in the film but contributions from other forces that minimize the free energy cannot be discarded. If V is the volume of the system, the small-grained and defective state is at an energy level $f \times V$ lower than the large-grained state. To achieve this level the system must overcome an energy barrier G_a^{RX}. This process is supported by the diffusion of cations. This means that the anion sublattice remains, in first approach, unmodified. The diffusion of cations can be enhanced by:

   - Increasing the concentration of cation vacancies, V_{Cat}. Increasing S pressure during processing results in the creation of cation vacancies at the surface of the sample that can diffuse into the bulk of the material. The presence of a $Cu_{2-x}S$ phase on the surface may accelerate the creation of cation vacancies at the surface of the $CuInS_2$ film because it enhances the incorporation of S in the $CuInS_2$ lattice. The experimental results lead to the supposition that an increased cation vacancy concentration yields a decrease in the energy barrier G_a^{RX};
   - Increasing the overall cation mobility. This can be achieved by alloying with more mobile cations like Ag.

3. Cu-Au to chalcopyrite cation ordering transition: cations re-order to achieve the stable chalcopyrite structure (abbreviated as CH in Figure 5.41). The driving force for this transition is $\Delta G_{CuAu \rightarrow CH}$, and the free energy barrier is $G_a^{CuAu \rightarrow CH}$.

The color-coded arrows in Figure 5.41 represent possible paths for the recrystallization.

- Path A: This corresponds to the case where the system goes completely through each step as temperature increases. This is achieved in the sulfurizations where the sulfur pressure is low so that the $2CuS \rightarrow Cu_2S + S$ occurs at a temperature lower than the domain and grain growth one. The latter will take place at higher temperatures followed by the copper-gold to chalcopyrite ordering transition. This corresponds to Figures 5.32b) and 5.35, i.e. experiment c of Table 5.5.
- Path B: This path corresponds to the case where the cation vacancy concentration is low. This can be achieved by reducing the S activity in the film considerably. After the $CuIn_5S_8$

phase is consumed the energy barrier G_a^{RX} is so large that, at a given temperature, the system can skip the metastable state where the cations are organized in the Cu-Au ordering and will achieve the state where the cations are organized in the chalcopyrite ordering and the domains and grains are large. This corresponds to the thin-film recrystallization shown in Figure 5.36b), i.e. experiment g of Table 5.5.

- Path C: This path corresponds to the extreme case where there is no $2CuS \rightarrow Cu_2S + S$ transition. This can be achieved by increasing considerably the sulfur pressure. In this case the $CuIn_5S_8$ phase will be consumed by the proposed reaction $4CuS + CuIn_5S_8 \rightarrow 5CuInS_2 + S_2$. The temperatures required for this are probably so high that the consumption of the $CuIn_5S_8$ phase, the domain and grain growth and the Cu-Au to chalcopyrite ordering transition will occur simultaneously. This path has to be confirmed in the future in an experimental setup that allows the separate heating of the samples and a high sulfur pressure.

These exemplary paths are the basis for process design that include a thin-film recrystallization step. For example, a film that does not present important amounts of the Cu-Au ordering (path B) during growth may have lower concentration of point defects of the type Cu_{In} or In_{Cu} than a film that completely transforms into the Cu-Au ordering before achieving the chalcopyrite ordering (path A) (assuming this last transition is incomplete). Attempting to achieve path C by increasing considerably the sulfur pressure could be deleterious for the homogeneity of the film. At high temperatures, a locally induced $2CuS \rightarrow Cu_2S + S$ transition would trigger an inhomogeneous domain and grain growth. This becomes even more critical when the secondary CuS phase does not completely cover the underlying $CuInS_2$ film. It is known that CuS tends to form very large grains with an Island-like morphology on top of the $CuInS_2$ films (see Figure 5.28). On the other hand, path C could be interesting if a laterally-evolving recrystallization front is desired. This would have the advantage of a clear division between the precursor stage and the recrystallized stage. This recrystallization front could be monitored optically (via the $2CuS \rightarrow Cu_2S + S$ transition).

A further important point is the cation mobility. Alloying with a more mobile cation like Ag increases the velocity of the transition. This can result in a clear reduction of the thin-film recrystallization temperature (including consumption of the $CuIn_5S_8$ phase, domain and grain growth and transition to the chalcopyrite ordering of the cations): from 440°C to 270°C in case of the experiments e and h of Table 5.5. The increase in the overall cation mobility is difficult to represent in the free energy vs. transition coordinate diagram of Figure 5.41. However, the increase in cation mobility has a similar effect as an increase in the temperature and can be translated in the diagram of Figure 5.41 with such an analogy.

The last question to be addressed is the role of the secondary Cu-S phases. First, the $2CuS \rightarrow Cu_2S + S$ transition plays a very important role in the thin-film recrystallization (see Figure 5.41). On one hand it triggers the consumption of the $CuIn_5S_8$ phase, and on the other it liberates S that can be incorporated in the $CuInS_2$ lattice creating cation vacancies and lowering G_a^{RX}. The $Cu_{2-x}S$ may also enhance the further incorporation of S from the gas phase, introducing further cation vacancies. However, this phase is not absolutely necessary for the domain and grain growth in the film (as was proposed by Klenk[68] and Wada[136] for the Se system). If the $CuIn_5S_8$ phase is not present and if enough cation vacancies are available, domain and grain growth may take place. In this case the domain and grain growth can be enhanced by other means other than the $Cu_{2-x}S$-supported cation-vacancy creation; for example by increasing the cation mobility.

The $Cu_{2-x}S$ phase can also be deleterious for the $CuInS_2$ thin film if it does not remains at the surface. It can be responsible for the creation of pinholes in the final device (see Figure 5.28). One way to block the mobility of this phase is to reduce the sulfur pressure. Indeed, when working at low sulfur activity (bringing the copper excess on the Cu-poor $CuInS_2$ thin films as a pure

Cu layer) the secondary Cu-S phases remain at the surface of the $CuInS_2$ film as a closed layer and no pinholes are formed (see Figure 5.34). It seems that the presence of Cu-S phases within the film is a pure consequence of the high cation mobility both in the $CuInS_2$ and in the $Cu_{2-x}S$ phases. The experimental results indicate that the secondary $Cu_{2-x}S$ phase enhances, but is not directly involved in the domain and grain growth of the $CuInS_2$ films (step 2 of the thin-film recrystallization model of Figure 5.41).

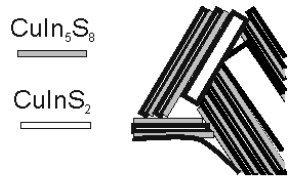

- As long as the ternary $CuIn_5S_8$ is within the film no significant thin-film recrystallization will take place. This phase is stabilized by the CuS phase. Once the 2CuS->$Cu_{2-x}S$ +S transition occurs the $CuIn_5S_8$ will be consumed.This results in a defective $CuInS_2$ thin film.

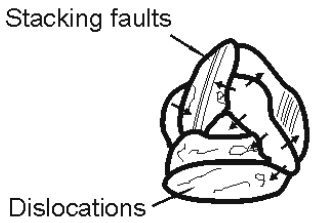

- The driving force for domain and grain growth is well described by a constant. A large density of linear and planar defects within the grains could account for the driving force. However elastic, electrochemical forces and the force for normal grain growth can also contribute to the total driving force.
The driving force pushes the grain boundaries in the direction that minimizes the total energy of the system.

- There is no long range cation ordering.

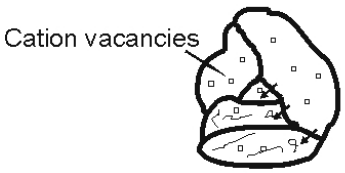

- Healing of structural defects and movement of grain boundaries is supported by cation diffusion. This is assured by the presence of cation vacancies. These vacancies can be created at the surface of the film. The $Cu_{2-x}S$ phase may accelerate their creation. At this stage the cations are organized in the metastable Cu-Au ordering.

- Diffusion of cations can be enhanced by increasing their mobility or by increasing the cation vacancy concentration.

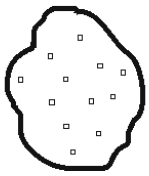

- At higher temperatures the cations will rearrange within the anion sublattice to achieve the stable chalcopyrite ordering.

Figure 5.40.: Morphology evolution during the recrystallization of defective Cu-poor $CuInS_2$ thin films in presence of copper excess.

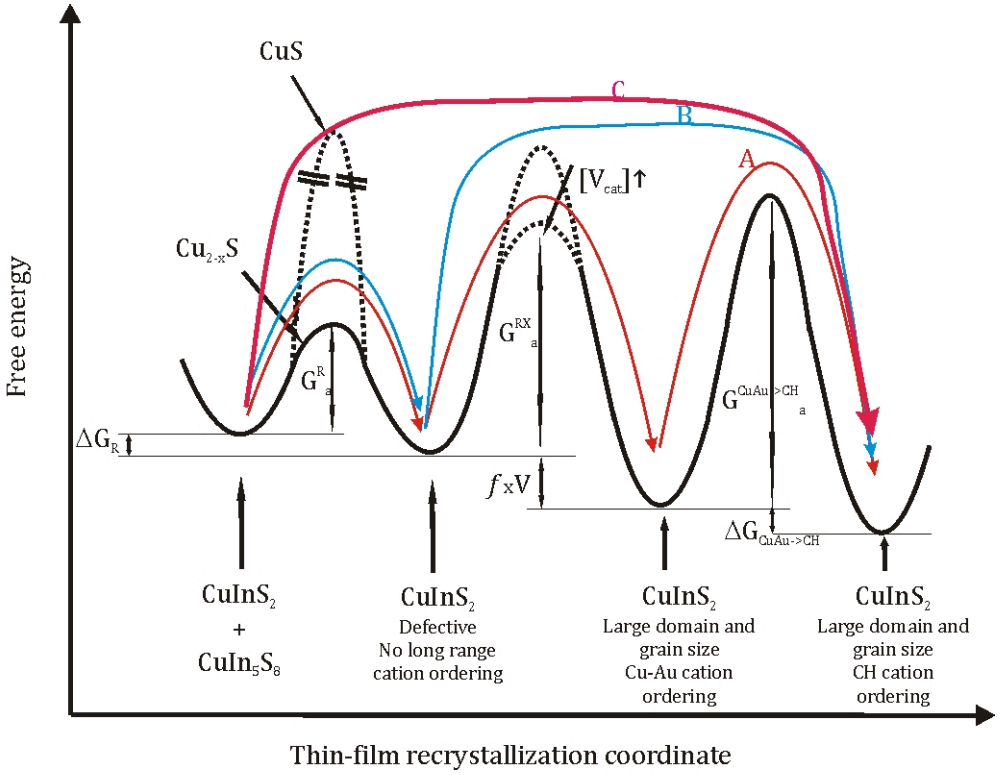

Figure 5.41.: Model for the thin-film recrystallization of defective Cu-poor $CuInS_2$ thin films in presence of copper excess in the free energy vs. transition coordinate diagram. The model is divided in three steps: the consumption of the $CuIn_5S_8$ phase controlled by the $2CuS \rightarrow Cu_2S + S$ transition, the domain and grain growth of the $CuInS_2$ phase and the transition from the Cu-Au to the chalcopyrite cation ordering. G_a^R, G_a^{RX}, and $G_a^{CuAu \rightarrow CH}$ stand for the free energies of activation and ΔG_R, $f \times \Delta V$, and $\Delta G_{CuAu \rightarrow CH}$ for the driving forces for each step. G_a^{RX} can be reduced by increasing the cation vacancy concentration $[V_{cat}]$. This enhances domain and grain growth. An increased cation mobility (for example through Ag alloying) enhances the complete thin-film recrystallization mechanism. An increase in the mobility has a similar effect as an increase in the temperature. The color-coded arrows represent the possible thin-film recrystallization paths. Path A represents a step-by-step transition as temperature increases under constant sulfur pressure conditions, path B represents a transition that skips the Cu-Au ordering by lowering the S activity in the film and path C represents a transition where the consumption of the $CuIn_5S_8$ phase, the domain and grain growth and the Cu-Au to the chalcopyrite cation ordering transition occur almost simultaneously. This can be achieved by increasing the sulfur pressure to stabilize the CuS phase.

5.4.3. Conclusions

The recrystallization of a Cu-poor $CuInS_2$ thin film was monitored in real time thanks to the *in situ* EDXRD setup. This is the first time that this mechanism that can be isolated and investigated for any $A^IB^{III}X_2^{VI}$ chalcopyrite compound. The conclusion of these investigations are summarized by the model proposed in Figure 5.41. This model serves as a basis for the design of fabrication processes that include a thin-film recrystallization step. Two concrete consequences for the fabrication of $CuInS_2$ thin films emerge from these investigations.

- The sulfur activity plays a determining role in the recrystallization of Cu-poor $CuInS_2$ thin films: it can delay it by means of the $2CuS \rightarrow Cu_2S + S$ transformation and it can enhance domain and grain growth by increasing the cation vacancy concentration.
- The recrystallization of the thin film can be induced at low temperatures (as low as 270°C) and without having to segregate Cu-S phases within the film. To do this the film must contain only one ternary phase and the cation mobility must be enhanced. A clear increase in the cation mobility can be achieved by alloying with Ag.

The activation energy for the domain and grain growth step was estimated to be between 3 and 3.4eV. This is more than three times the activation energy of the reaction $2Cu_2S + CuIn_5S_8 \rightarrow 5CuInS_2$ (between 0.5 and 1eV) studied in the previous section and that constitutes the first step of the model. This indicates that microscopical processes supporting both mechanisms are fundamentally different.

Once the films have recrystallized, the $CuInS_2$ and $Cu_{2-x}S$ phases can interdiffuse. This can affect the surface of the $CuInS_2$ grains and will be discussed in the next section.

5.5. Sulfide Interdiffusion

The interdiffusion between $Cu_{2-x}S$ and $CuInS_2$ cannot be probed by the bulk X-ray diffraction methods used during this work. The proof of dissolution of $CuInS_2$ by $Cu_{2-x}S$ is done by means of morphological consideration of films containing both phases.

5.5.1. Dissolution of $CuInS_2$ by Cu_2S

Figure 5.42a) presents an SEM plane view of a sample that was processed in the same way as that described for experiment *b* of Table 5.5 of the previous section, i.e. recrystallization of a Cu-poor $CuInS_2$ thin film in presence of $Cu_{2-x}S$ (heating rate of 1.44 $Kmin^{-1}$ under closed volume pressure conditions). Figure 5.42b) presents the plane view of a sample heated with increased sulfur pressure, i.e. experiment *d* of Table 5.5. Figure 5.42c) and d) presents the plane view of the same Cu-poor $CuInS_2$ /CuS bilayers after heating in vacuum with rates of 1.44$Kmin^{-1}$ and 46$Kmin^{-1}$ respectively. All samples were etched with KCN to remove the Cu-S phases. Figure 5.42a) corresponds to the cross-section presented in Figure 5.28, but without the CuS sulfide phases that are seen as islands on the surface of the $CuInS_2$ in the TEM image.

The $CuInS_2$ grains are evenly distributed in every case. There are pinholes, encircled in the figures, that may traverse the whole film. This means that Cu-S phases were also present between $CuInS_2$ grains. On the top of some grains, indicated by an arrow in the figure, irregular structures are identified. This structures occupy larger areas and, qualitatively, penetrate deeper in the $CuInS_2$ grains in the case of increased sulfur pressure (plane view b with respect to plane view a) and in the case of slower heating ramps (plane view d with respect to plane view c).

Controlling the dissolution

Given the asymmetrical solubilities, it is expected[121] that $Cu_{2-x}S$ dissolves $CuInS_2$ while it advances in the direction of the $CuInS_2$ grains. Therefore, etching of the samples reveals the irregular penetration of the $Cu_{2-x}S$ phase in the $CuInS_2$ grains. Because there is no chemical reaction, interface growth is probably limited by the diffusion indium in the $Cu_{2-x}S$ matrix. Based on the ionic radii, Mansour[79] proposes that In may occupy Cu sites in the $Cu_{1.8}S$ phase. Based on this criterion the same can be hypothesized for the cubic $Cu_{2-x}S$ phase. Rau[100] and Pareek *et al.*[95] propose that Cu vacancy concentration in $Cu_{2-x}S$ increases with sulfur pressure. Therefore increasing the sulfur pressure may enhance the diffusion of In in this phase. To summarize, the evolution of the interface between $Cu_{2-x}S$ and $CuInS_2$ depends on:

- Temperature, it determines the solubility of $CuInS_2$ in $Cu_{2-x}S$;
- Sulfur pressure, it determines the copper vacancy concentration in the $Cu_{2-x}S$ phase;
- Time.

Figure 5.43 proposes the moving interface during the interdiffusion as well as the direction of the diffusing In cations. A plausible hypothesis is that when using the same times and temperatures a variation in the sulfur pressure could lead to different point defect concentrations (related to In) near the surface of the $CuInS_2$ films. This because the diffusion of In in the $Cu_{2-x}S$ phase is probably enhanced by increasing the sulfur pressure. This effect should be investigated in the future by more sensitive and space-resolved methods.

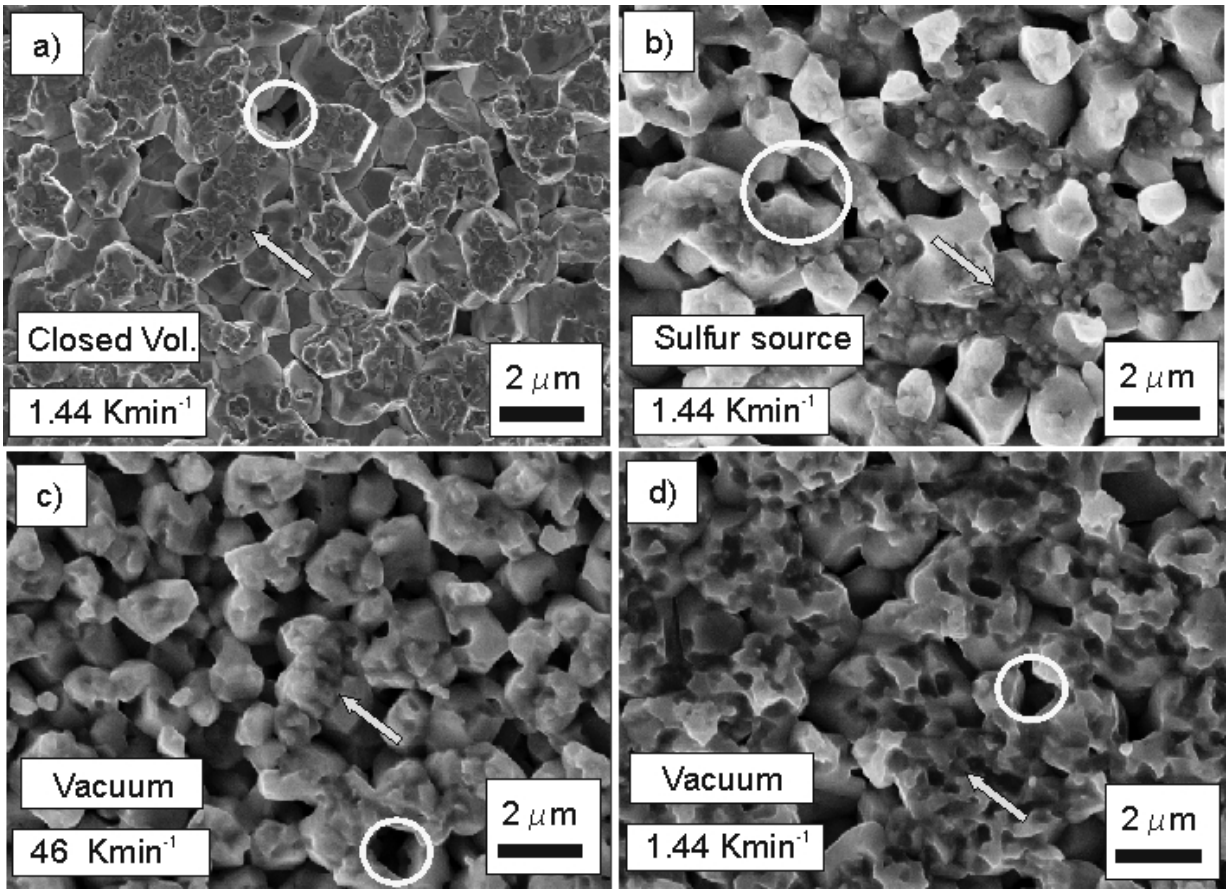

Figure 5.42.: Scanning electron micrographs in plane view of a $CuInS_2$ sample after a recrystallization in presence of $Cu_{2-x}S$. The samples were etched with KCN to remove the Cu-S phases. They correspond to: a) closed volume conditions, heating rate 1.44Kmin^{-1}, b) sulfur source conditions, heating rate 1.44Kmin^{-1}, c) vacuum conditions, heating rate 46.1Kmin^{-1}, d) vacuum conditions, heating rate 1.44Kmin^{-1}. For the description of the pressure conditions see Section 5.4.

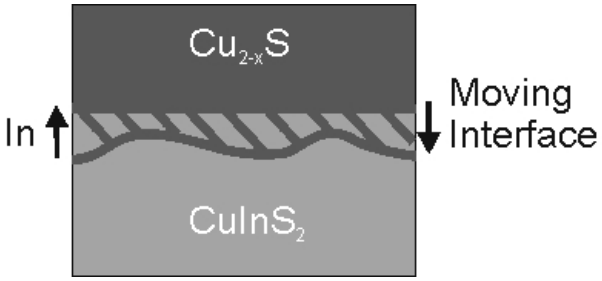

Figure 5.43.: Schematic representation of the dissolution of $CuInS_2$ by the $Cu_{2-x}S$ phase. The interface moves in direction of the $CuInS_2$ phase. The interface movement is supported by the diffusion of In in the $Cu_{2-x}S$ phase.

5.5.2. Conclusions

The interdiffusion of two phases is a process that occurs when there is a range of solubility of one phase in the other, or when a mixed phase can be formed. $Cu_{2-x}S$ does dissolve $CuInS_2$. This process depends on time, temperature and sulfur pressure and may affect the defect concentration at the surface of the $CuInS_2$ grains that are covered by the secondary $Cu_{2-x}S$ phase. This is of high relevance for the fabrication of solar cell absorbers because the surface of the film determines the band alignment at the heterojunction with the CdS buffer layer. If the time is reduced (for example in RTP fabrication) such effects are restricted to a narrow range near the surface of the films. These effects should be studied in the future with surface-sensitive and space-resolved techniques.

5.6. Summary

The sulfurization process consists of heating metallic precursors in presence of sulfur vapor. This chapter studied five mechanisms whose interaction determines the microstructure of the resulting $CuInS_2$ when using such a process. Figure 5.44 summarizes the different mechanisms and the temperature ranges where they are relevant.

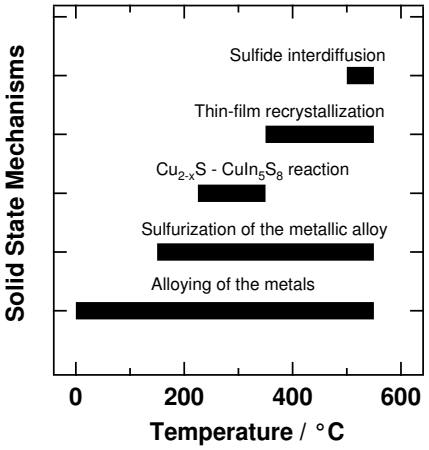

Figure 5.44.: Active mechanisms during the sulfurization in a closed space of Cu-In thin films and their relevant temperature ranges.

The sulfur pressure controls the majority of the mechanisms. For example, the presence of intermediate sulfides will be avoided if sulfur is offered at low pressures (p_S<10^{-3}mbar) only once the metals have reached 500°C. In this case the risk of a deleterious enrichment in Cu of the metallic phases (initially Cu-rich) increases and a bad adhesion of the films is always observed. If sulfur is offered at low temperatures (T< 220°C) and for sufficient times (depending on the sulfur pressure), the alloy will decompose in CuS and InS. This two intermediate phases lead to a $CuInS_2$ film that is unusable as a solar cell absorber. Sulfurizing at high pressures (p_S∼1mbar) and intermediate temperatures (T∼330°C) leads to the presence of an intermediate step where defective $CuInS_2$ and $CuIn_5S_8$ coexist. The $CuIn_5S_8$ phase must be consumed to obtain a pure $CuInS_2$ film (with eventual Cu-S phases that can be removed by a chemical etching procedure). This can be done at high rates (12min at ∼340°C and low pressures p_S<10^{-3}mbar) if the $Cu_{2-x}S$ phase is available. The thin-film recrystallization (meaning healing of structural defects, growth of domain and grain sizes and the Cu-Au to chalcopyrite cation ordering transition) of the $CuInS_2$ phase follows. This mechanism is at a great extent controlled by the sulfur activity (see the thin-film recrystallization model in Figure 5.41). In the last step the sulfur activity will probably modify the defect concentration near the surface of the films through the interdiffusion between the $CuInS_2$ and the $Cu_{2-x}S$ phases.

These are some selected examples of the importance of the sulfur pressure on the processing of the Cu-In thin films. They make clear that the focus of this process must be widened to cover not only the time and the temperature (as was done until now, see Section 2.6 of Chapter 2) but also the sulfur pressure. If this is made, deliberate microstructure engineering can be aimed at using the qualitative and quantitative information gathered in this chapter. These facts and models constitute a toolbox necessary for further microstructure improvement. A known deficiency of these films is the void formation near the Mo back contact (see Figure 1.1 of Chapter 1). This problem was addressed during this work using the breakdown of the sulfurization as proposed in Figure 5.44. The next chapter presents a new rapid thermal sulfurization process that bypasses

this void formation.

6. A New Rapid Thermal Process for Increased Adhesion

In this chapter a new rapid thermal sulfurization process will be presented. This sulfurization solves the problems of bad adhesion of the $CuInS_2$ films due to the presence of voids between the film and the Mo back contact (see Figure 1.1 of Chapter 1). This sulfurization was monitored *in situ* by means of the EDXRD method presented in Chapter 3. The mechanisms exposed in Chapter 5 are active during this rapid thermal sulfurization and will be exposed in detail.

The sulfurization process

The precursor films consisted of bilayers of Cu and In sputtered on Mo-coated soda-lime glass with a [Cu]/[In]≈1.6. After some days of storage the precursor film stack transformed to $Mo/Cu/CuIn_2$. Figure 6.1 presents the morphology of the precursor film. The $CuIn_2$ phase is distributed in a mountain-valley morphology on top of the Cu film.

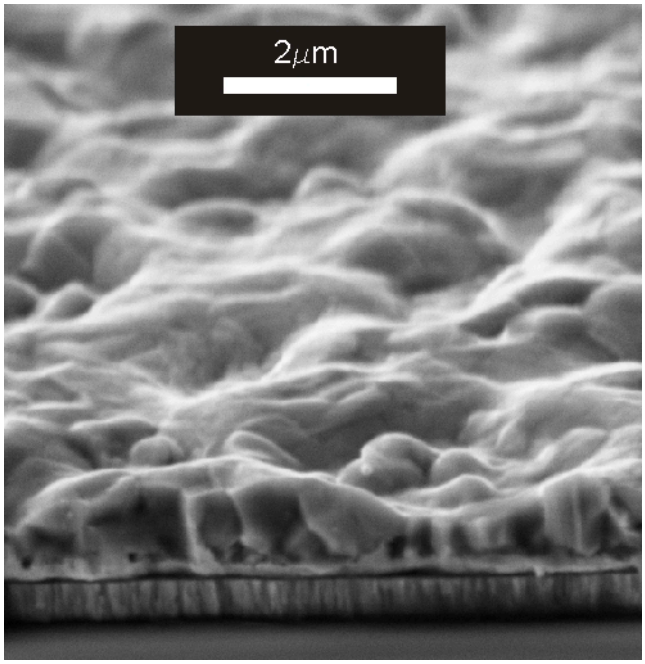

Figure 6.1.: Precursor $Mo/Cu/CuIn_2$ film before the rapid thermal sulfurization. The $CuIn_2$ phase has a mountain-valley-like morphology.

The precursor film was heated in the in situ chamber (see Section 3.1 of Chapter 3) together with 6mg of elementary sulfur inside of the reaction box. The overall S to In ratio was 3.3. The total heating time was restricted to 4.6min. During the sulfurization the temperature was recorded by a thermocouple placed in contact with one of the films. This temperature measurement does not give the exact temperature of the film but can be taken as a rough indicator of its evolution. The sulfur pressure profile was optimized by means of the valve that seals the reaction box (see Figure

3.1 of Chapter 3). To do this, the position of the valve was fixed so that it remained slightly opened during the lower temperature regime and closed at higher temperatures. Complementary RTP sulfurizations (and solar cell results) showed that an adequate time to seal completely the reactor by means of the valve is $t \sim 2.8$min. A more precise determination of the sulfur pressure is not possible in the configuration of the RTP chamber shown in Figure 3.1 of Chapter 3. A controlled sulfur pressure profile and its measurement belongs to the future developments of the RTP sulfurization technology.

Figure 6.2 presents the phase sequence evolution during the sulfurization together with the measured temperature. This was obtained by fitting the indicated reflections by Gaussian profiles and by plotting their normalized intensities against time. The evolution of the metallic and of the sulfide phases is separated in the graph (top and bottom respectively).

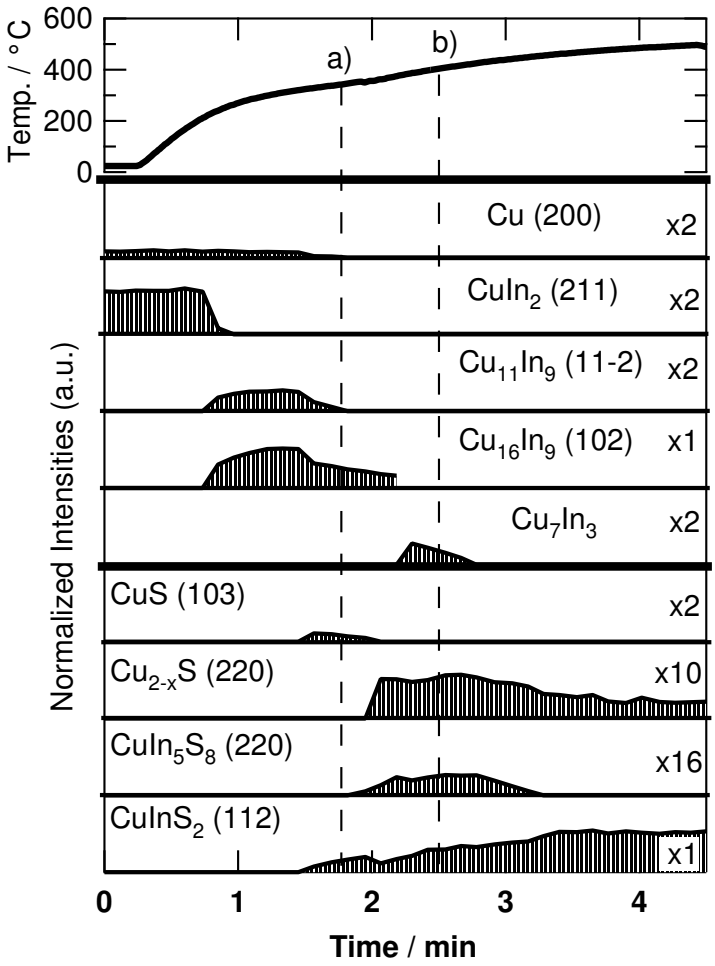

Figure 6.2.: Phase existence plot during the rapid thermal sulfurization of a Mo/Cu/$CuIn_2$ layered stack. The data corresponds to the intensities of the indicated X-ray reflections normalized to the Mo$K\alpha$ signal. The temperature corresponds to the measurement of a thermocouple placed in the vicinity of the samples. The dashed lines indicate the times of the break-off experiments.

Growth mechanisms

The formation of the microstructure of the resulting $CuInS_2$ can be understood if the process is broken down into the five mechanisms depicted in Chapter 5 and if their interaction is analyzed.

1. Alloying of the metals: between the process-start and t=2.8min the metals react and form $Cu_{11}In_9$ then $Cu_{16}In_9$ and then Cu_7In_3. This follows the same reaction schema of Figure 5.1 of Chapter 5. A first reaction, $CuIn_2(s) \rightarrow Cu_{11}In_9(s) + In(l)$, liberates In in the liquid state. This is of relevance because In can be lost in form of the volatile In_2S(g) phase. An coating (β-In_2S_3) is usually found in the walls of the reaction box after RTP processing indicating such a loss. The second reaction that can liberate In is the $Cu_{11}In_9$ to $Cu_{16}In_9$ transition. In this case the sulfurization has already started and a closed CuS layer on the surface inhibits further In loss. It is concluded that indium loss can be avoided if the starting alloy is $Cu_{11}In_9$. The second important issue of the intermetallic alloying is the formation of a solid solution of In in Cu. If this phase appears, large opposite strains between metals and sulfides are possible (see Section 5.1 of Chapter 5). Figure 6.2 shows that no Cu(In) phase was detected at high temperatures. This is the result of an optimization of the rapid thermal processing parameters.

2. Sulfurization of the metallic alloy: the sulfurization starts at t=1.5 and ends at t=2.8 with the consumption of the metals. The first detectable sulfides are CuS and $CuInS_2$. A break-off experiment at marker a) of Fig. 6.2 exposes the morphology at the beginning of the sulfurization. At this point the film is composed of a closed CuS layer on the surface, a porous intermediate layer and a continuous metallic layer at the bottom. Ex-situ X-ray diffraction revealed that the porous intermediate layer contained both $CuInS_2$ and $CuIn_5S_8$. Figure 6.3 presents the cross-section of the break-off experiment at marker a). The figure also shows a plane view of the porous layer. This was obtained by etching away the CuS phase with KCN. This layer is composed by very small grains. Plate-like structures are identified through out the plane view. At a later stage in the sulfurization the same configuration is maintained. Figure 6.4a) presents the cross-section of a film that resulted from a break-off experiment at t=2.5. Figure 6.4b) shows the mapping of the Cu fluorescence line in the same cross-section. This mapping serves to distinguish the phases within the film. In this case, both ternary $CuInS_2$ and $CuIn_5S_8$ phases were clearly identified in the in situ and in the *ex situ* X-ray diffraction spectra. The cross-section is characterized by a closed CuS layer (the CuS stems from the $Cu_{2-x}S$ phase at high temperatures present in Figure 6.2), an intermediate porous layer and of metallic phases in form of islands (characterized by a higher Cu fluorescence signal) near the back Mo film. The intermediate porous layer is qualitatively thicker than the one shown in Fig. 6.3. The Cu fluorescence line shows a Cu depletion near the CuS. This can be understood as a predominance of the $CuIn_5S_8$ phase near the Cu-S phases during sulfurization. The layer sequence Mo/metals/$CuInS_2$-$CuIn_5S_8$/CuS is typical of high sulfur pressure sulfurizations (p_S∼1mbar) at intermediate temperatures.

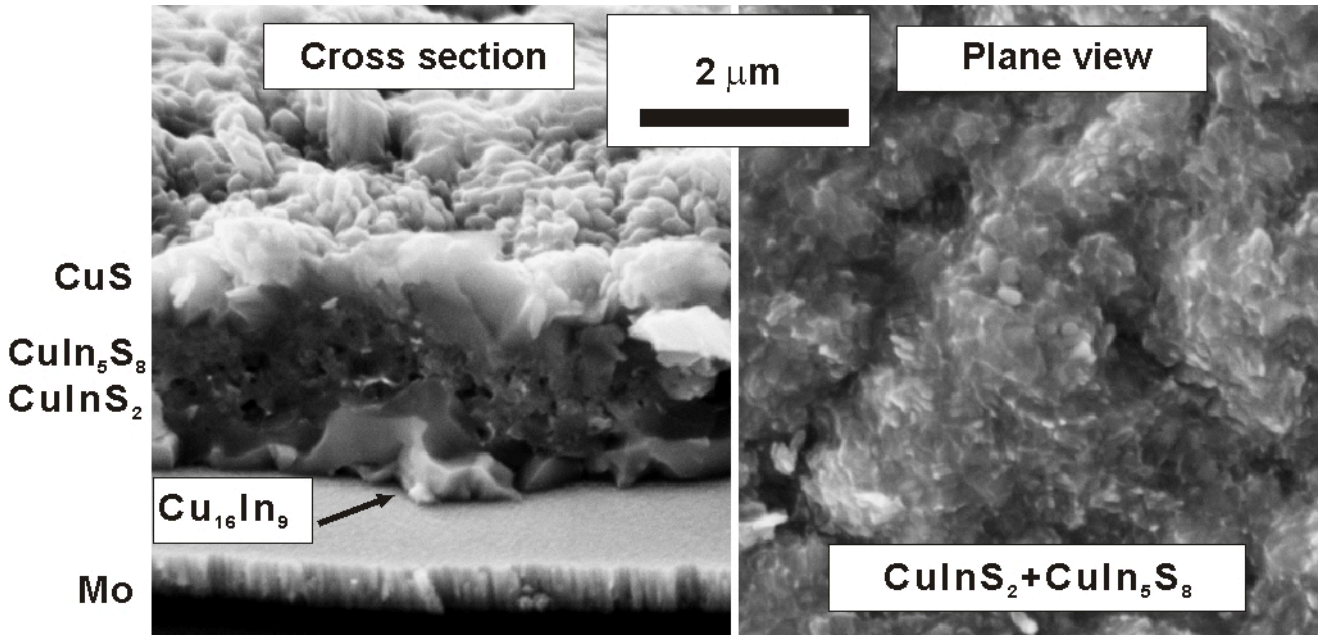

Figure 6.3.: Break-off experiment at marker a) of the RTP sulfurization shown in Figure 6.2 . The layer sequence is metals/porous $CuInS_2$-$CuIn_5S_8$/CuS. The plane view was taken after removing the CuS phase with KCN and reveals small grains in a plate-like morphology.

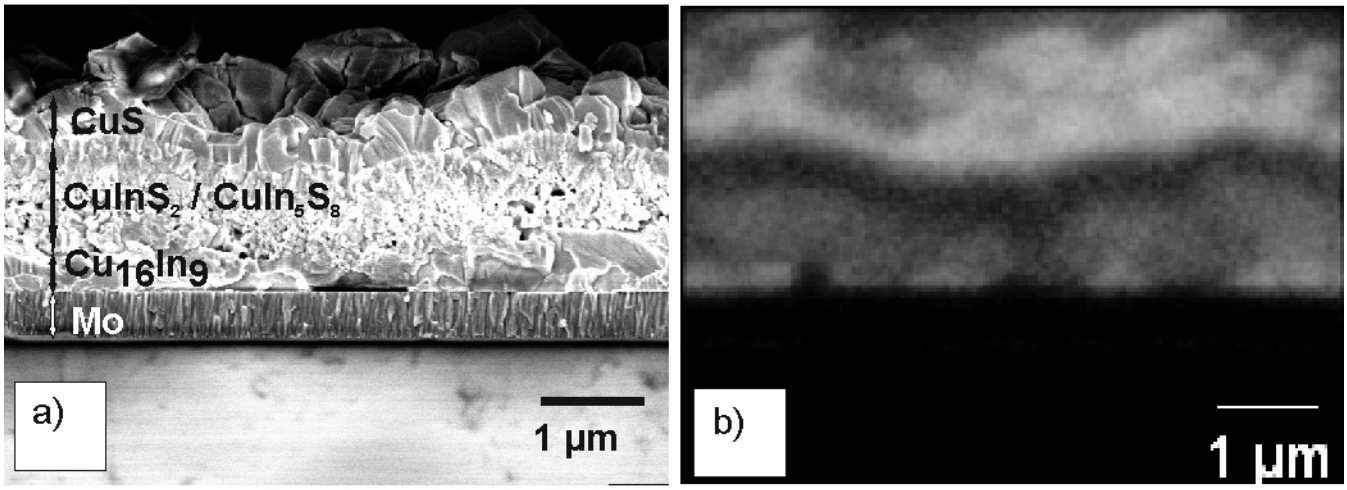

Figure 6.4.: Break-off experiment at marker b) of the RTP sulfurization shown in Figure 6.2: a) morphology and b) Cu L fluorescence mapping.

3. $2Cu_{2-x}S + CuIn_5S_8 \rightarrow 5CuInS_2$ reaction: between t=2.8 and t=3.2 $CuInS_2$ forms at expenses of the $Cu_{2-x}S$ and $CuIn_5S_8$ phases. This corresponds to the reaction whose kinetic was studied in Section 5.3 of Chapter 5. This reaction consumes the $CuIn_5S_8$ phase that coexists with the $CuInS_2$ one.

4. Thin-film recrystallization: this process could not be clearly resolved by the *in situ* measurement. A possible explanation is that this mechanism does not occur homogeneously through out the whole film. The accurate measurement of a reflection broadening becomes also more difficult for high noise to signal ratios (of the order of ∼50% as was shown in Figure 3.13 of Chapter 3) typical of the beginning of the sulfurization in fast experiments (short integration times). The cross-sections of Figure 6.4a) and Figure 6.5 serve as a concluding proof that domain and grain growth does take place. In the final film the only phases present are $CuInS_2$ and CuS. The CuS phase is evenly distributed on the surface of the film. The $CuInS_2$ is divided into two layers: a large-grained ∼1 μm thick layer that lies on top of a small-grained layer[1]. There are two possibilities that explain this bilayered morphology:

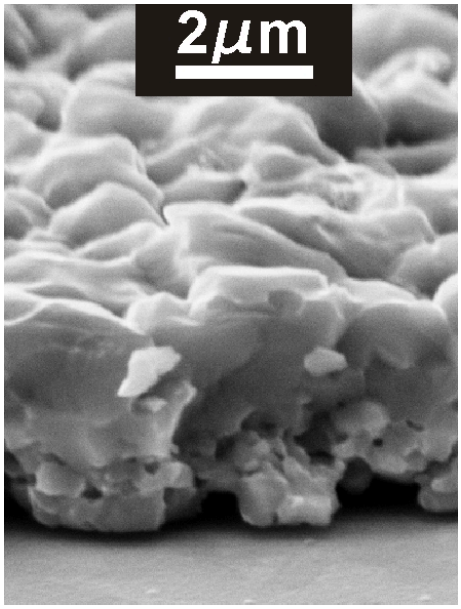

Figure 6.5.: Morphology of a rapid thermally processed $CuInS_2$ film. The small grain size near the back contact increases the adhesion of the film. The large grains near the surface assure a good electrical performance.

   a) a sulfur activity gradient: from Section 5.4 of Chapter 5 it resulted that the sulfur activity can reduce the activation energy for the domain and grain growth in the thin-film recrystallization. The sulfur activity, on its turn, decreases with depth when sulfurizing metallic films. In the idealized case of the steady state sulfurization (Figure 5.13 of Chapter 5), a sulfur activity gradient within the film supports growth and explains the observed layer sequence (metals/$CuInS_2$+$CuIn_5S_8$/CuS). If the porous intermediate layer presents a strong sulfur activity gradient, it is possible that the domain and grain growth will be inhomogeneous throughout the thin film. The grains near the sulfur source (the $Cu_{2-x}S$ phase at the surface) are expected to grow at lower temperatures compared to those near the back contact.

[1]The presence of a small-grained layer does not affect the solar cell device significantly, since this layer is far from the heterojunction situated at the surface. In contrast to this, the layer does improve significantly the adhesion to the Mo film as compared to a mono-layered $CuInS_2$ film (see Fig. 5.10 of Chapter 5 for an example of such morphology).

b) presence of the $CuIn_5S_8$ phase throughout the porous intermediate layer: there is a In enrichment near the Cu-S phases at the surface of the intermediate porous layer (see Fig. 6.4). The In enrichment can be shifted with growing $CuInS_2$ grains towards the back of the layer. This might stabilize the $CuIn_5S_8$ and block progressively the recrystallization near the back of the film.

5. Sulfide interdiffusion: at high temperature a dissolution of $CuInS_2$ by the $Cu_{2-x}S$ phase is possible. This affects the stoichiometry of the film near the surface. However, this cannot be resolved by bulk X-ray diffraction methods. Proof of this can be make in the future by analyzing the defect concentrations at the surface of the films.

Figure 6.6 shows a representation of the microstructure evolution through the rapid thermal sulfurization shown in Figure 6.2. An important observation is that the intermediate porous layer that results from the alloy sulfurization has small grains and contains both the $CuInS_2$ and the $CuIn_5S_8$ phases. The final $CuInS_2$ layer is formed from this mixed layer after the subsequent thin-film recrystallization that includes the $2Cu_2S + CuIn_5S_8 \rightarrow 5CuInS_2$ reaction. This happens inhomogeneously leading to the bilayered morphology.

The thin films that resulted from this sulfurization were used to fabricate solar cells. This procedure was done following these steps[120]:

- KCN etching to remove Cu-S phases;
- 50nm CdS deposition;
- 100 intrinsic and 500nm doped ZnO deposition;
- Ni/Al grid fingers deposition.

The current-voltage characteristic of the best $0.5cm^2$ solar cell are shown in Figure 2.1 of Chapter 2. The solar cell has an efficiency of 9.1%. This reflects that the microstructure that was obtained by this RTP sulfurization is susceptible of delivering good solar cell results with enhanced adhesion properties. This also confirms the capability of the *in situ* method to deliver information relevant for solar cell fabrication.

This chapter serves as an example of the description of the microstructure formation during RTP processing through the five mechanisms proposed in Chapter 4 and investigated in Chapter 5. It was emphasized that the sulfur pressure plays a key role in the alloy sulfurization and in the thin-film recrystallization. An optimization of the sulfur pressure profile (done by means of the valve that closes the reaction box shown in Figure 3.1 of Chapter 3) yields a two-layered $CuInS_2$ morphology where large grains lie on top of a small-grained layer. To achieve this the sulfur pressure must be high enough at low temperatures to achieve the formation of the $CuIn_5S_8$ intermediate phase, but not so high that it decomposes the alloy in CuS and InS. This bilayered morphology improves significantly the adhesion of the film to the Mo back contact.

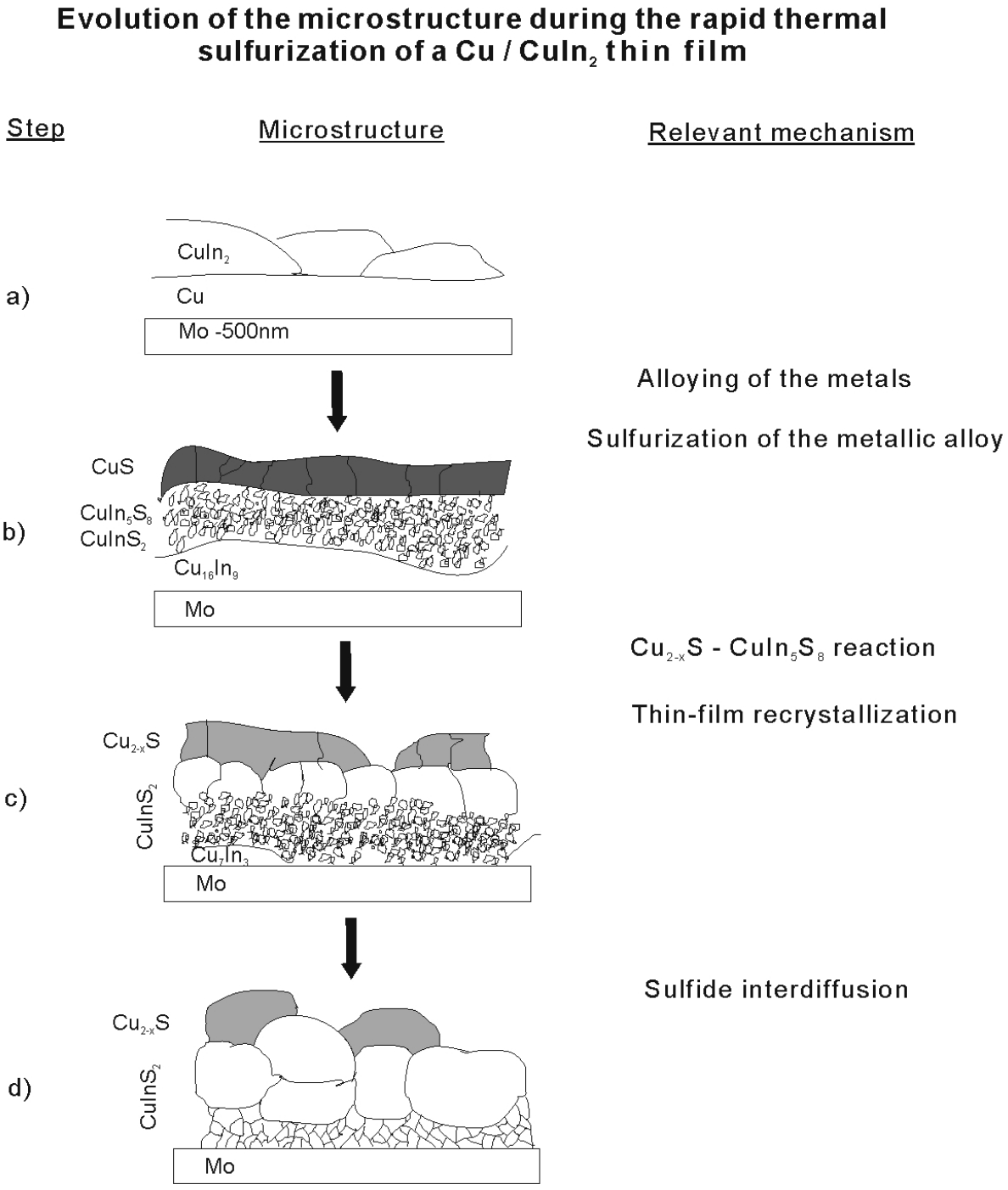

Figure 6.6.: Evolution of the microstructure during the rapid thermal sulfurization to produce $CuInS_2$ presenting an enhanced adhesion to the Mo. The high pressures at intermediate temperatures are responsible for the layer sequence: metals/porous $CuInS_2$-$CuIn_5S_8$/CuS represented in step b) (see the section 5.2 of Chapter 5). The recrystallization of the $CuInS_2$ thin film starts near the Cu-S phases and is not homogeneous through the film as seen in step c). The result is a bilayered $CuInS_2$ film with smaller grains near the Mo (step d).

7. Conclusions

This thesis makes two contributions to the rapid thermal sulfurization technology:

- An *in situ* energy-dispersive X-ray diffraction method to monitor the microstructural changes of a thin film during solid state transitions or reactions. The method can be used to monitor rapid thermal sulfurizations of metallic precursors under industrially relevant processing conditions. It is also suited to investigate and quantify isolated solid state mechanisms.
- The breakdown of the sulfurization process into five growth mechanisms. The qualitative and quantitative information concerning these mechanisms clarifies the microstructure formation during the growth of the $CuInS_2$ thin film and lays the ground for new process design. These growth mechanisms were studied by means of the *in situ* method. The most outstanding results concerning the individual mechanisms are summarized in the following:

    1. Alloying of the metals: the possible strain caused by the solid solution of In in Cu must be considered as a possible source of stress and pore formation. The contraction or expansion of this phase can be up to 100 times the expansion of the $CuInS_2$ phase. It would be desirable to avoid the formation of the Cu(In) solid solution.
    2. Sulfurization of the metallic alloy: the formation of different sulfide layered-stacks during the sulfurization of a metallic alloy was monitored as a function of pressure and temperature. The sulfurization mode depends on the temperature. At low temperatures (T<250°C) the layer formation depends on the growth rate of the individual phases. This sulfurization leads to the formation of CuS and InS. At high temperatures (T>∼400°C) the sulfurization depends on the local thermodynamic stability of the sulfide phases. The thermodynamic stability depends on the local sulfur activity. The sulfur pressure (interpreted as activity) vs. composition phase diagram serves to understand the formation of the stack of sulfide layers during the steady state sulfurization. At intermediate temperatures, a crossover is observed. In the case where the sulfurization occurs at 330°C and the sulfur pressure is ∼1mbar, the layer sequence is Cu_xIn_y/$CuInS_2$-$CuIn_5S_8$ /CuS.
    3. Reaction of the sulfides: the reaction $2Cu_{2-x}S + CuIn_5S_8 \rightarrow 5CuInS_2$ was identified as being important for the rapid thermal sulfurization because: a) the $CuIn_5S_8$ phase was identified as a possible product of the sulfurization mechanism under rapid thermal processing conditions, and b) through this reaction $CuInS_2$ thin films can be obtained with rates of the order of $\sim 0.1 \mu msec^{-1}$ at 550°C. The activation energy for this reaction was estimated to be between 0.5 and 1eV. It was found that the product of this reaction, $CuInS_2$, preserves the initial preferred orientation of the $CuIn_5S_8$ educt.
    4. Thin-film recrystallization: this mechanism ensures grain sizes of the order of the thickness of the films, low structural defect densities and the stable chalcopyrite ordering of the cations. A model for the thin-film recrystallization was proposed. The model consists of three steps: a) the consumption of the $CuIn_5S_8$ phase, b) an increase in domain and grain sizes: the activation energy was estimated to be between 3 and 3.4eV, c) the Cu-Au ordering to chalcopyrite ordering transition. The sulfur pressure profile

can be used to control the recrystallization of $CuInS_2$ thin films. Decreasing the sulfur activity at low temperatures can delay the transition so that the metastable Cu-Au ordering does not appear. Increasing the sulfur activity at lower temperatures can delay the recrystallization of the thin film by stabilizing the $CuIn_5S_8$ phase. Domain and grain growth in the $CuInS_2$ thin films is controlled by the cation mobility and the cation vacancy concentration. The sulfur activity enhances domain and grain growth by increasing cation vacancy concentration. The secondary $Cu_{2-x}S$ phase enhances the cation vacancy creation but is not necessary to trigger the domain and grain growth. Under this perspective the $Cu_{2-x}S$ phase does enhance, but it is not a necessary condition for grain growth. Alloying with Ag increases the cation mobility and enhances domain and grain growth. The use of Ag makes possible the fabrication of thin films with large grains at temperatures as low as 270°C.

5. Sulfide interdiffusion: the $Cu_{2-x}S$ can dissolve the $CuInS_2$ phase and may affect the In-related defect concentration near the surface of the thin film.

The objective of future investigations must be the controlled microstructure modification of $CuInS_2$ films using these tools. This includes avoiding the Cu-Au ordering through a controlled thin-film recrystallization (see the thin-film recrystallization paths proposed in Figure 5.41 of Chapter 5). The creation of pinholes can also be strongly reduced if the thin-film recrystallization is triggered without the presence of a secondary Cu-S phase. Innovative paths to enhance the cation mobility must be explored to achieve this. Optimizing the defect concentration near the surface of the $CuInS_2$ film by controlling the sulfur pressure at the highest temperature should also be addressed. When attempting to incorporate other elements in the $CuInS_2$ films via the sulfurization of metallic precursors, careful attention should be given to the sulfurization mode. The sulfur pressure and temperature do determine the resulting layered-stack and its morphology. The stack of sulfide layers may change if an alloy (or dopant) -containing sulfide phase is more stable at higher sulfur activities or if the free energies of formation vary with the addition of the alloying (or doping) element. Furthermore, if the alloying (or doping) element forms a very fast growing sulfide careful attention shall be given in avoiding an uncontrollable exclusive sulfurization at low temperatures. The analysis of the free energies of formation and the sulfur activity vs. composition diagrams should be part of the preliminary work when designing sulfurization processes.

The rapid thermal sulfurization of Cu-In films is a process that must be looked at in the three-dimensioned parameter field: time, temperature and sulfur pressure. A restricted control of the sulfur pressure inside an RTP reactor can be achieved by a valve similar to the one presented in Figure 3.1 of Chapter 3. However, a controllable sulfur source should be designed and fabricated for future processing. As for the measurement of the process pressure, no reliable sulfur pressure gauge for the 10^{-3} to 10mbar range is available. To address this issue a pressure gauge was conceived during this work. It was designed for the rapid thermal sulfurizations or selenizations of thin films and is subject to a German patent claim. Appendix F describes the measuring principle and a possible technical description of such a sensor. A controlled sulfur supply and a measurement of the process pressure must be the next two steps of the sulfurization technology. With these, a directed modification of the microstructure is possible.

Appendix

A. Thermodynamics of the Cu-In-S system

A.1. Definitions

A thermodynamic system is completely defined by a set of state variables. These are extensive (for example the volume) and intensive (for example the temperature). Functions of state use state variables to describe the system. The Gibbs free energy G is a function of state defined as:

$$G = U + pV - TS = H - TS \tag{A.1}$$

where U is the internal energy, H is the enthalpy, T the temperature, p the pressure and S the entropy. The total differential is

$$dG = Vdp - SdT \tag{A.2}$$

in a closed system (no mass transfer). At equilibrium the temperature and pressure are constants and no work is extracted. Then $dG = 0$. This means that G is at a minimum (a maximum of G implies an unstable equilibrium).

In a system with different atomic species found in ϕ different compounds, the minimization problem of Gibbs free energy can be expressed as

$$min(G = \sum_{\phi} N_{\phi} G_{\phi}) \tag{A.3}$$

where, N_ϕ is the molar quantity of the compound ϕ and G_ϕ^{Gibbs} its free energy. The closed system imposes the constancy of the number of atoms of each species. The Gibbs free energy of a compound as a function of temperature is

$$G_\phi^T = H_\phi^{298} + \int_{298}^{T} C_{p_\phi}(x)dx - T\left\{ S_\phi^{298} + \int_{298}^{T} \frac{C_{p_\phi}(x)}{x} dx \right\} \tag{A.4}$$

where C_p is the heat capacity at constant pressure, and H^0 and S^0 are the standard enthalpy and standard entropy. The temperature dependence of C_p is well described by

$$C_p = a + bT + cT^2 + dT^{-2} \tag{A.5}$$

where a,b,c,d are empirical parameters that are tabulated for a large quantity of compounds. CHEMSAGE[38] is a computer program that, based on a, b, c, d, H^0 and S^0, calculates the

equilibrium compositions by solving equation A.3. To solve equation A.3 in the ideal mixture model (IDMX) of CHEMSAGE, the pressure dependence of the Gibbs energy of the condensed phases is neglected. The pressure dependence of the gas phases is taken into account through the equation of state for the ideal gas

$$p_i V = N_i RT \tag{A.6}$$

with

$$p = \sum_i p_i \tag{A.7}$$

where p_i and N_i are the partial pressures and molar quantities of the i component of the gas phase, and p the total pressure in the system. Phase diagrams of the first (intensive vs. intensive) and of the second (intensive vs. extensive) kind were calculated with CHEMSAGE. The dataset and details on the calculations are given in Appendix B.

A.2. Sulfur vapor

Sulfur of 99.9995% purity was used in this work for the fabrication of the $CuInS_2$ films. Saturated sulfur vapor is composed of S_x(x=2..8) molecules. Figure A.1a) shows the saturated vapor pressure as a function of temperature[96] and the partial pressure of the molecules [31][1].

In a closed volume with a limited amount of sulfur, the sulfur pressure, and its composition, corresponds to the saturated vapor if a liquid phase is present. If the temperature rises further, so that only a gas phase is present, both composition and pressure of the gas phase deviate from the saturated pressure curve. Figure A.1b) shows thermodynamical calculations made with the software CHEMSAGE (see Appendix B for the dataset) of the pressure and composition of the vapor phase in a closed volume ($107cm^3$) containing 1 mg of solid S at room temperature. Figure A.1 also shows the total pressure evolution when using 32mg of solid S in the same volume. The temperature where the pressure deviates from the saturated vapor pressure is higher compared to the case of 1mg.

[1]The high vapor pressure of sulfur makes its direct measurement difficult. Operating under sulfur pressures S_{op} requires a sensor temperature of at least the temperature corresponding to the same pressure in the saturated vapor curve, T_{SV}. Lower temperatures imply condensation of the sulfur in the sensor.

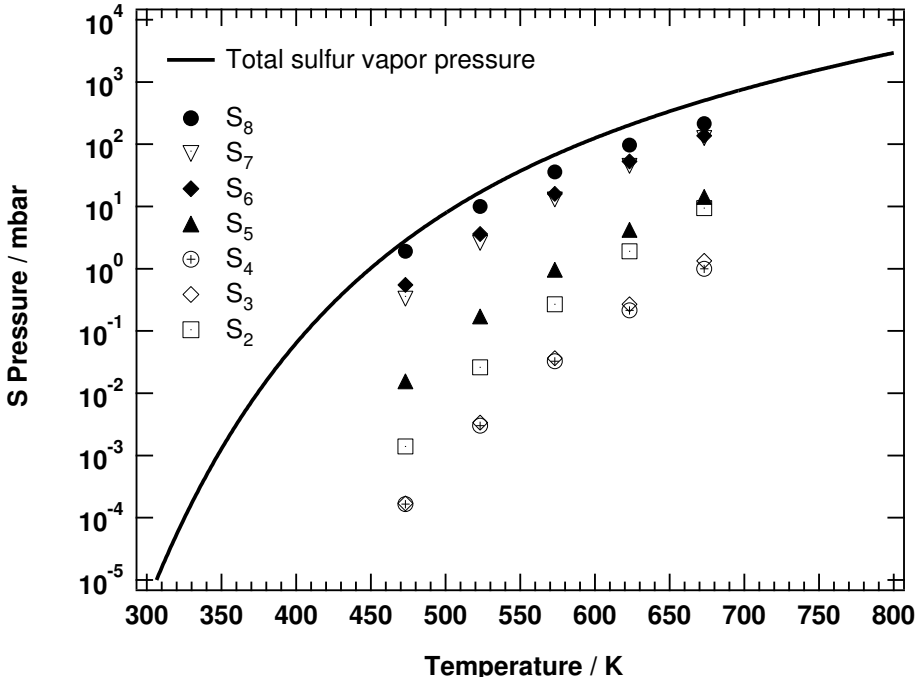

a)

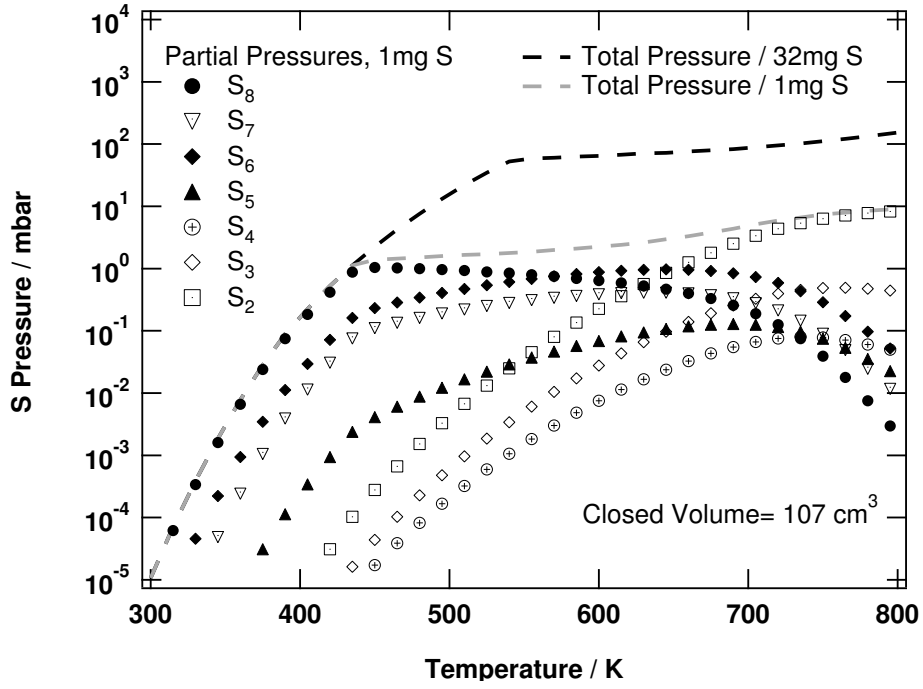

b)

Figure A.1.: a) Saturated vapor pressure of sulfur[96] and its composition[31], b) CHEMSAGE[38] calculation of the total pressure and the partial pressures inside a closed volume (107 cm^3) containing only sulfur.

A.3. Binary systems

The binary systems will be briefly described. For further information see [98].

A.3.1. Cu-In

The Cu-In system (see Figure A.2) presents four intermetallic phases at room temperature: (δ)Cu_7In_3, (η)$Cu_{16}In_9$, (ϕ)$Cu_{11}In_9$ and $CuIn_2$. The latter phase is not reported in the phase diagram[17] but is observed in thin films up to temperatures of 148°C[98].

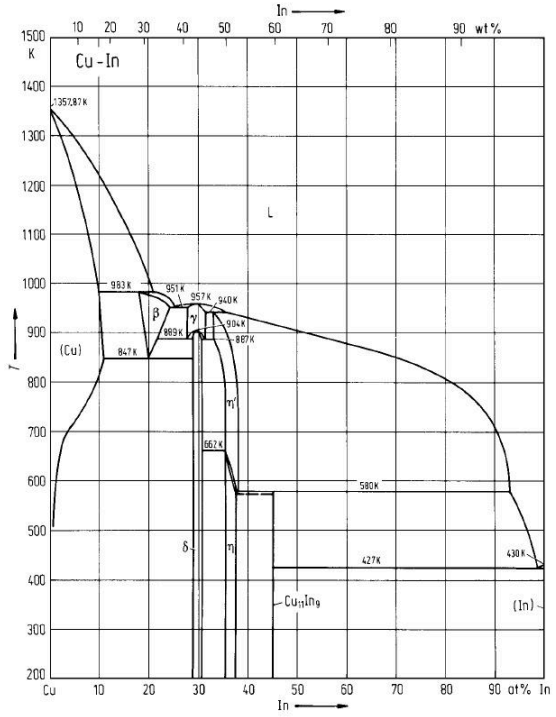

Figure A.2.: Cu-In phase diagram [17].

A.3.2. Cu-S

Figure A.3 presents the phase diagram of the Cu-S system. Cu-S crystallizes in the cubic digenite ($Cu_{2-x}S$) phase at high temperatures and in the orthorhombic or hexagonal chalcocite at lower temperatures. The more S-rich phase is the hexagonal covellite (CuS). The phase transition

$$2CuS(s) \rightarrow Cu_{2-x}S(s) + \frac{1}{2}S_2(g) \tag{A.8}$$

is sulfur pressure dependent. Figure A.4 presents the p-T phase diagram of the Cu-S system[11]. Lower S pressures shift transition A.8 to lower temperatures.

Djurle[34] shows that the lattice constant of the $Cu_{2-x}S$ phase decreases with increasing non-stoichiometry (x). Rau[100] proposes that the cation vacancy concentration (neutral, charged and a complex of both) increases with increasing S_2 pressure. Pareek *et al.*[95] observe the same trend. Their main conclusion is that the changes in stoichiometry are driven by addition or removal of copper vacancies and that the sulfur sublattice remains nearly unchanged.

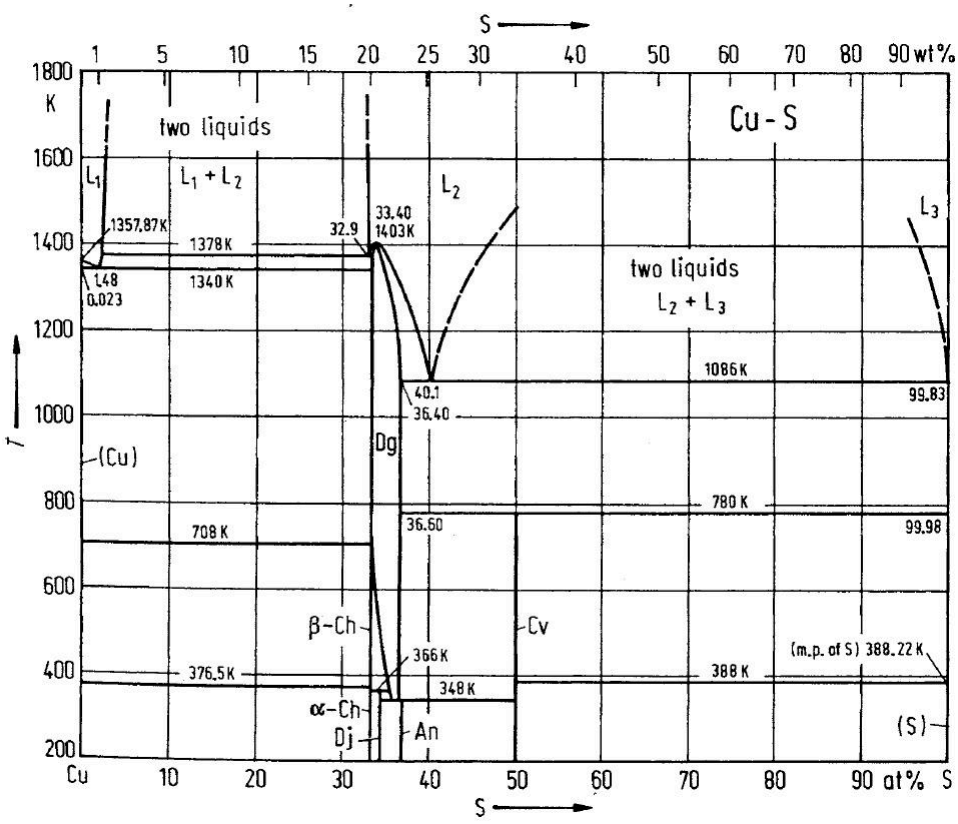

Figure A.3.: Cu-S phase diagram [23].

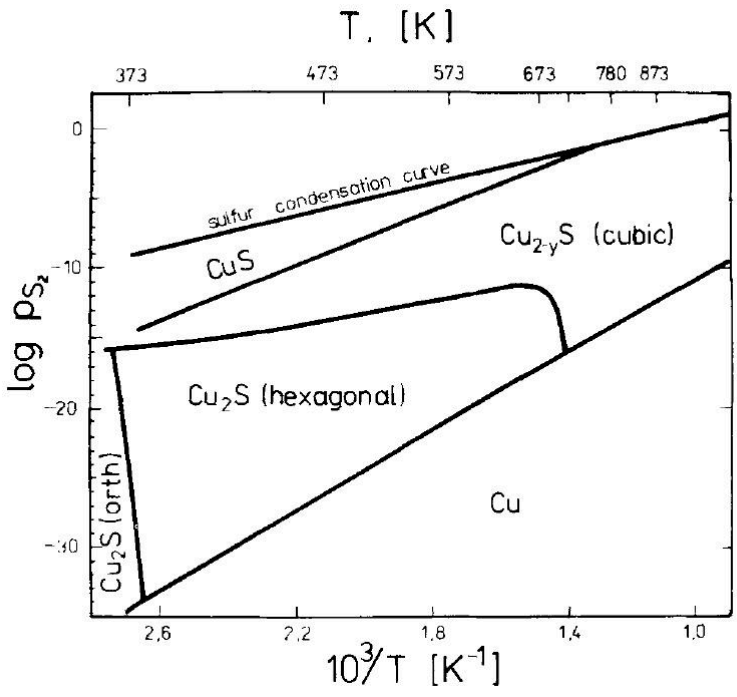

Figure A.4.: p-T phase diagram of the Cu-S system from [11].

A.3.3. In-S

Figure A.5 shows the binary In-S phase diagram. The β-In_2S_3 phase crystallizes in the cubic system presenting a spinel structure[118]. This is composed of a cubic face-centered cubic sulfur sublattice with In cations occupying partially tetrahedral and octahedral voids. This phase is relevant for the fabrication of $CuInS_2$ by physical vapor deposition methods and is currently used as an alternative buffer layer in $Cu(In,Ga)Se_2$ devices[99]. A volatile compound, $In_2S(g)$, forms when exposing pure In to sulfur at low pressures[35]. This compound is responsible for In loss during $CuInS_2$ processing.

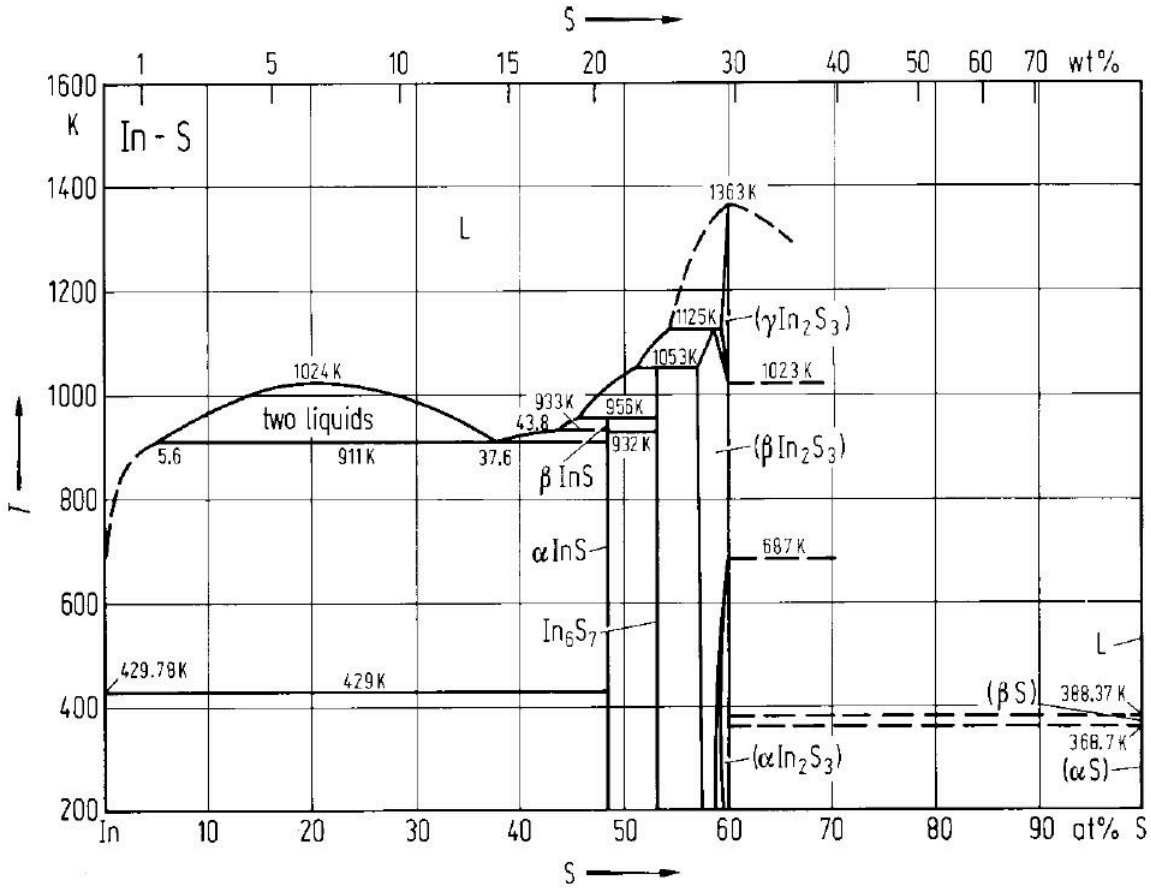

Figure A.5.: In-S phase diagram from [94].

A.3.4. Cu-In-S system

Figure A.6 shows a ternary phase diagram of the Cu-In-S system from [37]. The ternary phases stable at room temperature are chalcopyrite $CuInS_2$ and the spinel $CuIn_5S_8$.

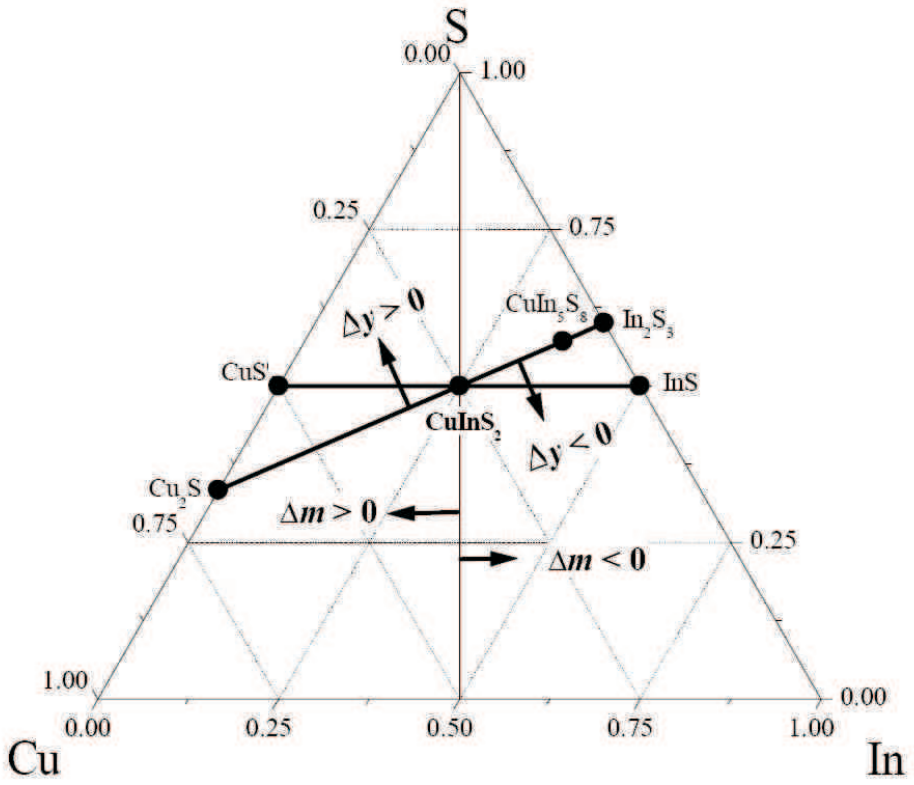

Figure A.6.: Cu-In-S phase diagram from [37].

Figure A.7 shows the quasi-binary Cu_2S-In_2S_3 cut. The homogeneity range is larger in the In-rich side of the chalcopyrite phase and can be read directly in the quasi-binary phase diagram. β-In_2S_3 and $CuIn_5S_8$ form a solid solution and share the same structure.

Figure A.8 shows the pressure dependent equilibrium phases calculated with CHEMSAGE for a Cu to In ratio of 1.6. For the calculation the elementary amounts were fixed and the volume of the virtual reactor was varied to obtain the desired pressure. The sulfur pressure corresponds to the sum of the partial pressures of all sulfur species, from S_2 to S_8. According to the calculations the In-richer $CuIn_5S_8$ phase can be stabilized by increasing the sulfur pressure even if the overall stoichiometry is Cu-rich. Free energies of formation used for the calculation are listed in Appendix B.

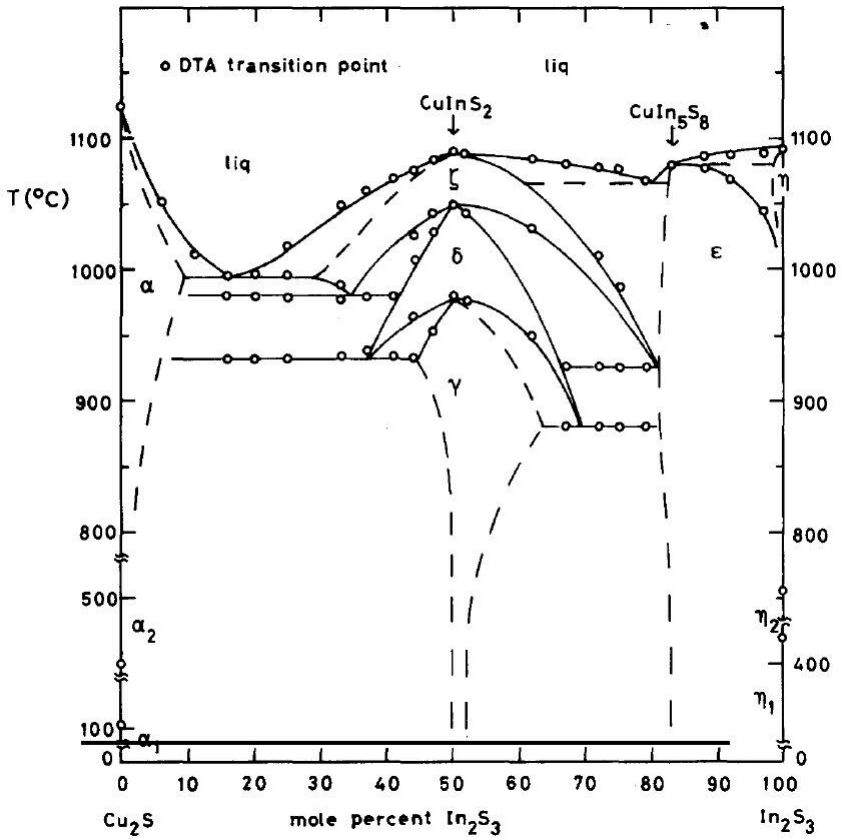

Figure A.7.: Quasi-binary Cu_2S-In_2S_3 phase diagram from [12].

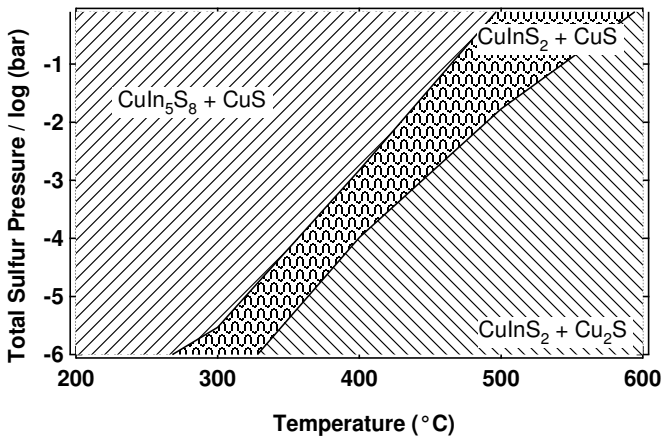

Figure A.8.: Pressure dependent equilibrium phases calculated with CHEMSAGE for a Cu to In ratio of 1.6.

B. Chemsage calculations

The software CHEMSAGE[38] was used to calculate phase equilibria. The ideal mixture model (IDMX) was used for the minimization of the free energy.

The input data for all simulations are given in the Figure B.1. For the Cu-S and In-S binary compounds the data were taken from [10]. The data for the ternary compounds were calculated by Villora[134] from the equilibrium reactions:

$$Cu_2S + In_2S_3 \rightleftharpoons 2CuInS_2 \tag{B.1}$$

and

$$\frac{1}{2}Cu_2S + \frac{5}{2}In_2S_3 \rightleftharpoons CuIn_5S_8\ . \tag{B.2}$$

The Cu_7In_3, $Cu_{16}In_9$, $Cu_{11}In_9$, $CuIn_2$ enthalpy, entropy, and heat capacity coefficients were estimated by Villora[134].

B.1. Sulfur pressure vs. Cu-In composition phase diagrams

The pressure-dependent phase equilibria were calculated at 500°C and at 330°C using the following input:

- Cu-rich: 1 to 5 mol Cu, 1 mol In, 100 mol S
- Cu-poor: 1 to 5 mol In, 1 mol Cu, 100 mol S
- The total pressure was imposed between 10^{-18} and 10^{-4} bar.

The calculated phase equilibria (presented in Figure B.2) served as a base to estimate the p_{S_2} vs. composition phase diagram of the Cu-In-S system in the 300°C-500°C range. To do this the following hypotheses were made:

- The total pressure corresponds to S_2(g). The pressure inside the virtual reactor is dominated by the S_2 species for both temperatures. At 500°C the S_2 pressure deviates the most from the total pressure. Figure B.3 presents the S_2 pressure as a function of the composition for the imposed total pressures (on the right). At low pressures and low Cu contents, the deviation is of maximal 10%. For intermediate and higher pressures and in the Cu rich case the deviation is negligible.
- The data for the Cu-In metallic phases is regarded with precaution. The data was estimated because no values are reported in the literature and is therefore subject to inaccuracies. Therefore the Cu_7In_3 regions should be interpreted as being any of the metallic Cu_xIn_y phases, or even a mixture of intermetallic phases.

Phase	Compound	H0	S0	a	b	c	d	Temperature
Gaz	**Cu**	339066	166.368	22.474634	-0.0030139	1.29e-06	-85813	3000
	Cu2	485344	241.718	37.388	0.000741	0	-9200	3000
	In	246304	173.719	22.679748	0.0023634	0	-237932	2500
	InS	233160	251.662	37.2554	7.53e-05	0	-2093	2000
	In2S	138138	318.397	59.94352	0.0012558	0	-8372	2000
	In2S2	93347.8	313.95	82.979078	0.00012977	0	-513204	2000
	S	272090	167.817	24.232754	-0.0041107	1.34e-05	-59022.6	2000
	S2	128594	228.179	35.061936	0.00282	0	-293020	2000
	S3	138862	269.5	53.781	0.004351	0	-649000	2000
	S4	145798	310.601	79.877252	0.003277	0	-1.18003e+06	2000
	S5	109380	308.592	106.935556	0.0010591	0	1.57687e+06	2000
	S6	99710.5	354.094	132.13109	0.00050232	0	-1.841e+06	2000
	S7	111515	407.675	155.120602	0.0024488	0	-2.03816e+06	2000
	S8	98245.4	430.321	180.316136	0.00172246	0	-2.24286e+06	2000
Condensed	**Cu**	0	33.1238	24.116802	0.0053711	-8.23e-07	-107329	1357
	Cu	13.27		31.395	0	0	0	2846
	Cu7In3	-20511.4	44.8321	17.60213	0.019808	0	0	700
	Cu16In9	-19381.8	44.8614	17.087252	0.01985	0	2511.6	700
	CuIn2	-38929.8	148.603	79.9526	0.02093	0	0	421
	Cu11In9	-349950	885.339	564.2728	0.094185	0	0	580
	CuInS2	-232742	142.324	94.68732	0.027942	0	53622.7	1256
	CuIn5S8	-993756	468.832	399.51184	-0.068985	0	-4.186e+06	1358
	CuS	-73255	66.5574	44.3716	0.011051	0	0	1000
	Cu2S	-79534	117.208	52.82732	0.078739	0	0	376
	Cu2S	3851.12		112.05922	-0.030767	0	0	717
	Cu2S	1201.38		84.64092	0	0	0	1402
	In	0	57.8087	10.958948	0.039838	0	-346894	430
	In	3.26	57.8087	29.86711	-0.00089078	0	0	900
	In2S3	-355810	163.673	128.9288	0.0032651	0	-10465	660
	In2S3	108.84		97.8268	0.055423	0	0	1100
	In3S4	-503157	234.416	94.1855	0.12139	0	0	1113
	In5S6	-774410	374.647	256.6018	0.05986	0	-1.06743e+06	1043
	S	0	34.3252	14.793324	0.024074	0	71162	368
	S	400.98		17.55898	0.019607	0	0	388
	S	1723		45.032988	-0.016635	0	0	717

Figure B.1.: Standard formation enthalpies, H^0 in $Jmol^{-1}$(and eventual transformation enthalpies H^T), entropies S^0 in $JK^{-1}mol^{-1}$, C_p coefficients according to Equation A.5, together with the temperatures ranges (in Kelvin) of validity of the phases in the Cu-In-S system.

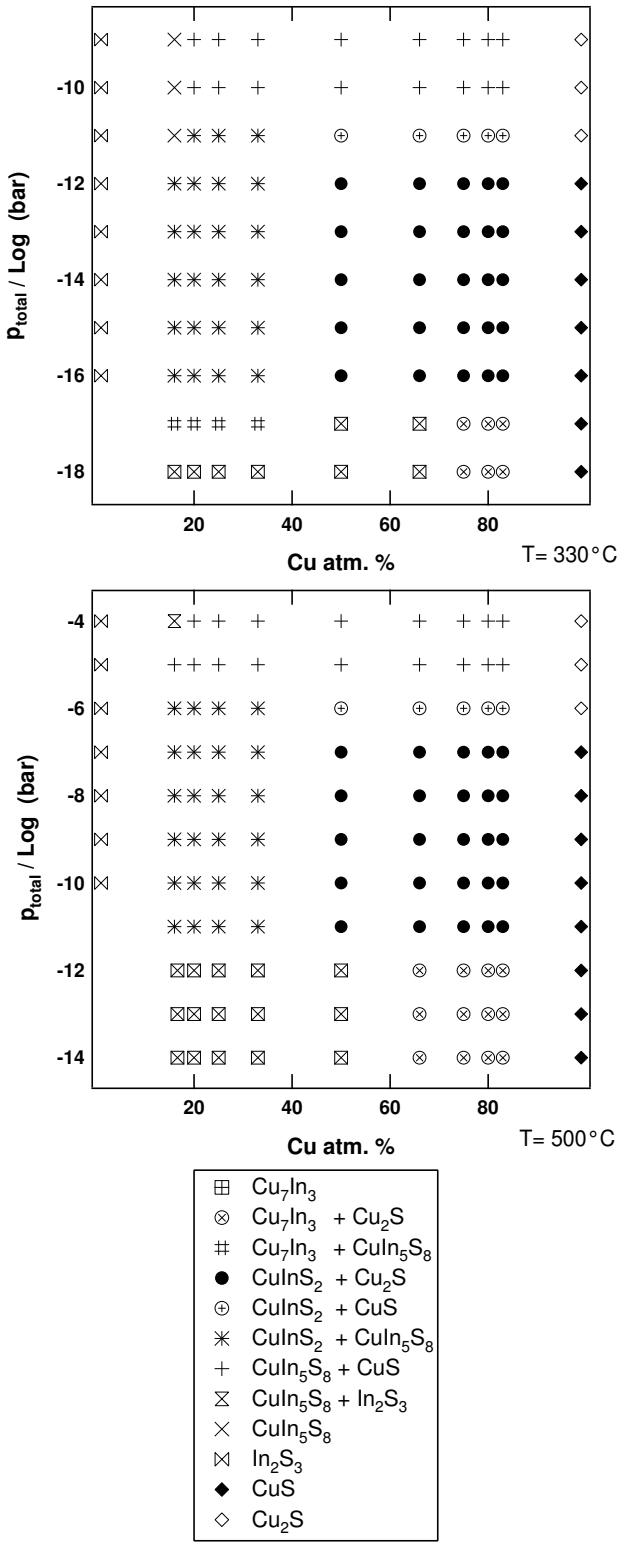

Figure B.2.: Total pressure and composition dependent phase equilibria at 330°C and 500°C in the Cu-In-S system. The markers indicate the phases that are stable at the given pressures and compositions. The schematic sulfur pressure vs. composition Cu-In shown in Figure 5.2 of Chapter 5 was extracted from these phase equilibria.

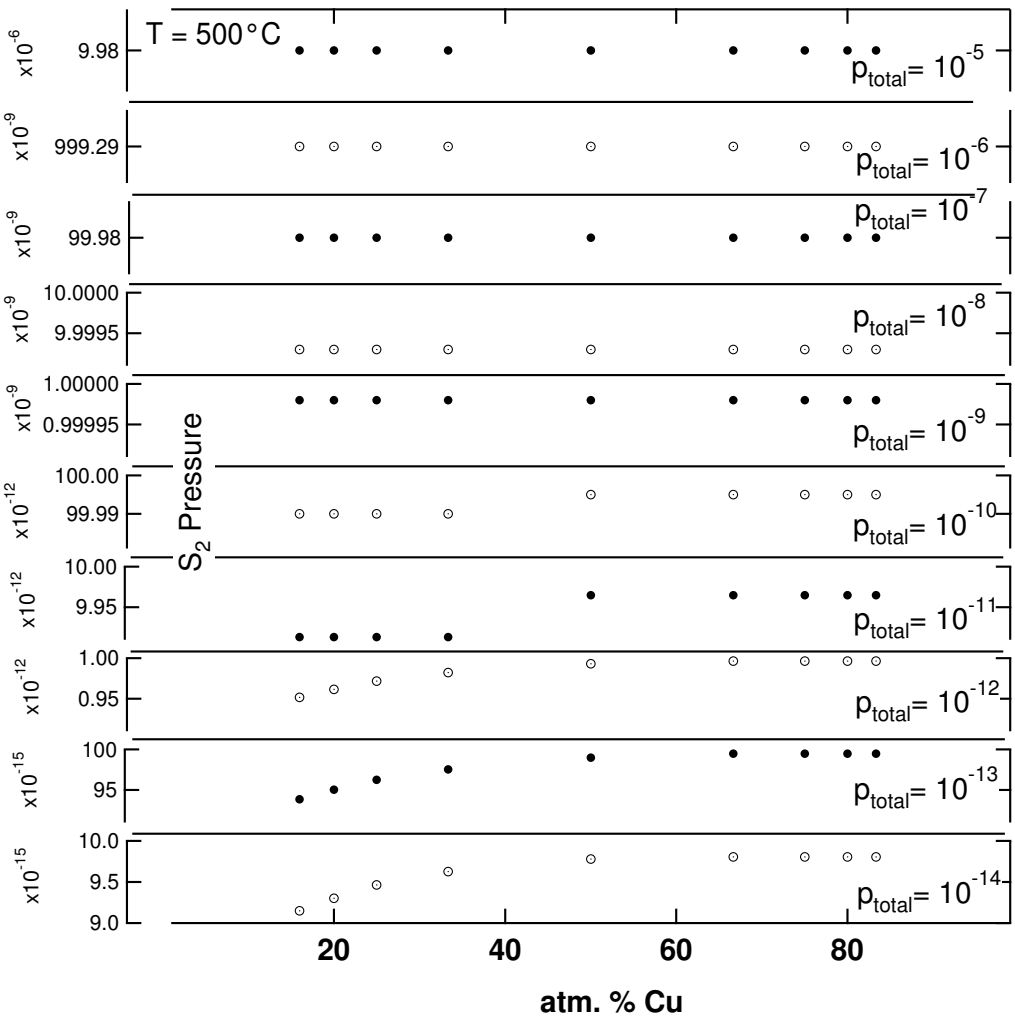

Figure B.3.: S_2 pressure as a function of composition for the equilibria calculated at 500°C presented in Figure B.2.

C. Definition of XRD profiling functions

$2w$ and β stand for full width at half maximum and integral breadth.

C.1. Gauss

$$y(x) = a_1 exp(-\frac{(x-a_2)^2}{2a_3^2}) \tag{C.1}$$

with

$2w = 2\sqrt{2ln2}a_3$ and $\beta = \sqrt{2\pi}a_3$.

C.2. Cauchy

$$y(x) = \frac{a_1}{1 + (\frac{2(x-a_2)}{a_3})^2} \tag{C.2}$$

with

$2w = a_3$ and $\beta = a_3\frac{\pi}{2}$.

C.3. Simplified Pearson VII

$$y(x) = \frac{a_1}{\left[1 + \frac{(x-a_2)^2}{2a_4a_3^2}\right]^{a_4}} \tag{C.3}$$

with

$2w = 2a_3\sqrt{2a_4(2^{\frac{1}{a_4}} - 1)}$ and $\beta = \frac{a_3\sqrt{2\pi a_4}\Gamma(a_4 - \frac{1}{2})}{\Gamma(a_4)}$, where Γ stands for the gamma function.

D. Determination of the kinetic parameters for the consumption of $CuIn_5S_8$

Figure D.1 presents the data used for the determination of the Avrami kinetic parameters of the reaction:

$$2Cu_2S + CuIn_5S_8 \rightarrow 5CuInS_2 \ . \tag{D.1}$$

In a), c) and e) the figure presents the best fit for the Avrami exponent and the corresponding χ^2 value as a function of τ (see Equation 5.6 of Chapter 5). In b) and d) the figure presents the fractional reaction data together with the best fit for n and τ for the experiments $Binary_{300}$ and $Binary_{325}$ described in Table 5.2 of Chapter 5. Experiment $Binary_{340}$ (listed in the same table) presents fractional reaction values higher than 0.75. The corresponding χ^2 of the fitting procedure presents no minimum as a function of τ. In this case the fractional reactions are at best fitted for low τ, with a clear increase in the Avrami exponent.

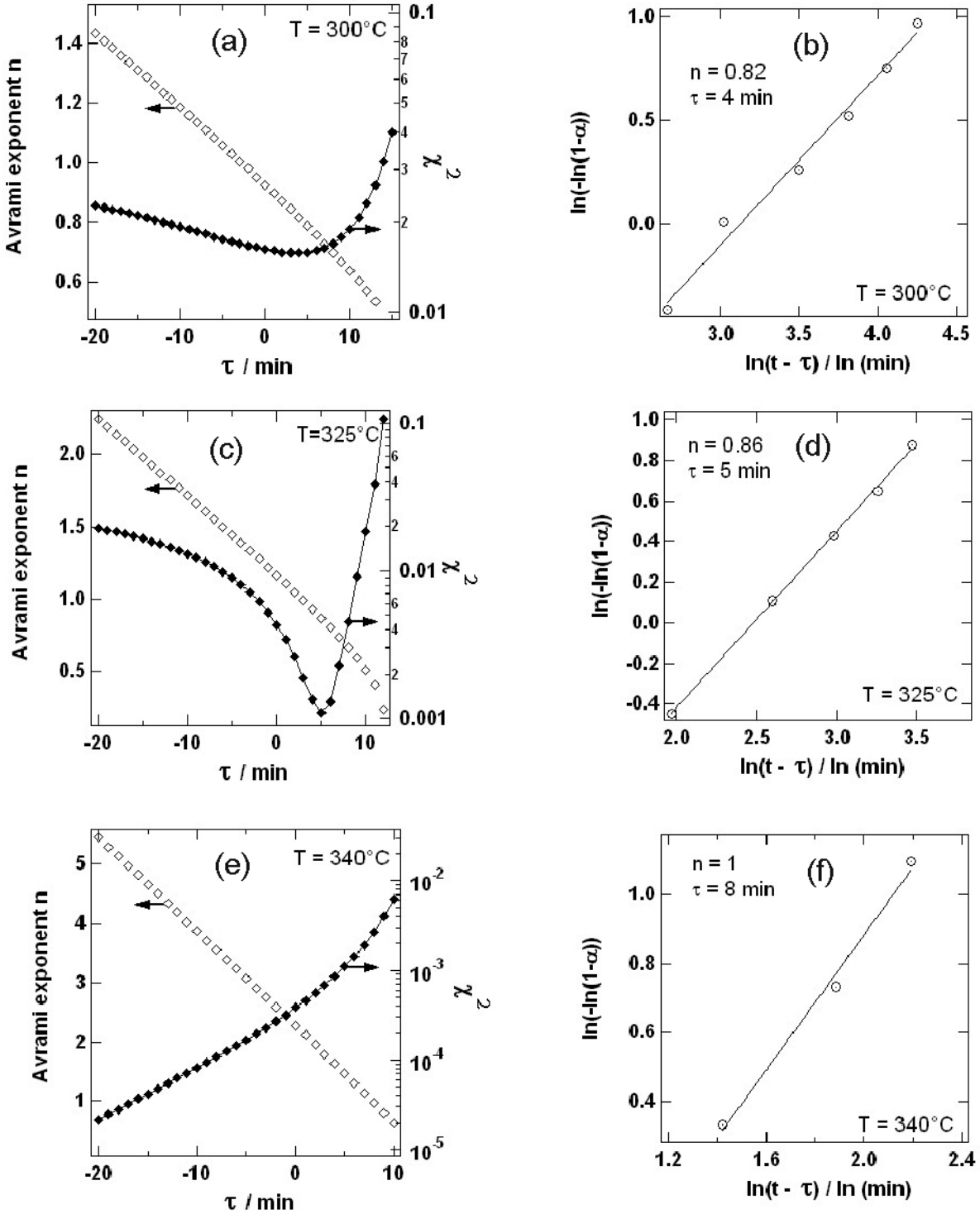

Figure D.1.: Determination of kinetic parameters using the Avrami model. Figures a),c) and e) show the best fit for the Avrami exponent n as a function of τ, together with the χ^2 value that mirrors the quality of the fit. Figures b) d) and f) show the fits at the n and τ values given in each figure. Such linear fits are used to extract k_p for the three annealing experiments.

E. Extraction of the Cauchy-breadth from EDXRD spectra

One way to evaluate the microstructure of a thin film is to quantify the broadening of its X-ray diffraction lines[1]. To the structural broadening of a diffraction line contribute principally: dislocation and stacking fault density, twinning, microstrain, chemical heterogeneity and crystallite size. These effects (other than twinning which is not considered in the following) can be separated in strain and size effects. In a first approach the strain-induced broadening is proportional to the microstrain and the size-induced broadening is inversely proportional to the average length of coherent scattering (measured in the direction of the scattering vector[13]). The latter correlation is called the Scherrer formula and will be described in Section E.3.

The length of coherent scattering, or domain size D_d, can be identified with the average size of the grains when considering crystallites of perfect quality separated only by grain boundaries. In this idealized case the domain sizes, D_d, are equivalent to the grain sizes, D_g. However, in general it is valid that

$$D_d \leqslant D_g \ . \tag{E.1}$$

E.1. Cauchy-breadth and domain size

Dehlez[29] proposes a procedure to separate strain and crystallite size effects. It is based on the separation of Gauss and Cauchy contributions to the breadth. Birkholz[13] proposes that the Gauss contribution is proportional to the strain, and the Cauchy contribution is inversely proportional to the average crystallite size. The proportionality constant depends on crystallite shape, size distribution and definition of crystallite size (see Scherrer formula below).

To obtain Gauss (β^G) and Cauchy (β^C) contribution to the breadth from a profile with full width at half maximum $2w$ and integral breadth β the following relations are used[29]:

$$\frac{\beta^C}{\beta} = 2.0207 - 0.4803(\frac{2\omega}{\beta}) - 1.7756(\frac{2\omega}{\beta})^2 \tag{E.2}$$

and

$$\frac{\beta^G}{\beta} = 0.6420 + 1.4187(\frac{2\omega}{\beta} - \frac{2}{\pi})^{\frac{1}{2}} - 2.2043(\frac{2\omega}{\beta}) + 1.8706(\frac{2\omega}{\beta})^2 \ . \tag{E.3}$$

The measured profile is the convolution of the microstructural profile and the instrumentation profile. From the relations of Section 3.2.1.5 of Chapter 3, it follows that

[1] Ungar[132] lists the possible aberrations of an X-ray diffraction line.

$$\beta^C_{Microstructre} = \beta^C_{Measured} - \beta^C_{Instrumentaion} \approx \beta^C_{Measured} \tag{E.4}$$

because the Cauchy contribution to the breadth of the instrumentation profile is negligible. Under this assumptions, the Cauchy-breadth of a diffraction line of the EDXRD setup described in Chapter 3 is:

a) a measure of domain size and

b) an indicator of the lower limit of grain size

E.2. Extraction of the $CuInS_2$ 112 Cauchy-breadth by multiple-line fit

Section 5.4 of this thesis presented results based on a multiple-line fit in the energy range 28.5-32.5 keV of EDXRD spectra recorded at the EDDI beamline. The suppositions of this fit concerned

- the reflection profiles: a Gaussian profile was assumed for the $CuIn_5S_8$ 311 and 222, the CuS 100, 101, 102 and the $Cu_{2-x}S$ 111 reflections and a Pearson VII-type profile was assumed for the $CuInS_2$ 112 reflection;
- the reflection positions: the positions of the $CuIn_5S_8$ 311 and 222 reflections were fixed by the position of the $CuIn_5S_8$ 400 reflection according to the JCPDS card 24-0361. The latter line was fitted independently ($\sim$35keV). The positions of the CuS 100, 101 reflections were fixed by the position of the CuS 102 reflection according to the JCPDS card 78-2121. The latter reflection was fitted independently. The position of the $Cu_{2-x}S$ 111 reflection was fixed by the position of the $Cu_{2-x}S$ 220 according to the calculated values. The latter reflection fitted independently ($\sim$49keV) ;
- the reflection intensities: A fixed intensity ratio was assumed in the case of the 100, 101, 102 CuS reflections according to the JCPDS card 78-2121. The intensity ratio for the $CuIn_5S_8$ 311 and 222 was taken to be 1 as it was found for a thin film reference of this phase. The intensities of the $CuIn_5S_8$ lines in the fit range introduce the greatest uncertainty in the extracted $CuInS_2$ profile parameters;
- the reflection widths: The widths of the CuS and $CuIn_5S_8$ reflections were fixed at 0.2 keV and 0.3 keV respectively, by iteratively optimizing the fit at room temperature. The width of the $Cu_{2-x}S$ 111 was kept between 0.2 keV and 0.3 keV and given free for fitting when possible;
- The background determination: the background was determined for the spectrum taken at 500°C and assumed constant for every other temperature.

The fitting procedure was programed in IGOR Pro V5.0 that uses a built-in Levenberg–Marquardt algorithm. From the fitting procedure the full width at half maximum $2w$ and integral breadth β of the $CuInS_2$ 112 were extracted. These were used to extract the Cauchy contribution of the breadth.

E.3. Scherrer formula

The Scherrer formula is

$$\beta_\theta = \frac{k^{Scherrer} \cdot \lambda}{L \cdot cos\theta} \tag{E.5}$$

where β is the breadth of a reflection, L the crystallite size, λ the wavelength and $k^{Scherrer}$ the Scherrer constant. $k^{Scherrer}$ takes different values depending on

- the exact definition of breadth;
- the crystallite shape;
- the size distribution of the crystallites.

Langford[73] summarizes the $k^{Scherrer}$ values in the most common cases. L refers to a volume-weighted crystallite size. This differs from the mean crystallite size that can be measured from a cross-section[29, 13]. The correlation between volume- and area-weighted sizes depends on the crystallite shape and on the size distributions.

Taking the breadth as an incertitude on the angle θ and differentiating the Bragg equation (Equation 3.3 of Chapter 3), the Scherrer formula is written as

$$\beta_E = \frac{k^{Scherrer} \cdot hc}{2 \cdot L \cdot sin\theta} \tag{E.6}$$

in the energy-dispersive case, where β_E is an incertitude in the energy scale. Usually β_E is interpreted as the integral breadth[36, 42].

F. High temperature pressure gauge for rapid thermal chalcogenizations

A gauge for the measurement of the sulfur (or eventually selenium) pressure in the range from 10^{-2} to 10mbar inside an RTP reaction box was designed during this thesis. This design is the subject of a German patent (DE: 102008029028 B3). The pressure gauge fulfills the following requirements:

- Measurement range: from $\sim 10^{-2}$mbar to $\sim$10mbar;
- No condensation of sulfur (or selenium). This imposes a minimal temperature at the measuring gauge of 300°C if the maximal sulfur pressure is 50 mbar (500°C if the maximal Se pressure is 50mbar). This temperature corresponds to the temperature of the vapor pressure curves for the given maximal pressure;
- Acquisition and processing time are adequate for its application in rapid thermal processing;
- Uncoupled from the processing temperature.

A pressure gauge that fulfills these requirements did not exist. The design of such a high temperature pressure gauge was based on the decoupling of the measurement of the pressure and the process itself. The pressure measurement was realized in a measuring head that was shielded form the radiation of the lamps. This measuring head could be heated separately to the desired temperature T_g in function of the gas and maximal expected pressures. The measuring head was connected to the reaction box via a transfer channel that was heated to the same temperature T_g. During RTP sulfurizations, the S gas molecules build a pressure $p_{\Sigma Sx}$ in the reaction box. The number of molecules passing through the transfer channel to the measuring head depend on this pressure. The measuring head was designed to measure the number of the molecules. Via a calibration, the pressure $p_{\Sigma Sx}$ during processing can be recorded.

In the measuring head a sensor must be mounted. This can be of the capacitive type or, as realized in the prototype, of the resistive type (Pirani type). A heated W filament is the heart of the sensor. Its resistance changes as a function of the heat transfer from the filament to the walls of the measuring head. This is a function of the heat conductivity of the medium between both: the incoming process gas.

A first prototype of such a high temperature gauge was realized with the following characteristics:

- Measuring head temperature: 300°C;
- Sensor: 20 μm thick, 1 cm long W filament;
- Filament temperature in vacuum: 450°C;
- Wheatstone bridge based electronics;
- Transfer channel 8mm in diameter and 290mm long.

This prototype pressure gauge was compared to a full range pressure gauge from Balzers. Form this comparison a calibration curve for dry nitrogen was obtained. Figure F.2 shows this calibration.

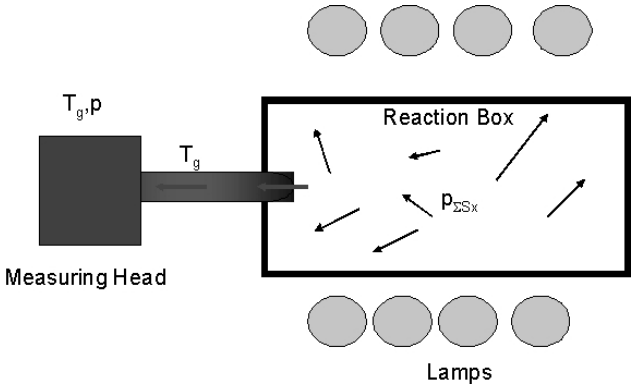

Figure F.1.: Representation of a pressure gauge for sulfurization (or selenization) processes in a closed volume. The measuring head is kept at a constant temperature T_g higher than the condensation temperature of the chalcogen at the maximal pressure and is decoupled from the processing temperature imposed by the lamps. The measuring head probes the gas in the reaction box.

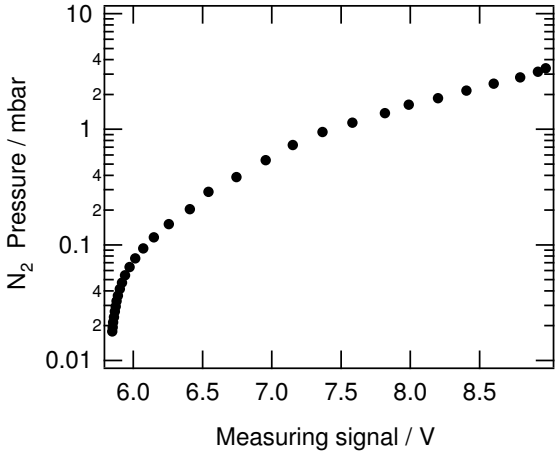

Figure F.2.: Calibration of the high temperature (300°C) Pirani-type gauge that was developed during this thesis. This gauge is capable of the pressure measurements in the range of $\sim 10^{-2}$ to 10mbar during rapid thermal sulfurizations.

The figure proofs that the protoype gauge is adequate to measure pressure in the 10^{-2} to 10mbar range. Furthermore it fulfills the requirements listed at the beginning of the appendix. Therefore, this prototype is suited to measure the pressure inside the reaction box during rapid thermal processes.

Bibliography

[1] D. Abou-Ras, R. Caballero, C. Kaufmann, M. Nichterwitz, K. Sakurai, S. Schorr, T. Unold, and H. W. Schock. Impact of the Ga concentration on the microstructure of $CuIn_{1-x}Ga_xSe_2$. *Physica Status Solidi (RRL)*, 2(3):135–137, 2008.

[2] D. Abou-Ras, S. Schorr, and H. W. Schock. Grain-size distributions and grain boundaries of chalcopyrite-type thin films. *Journal of Applied Crystallography*, 40:841–848, 2007.

[3] J. Alvarez Garcia. *Characterization of $CuInS_2$ films for solar cell applications by Raman spectroscopy*. PhD thesis, Universitat de Barcelona, 2002.

[4] J. Alvarez Garcia, B. Barcones, A. Romano-Rodriguez, L. Calvo-Barrio, A. Perez-Rodriguez, J. R. Morante, R. Scheer, and R. Klenk. Sulfurization of Cu/In precursors for $CuInS_2$-based solar cells. *Journal of the Electrochemical Society*, 150:G400, 2003.

[5] J. Alvarez Garcia, A. Perez-Rodriguez, A. Romano-Rodriguez, L. Calvo-Barrio, B. Barcones, J. R. Morante, K. Siemer, I. Luck, and R. Klenk. Microstructural characterization of $CuInS_2$ polycrystalline films sulfurised by rapid thermal processing. *Thin Solid Films*, 387:219–222, 2001.

[6] H. V. Atkinson. Theories of normal grain growth in pure single phase systems. *Acta Metallurgica*, 36(3):469–502, 1988.

[7] M. Avrami. Kinetics of phase change. I. General theory. *The Journal of Chemical Physics*, 7:1103, 1939.

[8] M. Avrami. Kinetics of phase change. II. Transformation time relations for random distribution of nuclei. *The Journal of Chemical Physics*, 8:212, 1940.

[9] B. Barcones, A. Perez-Rodriguez, L. Calvo-Barrio, A. Romano-Rodriguez, J. R. Morante, E. Rudigier, I. Luck, J. Djordjevic, and R. Scheer. In situ and ex situ characterization of thermally induced crystallization of $CuInS_2$ thin films for solar cells. *Thin Solid Films*, 480-481:362–366, 2005.

[10] I. Barin and O. Knacke. *Thermochemical properties of inorganic substances*. Springer-Verlag, Berlin, 1991.

[11] I. Bartkowicz and A. Stoklosa. Kinetics of copper sulfidation at temperatures 570-1123K. *Oxidation of Metals*, 25(5/6):305–311, 1985.

[12] J. J. M. Binsma, L. J. Giling, and J. Bloem. Phase relations in the system Cu_2S-In_2S_3. *Journal of Crystal Growth*, 50:429–437, 1980.

[13] M. Birkholz. *Thin film analysis by X-ray scattering*. Wiley-VCH Verlag Gmbh, 2006.

[14] I. V. Bodnar and N. S. Orlova. X-ray study of the thermal expansion in $CuAlS_2$, $CuGaS_2$, and $CuInS_2$ compounds over the temperature range from 90 to 650K. *Physica Status Solidi (a)*, 78(1), 1983.

[15] I. V. Bodnar and N. S. Orlova. X-ray study of the thermal expansion anisotropy in $AgGaS_2$ and $AgInS_2$ compounds over the temperature range from 80 to 650 K. *Physica Status Solidi (a)*, 91(2), 1985.

[16] I. V. Bodnar, L. V. Yasyukevich, B. V. Korzoun, and A. G. Karoza. The $Ag_xCu_{1-x}InS_2$ solid solutions with 0<x<1. *Journal of materials science*, 33:183–189, 1998.

[17] A. Bolcavage, S. W. Chen, C. R. Kao, Y. A. Chang, and A. Roming-Jr. Phase equilibria of the Cu-In system. I. experimental investigation. *Journal of Phase Equilibria*, 14(1):14–21, 1993.

[18] K. Bozhilov, V. Dimov, A. Panov, and H. Haefke. Thin film growth of silver sulphide. II. structure models of epitaxial contact layers. *Thin Solid Films*, 190(1):129–138, 1990.

[19] A. Brueckman. The mechanism of transport of matter through the scales during oxidation of metals and alloys. *Corrosion Science*, 7:51–60, 1967.

[20] S. Brunken, R. Mientus, S. Seeger, and K. Ellmer. The mechanism of nickel sulfide induced rapid crystallization of highly textured tungsten disulfide (WS_2) thin films: An in situ real-time diffraction study. *Journal of Applied Physics*, 103(063501), 2008.

[21] B. Buras and L. Gerward. Application of X-ray energy-dispersive diffraction for characterization of materials under high pressure. *Progress in Crystal Growth and Characterization*, 18:93–129, 1989.

[22] S. Cattarin, C. Pagura, L. Armelao, R. Bertocello, and N. Dietz. Surface characterization of $CuInS_2$ with lamellar morphology. *Journal of the Electrochemical Society*, 142(8):2818–2823, 1995.

[23] R. Chakrabarti and D. Laughlin. The Cu-S (copper-sulfur) system. *Bulletin of Alloy Phase Diagrams*, 4(3):254, 1983.

[24] R. Chakrabarti, A. B. Maity, R. Pal, D. Bhattacharyya, S. Chaudhuri, and A. K. Pal. Estimation of stress in polycrystalline $CuInSe_2$ films deposited on Mo-coated glass substrates. *Physica Status Solid*, 160:67–77, 1997.

[25] D. M. Chapin, C. S. Fuller, and G. L. Pearson. A new silicon p-n junction photocell for converting solar radiation into electrical power. *Journal of Applied Physics*, 25:676, 1954.

[26] A. W. Coats and J. P. Redfern. Kinetic paremeters form thermogravimetric data. *Nature*, 201:68–70, 1964.

[27] M. A. Contreras, B. Egaas, D. King, A. Swartzlander, and T. Dullweber. Texture manipulation of $CuInSe_2$ thin films. *Thin Solid Films*, 361-362:167–172, 2000.

[28] B. Cullity. *Elements of X-ray diffraction.* Adison-Wesley Publishing Company, 1978.

[29] R. Delhez, T. H. de Keijser, and E. J. Mittemeijer. Determination of crystallite size and lattice distortions through X-ray diffraction line profile analysis. *Fresenius Zeitschrift fuer Analytische Chemie*, 312:1–17, 1982.

[30] I. A. Denks and C. Genzel. Enhancement of energy dispersive residual stress analysis by consideration of detector electronic effects. *Nuclear Instruments and Methods in Physics Research B*, 262(1):87–94, 2007.

[31] D. Detry, J. Drowart, P. Goldfinger, H. Keller, and H. Rickert. Zur Thermodynamik von Schwefeldampf - Massenspektrometische Untersuchungen mit der Elektrochemischen KNUDSEN-zelle. *Zeitschrift fuer Physikalische Chemie*, 55:314–320, 1967.

[32] J. Djordjevic, E. Rudigier, and R. Scheer. Real-time studies of phase transformations in Cu-In-Se-S thin films. 3: Selenization of Cu-In precursors. *Journal of Crystal Growth*, 294:218–231, 2006.

[33] S. Djurle. An X-ray study on the system Ag-Cu-S. *Acta Chemica Scandinavica*, 12:1427–1436, 1958.

[34] S. Djurle. An X-ray study on the system Cu-S. *Acta Chemica Scandinavica*, 12:1415–1427, 1958.

[35] C. Dzionk, H. Metzner, S. Hessler, and H. Mahnke. Phase formation during the reactive annealing of Cu-In films in H_2S atmosphere. *Thin Solid Films*, 299:38–45, 1997.

[36] K. Ellmer, R. Mientus, V. Weiss, and H. Rossner. In situ energy-dispersive X-ray diffraction system for time-resolved thin-film growth studies. *Measurement Science and Technology*, 14:336–346, 2003.

[37] T. Enzenhofer. *Festkoerperreaktionen und Diffusionprozesse bei der schnellen Bildung Halbleiterschichten im System Cu-In-S*. PhD thesis, Technische Universitaet Berlin, 2006.

[38] G. Eriksson and K. Hack. ChemSage - a computer program for the calculation of complex chemical equilibria. *Metallurgical Transactions B*, 21B:1013–1024, 1990.

[39] P. Erslev, G. M. Hanket, W. N. Shafarman, and J. D. Cohen. Characterizing the effects of silver alloying in chalcopyrite CIGS solar cells with junction capacitance methods. *Proceedings of the Materials Research Society Spring Meeting 2009, Symposium M*, 1165-M01-07, 2009.

[40] S. Fiechter. Thermodynamic data base of the Cu-In-S-Ar system. *Personal communication*, 2007.

[41] C. Genzel, I. A. Denks, J. Gibmeier, M. Klaus, and G. Wagener. The materials science synchrotron beamline EDDI for energy-dispersive diffraction analysis. *Nuclear Instruments and Methods in Physics Research A*, 2007.

[42] L. Gerward, S. Morup, and H. Topsoe. Particle size and strain broadening in energy dispersive x-ray powder patterns. *Journal of Applied Physics*, 47(3):822–825, 1976.

[43] F. Gesmundo, Y. Niu, and F. Viani. Possible scaling modes in high-temperature oxidation of two-phase binary alloys. 2: Low oxidant pressures. *Oxidation of Metals*, 43:379–395, 1995.

[44] F. Gesmundo, F. Viani, and Y. Niu. The possible scaling modes in the high-temperature oxidation of two-phase binary alloys. 1: High oxidant pressures. *Oxidation of Metals*, 42:409–430, 1994.

[45] F. Gesmundo, F. Viani, and Y. Niu. The internal oxidation of two-phase binary alloys under low oxidant pressures. *Oxidation of Metals*, 45:51–77, 1996.

[46] N. A. Gorjunowa. *Halbleiter mit diamantaehnlicher Struktur*. BSB B. G. Teubner Verlagsgesellschaft, 1971.

[47] G. Gottstein. *Physikalische Grundlagen der Materialkunde*. Springer, Berlin, 2005.

[48] Q. Guo, G. M. Ford, H. W. Hillhouse, and R. Agrawal. Sulfide nanocrystal inks for dense $Cu(In_{1-x}Ga_x)(S_{1-y}Se_{\ y})_2$ absorber films and their photovoltaic performance. *Nano Letters*, pages 462–465, 2009.

[49] I. Hengel, A. Neisser, R. Klenk, and M. C. Lux-Steiner. Current transport in $CuInS_2$:Ga/CdS/ZnO solar cells. *Thin Solid Films*, 361:458–462, 2000.

[50] C. Herinckx, W. De Sutter, A. Fourdeux, and N. Terao. La recristallisation des films evapores de sulfure de cadmium dopes a l'argent. *Physica Status Solidi (a)*, 10:387–390, 1972.

[51] J. H. Hubbel and S. M. Seltzer. Tables of X-ray mass attenuation coefficients and mass energy-absorption coefficients, http://physics.nist.gov/physrefdata/xraymasscoef/cover.html, 2009.

[52] K. A. Jackson. *Kinetic Processes*. Wiley-VCH Verlag, Weinheim, 2004.

[53] P. Jackson, R. Wuerz, U. Rau, J. Mattheis, M. Kurth, T. Schloetzer, G. Bilger, and J. H. Werner. High quality baseline for high efficiency, $Cu(In_{1-x}Ga_x)Se_2$ solar cells. *Progress in Photovoltaics: Research and Applications*, 15:507–519, 2007.

[54] J. E. Jaffe and A. Zunger. Anion displacements and the band-gap anomaly in ternary ABC_2 chalcopyrite semiconductors. *Physical Review B*, 27(8):5176–5179, 1983.

[55] S. Jost, R. Schurr, A. Hoelzing, F. Hergert, R. Hock, M. Purwins, and J. Palm. The formation of the thin-film solar cell absorber $CuInS_2$ by annealing of Cu-In-S stacked elemental layer precursors - a comparison of selenization and sulfurization. *Thin Solid Films*, 517:2136–2139, 2009.

[56] W. Keppner, T. Klas, W. Koerner, R. Wesche, and G. Schatz. Formation at Cu-In thin-film interfaces detected by perturbed angular correlations. *Physical Review Letters*, 78(4):2392, 1985.

[57] H. J. Kim and C. V. Thompson. Compensation of grain growth enhancement in doped silicon films. *Applied Physics Letters*, 48:399–402, 1986.

[58] S. Kim, W. K. Kim, R. M. Kaczynski, R. D. Acher, S. Yoon, T. J. Anderson, O. D. Crisalle, E. A. Payzant, and S. S. Li. Reaction kinetics of $CuInSe_2$ thin films grown from bilayer InSe/CuSe precursors. *Journal of Vacuum Science and Technology A*, 23:210–216, 2005.

[59] W. K. Kim, S. Kim, E. A. Payzant, S. A. Speakman, S. Yoon, R. M. Kaczynski, R. D. Acher, T. J. Anderson, O. D. Crisalle, S. S. Li, and V. Craciun. Reaction kinetics of α-$CuInSe_2$ formation from In_2Se_3/CuSe bilayer precursor film. *Journal of Physics and Chemistry of Solids*, 66:1919–1924, 2005.

[60] W. K. Kim, E. A. Payzant, T. J. Anderson, and O. D. Crisalle. In situ investigation of the selenization kinetics of Cu-Ga precursors using time-resolved high-temperature X-ray diffraction. *Thin Solid Films*, 515:5837–5843, 2007.

[61] W. K. Kim, E. A. Payzant, S. Yoon, and T. J. Anderson. In situ investigation on the selenization kinetics of Cu-In precursor using time-resolved, high-temperature X-ray diffraction. *Journal of Crystal Growth*, 294:231–236, 2006.

[62] P. Kistaiah, Y. C. Venudhar, K. S. Murthy, L. Iyengar, and K. V. K. Rao. Anisotropic thermal expansion of copper gallium selenide. *Journal of Physics D: Applied Physics*, 14(3):457–461, 1981.

[63] P. Kistaiah, Y. C. Venudhar, K. S. Murthy, L. Iyengar, and K. V. K. Rao. Temperature dependence of tetragonal distortion and thermal expansion of copper indium selenide. *Journal of Physics D: Applied Physics*, 14(7):1311–1316, 1981.

[64] J. Klaer, J. Bruns, R. Henninger, M. Weber, K. Ellmer, R. Klenk, R. Scheer, and D. Braeunig. $CuInS_2$ solar cells from sputtered CuIn precursors reacted in sulphur vapour. *Proceedings of the 14th European Photovoltaic Solar Energy Conference, Barcelona*, page 4, 1997.

[65] M. Kleinfeld and H. D. Wiemhoefer. Chemical diffusion coefficients and stability of $CuInS_2$ and $CuInSe_2$ from polarization measurements with point electrodes. *Solid State Ionics*, 28-30:1111–1116, 1988.

[66] R. Klenk. Characterization and modeling of chalcopyrite solar cells. *Thin Solid Films*, 387:135–141, 2001.

[67] R. Klenk, J. Klaer, R. Scheer, M. C. Lux-Steiner, I. Luck, N. Meyer, and U. Ruehle. Solar cells based on $CuInS_2$ - an overview. *Thin Solid Films*, 480-481:509–515, 2005.

[68] R. Klenk, T. Walter, H. W. Schock, and D. Cahen. A model for the succesful growth of polycrystalline films of $CuInSe_2$ by multisource physical vacuum evaporation. *Advanced Materials*, 5(2):114–119, 1993.

[69] C. v. Klopman, J. Djordjevic, E. Rudigier, and R. Scheer. Real-time studies of phase transformations in Cu-In-S thin films. 2: Sulfurization of Cu-In precursors. *Journal of Crystal Growth*, 289:121–134, 2006.

[70] W. Kraus and G. Nolze. Powder cell-a program for the representation and manipulation of crystal structures and calculation of the resulting x-ray powder patterns. *Journal of Applied Crystallography*, 29(3):301–303, 1996.

[71] M. Krunks, V. Mikli, O. Bijakina, and E. Mellikov. Growth and recrystallization of $CuInS_2$ films in spray pyrolitic process. *Applied Surface Science*, 142:356–361, 1999.

[72] V. Kumar, G. M. Prasad, and D. Chandra. Bulk modulus of ternary chalcopyrite semiconductors. *Physica Status Solidi (b)*, 186:45–48, 1994.

[73] J. I. Langford and A. J. C. Wilson. Scherrer after sixty years: A survey and some new results in the determination of crystallite size. *Journal of Applied Crystallography*, 11:102–113, 1977.

[74] N. S. Lewis. Powering the planet. *MRS BULLETIN*, 32:808–820, 2007.

[75] D. C. Look and J. C. Manthurutil. Electron and hole conductivity in $CuInS_2$. *Journal of Physics and Chemistry of Solids*, 37:173–180, 1976.

[76] R. Mainz. *In-situ Analyse und Wachstum photovoltaischer Absorber mit Bandlueckengradienten*. PhD thesis, Freie Universitaet Berlin, 2008.

[77] R. Mainz, R. Klenk, and M. C. Lux-Steiner. Sulphurisation of gallium-containing thin-film precursors analysed in-situ. *Thin Solid Films*, 515:5934–5938, 2007.

[78] J. Major, Y. Proskuryakov, and K. Durose. Nucleation and gran boundaries in CdTe/CdS solar cells. *Materials Research Society Symposium M Proceedings*, 1165-M06-01, 2009.

[79] B. Mansour. Electrical and thermoelectric properties of In and Cd doped $Cu_{1.8}S$. *Physica Status Solidi (a)*, 136:153–159, 1993.

[80] H. Matsushita and T. Takizawa. Phase diagram of the CuIn-2Se system for $CuInSe_2$ crystal growth by controlling Se contents. *Journal of Crystal Growth*, 179:503–509, 1997.

[81] H. Mehrer. *Diffusion in Solids*. Springer, Berlin, 2007.

[82] N. Meyer, A. Meeder, and D. Schmid. Pilot production of large-area $CuInS_2$-based solar modules. *Thin solid films*, 515:5979–5984, 2007.

[83] H. Moeller. *Semiconductors for solar cells*. Artech House, Norwood, 1993.

[84] S. Mrowec. On the mechanism of high temperature oxidation of metals and alloys. *Corrosion Science*, 7:563–578, 1967.

[85] S. Mrowec. Sulphidation of alloys at high temperatures. *Materials Science*, 4:99–119, 1976.

[86] S. Mrowec. Mechanism of high-temperature sulphide corrosion of metals and alloys. *Werkstoffe und Korrosion*, 31:371–387, 1980.

[87] S. Mrowec and K. Przybylski. Transport properties of sulfide scales and sulfidation of metals and alloys. *Oxidation of Metals*, 23:107–140, 1985.

[88] K. Mueller, Y. Burkov, and D. Schmeisser. Spectromicroscopic characterisation of $CuInS_2$ surfaces. *Thin Solid Films*, 480-481:291–294, 2005.

[89] A. Neisser. *Gallium as an isovalent substitution in $CuInS_2$ absorber layers for photovoltaic applications*. PhD thesis, Freie Universitaet Berlin, 2001.

[90] H. Neumann, W. Hoerig, V. Savelev, J. Lagzdonis, B. Schumann, and G. Kuehn. The optical properties of $CuInS_2$ thin films. *Thin Solid Films*, 79(2):167–171, 1981.

[91] M. Nichterwitz, D. Abou-Ras, K. Sakurai, J. Bundesmann, T. Unold, R. Scheer, and H. Schock. Influence of grain boundaires on current collection in $Cu(In,Ga)Se_2$ thin-film solar cells. *Thin Solid Films*, 517:2554–2557, 2009.

[92] S. Nishiwaki, S. Siebentritt, M. Giersig, and M. C. Lux-Steiner. Growth model of $CuGaSe_2$ in a Cu-poor / Cu-rich bilayer process. *Journal of Applied Physics*, 94(10):6864–6881, 2003.

[93] F. Nix and D. MacNair. The thermal expansion of pure metals. 2: Molybdenum, palladium, silver, tantalum, tungsten, paltinum, and lead. *Physical Review*, 61:74–78, 1942.

[94] Okamoto. Indium-sulfur. *Binary alloy phase diagrams*, pages 2283–2285, 1983.

[95] V. K. Pareek, T. A. Ramanarayanan, S. Ling, and J. D. Mumford. Electrical conductivity of high digenite ($Cu_{2-x}S$) at controlled sulfur activities. *Solid State Ionics*, 74:263–269, 1994.

[96] D. Peng and J. Zhao. Representation of the vapour pressure of sulfur. *Journal of Chemical Thermodynamics*, 33:1121–1132, 2001.

[97] J. R. Petit, J. Jouzel, D. Raynaud, N. I. Barkov, J. M. Barnola, I. Basile, M. Bender, J. Chappellaz, M. Davis, and G. Delaygue. Climate and atmospheric history of the past 420 000 years from the Vostok ice core, Antarctica. *Nature*, 399(6735):429–436, 1999.

[98] C. Pietzker. *In-situ Wachstumsuntersuchungen beim reaktiven Anlassen von Cu, In Schichten in elementarem Schwefel*. PhD thesis, Universitaet Potsdam, 2003.

[99] P. Pistor, N. Allsop, R. Caballero, C. Camus, C.-H. Fischer, M. Gorgoi, A. Grimm, B. Johnson, T. Kropp, I. Lauermann, S. Lehmann, H. Moenig, S. Schorr, A. Weber, and R. Klenk. Cu in In_2S_3: interdiffusion phenomena anlysed by high kinetic X-ray photoelectron spectroscopy. *Physica Status Solidi (a)*, 206(5):1059–1062, 2009.

[100] H. Rau. Defect equilibria in cubic high temperature copper sulfide (digenite). *Journal of Physics and Chemistry of Solids*, 28:903–917, 1967.

[101] H. Rickert. Thermodynamische und kinetische Untersuchungen an Systemen Festkoerper/Gas insbesondere mit elektrochemischen Methoden. *Werkstoffe und Korrosion*, 10:869–884, 1968.

[102] H. Rodriguez-Alvarez, I. M. Koetschau, and H. W. Schock. Pressure-dependent real-time investigations on the rapid thermal sulfurization of Cu-In thin films. *Journal of Crystal Growth*, 310(15):3638–3644, 2008.

[103] E. Rudigier. *Phase transformations and crystalline quality in $CuInS_2$ thin films*. PhD thesis, Phillips-Universitaet Marburg, 2004.

[104] E. Rudigier, B. Barcones, I. Luck, T. Jawhari-Colin, A. Perez-Rodriguez, and R. Scheer. Quasi real-time Raman studies on the growth of Cu-In-S thin films. *Journal of Applied Physics*, 95:5153–5159, 2004.

[105] R. Scheer. *Korrelation von Struktur und elektronischen Eigenschaften mehrphasiger Cu-In-S Schichten fuer die Photovoltaik*. PhD thesis, Technishe Universitaet Berlin, 1993.

[106] R. Scheer, K. Diesner, and H. J. Lewerenz. Experiments on the microstructure of evaporated $CuInS_2$ thin films. *Thin Solid Films*, 268:130–137, 1995.

[107] R. Scheer and H. J. Lewerenz. Photoemission study of evaporated $CuInS_2$ thin films. I. surface stoichiometry and phase segregation. *Journal of Vacuum Science and Technology A*, 12:51–56, 1994.

[108] R. Scheer, I. Luck, H. Sehnert, and H. J. Lewerenz. Scavenging of excess Cu atoms in $CuInS_2$ films by sulphur annealing. *Solar Energy Materials and Solar Cells*, 41/42:261–271, 1996.

[109] H. Schmalzried. *Festkoerperreaktionen. Chemie des festen Zustandes*. Verlag Chemie, Weinheim, 1971.

[110] H. Schmalzried. *Chemical kinetics of solids*, volume 1. VCH Verlaggesellscaft mBH, Weinheim, 1995.

[111] H. W. Schock. Thin film photovoltaics. *Applied Surface Science*, 92:606–616, 1996.

[112] J. Schoeldstroem, J. Kessler, and M. Edoff. Two-stage growth of smooth $Cu(In,Ga)Se_2$ films using end-point detection. *Thin Solid Films*, 480:61–66, 2005.

[113] S. Schorr. X-ray and neutron scattering Rietveld refinement results. *Personal Communication*, 2009.

[114] S. Schorr and G. Geandier. In-situ investigation of the temperature dependent structural phase transition in $CuInSe_2$ by synchrotron radiation. *Crystal Research and Technology*, 41(5), 2006.

[115] S. Schorr, M. Tovar, H.-J. Hoebler, and H. W. Schock. Structure and phase relations in the $2(CuInS_2)$-Cu_2ZnSnS_4 solid solution system. *Thin Solid Films*, 517:2508–2510, 2009.

[116] M. Schuetze. *Corrosion and enviromental degradation*, volume 1. Wiley-VCH Verlag, Weinheim, 2000.

[117] R. C. Sharma and Y. A. Chang. The Ag-S (silver-sulfur) system. *Bulletin of Alloy Phase Diagrams*, 7(3):263, 1986.

[118] K. Sickafus and J. Wills. Structure of spinel. *Journal of the American Ceramic Society*, 82(12):3279–3292, 1999.

[119] S. Siebentritt. Wide gap chalcopyrites: material properties and solar cells. *Thin Solid Films*, 403-404:1–9, 2002.

[120] K. Siemer, J. Klaer, I. Luck, J. Bruns, R. Klenk, and D. Braeunig. Efficient $CuInS_2$ solar cells from a rapid thermal process (RTP). *Solar Energy Materials and Solar Cells*, 67:159–167, 2001.

[121] D. Smith. *Thin-Film Deposition*. Mc-Graw-Hill Inc, 1995.

[122] S. A. Somadossi. *Investigation on diffusion soldering in Cu/In/Cu and Cu/In-48Sn/Cu systems*. PhD thesis, Universitaet Stuttgart, 2002.

[123] H. Spiess, U. Haeberlen, G. Brandt, A. Raueber, and J. Schneider. Nuclear magnetic resonance in IB-III-VI_2 semiconductors. *physica status solidi (b)*, 62(1):183–192, 1974.

[124] M. E. Straumanis and L. S. Yu. Lattice parameters, densities, expansion coefficients and perfection of structure of Cu and of Cu-In phases. *Acta Crystallographica Section A: Crystal Physics, Diffraction, Theoretical and General Crystallography*, 25(6):676–682, 1969.

[125] K. Taretto and U. Rau. Numerical simulation of carrier collection and recombination at grain boundaries in Cu(In,Ga)Se_2 solar cells. *Journal of Applied Physics*, 103:094523, 2008.

[126] B. Tell, J. L. Shay, and H. M. Kasper. Electrical properties, optical properties and band structure of $CuGaS_2$ and $CuInS_2$. *Physical review B*, 4(8):2463–2471, 1971.

[127] B. Tell, J. L. Shay, and H. M. Kasper. Room-temperature electrical properties of ten I-III-VI_2 semiconductors. *Journal of Applied Physics*, 43(5):2469–2470, 1972.

[128] C. V. Thompson. Secondary grain growth in thin films of semiconductors: Theoretical aspects. *Journal of Applied Physics*, 58:763–773, 1985.

[129] C. V. Thompson. Grain growth in thin films. *Annual Review of Materials Research*, 20:245–269, 1990.

[130] T. Tinoco, A. Polian, D. Gomez, and J. P. Itie. Structural studies of $CuInS_2$ and $CuInSe_2$ under high pressure. *Physica Status Solidi (b)*, 198:433–438, 1996.

[131] R. Triboulet. Solid state recrystallization: a promising technique for the growth of semiconductor materials. *Crystal Research and Technology*, 38(3-5):215–224, 2003.

[132] T. Ungar. Microstructural parameters from X-ray diffraction peak broadening. *Scripta Materialia*, 51:777–781, 2004.

[133] A. Vecht. Recrystallization in thin films of zinc sulphide. *Journal of vacuum Science and Technology*, 6(4):773–777, 1969.

[134] E. Villora. *Charakterisierung und Optimierung der Mikrostruktur von $CuInS_2$-Duennschichten*. Undergraduate Thesis, Technische Universitaet Berlin, Berlin, 1998.

[135] O. Volobujeva, J. Kois, R. Traksmaa, K. Muska, S. Bereznev, M. Grossberg, and E. Mellikov. Influence of annealing conditions on the structural quality of $CuInSe_2$ films. *Thin Solid Films*, 516:7105–7109, 2008.

[136] T. Wada, N. Kohara, T. Negami, and M. Nishitani. Growth of $CuInSe_2$ crystals in Cu-rich Cu-In-Se thin films. *Journal of Materials Research*, 12(6):1456, 1997.

[137] C. Wagner. Theoretical analysis of the diffusion processes determining the oxidation rate of alloys. *Journal of the Electrochemical Society*, 99:369–381, 1952.

[138] C. Wagner. Oxidation of alloys involving noble metals. *Journal of the Electrochemical Society*, 103:571–581, 1956.

[139] T. Walter, D. Braunger, H. Dittrich, C. Koeble, R. Herberholz, and H. W. Schock. Sequential processes for the deposition of polycrystalline Cu(In,Ga)$(S,Se)_2$ thin films: Growth mechanism and devices. *Solar Energy Materials and Solar Cells*, 41/42:355–373, 1996.

[140] B. E. Warren. *X-ray diffraction*. Dover Publications Inc., New York, 1990.

[141] M. Weber, R. Scheer, H. J. Lewerenz, H. Jungblut, and U. Stoerkel. Microroughness and composition of cyanide-treated $CuInS_2$. *Journal of the Electrochemical Society*, 149:G77–G84, 2002.

[142] A. Werner, I. Luck, J. Bruns, J. Klaer, K. Siemer, and D. Braeunig. Investigation of the influence of silver on the crystal growth of $CuInS_2$ thin films. *Thin Solid Films*, 361-362:88–93, 2000.

[143] S. Wissmann and K. D. Becker. Tracer diffusion of indium in $CuInS_2$. *Solid State Ionics*, 101-103:539–545, 1997.

[144] P. Wuerfel. *Physik der Solarzellen*. Spektrum, Heidelberg, 2000.

[145] B. R. York. New X-ray diffraction line profile function based on crystallite size and strain distributions determined from mean field theory and statistical mechanics. *Advances in X-ray Analysis*, 41:544–554, 1997.

Publications

Parts of this work have already been published

- Rodriguez-Alvarez H., Koetschau I. M., Schock, H. W.. Pressure-dependent real-time investigations on the rapid thermal sulfurization of Cu-In thin films. *Journal of Crystal Growth.* 310(15):3638-3644, 2008.
- Rodriguez-Alvarez H., Koetschau I. M., Genzel Ch., Schock, H. W.. Growth paths for the sulfurization of Cu-rich Cu/In thin films. *Thin Solid Films.* 517(7):2140-2144 , 2009.
- Rodriguez-Alvarez H., Mainz R., Marsen B., A.Weber, Schock, H. W.. Copper sulfide assisted recrystallization of Cu-poor $CuInS_2$ observed in situ by polychromatic X-ray diffraction. *Proceedings of the Materials Research Society Spring Meeting 2009.* ID 1165-M02-07.
- Koetschau I.M., Rodriguez-Alvarez H., Streeck C., A.Weber, Klaus M., Denks I.A., Gibmeier J., Genzel C., Schock, H. W.. Pressure dependent rapid thermal processing of $CuInS_2$ thin films investigated by in situ energy dispersive X-ray diffraction. *Proceedings of the Materials Research Society Spring Meeting 2007.* ID 1012-Y13-09.

Acknowledgements

An dieser Stelle möchte ich mich bei Herrn Prof. Dr. Schock für das Vertrauen bedanken, das er bei mir gelegt hat. Für seine Betreuung, für sein kontinuierliches Interesse und für die wertvollen Diskussionen bedanke ich mich ebenso.

Bei Herrn Prof. Dr. W. Reimers bedanke ich mich ganz herzlich für die Übernahme des Gutachtens und das Interesse an dieser Arbeit.

Ich danke die Firma SULFURCELL Solartechnik GmbH, die diese Arbeit finanziell unterstützt hat.

Dankbar bin ich auch allen Mitarbeitern der Abteilung Technologie des Helmholtz-Zentrums Berlin für die sehr gute Arbeitsatmosphäre. Insbesondere danke ich J. Klaer und die ganze Baseline-gruppe für die Herstellung von zahlreichen Dünnschichten und Solarzellen, Dr. B. Marsen und L. Steinkopf für die aufgedampften Schichten, und D. Abou-Ras für mehreren EBSD- und REM-Aufnahmen. Insbesondere danke ich Ing. J. Lauche für die immer freundliche und sehr kompetente technische Unterstützung. Dr. I. Kötschau danke ich für die Einführung in der Vakuumtechnik und Herstellung von Dünnschichten.

Prof. Dr. Ch. Genzel, Dr. M. Klaus, Dr. I. Denks und die BESSY-Gruppe danke ich für die Betreuung während der Strahlzeiten an der EDDI-Beamline.

An meinen Kollegen und Freunden A.Weber, S. Brunken und Dr. S. Gledhill auch ein herzliches Dank für die unzählbaren Diskussionen, Korrekturen, und Überstetzungen dieser Arbeit. Dr. R. Mainz danke ich herzlich für eine sehr angenehme Zusammenarbeit, die kritische Korrektur dieser Arbeit und für seine wissenschaftlichen Vorschläge.

A Rosita, Humberto, Pilar y Ximena les agradezco su apoyo incondicional y constante motivación.

Mi agradecimiento mas grande va para Francesca no solo por corregir esta tesis pero por darme la fuerza necesaria para llevar acabo este proyecto.